Universiteit Antwerpen

Faculteit Wetenschappen
Departement Chemie

Generation, transport and molecular interactions of reactive species in plasma medicine

Proefschrift voorgelegd tot het behalen
van de graad doctor in de wetenschappen: chemie
aan de Universiteit Antwerpen
te verdedigen door

Jonas Van der Paal

Promotor: prof. dr. Annemie Bogaerts
Co-promotor: prof. dr. Erik Neyts

Contents

Acknowledgements

Obtaining this PhD marks the end of a four-year ride. Although seemingly not that long, it does feel like it has been a crazy journey. During this period, I learned a lot, not only scientifically but also personally. Obviously, there are numerous people I need to thank for making this possible, so here we go!

First and foremost, the two people who by far have had the most impact on my PhD. Annemie and Erik, I can't thank you enough for this amazing chance you have provided me. You always gave me the freedom to pursue my own research, to focus on what I was most interested in, yet whenever I hit a wall, you were there to support me, to provide feedback and to encourage me to keep on going. Although I look forward to the next step in my young 'career', it does feel like leaving what has become a second home to me throughout these past years, which is in big part thanks to you.

Next, I want to thank my fellow PLASMANT members. All of you make PLASMANT an awesome place to work in. Special thanks goes out to the residents of B2.28, Kristof, Stijn and Yannick. Although others might not survive in here, I couldn't have wished for any other colleagues/friends to have spent the past four years with.

I also want to thank the people from UniSA, with whom I had the pleasure to work with during my research stay in Adelaide. Endre, Sunny and Nishta, thank you so much for teaching me all about the vesicle work, but also for making Maksud and me feel so welcome with you. You made my time in Adelaide one of the best experiences I've had so far. I truly enjoyed my time with you guys.

Next, my former classmates of 6 WeWiB. Now, almost 10 years after graduation, you guys really feel like a second family. I hope we can continue our skiing tradition, and hopefully launch a second one with the Ardennes-weekend. Special thanks to Matthias and Charlotte for being my babysit when Linsey was working late.

Of course, I also can't go past my former Chemistry classmates: Nick, Liesbeth T, Yannick, Michael, Sarah, Liesbeth S and Filip, who have given me so many great nights, weekends and holidays in the past years.

My time as a PhD student also went hand-in-hand with my time as the coach of the ladies team of SK Nieuw Stabroek. This has been a crazy ride, but I am truly grateful for this experience. Next to some amazing nights and weekends together, I learned so much from this time with you girls. Special thanks also to Bert, for starting this journey together with me.

Last, my family, as well as my family in law. My parents, for providing a safe haven I could always return to. You have always put us first, no matter what. This always seemed evident, and although I didn't realize it at that time, I do see it now, and I can't thank you enough for this. My sisters, for being sisters. Fighting when we were younger but now we're all moved out, actually growing closer together. My family in law, for being the best family in law one could ever wish for. From day one you have welcomed me in your home and treated me like your own child.

Last of all, Linsey. Words can't express how much you mean to me, and how important you have been to me in these past 10 years. Your support and unconditional love means the world to me!

Summary

In the last decades, the field of plasma medicine, in which cold atmospheric pressure plasmas (CAPs) are used for medical applications, has grown significantly. The applications investigated in this field cover many topics, including, *e.g.*, wound decontamination, transdermal drug and anti-cancer treatment. Although very promising results are being obtained from *in vitro* to *in vivo* studies, and even some first clinical trials, the need for more fundamental insight in the underlying mechanisms remains at large. In general, three groups of questions can be identified:

1. Which components (*e.g.* reactive species or electric fields) are generated during treatment and which survive the transport to the substrate of interest?
2. How do these components interact or react with molecules present in the biological substrate (*e.g.*, lipids, proteins, DNA or elements of the extracellular matrix)?
3. What are the effects of these modifications in the substrate on the short and longer timescale?

In the first part of this thesis, we have focused on the first class of research questions (cf. Chapter 3 and 4). Indeed, in these chapters, the development of chemical kinetics models for the kINPen IND and COST-jet is discussed, two CAP sources that are often used in the field of plasma medicine. These models are used to investigate both (i) the plasma chemistry, (ii) the transport of reactive species to a liquid substrate, as well as (iii) the chemistry occurring in the liquid substrate. Obtaining knowledge into the chemistry occurring in this source, under different operating conditions, is very important, as depending on the source or conditions used, very different biological outcomes can be obtained. Once such models are developed and validated, we can use them to obtain detailed knowledge into the reactions/species leading to the generation of important, biomedical active reactive oxygen and nitrogen species (RONS), but we can also try to use the model to predict optimal conditions to achieve a

desired chemical cocktail of RONS. In Chapter 3, different operating conditions of the kINPen IND were investigated, to study the effect of (i) the flow rate, (ii) the treatment gap distance and (iii) the treatment time, on the generation of RONS and the treatment of different cancer cell lines. By comparing between different conditions, we showed that the H_2O_2 concentration is mostly determined by the time needed for $^{\bullet}OH$ to reach the liquid (increases when decreasing the gap or increasing flow rate). Indeed, the transportation time from jet to substrate determines the fraction of $^{\bullet}OH$ that will recombine into H_2O_2 (at high $^{\bullet}OH_{liquid}$ concentrations) and what fraction will be consumed by N-species, forming HNO_2-HNO_3. For the NO_2^- concentration, on the other hand, our model predicts that (i) by increasing the flow rate, fewer ambient air species are able to diffuse into the effluent, thereby lowering the NO_2^- concentration, and (ii) by increasing the gap, more O_3 will be generated, which will consume NO_2^-, hence again lowering the NO_2^- concentration. Increasing the plasma treatment time yields a more or less linear increase in both the NO_2^- and H_2O_2 concentrations in pPBS, and in the percentage cell cytotoxicity.

Furthermore, by also treating different cancer cell lines after the creation of plasma-treated liquid (PTL), our experiments (performed by Wilma Van Boxem) revealed that H_2O_2 is a major contributor to cancer cell cytotoxicity, while NO_2^- plays a minor role, but other reactive species should also play a role in the anti-cancer activity of pPBS, as a liquid containing solely these stable species does not have the same effect as PTL.

The validation of the model by liquid measurements of H_2O_2 and NO_2^-, two of the most relevant RONS, showed that although the general trends of the experimental results could be captured in the chemical kinetics models, for certain treatment conditions, the overlap was not entirely satisfactory. Therefore, in Chapter 4 we discuss the development of an improved version of this chemical kinetics model. In contrast with the model discussed in Chapter 3, the liquid is now divided into two regions, *i.e.*, the interface and the bulk liquid. This is a very important step, as the chemistry in these two regions can be completely different (dominated by short- or long-lived RONS,

respectively). Furthermore, we also discuss the development of a gas phase kinetic model for the COST-jet, which is validated by measurements of short- and long-lived RONS trapped in a liquid substrate. After validating both the gas and liquid phase model by comparing the obtained densities with experimental measurements, we were able to use these models to investigate the chemistry occurring in both phases in detail. By combining these experimental (performed by Yury Gorbanev) and modelling approaches, we were able to investigate (i) a new reaction of Cl^- with atomic oxygen, yielding ClO^-, as well as (ii) the high dependence of ClO^- stability in PTM on other CAP-generated RONS. Furthermore, we showed that the concentration of H_2O_2 increased when increasing the feed gas humidity due to an increase of the $^{\bullet}OH$-density inside the source, whereas the HNO_2/NO_2^- concentration remained constant as $^{\bullet}OH$ is involved in both source and loss terms of these species.

The following chapters of this thesis combine research questions 2 and 3, mentioned above. Indeed, although we did not perform reactive MD simulations, we did study how elements present in CAPs interact with biomolecules (lipids) present in cells. Furthermore, we also used the knowledge existing in literature on how RONS react with lipids (induction of lipid peroxidation) to study the longer-term effects of these oxidized lipids in membranes.

More specifically, in Chapter 5, we applied united-atom molecular dynamics (MD) simulations to study how the cholesterol fraction in cell membranes affects the permeation of important ROS (including $^{\bullet}OH$, $^{\bullet}OOH$, H_2O_2 and O_2) present in CAPs. This was investigated as literature shows that cancer cells possess lower amount of cholesterol in their cell membrane, in comparison to their healthy counterpart. The results illustrated that, depending on the specific species, cholesterol is able to affect multiple aspects of the FEP, including (i) the height and (ii) width of the barrier, and (iii) the overall shape of the FEP (including the shape at the head group region, at the centre of the membrane and at the sterol rings). Although all FEPs indicate that cholesterol definitely has an influence on the penetration of certain ROS,

even for systems without cholesterol, the free energy barriers are still significantly high for species to impede travelling through the membrane, hence the permeation barrier role of each membrane. This led to the conclusion that additional elements should be in play to explain the observed selectivity in CAP treatment of cancer cells over healthy cells, which could be an increased expression of aquaporines in cancerous membranes, or the generation of nanopores due to lipid oxidation (as we have shown previously[1]). In conclusion, these results aided in the search of a possible explanation as to why cancer cells, containing lower amounts of cholesterol, would absorb RONS faster compared to their healthy counterparts (containing higher levels of cholesterol), which is assumed to be one of the primary reasons behind the experimentally observed selectivity of CAP cancer treatment[2–4], although this selectivity might be dependent on the type of cancer cell line, as other researchers report contradictory results.[5–7]

In Chapter 6, in collaboration with Maksudbek Yusupov, we investigated yet another element present in certain CAP sources, which is the generation of an electric field over the treated substrate. More specifically, united-atom MD simulations were performed to obtain a better insight in the synergistic effect of an electric field in combination with lipid oxidation on the formation of pores in a phospholipid bilayer (PLB). First, the translocation of ROS through native and oxidized PLBs was investigated in the absence of an electric field. It was found that oxidation of the PLs leads to an overall decrease of the permeation free energy barriers of the ROS, especially in the case of aldehyde oxidation. This is due to the increasing fluidity of the PLB, thereby increasing the permeability of the bilayer to ROS. However, the energy barriers are still relatively high, and thus the ROS will still not be able to easily travel through the oxidized PLB. However, when applying an electric field, the formation of pores occurs, which is a process called electroporation. Our calculations reveal that a stronger electric field yields a shorter time required to induce pore formation in the simulations. Moreover, oxidation of lipid tails leads to a drop in the average time needed to initiate electroporation, as well as a lower threshold electric field needed for pore formation to occur within the

timescale of the simulation. This effect was most apparent for aldehyde oxidation, while it was rather minor for peroxidation of the PLB. The latter may be explained by the higher permeation free energy barrier of water through a peroxidized PLB, as the pore formation process is initiated by the creation of water defects.

Whereas in Chapters 5 and 6, the main focus was on the use of CAPs as an anti-cancer therapy, in Chapter 7 we tried to obtain deeper insight in the processes occurring when CAPs interact with skin lipids, for the use in transdermal drug delivery (TDD) systems. TDD possesses many advantages over other drug administration methods, including, *e.g.*, avoiding the first-pass effect of the liver, reducing side effects and the ease of application of the drug. Enhancers are nowadays used to be able to enhance the drug uptake rate, or to be able to use TDD for, *e.g.*, bigger drug molecules. Recently, CAP has been demonstrated to enhance the transdermal uptake of drugs in a very gentle way, *i.e.*, while avoiding side effects such as deeper tissue damage. In this research, we performed coarse-grained MD simulations in search of the mechanism behind CAP-enhanced TDD. The hypothesis put forward is that lipid tail oxidation, induced by plasma-generated ROS, leads to the formation of cross-linkages between neighboring ceramides. This, in turn, leads to the generation of nanopores, which facilitate the diffusion of drug molecules through skin tissue, as observed experimentally. Our MD simulations reveal that cross-linking of the ceramides indeed induces the creation of voids in the SC structure, which can facilitate the diffusion of drugs. Furthermore, our results predict that there will be an optimal treatment time to achieve maximum enhancement of the SC permeability, which, experimentally, will depend on the exact composition of the SC, as well as on the plasma source used. Overall, our results indicate that the induction of ceramide cross-linking can be an explanation for the experimentally observed ability of CAP to enhance transdermal drug delivery.

The final chapter of this thesis (Chapter 8) distinguishes itself from the other chapters regarding the methodology used, as in this research we mainly focussed on experimental techniques. More specifically, we combined lipid

vesicle experiments with MD simulations to study the effect of variable membrane lipid composition on the ability of plasma-generated ROS to diffuse through these membranes. However, although the methodology is different, these results are valuable for other investigations presented in this thesis (or performed earlier), as they allowed us to test some of the hypotheses put forward regarding the selectivity of CAP treatment towards cancer cells in a very controlled environment. Indeed, by applying lipid vesicle experiments we could tune the saturation degree of the lipid tails, the cholesterol content of the membrane, and the type of lipid head group (*i.e.*, PE vs. PC head group), without having to deal with other variations present between real cell lines. These characteristics were selected because different cell types, including healthy and cancerous human cells, also show variations in these types of lipid characteristics.

The results presented in Chapter 8 clearly indicate that potential cellular effects from application of oxidative stress strongly depend on the cell membrane lipid composition. Broad-range ROS measurements showed that the vulnerability of vesicles towards ROS ingress strongly depends on the membrane lipid composition, but also that the addition of certain elements (cholesterol or PE-lipids) can have opposite effects depending on the main lipid type of the membrane. To determine the possible underlying mechanisms causing these observations, Maksudbek Yusupov performed MD simulations. The latter showed that multiple effects play a role, including (i) lipid oxidation of unsaturated phospholipids and cholesterol, (ii) lipid packing due to the head group volume, and (iii) formation of lipid rafts due to strong interactions between lipids of the same type.

Furthermore, we assessed the ability of plasma to induce DNA strand breaks within vesicles encapsulating a MB. This led to the surprising observations that the vulnerability towards ROS ingress does not necessarily links with the susceptibility towards DNA damage. This could be explained by the fact that the double bonds present in DOPC serve as scavenging sites for short-lived ROS, thereby preventing them from entering the vesicle interior. On the other hand, due to the reaction of the double bonds with these

short-lived species, the polarity of the bilayer interior increases, facilitating the overall permeation of other impinging ROS. In DPPC vesicles, no reactive sites are present, which allows short-lived ROS to diffuse through the membrane. Once they reach the vesicle interior, these species are very efficient in inducing DNA strand breaks. However, without lipid oxidation occurring, the membrane's hydrophobic environment is sustained, thereby hindering the overall ingress of impinging larger and more stable ROS (e.g., H_2O_2).

Taken together, this thesis provides insight in the generation mechanisms of RONS in different sources often used in the field of plasma medicine. Furthermore, multiple hypotheses have been put forward on how these species interact with biomolecules present in substrates of interest in the use of CAPs as an anti-cancer therapy, as well as in the enhancement of transdermal drug delivery, which can be used as possible explanations for experimental observations.

Samenvatting

Gedurende de afgelopen decennia is plasma-geneeskunde, een onderzoeksveld waarin koude atmosferische-druk plasma's (CAPs) gebruikt worden voor medische toepassingen, sterk gegroeid. De toepassingen waar momenteel onderzoek naar wordt gedaan zijn zeer uitgebreid, waaronder bijvoorbeeld het gebruik van CAPs in de decontaminatie van wonden, het bevorderen van de transdermale toediening van geneesmiddelen of het gebruik van CAPs als methode om kankercellen te bestrijden. In elk van deze toepassingsgebieden worden zeer veelbelovende resultaten behaald, gaande van in vitro tot in vivo studies, en zelfs de eerste klinische testen. De vraag naar meer fundamenteel onderzoek naar de onderliggende processen blijft echter groot. In het algemeen kunnen drie onderzoeksvragen vooropgesteld worden in het onderzoek naar het gebruik van CAPs voor medische doeleinden:

1. Welke componenten (reactive deeltjes of elektrische velden, bijvoorbeeld) worden gegenereerd in verschillende plasmabronnen, en welke zijn ook in staat om het te behandelen substraat (celmedium of cellen/weefsels, bijvoorbeeld) te bereiken?
2. Hoe interageren of reageren deze componenten met de biomoleculen aanwezig in deze substraten? Dit kunnen bijvoorbeeld lipiden, proteïnen, DNA of elementen uit de extracellulaire matrix zijn.
3. Welke effecten hebben deze modificaties in het substraat op de korte en lange termijn?

In het eerste deel van deze thesis wordt er gefocust op de eerste klasse van hierboven genoemde vraagstukken (cfr. Hoofdstuk 3 en 4). In deze hoofdstukken wordt de ontwikkeling van *chemisch kinetische modellen* besproken voor de kINPen IND en COST-jet, twee plasmabron die vaak gebruikt worden voor medische toepassingen. Dergelijk modellen worden gebruikt om zowel (i) de chemie in het plasma, (ii) het transport van de

gevormde reactieve deeltjes naar een vloeistofsubstraat, als (iii) de vloeisstoffase chemie in het te behandelen substraat te onderzoeken. Het ontwikkelen van dergelijke kennis omtrent de chemie die optreedt onder verschillende behandelcondities is zeer belangrijk, omdat, afhankelijk van de bron of behandelcondities die gebruikt worden, zeer uiteenlopende biologische resultaten bekomen worden. Eens dergelijke modellen ontwikkeld en gevalideerd zijn, kunnen we deze aldus gebruiken om een gedetailleerd inzicht te krijgen in de belangrijkste vormingsprocessen van bepaalde belangrijke reactieve deeltjes, en kunnen we trachten om optimale werkingscondities te bepalen om een gewenste samenstelling van reactieve deeltjes te verkrijgen.

In Hoofdstuk 3, verschillende behandelingscondities werden onderzocht om het effect na te gaan van (i) de gasstroomsnelheid, (ii) de afstand tot het substraat en (iii) de behandeltijd om de vorming van reactieve deeltjes en de behandeling van verschillende kankercellijnen. Dit toonde aan dat de H_2O_2 concentratie in het substraat voornamelijk afhankelijk is van de tijd die plasma-gegenereerde $^{\bullet}OH$-radicalen nodig hebben om het substraat te bereiken. Deze H_2O_2 concentratie neemt namelijk toe wanneer de afstand tot het substraat afneemt, of wanneer de gasstroomsnelheid toeneemt. Dit kan verklaard worden doordat $^{\bullet}OH$-radicalen tijdens transport naar het substraat voornamelijk zullen recombineren met stikstof(N)-deeltjes, waarbij HNO_2 of HNO_3 uiteindelijk gevormd wordt. Echter, in het geval van NO_2^- voorspelt het model dat de concentratie in het substraat zal afnemen, zowel wanneer (i) de gasstroomsnelheid verhoogt, als wanneer (ii) de afstand tot het substraat toeneemt. In het eerste geval komt dit doordat minder omgevingslucht (rijk aan N_2) in de plasmapluim kan diffunderen, in het tweede geval doordat er meer ozon (O_3) gevormd zal worden, wat zal wegreageren met NO_2^-. Het verhogen van de behandeltijd zorgt voor een quasi lineaire toename van de concetratie van zowel H_2O_2 als NO_2^-, en tevens voor een quasi lineaire toename van de celtoxiciteit.

In het laatste deel van dit onderzoek werd gekeken naar de celtoxiciteit voor de verschillende condities (experimenten uitgevoerd door Wilma Van

Boxem). Door te vergelijken met de vloeisstoffase metingen van de twee belangrijkste reactieve deeltjes volgde hieruit dat H_2O_2 de grootste bijdrage heeft in het bepalen van de celtoxiciteit. De bijdrage van NO_2^- is veel kleiner, hoewel er ook dient benadrukt te worden dat andere deeltjes ook wel degelijk een bijdrage hebben. Dit werd duidelijk doordat een vloeistof die enkel H_2O_2 en NO_2^- bevatte niet hetzelfde effect had als de met plasma behandelde vloeistoffen.

De validatie van het model, aan de hand van een vergelijking met experimentele metingen van de H_2O_2 en NO_2^- concentratie in de behandelde vloeistof, toonde aan dat, hoewel de algemene trends van de experimentele metingen ook bekomen werden in de simulaties, voor bepaalde condities de overlap niet optimaal was. Om deze reden hebben we in Hoofdstuk 4 de ontwikkeling van een verbeterd model besproken. Ten opzichte van het model uit Hoofdstuk 3 wordt in deze nieuwe versie de vloeistoffase opgesplitst in twee aparte regio's, namelijk de *interface* en de bulk van de vloeistof. Dit werd gedaan omdat de chemie in deze twee gebieden gedomineerd wordt door respectievelijk de kort- en langlevende reactieve deeltjes. Verder werd in Hoofdstuk 4 ook de ontwikkeling van een chemisch kinetisch model voor de gasfase van de COST-jet besproken, hetwelke gevalideerd werd aan de hand van metingen van kortlevende deeltjes die vanuit de gasfase in een vloeistof gevangen worden. Na validatie van zowel het gasfase- als vloeistoffasemodel, werden beide in combinatie gebruikt om de chemie in beide fasen in detail te onderzoeken. Door een combinatie van deze modellen met experimentele waarnemingen (uitgevoerd door Yury Gorbanev) hebben we (i) een nieuwe reactie kunnen aantonen tussen Cl^- en zuurstofatomen (O), waarbij ClO^- gevormd wordt, maar ook (ii) de grote afhankelijkheid van ClO^- in plasma-behandelde vloeistoffen van andere CAP-gegenereerde reactieve deeltjes. Verder toonden we ook aan dat de H_2O_2 concentratie sterk afhankelijk is van de toevoeging van H_2O in het toevoergas, vanwege een sterke toename van de $^{\bullet}OH$-concentratie binennin de bron. De concentratie van HNO_2/NO_2^-, anderzijds, is quasi onafhankelijk van deze

wijzigingen in toevoergas, aangezien •OH zowel belangrijk is in de vorming van deze deeltjes, als in de afbraak ervan.

In de volgende hoofdstukken werd dieper ingegaan op onderzoeksvragen 2 en 3 die hierboven zijn opgesomd. Hoewel geen reactieve MD simulaties werden uitgevoerd, werd in deze hoofdstukken wel nagegaan hoe bepaalde elementen aanwezig in CAPs interageren met biomoleculen (lipiden) aanwezig in cellen. Bovendien werd er ook gebruik gemaakt van de kennis in de literatuur omtrent de reacties die optreden tussen RONS en lipiden (lipide peroxidatie) om na te gaan wat de meer lange-termijn effecten van dergelijke processen zijn op membranen.

In Hoofdstuk 4 werden *united-atom* moleculaire dynamica (MD) simulaties gebruikt om na te gaan hoe het cholesterolgehalte in membranen de diffusie van enkele belangrijke reactieve deeltjes (•OH, •OOH, H_2O_2 and O_2) beïnvloedt. Dit werd onderzocht aangezien uit de literatuur volgde dat kankercellen een verlaagde concentratie aan cholesterol bezitten in hun celmembraan, in vergelijking met gezonde cellen. De resultaten van dit onderzoek toonden aan dat, afhankelijk van het deeltje in kwestie, cholesterol verschillende aspecten van het vrije-energie profiel doorheen het membraan beïnvloedt. Dergelijk profiel toont aan waar bepaalde barrières voor difussie liggen, en hoe groot deze barrières zijn. Zo zorgt cholesterol bijvoorbeeld voor (i) het verhogen en (ii) het verbreden van de barrière, alsook voor (iii) een verandering van de algemene vorm van de barrière. Hoewel uit dit onderzoek volgde dat cholesterol dus duidelijk een invloed heeft op de barrière voor diffusie, kon ook worden vastgesteld dat in eender welk systeem (hoge of lage cholesterolfractie) de barrière steeds significant was voor polaire deeltjes (wat de beschermende of controlerende rol van het celmembraan illustreert). Dit betekent dat, om de selectiviteitsverschillen tussen gezonde cellen en kankercellen tijdens CAP behandeling te verklaren, er (ook) andere elementen aanwezig moeten zijn, zoals bijvoorbeeld: een verhoogde expressie van aquaporines in kankercelmembranen of het genereren van nanoporiën ten gevolge van lipide peroxidatie, zoals we eerder reeds hebben aangetoond[1]. Als conclusie kon gesteld worden dat dit onderzoek een bijdrage leverde in de

zoektocht naar een mogelijke verklaring voor de verhoogde opname van reactive deeltjes door kankercellen, waarvan geweten is dat ze een lagere cholesterolfractie bezitten. Dit verschil in lipidesamenstelling van de membranen zou een mogelijke verklaring kunnen zijn voor de waargenomen selectiviteit van CAPs ten aanzien van kankercellen, geraporteerd door meerdere onderzoekers.[2–4] Er moet echter ook opgemerkt worden dat deze selectiviteit mogelijks ook afhangt van het type cellijn, aangezien contradictorische resultaten bekomen worden in andere onderzoeken.[5–7]

In Hoofdstuk 6 werd, in samenwerking met Maksudbek Yusupov, gefocust op het effect van elektrische velden, aanwezig in bepaalde CAP bronnen, op biologische substraten. Hiervoor werden opnieuw *united-atom* MD simulaties gebruikt, om een inzicht te verkijgen in het synergetisch effect van het aanleggen van een elektrisch veld in samenwerking met de aanwezigheid van geoxideerde lipiden op de vorming van poriën in celmembranen. In een eerste fase werd er gekeken naar de permeatie van reactieve deeltjes in membranen die al dan niet geoxideerde lipiden bevatten, in de afwezigheid van een elektrisch veld. Dit toonde aan dat het oxideren van lipiden in het algemeen leidt tot een verlaging van de permeatiebarrière, voornamelijk in de aanwezigheid van een aldehydefunctie in de geoxideerde lipiden. Dit kon verklaard worden door een verhoging van de fluïditeit van het membraan, wat permeatie bevordert. De waargenomen energiebarrières waren in alle systemen echter nog steeds significant, wat aantoonde dat passieve permeatie nog steeds zeer moeilijk is. Bij het aanleggen van een elektrisch veld daarentegen, treedt elektroporatie van de membranen op, waarbij poriën gevormd worden waarlangs de reactieve deeltjes zeer makkelijk kunnen diffunderen. Onze simulaties toonden hierbij aan dat het verhogen van de elektrische veldsterkte dit proces zal versnellen, en bovendien, dat de aanwezigheid van geoxideerde lipiden ervoor zorgt dat de threshold veldsterkte, nodig om elektroporatie te initiëren, ook verlaagt. Dit effect was opnieuw het sterkste in het geval van de aanwezigheid van een aldehydefunctie.

Terwijl in Hoofdstukken 5 en 6 de focus lag op het gebruik van CAPs voor de behandeling van kanker, werd er in Hoofdstuk 7 getracht een dieper inzicht te krijgen in de onderliggende processen die optreden wanneer CAPs interageren met de huid, met als toepassingen het bevorderen van de transdermale opname van geneesmiddelen. Dergelijke toedieningsmethode heeft vele voordelen ten aanzien van andere bestaande methoden, zoals bijvoorbeeld het vermijden van het *first-pass* effect in de lever, het verminderen van neveneffecten en het gemak van toediening aan de hand van huidpatches. Bij dergelijke methode worden typisch extra technieken gebruikt die de opname dienen te bevorderen, zodat een hogere concentratie van het geneesmiddel door de huid geraakt, of zodat grotere geneesmiddel moleculen ook via deze methode kunnen worden toegediend. Zeer recent werd aangetoond dat ook CAPs als dergelijke bevorderende techniek kunnen worden toegepast op een zeer 'zachte' manier, waarbij bijvoorbeeld neveneffecten als schade aan onderliggend weefsel kunnen vermeden worden. In dit onderzoek werden *coarse-grained* MD simulaties aangewend om het onderliggende mechanisme te onderzoeken. De hypothese die werd vooropgesteld, stelt dat CAP-gegenereerde reactieve deeltjes zorgen voor lipide oxidatie, wat uiteindelijk zal leiden tot het vormen van *cross-links* tussen naburige ceramiden (lipiden aanwezig in de huidlaag). Deze *cross-links* zullen er op hun beurt voor zorgen dat kleine poriën ontstaan in de huidlaag, waarlangs geneesmiddelen makkelijker kunnen diffunderen in de bloedbaan. Deze hypothese werd bevestigd door onze MD simulaties, die aantoonden dat *cross-links* tussen ceramiden inderdaad kleine poriën zullen doen onstaan. Verder werd ook aangetoond dat er een optimale behandeltijd bestaat om de permeatie van geneesmiddelen maximaal te bevorderen.

Het laatste deel van deze thesis (Hoofdstuk 8) onderscheidde zich van alle anderen, aangezien hier de focus werd gelegd op het gebruik van experimentele technieken. Lipide vesikels werden in dit onderzoek gebruikt, in combinatie met MD simulaties, om het effect van veranderingen in de lipidesamenstelling van membranen op de diffusie van plasma-gegenereerde reactieve deeltjes doorheen deze membranen na te gaan. Hoewel de

methodologie anders is dan voorgaande hoofdstukken, zijn deze resultaten enorm waardevol in combinatie met enkele waarnemingen in de andere onderzoeken, aangezien deze studie ons in staat stelde om enkele van de vooropgestelde hypotheses omtrent de selectiviteit van CAPs ten aanzien van kankercellen na te gaan in een zeer gecontroleerde omgeving. Door te werken met lipid vesikels konden we namelijk specifiek het effect van het cholesterolgehalte, de verzadigingsgraad van de lipiden en het type lipide-hoofdgroep nagaan, zonder rekening te moeten houden met andere variaties die altijd aanwezig zijn wanneer gewerkt wordt met echte cellijnen. De vermelde karakteristieken werden gekozen omdat dergelijke variaties typisch bestaan tussen gezonde cellijnen, en kankercellen.

De resultaten in Hoofdstuk 8 toonden aan dat mogelijke cellulaire effecten, geïnduceerd door het aanbrengen van oxidatieve stress, sterk afhangen van de lipide samenstelling van membranen. Zo hangt de hoeveelheid reactieve deeltjes die in staat zijn om door het membraan te diffunderen sterk af van de lipide samenstelling van dit membraan. Bovendien werd ook waargenomen dat het toevoegen van bepaalde lipiden (cholesterol of PE-lipiden) tegenovergestelde effecten kan hebben, afhankelijk van wat de voornaamste component van het membraan is. Om de onderliggende mechanismen te onderzoeken werden ook hier MD simulaties aangewend (uitgevoerd door Maksudbek Yusupov). Deze toonden aan dat er meerdere elementen een rol spelen, zoals (i) de lipide oxidatie van onverzadigde lipiden, (ii) de lipide pakking die afhankelijk is van het volume van de hoofdgroep en (iii) de vorming van lipide raften door sterke interacties tussen gelijkaardige lipiden.

Verder werd ook gekeken naar de mogelijkheid van CAP-gegenereerde reactieve deeltjes om DNA schade aan te richten, aan de hand van een klein DNA fragment dat opgenomen werd in de vesikels. Dit leidde tot de verrassende ontdekking dat de hoeveelheid reactieve deeltjes die door het membraan kunnen diffunderen (zoals hierboven besproken) niet noodzakelijk gelinkt is aan de hoeveelheid DNA schade die kan worden aangericht. Een mogelijke verklaring hiervoor zijn de dubbele bindingen aanwezig in

onverzadigde lipiden, dewelke als *scavengers* dienden voor kortlevende reactieve deeltjes (bijvoorbeeld $^{\bullet}OH$). Door met deze deeltjes te reageren kunnen zij het intracellulaire DNA niet bereiken, waardoor minder DNA schade werd waargenomen. Deze lipide-oxidatie zorgde er daarentegen wel voor dat de diffusie van langer-levende reactieve deeltjes (bijvoorbeeld H_2O_2) verhoogde. In membranen die meer verzadigde lipiden bevatten daarentegen, werden deze kortlevende deeltjes minder efficiënt tegengehouden, waardoor er meer DNA schade kon worden aangericht. De hydrofobe barrière van het membraan bleef echter wel meer behouden, waardoor globaal gezien minder reactieve deeltjes in staat waren door het membraan heen te diffunderen.

Samengevat kan gesteld worden dat deze thesis dieper inzicht geeft in de vormingsmechanismen van biomedisch relevante reactieve deeltjes in verschillende bronnen die worden gebruikt in medische toepassingen van CAPs. Verder werden ook verschillende hypothesen ontwikkeld omtrent hoe deze deeltjes interageren met bepaalde biomoleculen, zowel in het gebruik van CAPs als anti-kanker therapie, alsook in het bevorderen van de transdermale opname van geneesmiddelen. Deze hypothesen kunnen gebruikt worden als mogelijke verklaringen voor bepaalde experimentele waarnemingen.

CHAPTER 1
INTRODUCTION

1.1 Introduction to plasma

The term `plasma`, which will be used throughout this thesis, refers to an ionized gas. The first reference to these physical plasmas in history dates back to 1879, when, based on its visual properties, Sir William Crookes described these as *radiant matter*, *i.e.*, a gas able to emit a constant stream of photons.[8] It took almost 50 years, until 1928, before Irvin Langmuir introduced the term 'plasma' for the first time:[9]

> *"We shall use the name plasma to describe this region containing balanced charges of ions and electrons."*

From then on, our understanding of plasmas has increased significantly. Nowadays, we know that plasma is much more than just a balance of ions and electrons. Indeed, many more components are present, including, *e.g.*, excited species, atomic or molecular radicals, UV-radiation and electromagnetic fields. In general, physical plasmas are generated by the addition of energy to a gas, as is illustrated in Figure 1.1.

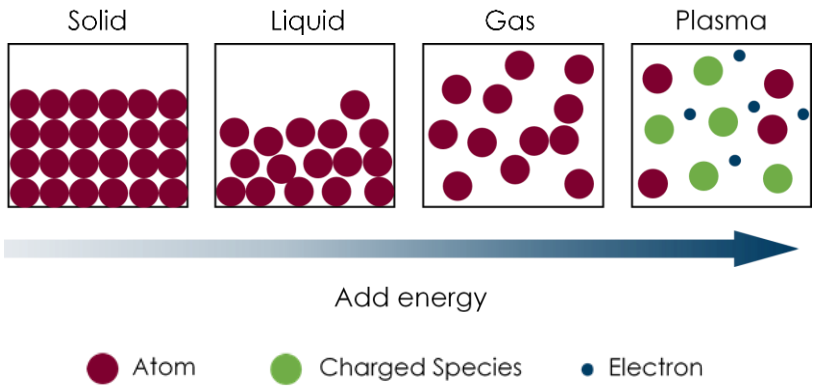

FIGURE 1.1: Addition of energy to a solid initiates a phase transition into a liquid, and eventually a gas. Further addition will ionize this gas, leading to the creation of plasma.

Depending on the operating conditions when generating plasma (*e.g.*, the pressure, the discharge configuration or the working gas), plasmas can be divided into two categories, *i.e.*, local thermal equilibrium plasma (LTE plasma, also called thermal plasma) and non-local thermal equilibrium plasma

(non-LTE plasma, also called non-thermal plasma).[10] In non-LTE plasmas, the temperature of the electrons is much higher compared to that of the heavy particles. As the gas temperature depends on the temperature of the heavy particles, this means that while the electron temperature in non-LTE plasmas can be in excess of 10,000 K, the gas temperature will be much lower, *i.e.*, typically ranging from room temperature to a few hundreds of K. In LTE plasmas, on the other hand, thermal equilibrium between the electrons and heavy particles is established, which means that the gas temperature is much higher than in non-LTE plasmas, reaching temperatures of up to tens of thousands of K. It has to be noted that the gas temperature of such LTE plasmas is still orders of magnitude lower compared to the temperature of high-temperature or fusion plasmas, in which values up to millions of K can be reached. Therefore, LTE and non-LTE plasmas are grouped as low-temperature, or cold plasmas. Figure 1.2 lists the different components present in cold plasmas, which illustrates the cocktail of ingredients a plasma typically comprises.

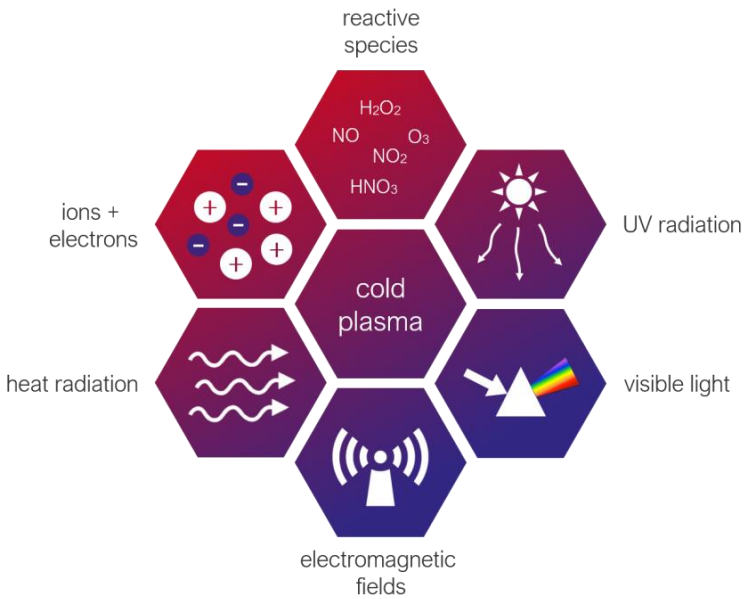

FIGURE 1.2: Different components present in cold plasmas.

In the field of plasma medicine, the goal is to use plasmas directly on patients (unless an indirect treatment method is used, see below). Therefore, to avoid

heating damage in living tissues, non-LTE plasmas, also referred to also cold atmospheric pressure plasmas (CAPs), are almost used exclusively in this field. In general, such plasmas are generated by a gas discharge upon applying an external voltage over two electrodes, which causes the electrons to be accelerated. If the applied voltage is high enough, the electrons will gain enough energy to ionize heavy particles upon collision, and hence create an ionized gas, or plasma. In this process, additional electrons are created, which can ionize even more gas molecules, thereby sustaining the created plasma. The initial electrons required to initiate this process are created naturally by photo-ionization of gas molecules due to cosmic radiation. Due to the large difference in mass of electrons and atoms, the energy transfer between electrons and heavy particles during collisions is minimal. Therefore, the electron temperature can become very high, while a very low gas temperature is maintained; hence non-LTE plasma is generated.

1.2 Plasma sources in plasma medicine

In medical applications of plasmas, a multitude of different plasma sources have been developed over the last decades. However, nearly all these sources can be divided into two different types: (i) atmospheric pressure plasma jets (APPJs) and (ii) dielectric barrier discharges (DBDs).[11,12] The general set-up of both sources is illustrated in Figure 1.3.

Fig 1.3.A shows the general set-up of an APPJ. In an APPJ, a feed gas is led between two powered electrodes, which are usually separated by a few millimetres in distance. The voltage applied over both electrodes will accelerate the electrons in the discharge gap, which leads to ionization of the feed gas and thus the creation of a plasma. After passing through the discharge zone (inside the source), the generated plasma is transported out of the source into the surrounding atmosphere by (i) the flow of the feed gas and (ii) the propagation of the ionization front. The substrate to be treated is thereby placed at a certain distance from the tip of the plasma jet (so-called nozzle), with typical treatment distances in the range of millimetres to

centimetres. Different carrier gases, or a mixture of different gases, can be used in this approach. In most applications, either helium (*e.g.*, the COST Reference Microplasma jet[13]), argon (*e.g.*, the kINPen IND[14]) or air (*e.g.*, the so-called SOFT-jet[15]) is used as main carrier gas, to which traces of O_2, N_2 or H_2O are sometimes added.[12] Furthermore, APPJs can be classified into different categories according to parameters such as discharge geometry, electrode arrangement, excitation frequency or pattern.[12,16] Depending on the exact configuration of the electrodes, there can be a visual plasma effluent outside the plasma source. If in this case, the substrate is placed close to the nozzle of the jet, a discharge onto the substrate can occur.

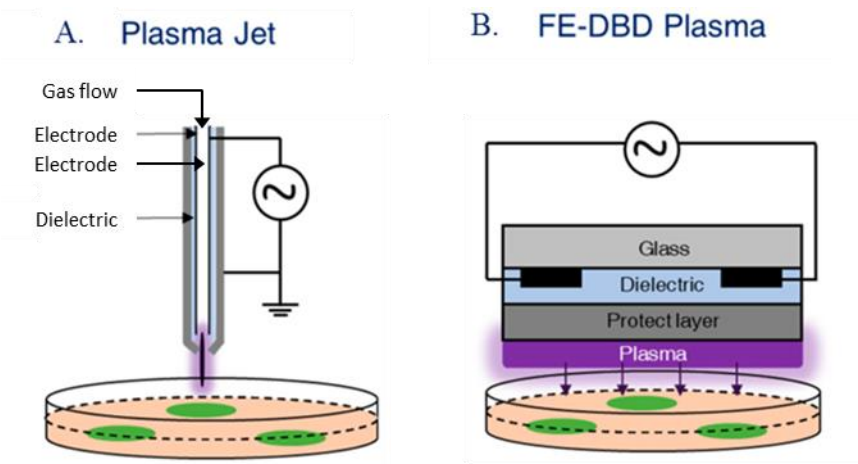

FIGURE 1.3: Schematic illustration of the electrode set-up in the two main plasma sources used for medical applications, *i.e.*, (A) a plasma jet (APPJ), and (B) a floating-electrode DBD (FE-DBD). Figure was adopted from[17].

In general, a few important advantages and disadvantages of using APPJs can be identified:

- ✓ APPJs have the ability to treat very narrow cavities or substrates that are difficult to reach, which is due to (i) the compact, light-weight design of APPJs and (ii) the presence of the effluent.
- ✓ By making small modifications to the operational parameters (feed gas composition, flow rate, treatment distance), the production of reactive species can be fine-tuned to optimize the treatment outcome. As will be demonstrated in Chapter 3 and 4, each of these

operational parameters can have a large effect on the generation of reactive oxygen and nitrogen species (RONS).

- ✗ The concentration of RONS generated is in general lower compared to DBDs.[18]

In DBD plasma sources (Fig 1.3.B), the substrate to be treated is placed underneath the powered electrode. In this configuration, which is also called a floating-electrode DBD (FE-DBD), the substrate treated serves as a counter (grounded) electrode, and the discharge takes place in ambient air. When comparing with APPJs, both advantages and disadvantages of using DBDs can be identified (next to the (dis)advantages discussed above):

- ✓ By upscaling the dimensions of the powered electrode, DBD sources have the ability to treat large surface areas.
- ✓ The discharge usually takes place in ambient air, by which expensive noble gases, more commonly used in APPJs, can be avoided.
- ✗ Using ambient air, however, makes the generation of RONS, and thus the exact treatment outcome, dependent on the local conditions (humidity, pressure, etc.), while in the case of (some) APPJs, there is a strong control over the composition of the feed gas and thus the treatment outcome.
- ✗ The powered electrode and substrate should always remain very close to each other (typically around 1-3 mm), which limits its use in applications that require reaching small areas inside the human body.[18]

In each of these CAP sources, due to the carrier gases used, and/or due to the contact of the plasma with ambient air (present in both types of plasma sources), RONS are generated. These species are created when energetic electrons or exited species, generated inside the plasma jet, come in contact with O_2, N_2 or H_2O present in ambient air or in the feed gas. These RONS include very reactive species (*e.g.* OH radicals ($^{\bullet}OH$), oxygen (O) or nitrogen (N) atoms, or singlet oxygen $^1O_2$) which have a typical half-life in the ns range,

and more stable, longer-lived species, *e.g.*, hydrogen peroxide (H_2O_2), nitrous acid (HNO_2) and nitric acid (HNO_3), with typical cellular half-lives in the ms range.[19] These species are very important, as the oxidative stress induced by CAP-generated RONS is thought to be the main mode-of-action in the induction of the biological effects observed in all medical applications.[20]

1.3 Indirect plasma treatment in plasma medicine

Besides the direct treatment of a substrate (cells or tissues, for example), in recent years, an indirect treatment method, in which a liquid is treated with CAP and afterwards administered to the substrate, is gaining interest (see Figure 1.4).[21–24]

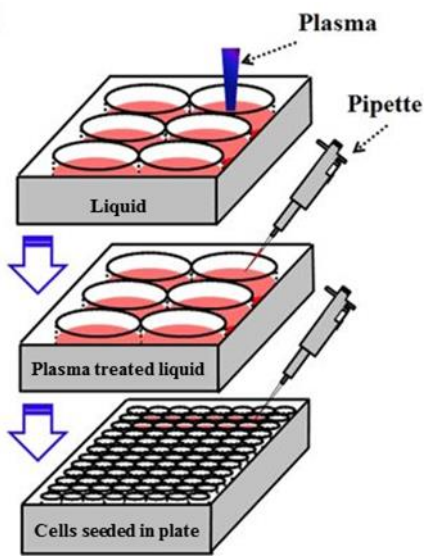

FIGURE 1.4: Schematic illustration of the use of CAPs in the indirect treatment of cells. Figure was adopted from[24].

The idea behind this approach is that plasma-generated RONS are stored in the treated liquid, to be used later when administering this liquid to the biological substrate of interest. Using such plasma-treated liquids (PTLs) possesses multiple advantages over direct treatments, although some drawbacks can be identified as well.[24]

- ✓ Plasma-generated species can be stored for a longer period of time, which allows these species to be applied at locations where no plasma sources are available. Indeed, H_2O_2, HNO_2 and HNO_3 are shown to survive up to several hours after CAP treatment.[22,25]
- ✓ Whereas direct treatment is only applicable for surface treatments, PTLs can be injected into a patient, thereby overcoming problems with difficult to reach targets.
- ✓ Using PTLs allows to measure the exact composition of certain species before administration to the patient. This control over the therapy is not possible in the direct treatment approach, in which many highly reactive, short-lived species are present. Such species often react with the first molecule they encounter, making any control over the homogeneity of the treatment impossible.
- × Short-lived species will not survive during storage, and even not after the plasma is switched off. Thus, only long-lived species can exert any biological effect. This makes PTLs somewhat less effective than direct CAP treatment, because research has shown that short-lived species generated by CAP are essential to utilize the full potential of CAP treatments.[22,24,26,27]

A lot of research is being performed regarding the exact contribution of short- and long-lived species when using PTLs. By comparing the effect of PTL with mock solutions containing only long-lived species, Girard *et al.* showed that long-lived species such as H_2O_2 and NO_2^- can fully account for the toxicity of CAP-treated liquid.[7] This would make the use of plasma redundant, as these mock-solutions can easily be synthesized in the lab, at a much cheaper price compared to PTL. However, as mentioned above, other researchers have shown that PTL is more efficient in killing cancer cells compared to mock solutions containing only H_2O_2 and NO_2^-.[22,24,26,27] In addition, when using CAP for disinfection, similar observations have been made, which again illustrates the versatile nature of PTL.[28] Furthermore, although the concentration of oxidizing species is seen to drop during storage, the bactericidal properties are maintained for up to four weeks.[28] This clearly illustrates that although H_2O_2

is thought to be the major species in PTLs, other components of PTL (*e.g.*, nitrites, nitrates, peroxynitrites or peroxynitrates) may also be important, which makes PTLs more effective than mere H_2O_2 mock solutions. Moreover, it also stresses the need for more fundamental knowledge of the plasma chemistry occurring in the treated liquids.

In the literature, a number of different liquids have been investigated regarding this approach, ranging from pure water, leading to the creation of plasma-treated water (PTW), to complex cell media, which are then called plasma-treated media (PTM).[22,29–34] The exact composition of the treated liquid strongly affects the generation of reactive species.[22,24,33] Non-buffered media, for example, show a strong decrease in pH during plasma treatment, due to the generation of strong acids, such as HNO_2 and HNO_3.[35] The biomolecules present in cell media, on the other hand, serve as scavengers of short-lived species, such as atoms and radicals. The secondary oxidation products generated from these reactions can afterwards pass the oxidative stress signal down to the treated cells. Furthermore, the presence of chlorine species in some treated liquids, such as phosphate buffered solutions (PBS), can also affect the outcome of an indirect treatment. Chloride ions (Cl^-), for example, can form hypochlorous acid (HOCl), which is known for its strong antibacterial effect.[36] The chemistry induced between CAP-generated RONS and Cl^--ions (present in PBS) will be discussed in the first part of Chapter 4.

Furthermore, although not investigated in this thesis, multiple researchers have shown that, whichever treatment method (direct or indirect) or CAP device (*e.g.*, plasma jet or DBD) is used, the effect of the substrate on the plasma has to be taken into account.[37,38] Indeed, Stancampiano et al. have shown that placing the substrate either on a dielectric table or a metallic cabinet has a drastic impact on the generation of RONS in a liquid substrate.[37] Therefore, they developed an electric circuit that can compensate electric differences between *in vitro* or animal models and the human body, which should facilitate the transition from one to the other.[37]

The above discussion clearly illustrates that, even when only focussing on the plasma chemistry and physics, a very large number of parameters have to be taken into account in the field of plasma medicine. Moreover, the development of many different plasma sources, and large variations in operating conditions, makes a comparison of results obtained in different labs extremely difficult. In this thesis, chemical kinetics models were developed for two different sources often used for medical applications, *i.e.*, the kINPen IND and the COST-jet. The results of these models will be discussed in Chapter 3 (kINPen IND) and Chapter 4 (COST-jet).

1.4 Research in plasma medicine

The usage of CAPs on human bodies dates back to Nikola Tesla in the 19th century.[39] In his research, Tesla showed that high frequency currents could pass through a human body without causing any damage or pain. Back then, he already suggested the potential medical use of such currents. A century later, in the mid-90s of last century, the field of plasma medicine really started evolving when researchers showed that such plasmas could be used to inactivate bacteria.[40] Since then, this field has grown rapidly, leading to the discovery of many potential medical applications of plasmas, including the acceleration of wound healing, applications in dentistry, and even the use of CAPs as an anti-cancer therapy.[11,21,23,41,42] Plasma medicine as such is a highly multidisciplinary field, involving the work of physicists, chemists, biologists, clinicians and engineers. Indeed, the research performed in the framework of plasmas for medical applications can be divided into four groups:

i. The development and characterization of plasma sources.
ii. The chemistry and physics occurring inside the plasma, as well as in the substrate treated, which is often covered by a liquid layer (*e.g.*, water or cell medium).
iii. The biological processes occurring when plasma-generated species or electromagnetic fields come in contact with biomolecules present in the substrate.

iv. The long-term effects of plasma treatments in living organisms.

The different processes occurring during CAP treatment of any biological substrate are illustrated in Figure 1.5.[5] Upon igniting the plasma, the generation of reactive species from the feed gas or surrounding atmosphere occurs immediately, *i.e.*, on the ps-ns timescale. Next, these species are transported to the biological substrate of interest, which is usually covered by a liquid layer. The recombination of species in the liquid, and the diffusion across this layer, occurs on the ms-min timescale. The time required to reach the biological substrate itself and to initiate any subsequent effects these species exert on cellular (or systemic) processes can range anytime from minutes to multiple days.[5]

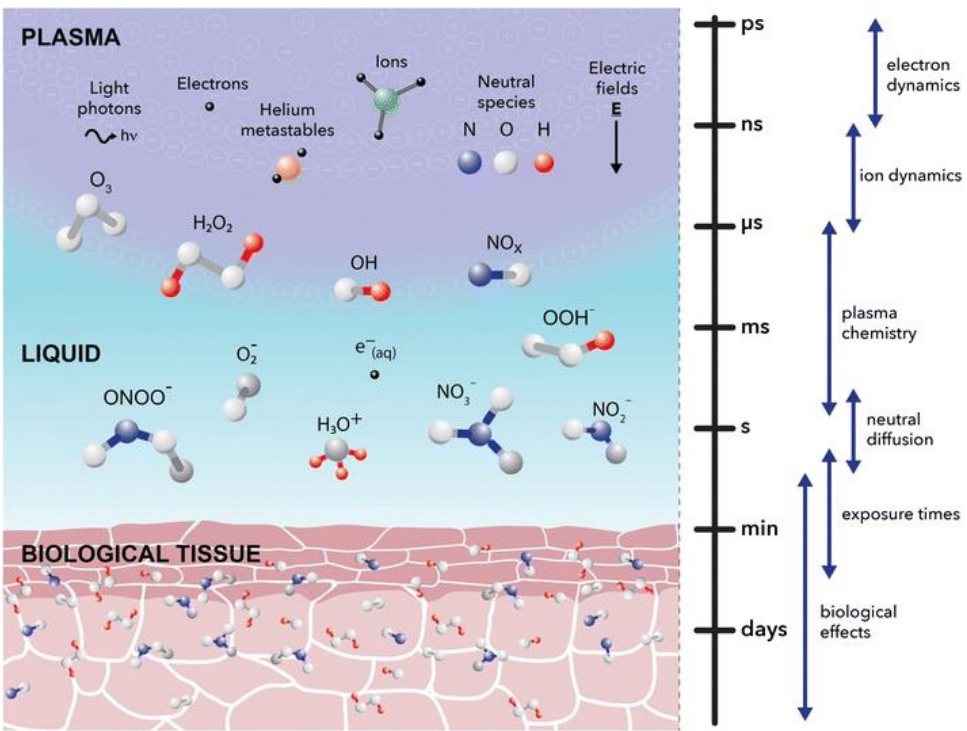

FIGURE 1.5: Illustration of the different physical, chemical and biological processes occurring during CAP treatment of biological tissues, as well as the timescale associated with each of these components.[5]

In recent years, plasma medicine has taken a huge step by moving from *in vitro* to more and more *in vivo* experiments.[21,43,44] However, fundamental research into (i) the plasma physics and chemistry occurring in different

plasma sources, as well as (ii) the processes occurring in the tissue or cells treated, remains essential. Indeed, although very promising results are being obtained in different medical applications, the need for a thorough understanding of the underlying processes is still very much present.

Depending on the plasma source used, different elements of plasmas can come in contact with biological substrates during treatment. Indeed, when PTLs are used in indirect treatments, only long-lived RONS will interact with biomolecules present in the substrate. When using plasma jets, on the other hand, also short-lived species are to be taken into account. If such jets have a discharge onto the liquid, or in the case of FE-DBDs, electromagnetic fields, photons and even solvated electrons enter the picture. Although in the case of direct plasma treatments using APPJs or DBDs, a certain degree of synergy between different plasma components can occur (see Chapter 6), throughout the literature, RONS produced by plasma are considered to be the main active agent inducing the biological effects observed.[45] These biological processes span a wide range of applications, including sterilization, treatment of chronic wounds, dental treatment, enhancement of transdermal drug delivery (TDD) (which is the focus of Chapter 7) and treatment of cancers. As the use of CAPs as an anti-cancer therapy is the main research focus of this thesis (see Chapters 3, 5, 6 and 8), as well as that of the PLASMANT research group (as far as plasma medicine is concerned), this application is discussed in more detail below.

1.5 Cancer biology and treatment therapies

The term 'cancer' refers to a series of diseases which are all characterized by two modifications of cells. First of all, in the development of cancer, cells need to establish the ability to ignore certain signals, allowing them to divide uncontrollably. Secondly, cancer cells need to develop the ability to invade and colonize territories normally reserved for other cells (making it a malignant tumour, which is then classified as cancer).[46] Without this invasive nature, a tumour is classified as benign, and removing or destroying the mass

locally usually achieves a complete cure. Based on the type of cells or the tissue in which the development of cancerous cells start, cancers can be classified into different categories, including, *e.g.*, carcinomas (arising from epithelial cells), sarcomas (arising from connective tissue or muscle cells) or leukaemia (arising from blood-forming tissue of the bone marrow).[46]

In a healthy organism, the cooperation between cells is regulated very strictly. Due to cell-to-cell communication, cells receive signals for, *e.g.*, cell division or cell death, which allows trillions of cells to work together and form tissues and organisms. However, during the life of a cell, mutations can be induced in the genetic carrier of cells, which is called deoxyribonucleic acid (DNA). These mutations can be caused by different factors, including, *e.g.*, environmental factors (such as UV radiation) or a faulty transcription during the replication of DNA. Such mutations occur very often in our body, which is why there are regulatory processes in place to detect these and, once they have detected mutated cells, either (i) repair the mutation or (ii) ensure that the mutated cell dies in a controlled manner, which is called apoptosis. However, if these regulatory processes do not succeed in repairing the mutation or in introducing cell death, the developed mutations can be passed on to the daughter cell during cell division. If the mutations succeed to survive over different generations of cells, multiple mutations can be piled up, which might eventually lead to the formation of a tumour.[46] Specific DNA-damaging molecular mechanisms are known to be involved in the development of cancer. These include, *e.g.*, the formation of DNA cross-links, single- or double-strand breaks or methylation of DNA-bases.[47] Moreover, certain genes (parts of the DNA) are also known to be especially vulnerable for tumour development if a mutation occurs on one them.[46]

1. Proto-oncogenes, which are involved during cell growth, cell division and cell differentiation.
2. Tumour suppressor genes or anti-oncogenes, which are involved in the regulation of the cell cycle and the promotion of apoptosis in diseased cells.

3. DNA maintenance genes, which are responsible for the repair of mutations in DNA.

Next to DNA mutations, also epigenetic changes are increasingly recognized for their roles in the development of cancers.[48] Such epigenetic alterations do not change the primary DNA sequence, but they play an essential role in modulating the expression of genes, *i.e.*, they can silence or upregulate the expression of genes. One of these epigenetic changes involves, *e.g.*, covalent modifications of amino acid residues in the histones around which the DNA is wrapped.[48]

Besides the ability of cancer cells to evade the immune system, responsible for repairing or introducing cell death in damaged cells, and their invasive nature towards neighboring tissues, many cancer cells typically also develop the ability to enter the circulatory systems of the body (blood vessels or lymph nodes), which allows them to travel through these systems to distant locations in the body, in which they can invade and start a new tumour. This process is called metastasis.

As mentioned before, cancers can be divided into different classes, based on the type of cell or tissue from which they originate. However, within each of these categories, an enormous amount of different cancers can be identified. Indeed, up to 1300 unique cancer cell lines have been identified in literature.[49] Regardless of the exact number, as each cell has its own specific modifications and behaviour, this clearly illustrates the extreme challenge of trying to find a treatment method for each different type of cancer. Moreover, besides variations in the initial mutations, cancer cells are able to continuously adapt themselves, which gives them the potential to develop resistance against any type of therapy used to treat them.

Traditionally, three cancer treatment therapies have been developed in the past, and are nowadays being used to treat a large number of cancers: surgery, chemotherapy and radiation therapy. Tremendous advances in the development of chemotherapeutics have improved survival rates, long-term remission and even led to a cure for a few cancers.[50,51] Combining these

chemotherapeutics with local treatment methods (radiotherapy and surgery) further improves the efficacy of the treatment.[52] However, while these methods are indeed able to treat a large number of different cancers, they are often harmful for healthy cells as well, which induces many side-effects during treatment. Radiation therapy, for example, relies on the generation of reactive oxygen species, such as H_2O_2 or $^{\bullet}OH$, inside the cancerous cells. By applying ionizing radiation, the chemical bonds of water (H_2O) molecules, present inside the cells, will be broken, eventually leading to the formation of the before mentioned ROS. As these ROS are generated inside the cells, they are able to oxidize the DNA of the cell, which will eventually lead to cell death. Selectively killing of cancer cells over healthy cells can be achieved as cancer cells divide much faster than healthy cells, which means their DNA is more vulnerable to oxidative damage.[53] However, the technique itself does not discriminate between specific cell types, meaning that healthy cells will also be damaged in the process. Especially fast dividing healthy cells (*e.g.*, blood cells or hair follicles) prove to be vulnerable to ionizing radiation, which leads to significant side-effects, such as hair loss, or even induction of new cancers in these cells. Traditional chemotherapy, which relies on the administration of drugs, suffers from similar problems as radiation therapy. Typically, these drugs target fast dividing cells, which results in them attacking fast dividing healthy cells as well. One remark to make regarding surgery is that when electrosurgical knives are used to cut tissue, a thermal plasma is generated in the process. This will most likely lead to a combined effect of both the heat as well as the reactive species chemistry on the tissue being treated.[54]

Besides these three traditional anti-cancer therapies, a lot of effort is put in research for new treatment modalities. In the past decades, new treatment methods have been added to this list, which include, *e.g.*, ion beam treatment[55], photodynamic therapy[56], gene-targeted therapies[57] (also called new-generation chemotherapy) or antibodies-based therapy[58,59]. This last one is particularly interesting in the case of antibody drug conjugates (ADCs), in which chemotherapeutics are linked to antibodies. By using antibodies that are specific to tumour cell surface proteins (the antigen), the conjugate will

target cancer cells specifically. After binding with the antigen, the chemotherapeutic will exert its anti-cancer effect. The combination of both makes this an extremely targeted and effective technique.[58]

Whichever therapy is being investigated, the ultimate goal is always to develop therapies which can be used against a broad range of different cancers, while avoiding the induction of damage in healthy cells. However, up until now, all of these methods still suffer from specific shortcomings. Indeed, in the case of photodynamic therapy, selectivity towards cancer cells is still a problem. With ion beam treatment, on the other hand, single cells can be treated, which should minimize the effect on healthy cells. However, the problem lies in the difficulty of finding each individual cell throughout the entire body, and with the harsh conditions used to induce cell death, which often induce necrosis in cancer cells (uncontrolled cell death, often leading to inflammation of the surrounding tissue). In the case of gene-targeted therapy, great knowledge of the individual cells is required for optimal treatment outcomes, which is often still missing. Moreover, the changing nature of cancer cells also has to be taken into account, which allows them to develop resistance towards all of these treatment therapies used (with the exception of ion beam treatment). If resistance is developed, the resistant cells will survive the treatment and can continue to grow and form new tumours. Indeed, it is estimated that around 90% of cancer deaths are not caused by the initial tumour, but rather by the spread of cancer cells from the primary tumour to surrounding tissues and distant organs.[60] This clearly stresses the importance of finding new treatment methods, which are able to (i) selectively kill cancer cells over healthy cells, (ii) throughout the entire organism, while at the same time (iii) avoiding the development of resistance in treated tumours. In this context, the ability of cold plasmas to satisfy all three of these requirements is being investigated intensively in the last decade.

As is the case in other cancer treatment therapies, the action of CAPs in the treatment of cancer cells is assumed to be based on the action of RONS generated during treatment. Indeed, in comparison to healthy cells, cancer cells are characterized by an increased level of intracellular RONS, which

promotes cell proliferation.[61–64] Homeostasis of RONS in the cell is crucial for cell growth and survival, as excessive amounts of RONS induce oxidative damage to lipids, proteins and DNA, which will eventually lead to cell death. One theory of how CAPs might induce a selective killing effect of cancer cells states that during CAP treatment, the exogenous supply of RONS will disturb the homeostasis of RONS, which will bring cancer cells over the cell death threshold. Healthy cells, on the other hand, possess lower levels of intracellular ROS, and will therefore remain under the threshold of oxidative stress induced cell death (see Figure 1.6).

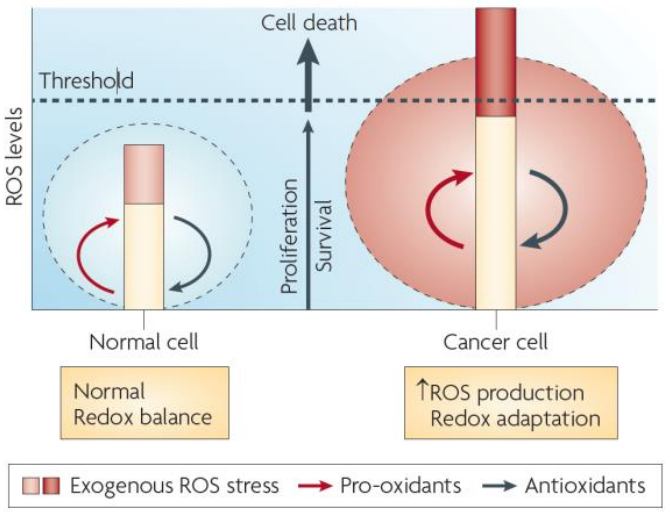

FIGURE 1.6: Possible explanation of how cancer cells can be targeted selectively over healthy cells by CAP-generated ROS.

However, this theory is being increasingly challenged, as different researchers have shown that antioxidants are also able to promote the invasiveness of tumours.[65,66] Indeed, the underlying biological processes are much more complicated. Besides differences in intracellular ROS levels, there are many more differences between healthy and cancer cells, which all play a role in determining how both types of cells will react on the plasma-induced oxidative stress. These differences include (and, this list is not exhaustive):

i. Alterations in lipid composition of the outer cell membrane.[67–70] These alterations include, *e.g.*, variations in the metabolism of cholesterol (a decreased concentration is observed in metastatic

cells[67–69], whereas multidrug resistant cells display elevated levels of cholesterol[69]) or increased expression of phosphatidylserine (PS) and phosphatidylethanolamine (PE) lipids in the outer leaflet of the membrane[69,70]. The effect of the lipid composition of the plasma membrane on the ability of CAP-generated RONS to penetrate through the membrane is the focus of Chapters 4 and 7 of this thesis.

ii. Alterations in the expression of different proteins, such as membrane-associated proteins. Cancer cells possess, *e.g.*, increased levels of aquaporines.[71–74] As these proteins allow diffusion of exogenous H_2O_2 into the cell interior, cancer cells will take up a higher amount of H_2O_2, which will eventually lead to cell death in these cells. Another possible pathway to target cancer cells selectively is through the interplay of increased levels in membrane-associated (i) catalase, (ii) NADPH oxidase (NOX1) and (iii) superoxide dismutase (SOD), present in cancer cells. This is discussed in great detail in the work of Georg Bauer.[75,76]

Furthermore, nowadays, a lot of research is spent in inducing an immune system response by plasma, rather than direct cell death in cancer cells.[27,77] Indeed, to achieve a systemic response in an entire organism, and to avoid the recurrence of a cancer, the immune system has to be activated to actively hunt cancer cells down in an entire organism.[78] As mentioned above, one prerequisite for cancer cells to survive and grow into large tumours is to become invisible for immune cells, as their role is to remove mutated cells before they become a problem. Only cells that are able escape this process because of their low immunogenicity can grow unchecked and, with accumulating mutations, become cancerous. Therefore, if these immune cells can be activated again to hunt down cancer cells, a systemic and selective treatment is achieved. Very promising results have been obtained so far, which show that short-lived species generated by plasma can indeed elicit immunogenic cell death in melanoma cells, which has also been validated in a

vaccination assay *in vivo*.[27] The overall process of how the immune system is involved in the development of tumours is illustrated in Figure 1.7.

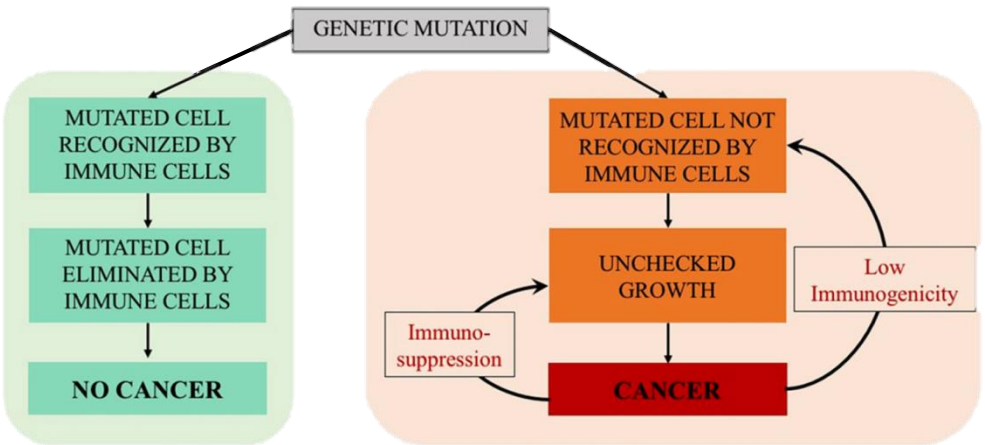

FIGURE 1.7: Role of the immune system in initiation, development, and control of cancer. Figure was adopted from[78].

The main difference between cold plasmas and the traditional cancer treatment therapies discussed above is that CAP offers the possibility to tune the composition of bioactive agents, a property which is not observed in any of the other therapies.[45,79–82] Indeed, biological effects caused by plasma, whether delivered by APPJs or DBDs, are believed to be mainly through a cocktail of RONS (as discussed above), but also charged particles, electric fields and shock waves can exert a synergistic effect.[45,81,82] In this context, it is suggested that by combining nitrosative stress with oxidative stress via air plasma might avoid the problem of cancer cells developing treatment resistance, as is often observed when using chemotherapeutics. Moreover, because of the non-equilibrium nature of plasma, the composition of plasma is easily adjusted in different combinations and permutations for optimal treatment. Hence, the selectivity required to deliver cytotoxic molecules to cancer cells, preferentially over normal cells, becomes possible. In fact, plasmas may be unique in their ability to trigger local effects that eventually produce systemic effects, which is the key to the approach for treatment of cancers with CAP. Indeed, in the last decades, researchers around the world have demonstrated the ability of CAP to induce cell death in many different cancer cell lines, including breast cancer[83], leukemia[84], lung cancer[85],

pancreatic cancer[86], melanoma[87], neuroblastoma[88], glioblastoma[26,30] and colorectal carcinoma[89–91].

1.6 Aim of this work

Although very promising results are being obtained in different applications of plasma medicine, the need for more fundamental insight in the underlying mechanisms remains at large. In general, three groups of questions can be identified:

1. Which components (*e.g.* reactive species or electric fields) are generated during treatment and which survive the transport to the substrate of interest?
2. How do these components interact or react with molecules present in the biological substrate (*e.g.*, lipids, proteins, DNA or elements of the extracellular matrix)?
3. What are the effects of these modifications in the substrate on the short and longer timescale?

To answer the research questions of group 1, the development of chemical kinetics models for the kINPen IND and the COST-jet, two CAP sources often used in the field of plasma medicine, is discussed in Chapter 3 and 4, respectively, of this thesis. Such models are used to investigate (i) the plasma chemistry, (ii) the transport of reactive species to a liquid substrate, as well as (iii) the chemistry occurring in the liquid substrate. Obtaining knowledge into the chemistry occurring in these plasma sources under different operating conditions is very important, as depending on the source or conditions used, very different biological outcomes can be obtained. Once such models are developed and validated, we can use them to obtain detailed knowledge into the reactions/species leading to the generation of important, biomedical active RONS. Furthermore, we can also try to use these models to predict optimal conditions to achieve the most desirable chemical cocktail of RONS.

The next chapters of this thesis discuss research questions of groups 2 and 3 discussed above. In Chapter 5, 6 and 7, molecular dynamics (MD) simulations are applied to study how RONS and electric fields, generated in CAPs, interact with biomolecules (lipids) present in cells. Furthermore, we also use the knowledge existing in literature on how RONS react with lipids (induction of lipid peroxidation) to study the longer-term effects of these oxidized lipids in membranes. In Chapters 5 and 6, the focus is on the use of CAPs as anti-cancer therapy, whereas in Chapter 7 we try to obtain deeper insight in the processes occurring when CAPs interact with skin lipids, for their use in transdermal drug delivery (TDD) systems.

The final chapter of this thesis, Chapter 8, is somewhat of a stand-alone chapter regarding the methodology used, as we mainly focus on experimental techniques. More specifically, we apply lipid vesicle experiments, in combination with additional MD simulations, to study the effect of a variable membrane lipid composition on the ability of plasma-generated RONS to diffuse through cellular membranes. Although the methodology is different, these results are extremely valuable for other investigations presented in this thesis (or performed earlier), as they allow us to test some of the hypotheses put forward regarding the selectivity of CAP treatment towards cancer cells in a very controllable environment. Indeed, by utilizing lipid vesicle experiments, we can tune the saturation degree of the lipid tails, the cholesterol content of the membrane, and the type of lipid head group (*i.e.*, PE vs. PC head group), without having to take other variations present between real cell lines in account. These characteristics are selected because different cell types, including healthy and cancerous human cells, also show variations in these types of lipid characteristics, as will be discussed in more detail in Chapter 8.

Before discussing the actual results of this work, Chapter 2 provides a very brief overview of the different techniques applied throughout this thesis. The main goal of this chapter is to introduce the different techniques, to clarify the differences between the methods used, as well as to explain why these specific techniques are selected for the research questions at hand. A more

detailed description regarding each of the techniques, however, will be given in the subsequent chapters.

CHAPTER 2

METHODOLOGY

2.1 General introduction

As mentioned in the previous chapter, there is a need for more insight in the underlying mechanisms of plasma oncology (and plasma medicine in general), for which modelling can be very useful. During the last decades, the increasing calculation capacity of computers has enabled us to investigate bigger systems on longer timescales, thereby increasing the overlap between simulations and experiment. This, in turn, has increased the importance and value of computational research significantly. Indeed, computational research possesses many advantages, including, *e.g.*, the ability to scan the effect of single parameters separately at low costs (both in time and money) or the avoidance of health, safety or waste regulations which have to be taken into account in experimental set-ups. It is important to note that in plasma medicine applications, very large biological substrates are treated (ranging from cultured cells in *in vitro* studies to human patients in clinical trials), whereas simulations often work with much smaller systems. This, of course, makes a direct correlation between model and experiments often extremely difficult. Nevertheless, by being very selective in choosing the model systems studied, the computational results presented in this thesis can be used to provide fundamental or atomistic-level insight in different processes occurring during CAP treatment of biological substrates. To get such an insight from experiments alone might be very difficult, as it is often impossible experimentally to focus on single parameters or to assign specific observations to, *e.g.*, certain processes or specific cellular alterations.[92] Nevertheless, it has to be kept in mind that these models are always an approximation or a subset of the real situation. This means that the conclusions drawn from the obtained results depend on the assumptions made in the development of the models. Therefore, we always try to combine or validate our results by experiments, to assess the validity of the approximations.

Besides being very selective regarding the system in the development of a model, at the same time, one has to choose which specific computational

technique is most suited to answer the research question at hand. Indeed, a wide variety of computational methods exist, all having their own specific advantages and limitations.[92] In general, two families of techniques can be identified in plasma medicine literature: atomic scale simulations and macroscopic simulations.[92] In this thesis, both types of techniques will be applied in different chapters, to investigate (i) the chemistry occurring in cold atmospheric plasmas and in their contact with liquids, as well as (ii) the interaction of CAP-derived species with biomolecules, and the effects of these interactions on the structure of lipid membranes. The first topic will be investigated by means of macroscopic simulations, more specifically chemical kinetics simulations, while the second topic is investigated by means of atomistic simulations, more specifically MD simulations. Finally, the last chapter will discuss the results of lipid vesicle experiments, performed to test different hypotheses discussed in Chapters 5 and 6. The concepts behind these simulation techniques, as well as the lipid vesicle experiments, are discussed below, while the research questions for which these models are employed will be discussed in more detail in the subsequent chapters.

2.2 Chemical kinetics models

Chemical kinetics models are used to describe the chemistry occurring inside a plasma source, in the gap between the source and a liquid substrate, as well as in the liquid substrate itself, on timescales up to several minutes. A chemical kinetics model describes a homogenous plasma, which means that processes such as diffusion or convection are not taken into account.[93] Indeed, typically, a chemical kinetics model will calculate the evolution of different species only over time, without giving any insight in the spatial distribution of these species. This is one of the major assumptions of a chemical kinetics model, especially when taking the effluent of a plasma jet into account, which is in most cases in contact with ambient air. Indeed, the latter induces mixing of the effluent with air species, which makes the spatial distribution very relevant. However, by relying on information obtained from more detailed 2D

simulations, chemical kinetics models can realistically mimic this situation, as will be discussed in more detail below.

The basis of a chemical kinetics model is solving the mass-conservation equations for all species included in the model.[93] Without taking transport processes into account, the following equation can be used:

$$\frac{\partial n_i}{\partial t} = S_i - L_i \tag{2.1}$$

in which n_i represents the density of species i, which is followed over time, t. On the right-hand side, S_i and L_i represent the source and loss terms respectively, *i.e.*, the reactions leading to the formation or loss of species i. In the case of heavy particles reactions, these source and loss terms are based on the rate coefficient (k) of these reactions and the densities of all reactants included. These rate coefficients, which are usually taken from literature, are often a function of the gas temperature. In the case of electron impact reactions, on the other hand, the rate coefficients of the source and loss reactions usually depend on the electron energy. To calculate the exact rate coefficient, the electron energy distribution function (EEDF, $f_e(\varepsilon)$) needs to be calculated, using the Boltzmann equation, and coupled with the cross-section ($\sigma(\varepsilon)$), taken from literature:

$$k = \int_0^{+\infty} \sigma(\varepsilon) f_e(\varepsilon) \sqrt{\frac{2\varepsilon}{m_e}} d\varepsilon \tag{2.2}$$

in which m_e represents the mass of an electron, and ε_e the electron energy.

When using these models to investigate the chemistry occurring (i) in plasma sources used in plasma medicine and (ii) in their interaction with liquids, a number of other assumptions are required. Indeed, as mentioned before, the rate coefficients of heavy particle reactions are mostly a function of the gas temperature. Therefore, the gas temperature profile needs to be known as an input parameter, both inside the jet, as well as in the effluent. Electron-impact reactions, as mentioned above, depend on the EEDF and therefore

require a power density profile as input. Furthermore, for both heavy and light species, a gas flow velocity profile is used to couple the time dependence of a chemical kinetics model with the position inside or outside the CAP source. Additional parameters include (i) the initial composition of the feed gas (impurities present in the feed) and (ii) the rate of mixing plasma with ambient air, once inside the effluent.

Afterwards, once the liquid surface to be treated is reached, the gas phase species are transported into the liquid phase. This diffusion is based on the model developed by Lietz et al.[94] and is described by the following equation:

$$n_{i+dt,l} = n_{i,aq} + C \,.\, D_i \,.\left(\frac{h_i \,.\, n_{i,aq} - n_{i,g}}{h_i}\right).dt \qquad (2.3)$$

in which $n_{i,aq}$ and $n_{i,g}$ represent the liquid and final gas phase (just above the liquid substrate) density of species i, respectively. D_i is the liquid phase diffusion coefficient of species i, while h_i is the Henry constant of species i. A constant C is used to scale the densities obtained from the chemical kinetics simulations to the experimental densities. Such a scaling constant is required, as chemical kinetics models do not include a spatial dimension in the gas nor in the liquid phase simulations. Therefore, this scaling constant is chosen so that the absolute densities obtained in the model match the concentrations measured experimentally. Note that throughout different simulations (*e.g.*, for different experimental conditions), the same scaling constant is always used. Furthermore, as the absolute densities obtained by the chemical kinetics models were matched to the experiments based on a scaling constant, any evaporation effects (which are observed in the experiments discussed in this thesis) are taken into account in this constant.

As mentioned above, multiple assumptions are made in the development of chemical kinetics models. Therefore, a thorough validation against experimental data is always required. Once an accurate model is developed, however, the main advantage of chemical kinetics models is their ability to investigate many different conditions and processes, while requiring a very limited amount of computational power. Indeed, using such models, complex

chemistry sets of thousands of reactions can be investigated on timescales of seconds to minutes (which would take months or years if attempted to simulate this in a two-dimensional model). By analysing the formation and loss processes of different species of interest, fundamental insight can be acquired in how different plasma sources lead to the generation of different combinations of species, how the operating conditions influence the plasma chemistry and how these can be fine-tuned to obtain the desired results (*e.g.*, most effective treatment in medicinal applications, or highest conversion or energy efficiency in greenhouse gas applications). Furthermore, knowledge of which species are present under which operating conditions can help us determining which species are actually involved in inducing certain biological effects (*e.g.*, cell death).

The development of different chemical kinetics models used to investigate the plasma and liquid chemistry in the kINPen IND, the COST-jet, the SOFT-jet and a FE-DBD source will be discussed in more detail in Chapters 3 and 4.

2.3 Molecular dynamics simulations

In contrast to chemical kinetics models, MD simulations follow the trajectory of individual atoms and molecules over time (typically in the ns to μs range), which is achieved by integrating the laws of motion.[92] In this thesis, classical MD simulations are performed, in which a force field is used that describes how different atoms interact with each other. Such a force field determines the force (F_i) acting upon each atom or particle i, based on its immediate environment (Eq. 2.4).

$$F_i = -\frac{\partial U}{\partial r_i} \tag{2.4}$$

Once these forces are known, Newton's laws can be used to derive the acceleration, and thereby the displacement, of each particle in the system (Eq. 2.5).

$$F_i = m_i \frac{\partial^2 r_i}{\partial t^2} \tag{2.5}$$

Indeed, once the potential energy, U, is defined (by the force field), the position r_i of each atom i can be updated, taking into account its mass, m_i, and the time-step, dt. Each particle is moved accordingly, and a subsequent iteration of the integration is performed. By repeating this integration many times, and moving all atoms in the system at each time step, the dynamic evolution of a system can be determined.

As is clear from the above discussion, the force field used in MD simulations is crucial in the outcome of such simulations. Throughout history, many different force fields have been developed, which are all validated against a certain training set of molecules.[92] The type of molecules used as a training set determines the applicability of a certain force field. Moreover, different types of force fields can be identified in literature. Two big families of force fields can be distinguished: (i) reactive and (ii) non-reactive force fields. Reactive force fields allow molecular bonds to be broken and created throughout simulations, and are therefore suited to investigate chemical reactions. This also means, however, that the connectivity between atoms needs to be re-evaluated on every time step, which makes such simulations far more computationally demanding compared to non-reactive MD simulations, where no bond breaking or formation occurs.

In this thesis, only non-reactive force fields will be used, while relying on existing literature regarding plasma-lipid interactions (as will be discussed in the following chapters in more detail). The interatomic potential used in those types of force fields is defined as the sum of bonded (U_{bonded}) and non-bonded energy terms ($U_{non\text{-}bonded}$). The non-bonded energy term can be subdivided further into the sum of Lennard-Jones (U_{LJ}) and Coulombic interactions (U_C). The bonded interaction potential (U_{bonded}), on the other hand, depends on a certain number of covalently bonded atoms, *i.e.*, bond stretching (between two atoms), bond angle (between three atoms) and (improper) dihedral angle (between four atoms) interactions (see Eq 2.6).

$$U = U_{bonded} + U_{non-bonded} = U_{bonds} + U_{angles} + U_{dihedrals} + U_{LJ} + U_C \quad (2.6)$$

Furthermore, the family of non-reactive force fields can be subdivided based on the level of detail at which individual molecules are described. One possibility is that each atom is described separately, leading to the generation of all-atom force fields. Another possibility is grouping multiple atoms into one particle, which are connected through pseudo-bonds. Based on the number of atoms used to create such a particle, united-atom and coarse-grained force field can be distinguished. These force-fields typically group around 3-4 or 12-15 in each particle, respectively (Figure 2.1).

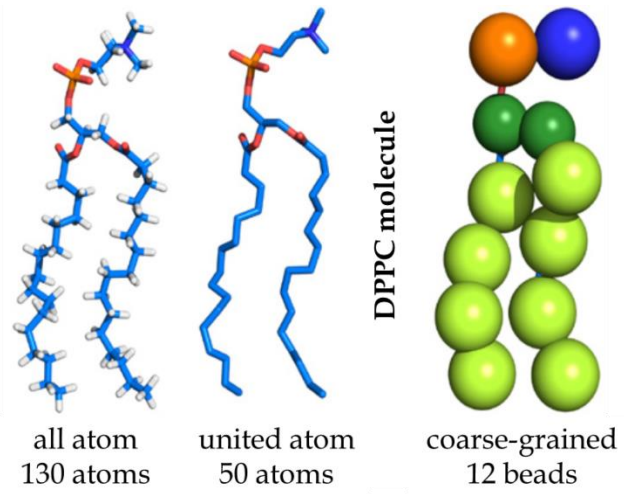

FIGURE 2.1: Different representations of a DPPC (1,2-dipalmitoyl-sn-glycero-3-phosphocholine) lipid in an all atom, united atom or coarse grained force field. Figure was adopted from[95].

It is clear that grouping multiple atoms in one particle will reduce the calculation time, which allows bigger systems to be investigated on larger timescales. However, at the same time, this also reduces the level of detailed insight that can be obtained from such simulations. Which force field is most suited will always depend on the exact point of interest of the study at hand.

Although the force field is the most important aspect of an MD simulation, other components of the simulation will also determine the validity of the results obtained. Indeed, before actually running an MD

simulation, one has to define, *e.g.*, which integrator to use, which boundary conditions to apply, which ensemble is most suitable, and afterwards, which specific thermostat and barostat to use (these are algorithms that ensure the MD system to generate a certain statistical ensemble at a predefined temperature and pressure). More information regarding the exact set-up used in the MD simulations performed in this thesis can be found in the specific Chapters, although not every different element will be discussed in great detail.

In this thesis, molecular dynamics (MD) simulations are used to investigate (i) the effect of the lipid composition of membranes on the permeation of RONS (Chapter 5), (ii) the synergistic effect of peroxidised lipids and electric fields on the permeation of RONS (Chapter 6) and (iii) the effect of cross-linking of ceramides in the skin on the transdermal drug delivery rate (Chapter 7). In Chapter 8, MD simulations are employed as well, in order to explain observations made in the lipid vesicle experiments, which are the main focus of that chapter. In most cases (Chapters 5, 6 and 8), united-atom force fields are employed. Although in these simulations the level of detail is lower compared to, *e.g.*, all-atom force fields, it proved to be sufficient for the required information. Furthermore, by comparing the obtained results with experimental data, we ensured the validity of the model for the study at hand in each Chapter (see further). In Chapter 7, on the other hand, the coarse-grained Martini force field is employed. This is required to study the cross-linking of ceramides, which involves too many lipids to be included in a united-atom force field.

Furthermore, as only non-reactive MD simulations are employed in this thesis, the oxidation or cross-linking degree is always taken as an input parameter in the simulations. Although no exact numbers are known regarding the ability of CAPs to produce a certain amount of oxidized lipids in cells, it always has to be taken into account that in the MD simulations, only a small patch of a membrane is investigated. Therefore, seemingly high oxidation degrees can be justified by taking into account that this is possibly

only a local effect, and therefore, the overall oxidation degree of the entire membrane will be much lower.

One last remark to make regarding the MD simulations performed in this thesis is the absence of a curved membrane structure. In real cells, the membrane is curved as the cells are spherical. However, in these MD simulations, we only look at planar bilayer structures (although small undulations can be present), which will in turn affect the physical properties of these membranes. Indeed, Yesylevskyy et al. showed that including the curvature of membranes in MD simulations affects properties such as the bilayer thickness or lipid order parameter.[96] Although these properties are very important in our simulations as well, it has to be noted that we don't focus on absolute values obtained in the simulations. Indeed, only different structures are compared to one another, to assess the effect of certain elements (*e.g.*, cholesterol content or lipid oxidation degree). Therefore, we believe that the conclusions drawn from these simulations are insensitive to the curvature of the membrane.

2.4 Lipid vesicle experiments

Lipid vesicle experiments are performed to model the cell membrane response when exposed to CAP-generated oxidative stress, upon altering the lipid composition of these membranes. More specifically, the permeation of reactive species, as well as their ability to subsequently induce DNA damage is investigated. Note that in these experiments, we only focus on DNA double strand breaks, but other types of DNA damage, *e.g.*, single strand breaks or chemical modifications to the DNA, can also cause cell death. These experiments can be used to test the validity of certain hypotheses, which are put forward based on the results of MD simulations obtained in the chapters preceding Chapter 8.

Applying lipid vesicle experiments allows us to have total control over all boundary conditions, which in turn makes it possible to exactly pinpoint differences observed in the cellular response to certain alterations in lipid

composition between different vesicles. This would not be possible when working with real cells or tissues, as in this case it is extremely difficult to pinpoint certain observations to specific elements of a cell, such as the lipid composition. Indeed, the extent of certain observed effects (such as the amount of cell death during treatment), is often difficult to explain as there are many differences between different cell lines. Even when only focussing on the lipids present in a cell membrane (and thereby ignoring, *e.g.*, differences in the expression of numerous proteins or the redox state of cells), the complex interplay between more than 1000 different membrane lipids has to be taken into account when working with any eukaryotic cell.[46] This is, of course, an impossible task, which means that observations made in cell experiments are always the combined effect of different elements.

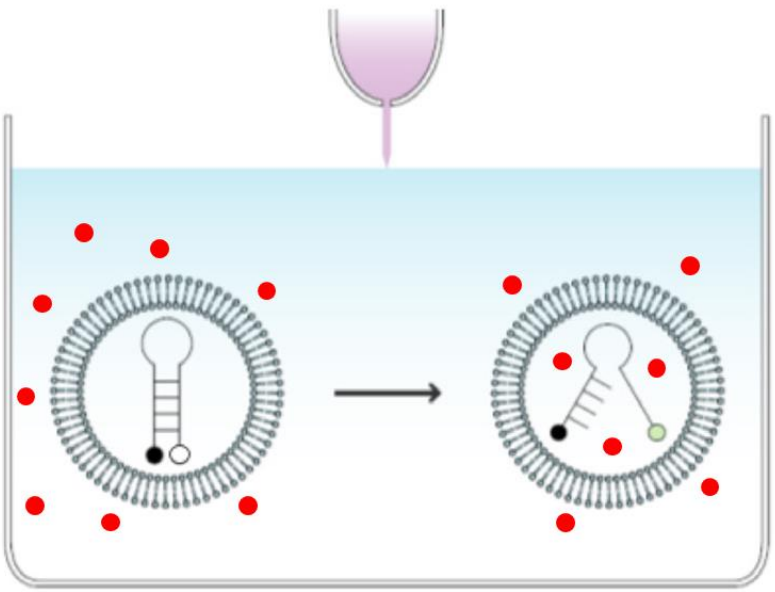

FIGURE 2.2: The MB consists of a single-stranded loop and double-stranded stem structure with a fluorophore and quencher moiety at the end of each DNA strand. With the MB intact, the quencher inhibits fluorescence of the fluorophore. If the DNA strand of the MB breaks, the quencher is separated from the fluorophore, resulting in a switch-on of fluorescence (as a positive indication of DNA strand breaks). The CAP-generated RONS are depicted as red spheres. Figure was adopted from[97].

In the lipid vesicle experiments, different molecular probes are used to measure (i) the stability of the vesicles during CAP treatment, (ii) the amount

of broad range ROS able to penetrate through the vesicle membrane and (iii) the ability of penetrated RONS to induce DNA damage. As we are interested in the ability of CAP-generated RONS to diffuse through the vesicle membrane, the molecular probes are first encapsulated in the vesicles during synthesis. If RONS are able to diffuse through the vesicle membrane, these species will be able to react with the encapsulated molecular probes, which generates a fluorescence signal. The idea of this set up is illustrated in Figure 2.2, in the case of an encapsulated DNA fragment (molecular beacon or MB), used to assess the ability of the intracellular RONS to induce DNA damage.

Following the same approach, encapsulated DCFH (2,7-dichlorodihydro-fluorescein) is used as a broad range molecular probe for RONS, in order to qualitatively determine the number of these molecules able to penetrate through the vesicle membrane during CAP treatment (Figure 2.3).

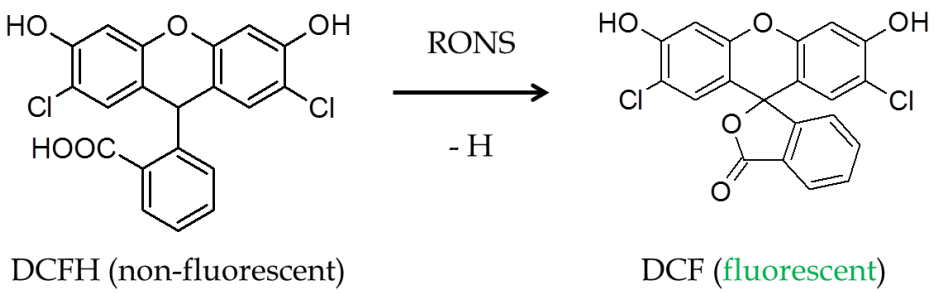

FIGURE 2.3: Reaction of CAP-generated RONS switches on the fluorescence signal by generating fluorescent DCF (2,7-dichlorofluorescein).

Lastly, vesicles encapsulating CF (carboxyfluorescein) are used to analyse the possibility of the vesicle membrane being ruptured by the plasma jet treatment. In these experiments, CF is encapsulated within the vesicles, at a concentration sufficiently high to be self-quenched inside the intact vesicles. However, if the vesicles are ruptured by the plasma jet treatment, the CF would be released and diluted into the HEPES buffer containing the vesicles, resulting in a switch-on of fluorescence (*i.e.* a positive indication of vesicle rupture). The validation of the stability of the vesicles during CAP treatment is required, as the above mentioned experiments rely on the molecular probes being encapsulated within the vesicles. If vesicle membrane rupture would

occur, on the other hand, the molecular probes can enter the liquid solution, which would negate the entire set up. More details regarding these lipid vesicle experiments and the results obtained are presented in Chapter 8 and Appendix A.

CHAPTER 3

Model development and applications of the kINPen IND

The results presented in this chapter were published in:

W. Van Boxem, J. Van der Paal, Y. Gorbanev, S. Vanuytsel, E. Smits, S. Dewilde and A. Bogaerts. Anti-cancer capacity of plasma treated PBS: effect of chemical composition on cancer cell cytotoxicity. *Sci. Rep.* **7**, 1647 (2017).

3.1 Introduction

As mentioned in the general introduction of this thesis, the delivery of reactive species to cells or organs can be achieved by a direct or an indirect treatment method, in which a direct treatment can deliver both short-lived and long-lived species, while in an indirect treatment, only long-lived species are still present in the liquid. As there are some clear drawbacks for the direct treatment method (*e.g.*, only applicable for easy-to-reach targets or in places where plasma devices are available), many investigations focus on the indirect method, by using plasma-treated cell media (PTMs) or other plasma-treated liquids (PTLs).[7,24,30–33] One of these PTLs can be plasma-treated phosphate buffered saline (pPBS), which is a very simple buffered solution (containing NaCl, KCl, KH_2PO_4 and $Na_2HPO_4{\bullet}2H_2O$). Using such simple liquids, such as PBS, over often very complex cell media offers multiple benefits. Firstly, in a clinical setting, they can be seen as more standardized solutions, and they are also more suitable for the investigation of the species and mechanisms playing an important role in the anti-cancer activity of PTL, because they are not cell line dependent (compared to cell media, of which multiples exist for different cell lines). Secondly, research has also shown that pPBS retains its biological activity longer than PTM, which is an advantage for the storage of this PTL.[31] Furthermore, Bekeschus *et al.* showed that pPBS significantly decreased cancer cell metabolisms and proliferation, whereas PTM (Dulbecco's Modified Eagle Medium) showed no effect.[98] Lastly, the multi-component cell culture media are unlikely to receive accreditation for use in clinics due to their complex formulation and unknown immunogenicity.[44,98] When using PBS, however, it has to be taken into account that certain elements present in this solution can act as scavengers of CAP-generated RONS. The radical products, which are generated in this process, can potentially be very reactive as well. Indeed, as will be shown in the next chapter, Cl^- present in PBS is able to scavenge O atoms, leading to the formation of the very reactive ClO^-.

Although the advantages of using PTLs are rather clear, however, as mentioned in the introduction of this thesis, when using PTLs it has to be

realized that short-lived species will not survive during storage, and thus, only long-lived species can exert any biological effect, while research has shown that short-lived species generated by CAP are essential to utilize the full potential of CAP treatments.[26,27] Furthermore, the anti-cancer potential of PTLs, whilst exciting, is still in early stages of development, which is mainly because the underlying mechanisms are largely unknown. Furthermore, the liquid phase chemistry of solutions exposed to plasma is quite complicated. Recently, a very comprehensive review paper was published on plasma-liquid interactions, stating the upcoming challenges, as well as the fact that there are many unresolved questions in plasma-liquid interaction.[99] Generally, when using PTL or PTM, H_2O_2[24,100,101] and NO_2^- [7,102] have been regarded as the key species in the anti-cancer activity. In the context of pPBS, only few studies on the effect of RONS on the cancer cells have been published. Girard *et al*.[7] measured the concentrations of H_2O_2, NO_2^- and NO_3^- in pPBS and found that H_2O_2 and NO_2^- have a synergistic effect on the anti-cancer capacity of pPBS, while NO_3^- does not contribute to the killing of cancer cells. They also investigated the effects of treatment time and gas flow rate on these concentrations, but they only considered one or two different operating conditions for plasma treatment. Yan *et al*.[34] showed that NO_2^- alone has no killing capacity for cancer cells, while H_2O_2 does.

In this chapter, we present a chemical kinetics model, developed to investigate the chemistry occurring in the gas phase of the kINPen IND, as well as in the liquid phase of a liquid substrate treated by this jet. Although a medically-certified kINPen MED exists, which is specifically developed for medical applications, the kINPen IND was used in this study as this is an in-house jet and, moreover, the characteristics of both jets (IND and MED) are very similar).[14] The validation of the model is based on the comparison of the H_2O_2 and NO_2^- concentrations obtained by the model and the liquid concentrations measured experimentally. The effect of the gas flow rate, treatment distance and treatment time on the chemistry is investigated. Furthermore, the anti-cancer capacity of pPBS is evaluated for all conditions investigated, by considering three different cell lines of glioblastoma

multiforme (GBM). GBM is the most common and lethal type of primary brain tumours[103], classified as the highest rank for tumours of the central nervous system, as issued by the WHO[104]. These tumours are characterised by a high invasiveness, molecular heterogeneity and rapid spreading throughout the brain.[104] Furthermore, they exhibit a particular resistance to surgical and medical treatment and are extremely susceptible to relapse, leading to a poor median life-expectancy of 14.6 months and a 5-year survival rate of only 9.8% when treated with conventional therapy.[105] These numbers indicate that the treatment remains palliative in most cases, demonstrating the need for alternative approaches, such as plasma treatment.

By comparing the results of the chemical kinetics model and liquid measurements of H_2O_2 (colorimetric assay using the titanium sulphate method[106]) and NO_2^- (Griess method[107]) with the cell cytotoxicity effects of pPBS for identical conditions, we try to correlate the anti-cancer capacity of pPBS with the presence of specific species. This knowledge will help future investigations to optimize CAP operating conditions to achieve the most effective treatment.

Note: All experiments included in this chapter were performed by Wilma Van Boxem (M. Sc.), and will therefore not be discussed in detail in this thesis.

3.2 Methodology

3.2.1 General set-up chemical kinetics model

As explained in Section 2.2 of Chapter 2, chemical kinetics model are based on solving a set of conservation equations (Eq. 3.1) for all individual species included in the model (see below)[93]:

$$\frac{\partial n_s}{\partial t} = \sum_{i=1}^{j} [(a_{s,i}^R - a_{s,i}^L) R_i] \tag{3.1}$$

in which n_s is the density of species s (m^{-3}) , j the total number of reactions, $a_{s,i}^L$ and $a_{s,i}^R$ the stoichiometric coefficients at the left hand side and right hand side of the reaction and R_i the rate of reaction (in $m^{-3}.s^{-1}$), given by:

$$R_i = k_i \prod_s n_s^{\alpha_{s,i}} \tag{3.2}$$

in which k_i is the rate coefficient ($m^3.s^{-1}$ or $m^6.s^{-1}$ for two-body or three-body reactions, respectively). The rate coefficients of the heavy particle reactions are either constant or dependent on the gas temperature, whereas the rate coefficients of the electron impact reactions depend on the electron temperature T_e or the reduced electric field $\frac{E}{N}$ (*i.e.*, the electric field E divided by the number density of all neutral species N, usually expressed in Townsend, Td = 10^{-21} V m^2). The rate coefficients of the electron impact reactions are generally calculated according to the following equation:

$$k_i = \int_{\varepsilon_{th}}^{\infty} \sigma_i(\varepsilon) v(\varepsilon) f(\varepsilon) d\varepsilon \tag{3.3}$$

with ε the electron energy (usually in eV), ε_{th} the minimum threshold energy needed to induce the reaction, $v(\varepsilon)$ the velocity of the electrons (in $m.s^{-1}$) , $\sigma_i(\varepsilon)$ the cross section of collision i (in m^2), and $f(\varepsilon)$ the (normalized) electron energy distribution function (EEDF; in eV^{-1}) calculated using a Boltzmann solver.

In this work we solve the balance equations (Eq. 3.1) of all species by means of the ZDPlaskin code, which also has a built-in Boltzmann solver, called BOLSIG+[108], to calculate the EEDF and the rate coefficients of the electron impact reactions[93] based on a set of cross sections, the plasma composition, the gas temperature and the reduced electric field (E/N). The electric field (E; in $V.m^{-1}$) is calculated from a given power density, using the so-called local field approximation[109]:

$$E = \sqrt{\frac{P}{\sigma}} \tag{3.4}$$

with P the input power density (in W.m^{-3}) and σ the plasma conductivity (A.V^{-1}.m^{-1}). The plasma conductivity is estimated at the beginning of the simulations as[109]:

$$\sigma = \frac{e^2 n_{e,init}}{m_e v_m} \tag{3.5}$$

with e the elementary charge (1.6022.10^{-19} C), $n_{e,init}$ the initial electron density (in m^{-3}), m_e the electron mass (9.1094.11^{-31} kg) and v_m the collision frequency (in s^{-1}) calculated using BOLSIG+. During the simulation the plasma conductivity is calculated as[109]:

$$\sigma = \frac{e v_d n_e}{(\frac{E}{N})_{prev} n_0} \tag{3.6}$$

with v_d the electron drift velocity (in m.s^{-1}), which is calculated using BOLSIG+ implemented in ZDPlaskin, and $(\frac{E}{N})_{prev}$ the reduced electric field at the previous time step (in V.m^2).

3.2.2 Chemical kinetics approach to a plasma jet

In the approach of using a chemical kinetics model to simulate the kINPen IND plasma jet studied in this work, a cylindrical volume element is followed along the jet stream. By doing this, we assume a homogenous plasma along the radial axis (cfr. plug flow reactor). Moreover, we assume that the axial transport of mass and energy due to drift and diffusion is negligible compared to convection. Due to the very high axial flow speed (order of several thousand cm.s^{-1}) compared to the radial flow speed this seems acceptable. Upon reaching the liquid substrate, the calculated gas phase densities of all plasma species are used as input for the liquid phase module. In this module, the accumulation of species in the liquid is determined by the diffusion from gas phase species into the liquid, which is based on Henry's law, as well as by the liquid-phase chemistry. This approach, which allows us to investigate the liquid chemistry using a chemical kinetics model, was introduced by Lietz *et*

al.[94] The general plasma jet set-up, assumed in the model, is shown in Figure 3.1.

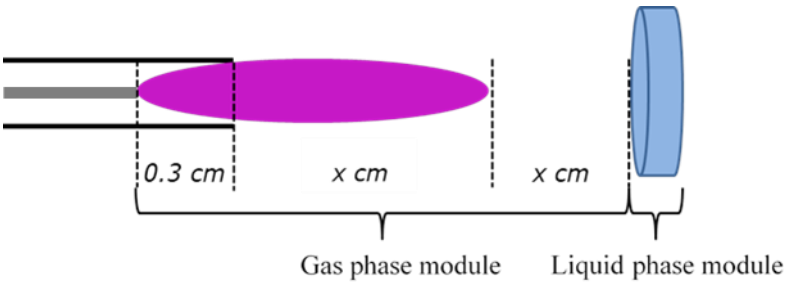

FIGURE 3.1: Plasma jet set-up used in the chemical kinetics model. The start of the simulation is 3 mm before the nozzle, which is at the tip of the inner electrode (thick gray line). The length of the visible effluent (indicated in purple) and the total distance between nozzle and liquid sample (both denoted as "x" cm, as they are both variables in different simulations) depend on the specific treatment conditions (see further).

3.2.3 Gas phase module

Conceptually, a chemical kinetics model calculates the density of all species as a function of time (see Eq. 3.1). However, by assuming a certain velocity profile of the feed gas, this time can be coupled to the position of the volume element along the axis, which allows us to obtain information on the species densities as a function of distance, and thus to investigate different treatment distances, as used in the experiments. An example of the gas flow velocity profile, which decreases along the axis due to gas expansion and obstruction by the relatively stationary surrounding atmosphere, is shown Figure 3.2, for a gas flow rate of 1 slm (standard litres per minute). The initial gas flow velocity, at the nozzle, is calculated based on the flow rate of the feed gas and the dimensions (diameter) of the plasma jet. Furthermore, as mentioned above, many of the gas phase reaction rate coefficients depend on the gas temperature. This means that a gas temperature profile along the plasma axis is required to calculate the exact rate of all reactions (see Figure 3.2). This temperature profile is based on experimental data[14], and assumptions of how the temperature decreases in the effluent. Note that small variations in this gas temperature had a negligible impact on the simulation results.

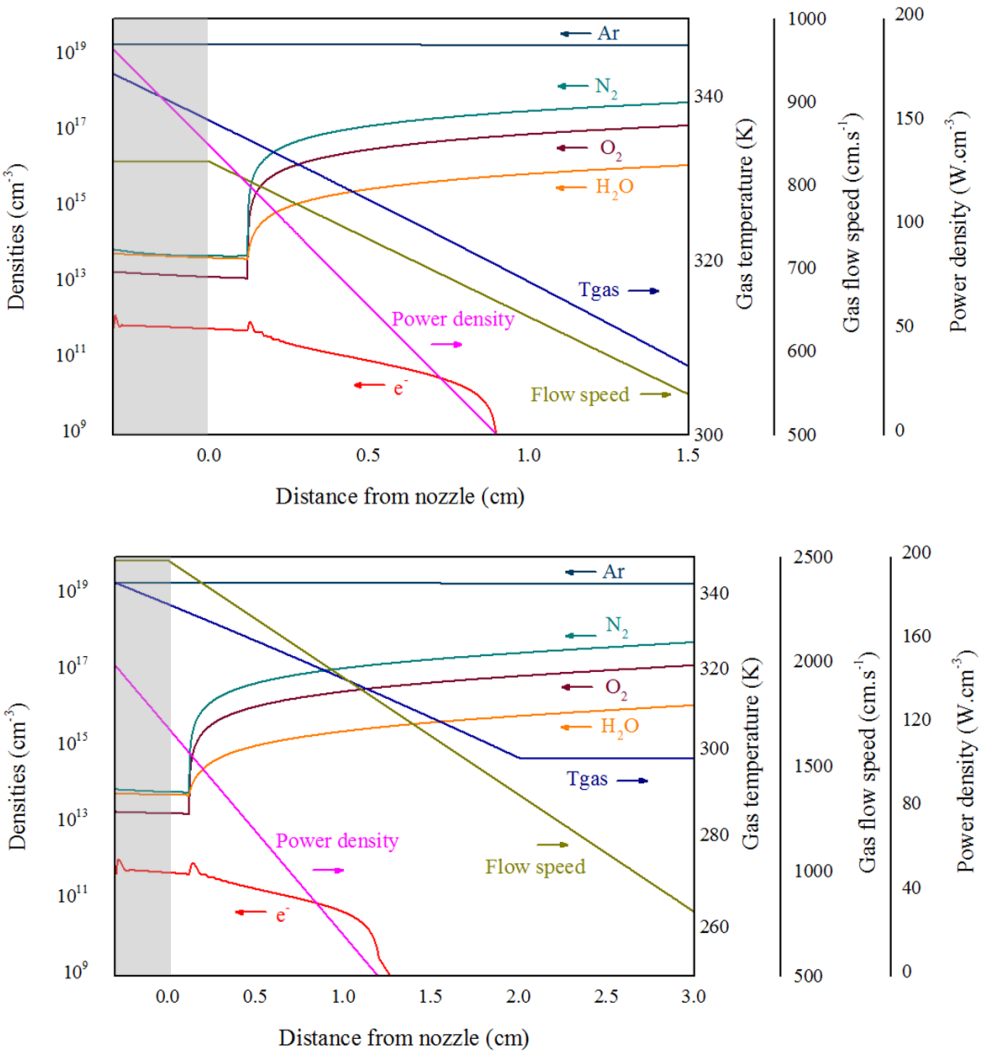

FIGURE 3.2: Plasma and gas characteristics as a function of the distance from the nozzle, along the plasma jet axis, for a flow rate of 1 slm and a treatment distance of 15 mm (top figure) and a flow rate of 3 slm and a treatment distance of 30 mm (bottom figure). The profiles of the power deposition and gas temperature are based on experimental data, whereas the density profiles of humid air species (O_2, N_2 and H_2O) in argon (Ar) and the velocity profile are based on more detailed 2D simulations.[110] The electron density is calculated throughout the simulation. The grey area indicates the interior of the plasma jet, starting from the electrode tip, where the simulation starts.

Moreover, as the electron impact reactions depend on the EEDF, the reduced electric field is also required. As mentioned above, this reduced field is

calculated based on the deposited power density, of which an example profile is also shown in Figure 3.2. The maximum value of the power density is achieved at the tip of the powered electrode. Subsequently, the power density decreases linearly along the plasma axis, reaching zero at the end of the visible effluent, which is observed experimentally. This is chosen as the simulation results indicate that the densities of the excited species quickly drop to zero when the power density drops to zero, due to which the visible effluent would also be lost. The length of the visible effluent depends on the gas flow rate, based on our experimental observations, *i.e.*, at 1 slm, the visible effluent propagates in general 9 mm into the surrounding atmosphere, whereas at 3 slm, this has a length of 12 mm. In the case of 1 slm and a treatment distance of 10 mm, plasma discharges onto the liquid substrate were observed, as mentioned in the main paper. This means that under these conditions, a discharge between two electrodes occurs, (i) the electrode tip from the plasma jet and (ii) the liquid surface. Therefore, we assume the power density profile to rise again slightly upon reaching the liquid surface (*i.e.* at the end of the gas phase simulation). In all cases, the total deposited power equals 3.5 W, as is the case in the experimental treatments.

Finally, to mimic the mixing of humid air species into the effluent of the plasma jet, these species (O_2, N_2 and H_2O) are added into the effluent, assuming a certain air mixing rate (based on 2D simulations). The profiles of the ambient air species along the axis are also shown in Figure 3.2. Note that the diffusion of ambient air species only starts after 0.12 cm in the effluent. This is because it will take some time before the ambient air species are able to diffuse up to the plasma axis. The initial densities of O_2, N_2 and H_2O inside the device (grey area in Figure 3.2) originate from the impurities of the feed gas (1, 4 and 3 ppm for O_2, N_2 and H_2O, respectively; corresponding to the feed gas used experimentally). The computational flowchart is illustrated in Figure 3.3.

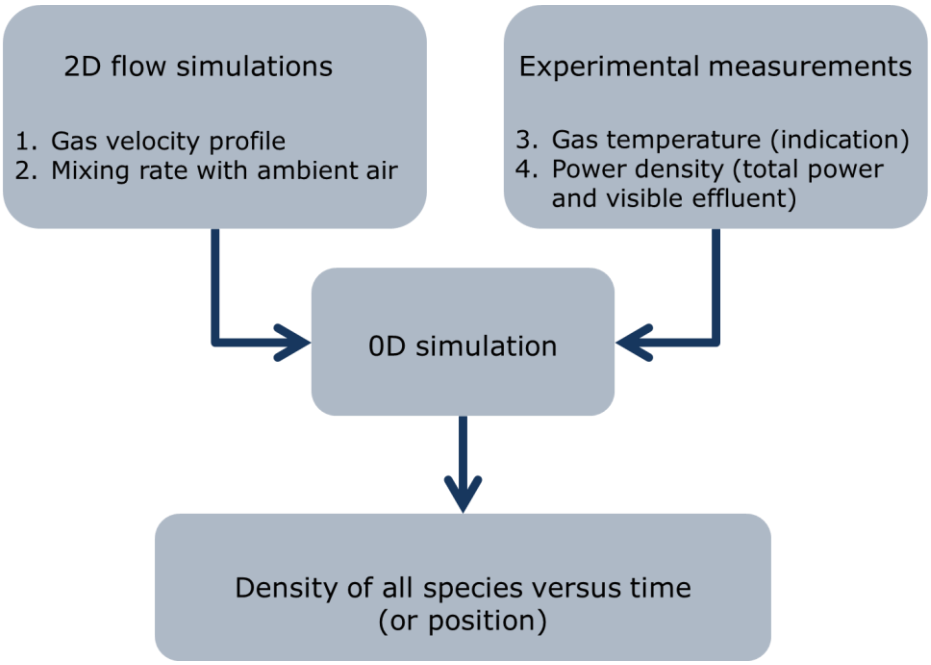

FIGURE 3.3: Overview of the computational flowchart.

TABLE 3.1: Species included in the chemical kinetics model for the gas phase. The species in bold are also taken into account in the liquid phase.

Ground state neutrals	Excited state neutrals	Charged species
Ar	$Ar(^4S[^3P_2])$, $Ar(^4S[^3P_1])$, $Ar(^4S[^3P_0])$, $Ar(^4S[^1P_1])$, Ar(4P)	$\mathbf{e^-}$, Ar^+, Ar_2^+, ArH^+
N, $\mathbf{N_2}$	$N(^2D)$, $N(^2P)$, $N_{2,\,vib(1\text{-}4)}$, $N_{2,rot}$, $N_2(A^3\sum_u^+)$, $N_2(a'^1\sum_u^-)$	N^+, N_2^+, N_3^+, N_4^+
O, $\mathbf{O_2}$, $\mathbf{O_3}$	$O(^1D)$, $O(^1S)$, $O_{2,vib(1\text{-}5)}$, $O_{2,rot}$, **$\mathbf{O_2(a^1\Delta_g)}$**, $O_2(b^1\sum_g^+)$	O^+, O_2^+, O_4^+, O^-, **$\mathbf{O_2^-}$**, O_3^-
NO, $\mathbf{NO_2}$, $\mathbf{NO_3}$, $\mathbf{N_2O}$, $\mathbf{N_2O_3}$, $\mathbf{N_2O_4}$, $\mathbf{N_2O_5}$		NO^+, NO_2^+, N_2O^+, NO^-, **$\mathbf{NO_2^-}$, $\mathbf{NO_3^-}$**
H, $\mathbf{H_2}$, OH, $\mathbf{H_2O}$, OOH, $\mathbf{H_2O_2}$	H^*, $H_{2,vib}$, $H_{2,rot}$, H_2^*, OH(A)	H^+, H_2^+, H_3^+, OH^+, H_2O^+, **$\mathbf{H_3O^+}$**, H^-, **$\mathbf{OH^-}$**, $O_2H_2O^-$, **$\mathbf{H_2O^-}$, $\mathbf{HO_2^-}$**
NH, HNO, $\mathbf{HNO_2}$, $\mathbf{HNO_3}$, HNO_4, **ONOOH**		$NO_2H_2O^-$, $NO_3H_2O^-$, **$\mathbf{ONOO^-}$**

The chemistry set of the gas phase reactions used in this study is largely taken from Murakami *et al*.[111] However, to include additional relevant biomedically active species (e.g. H_2O_2, $^{\bullet}OOH$, HNO_3 or HNO_2), we extended this chemistry set with the reactions describing the behaviour of these species, adopted from the chemistry set of Van Gaens and Bogaerts[112], yielding a total chemistry set of 91 different species and 1390 reactions. All species included in the gas phase are shown in Table 3.1.

3.2.4 Liquid phase module

To investigate the chemistry occurring in the PTL, a second set of species and a separate chemistry set[94] were included in the chemical kinetics model. First, a duplicate solvated species was added for each important gas phase species (*e.g.*, O_{3aq} for O_3). The choice was either based on the final gas phase density of these species or their relevance for the biomedical applications. These aqueous species and the liquid reactions are restricted to the liquid module only (and are thus not taken into account in the gas phase module). The species in these two modules can only interact through the gas-liquid interphase by means of diffusion into or out of the liquid. In general, the densities of the liquid species are given by[94]:

$$\frac{\partial n_{s,l}}{\partial t} = \sum_{i=1}^{j}\left[\left(a_{s,i}^{R} - a_{s,i}^{L}\right)R_i\right] + \frac{D_s n_{s,g}}{\Lambda^2} f_l S_{s,aq} \frac{V_p}{V_{aq}} - max\left[0, \frac{D_s(n_{s,aq} - h_s n_{s,g}}{\Lambda^2} \frac{V_p}{V_{aq}}\right] \tag{3.7}$$

in which the first term is similar to the calculation of the gas phase species densities (conservation of mass; see above). The second term represents the diffusion of gas phase species into the liquid. In this term, D_s is the liquid diffusion coefficient of gas phase species *s*, $n_{s,g}$ is the final gas phase density of species *s* and Λ is the diffusion length of the plasma. Furthermore, f_l is the fraction of the area of the plasma in contact with the liquid and $S_{s,aq}$ is the sticking coefficient of species *s* on the liquid, given by:

$$S_{s,aq} = \frac{h_s n_{s,g} - n_{s,aq}}{h_s n_{s,g}} \tag{3.8}$$

in which h_s represents the Henry constant of species *s*. This sticking coefficient is only used if $n_{s,aq}/n_{s,g} < h_i$ and accounts for a diminishing loss rate of the gas phase species into the liquid as the liquid density approaches its Henry's law equilibrium values. Finally, V_p and V_{aq} represent the volume of the plasma and the liquid, respectively. The third term of equation 7 is only non-zero if the liquid is oversaturated (*i.e.* if $n_{s,aq}/n_{s,g} > h_i$) and represents the flux from the liquid phase into the gas phase. The Henry constants were adopted from Lietz *et al*.[94], whereas the diffusion coefficients were taken from Verlackt *et al*.[110]

As mentioned before, the reaction chemistry of the liquid phase is taken from Lietz *et al*.[94] and includes in total 35 species and 89 reactions (see Table 3.2). It is impossible to take into account the transportation of plasma species from the gas-liquid interface into the bulk of the liquid by means of this 0D chemical kinetics model, but in reality, the density of the short-lived reactive species, such as $^{\bullet}$OH, will drop quickly from the interface towards the bulk. We mimic this drop in species densities in our model by decreasing the reaction rate coefficients of the reactions involving these short-lived species with longer-lived species. This approach is based on observations from more detailed 2D fluid simulations carried out in our group, in which short-lived species react mostly at the gas-liquid interface, generating more stable species, which are then rapidly transported towards the bulk of the liquid due to convection.[110] Nevertheless, as we do not exactly know how much we must reduce the reaction rates of certain reactions to account for this effect, this is one of the main limitations of this model. Therefore, in the next chapter, we tried to develop a new approach by which we can avoid this approximation (Chapter 4).

TABLE 3.2: List of reactions included in the liquid module. The unit of the rate coefficient is (s^{-1}), ($cm^3.s^{-1}$) or ($cm^6.s^{-1}$) for first, second or third order reactions, respectively.

Reaction	Rate coefficient
$ONOOH_{aq} + H_2O_{aq} \rightarrow H_3O^+_{aq} + ONOO^-_{aq}$	$5.0x10^{-15}$
$ONOO^-_{aq} + H_3O^+_{aq} \rightarrow H_2O_{aq} + ONOOH_{aq}$	$1.75x10^{-6}$
$HO_{2,aq} + H_2O_{aq} \rightarrow H_3O^+_{aq} + O_2^-{}_{aq}$	$1.43x10^{-17}$
$H_3O^+_{aq} + O_2^-{}_{aq} \rightarrow HO_{2aq} + H_2O_{aq}$	$5.0x10^{-11}$
$HNO_{2,aq} + H_2O_{aq} \rightarrow H_3O^+_{aq} + NO_2^-{}_{aq}$	$5.0x10^{-15}$
$H_3O^+_{aq} + NO_2^-{}_{aq} \rightarrow HNO_{2,aq} + H_2O_{aq}$	$3.9x10^{-10}$
$HNO_{3,aq} + H_2O_{aq} \rightarrow H_3O^+_{aq} + NO_3^-{}_{aq}$	$3.0x10^{-18}$
$H_3O^+_{aq} + NO_3^-{}_{aq} \rightarrow HNO_{3,aq} + H_2O_{aq}$	$7.0x10^{-16}$
$HO_2NO_{2,aq} + H_2O_{aq} \rightarrow O_2NO_2^-{}_{aq} + H_3O^+_{aq}$	$5.0x10^{-15}$
$O_2NO_2^-{}_{aq} + H_3O^+_{aq} \rightarrow HO_2NO_{2,aq} + H_2O_{aq}$	$1.05x10^{-7}$
$OH_{aq} + H_{aq} \rightarrow H_2O_{aq}$	$3.0x10^{-11}$
$H_2O^-_{aq} + H_2O_{aq} \rightarrow H_{aq} + OH^-_{aq} + H_2O_{aq}$	$3.0x10^{-20}$
$H_2O^-_{aq} + H_{aq} \rightarrow H_{2aq} + OH^-_{aq}$	$4.0x10^{-11}$
$H_2O^-_{aq} + O_{2aq} \rightarrow H_2O_{aq} + O_2^-{}_{aq}$	$3.0x10^{-11}$
$H_2O^-_{aq} + OH_{aq} \rightarrow H_2O_{aq} + OH^-_{aq}$	$5.0x10^{-11}$
$H_2O^-_{aq} + H_2O_{2aq} \rightarrow H_2O_{aq} + OH^-_{aq} + OH_{aq}$	$2.0x10^{-13}$
$H_2O^-_{aq} + HO_2^-{}_{aq} \rightarrow OH^-_{aq} + OH^-_{aq} + OH_{aq}$	$5.0x10^{-12}$
$H_2O^-_{aq} + H_2O^-_{aq} \rightarrow H_{2,aq} + OH^-_{aq} + OH^-_{aq}$	$1.0x10^{-11}$
$H_3O^+_{aq} + OH^-_{aq} \rightarrow H_2O_{aq} + H_2O_{aq}$	$5.0x10^{-15}$
$H_2O_{aq} + H_2O_{aq} \rightarrow H_3O^+_{aq} + OH^-_{aq}$	$3.02x10^{-32}$
$OH_{aq} + OH_{aq} \rightarrow H_2O_{2aq}$	$1.7x10^{-11}$
$OH_{aq} + H_{2,aq} \rightarrow H_{aq} + H_2O_{aq}$	$6.0x10^{-14}$
$OH_{aq} + HO_{2,aq} \rightarrow O_{2,aq} + H_2O_{aq}$	$2.0x10^{-11}$
$OH_{aq} + H_2O_{2,aq} \rightarrow HO_{2,aq} + H_2O_{aq}$	$0.45x10^{-15}$
$OH^+_{aq}\ O_2^-{}_{aq} \rightarrow O_{2,aq} + OH^-_{aq}$	$1.5x10^{-11}$
$OH_{aq} + HO_2^-{}_{aq} \rightarrow HO_{2,aq} + OH^-_{aq}$	$1.5x10^{-11}$
$OH_{aq} + NO_2^-{}_{aq} \rightarrow OH^-_{aq} + NO_{2,aq}$	$0.3x10^{-15}$
$OH_{aq} + NO_{aq} \rightarrow HNO_{2,aq}$	$3.3x10^{-11}$
$OH_{aq} + NO_{2,aq} \rightarrow HNO_{3,aq}$	$2.0x10^{-11}$
$OH_{aq} + HNO_{3,aq} \rightarrow NO_{3,aq} + H_2O_{aq}$	$2.17x10^{-15}$
$OH_{aq} + N_2O_{aq} \rightarrow HNO_{aq} + NO_{aq}$	$3.8x10^{-17}$
$H_{aq} + H_2O_{aq} \rightarrow H_{2aq} + OH_{aq}$	$1.5x10^{-21}$
$H_{aq} + H_{aq} \rightarrow H_{2aq}$	$1.5x10^{-11}$
$H_{aq} + OH^-_{aq} \rightarrow H_2O^-_{aq}$	$3.0x10^{-14}$
$H_{aq} + HO_{2,aq} \rightarrow H_2O_{2,aq}$	$3.0x10^{-11}$

$H_{aq} + H_2O_{2,aq} \rightarrow H_2O_{aq} + OH_{aq}$	$1.5x10^{-15}$
$H_{aq} + HNO_{aq} \rightarrow OH_{aq} + NH_{aq}$	$2.18x10^{-22}$
$H_{aq} + OH^-_{aq} \rightarrow E_{aq} + H_2O_{aq}$	$2.0x10^{-14}$
$H_{aq} + NO_2^-_{aq} \rightarrow NO_{aq} + OH^-_{aq}$	$7.5x10^{-15}$
$H_{aq} + HNO_{2,aq} \rightarrow NO_{aq} + H_2O_{aq}$	$3.52x10^{-14}$
$H_{2aq} + H_2O_{2,aq} \rightarrow H_{aq} + OH_{aq} + H_2O_{aq}$	$1.0x10^{-14}$
$O_{aq} + H_2O_{aq} \rightarrow OH_{aq} + OH_{aq}$	$2.2x10^{-17}$
$O_{aq} + O_{2aq} \rightarrow O_{3aq}$	$5.0x10^{-12}$
$O_{2aq} + H_{aq} \rightarrow HO_{2aq}$	$5.0x10^{-11}$
$O_2(a^1\Delta_g)_{aq} + H_2O_{aq} \rightarrow O_{2,aq} + H_2O_{aq}$	$5.0x10^{-15}$
$O_2^-_{aq} + HO_{2aq} + H_2O_{aq} \rightarrow O_{2,aq} + H_2O_{2,aq} + OH^-_{aq}$	$2.68x10^{-34}$
$O_2^-_{aq} + H_2O_{2aq} \rightarrow O_{2,aq} + OH_{aq} + OH^-_{aq}$	$2.16x10^{-24}$
$O_2^-_{aq} + NO_{aq} \rightarrow NO_3^-_{aq}$	$6.0x10^{-12}$
$O_{3,aq} \rightarrow O_{2,aq} + O_{aq}$	$3.0x10^{-6}$
$O_{3,aq} + OH^-_{aq} \rightarrow O_2^-_{aq} + HO_{2,aq}$	$1.16x10^{-19}$
$N_{aq} + N_{aq} \rightarrow N_{2,aq}$	$5.0x10^{-14}$
$N_{aq} + H_2O_{aq} \rightarrow NH_{aq} + OH_{aq}$	$6.93x10^{-39}$
$NH_{aq} + NO_{aq} \rightarrow N_2O_{aq} + H_{aq}$	$1.3x10^{-12}$
$NH_{aq} + O_{2,aq} \rightarrow HNO_{aq} + O_{aq}$	$2.3x10^{-13}$
$NO_{aq} + NO_{aq} + O_{2aq} \rightarrow NO_{2,aq} + NO_{2,aq}$	$6.28x10^{-36}$
$NO_{aq} + NO_{2,aq} + H_2O_{aq} \rightarrow HNO_{2,aq} + HNO_{2,aq}$	$5.55x10^{-34}$
$NO_{aq} + HO_{2,aq} \rightarrow HNO_{3,aq}$	$5.33x10^{-12}$
$NO_{aq} + HO_{2,aq} \rightarrow ONOOH_{aq}$	$5.33x10^{-12}$
$NO_{aq} + O_2^-_{aq} \rightarrow ONOO^-_{aq}$	$7.14x10^{-12}$
$2\ NO_{2,aq} + 2\ H_2O_{aq} \rightarrow H_3O^+_{aq} + NO_3^-_{aq} + HNO_{2,aq}$	$1.26x10^{-56}$
$2\ NO_{2,aq} + 3\ H_2O_{aq} \rightarrow 2\ H_3O^+_{aq} + NO_3^-_{aq} + NO_2^-_{aq}$	$1.30x10^{-79}$
$NO_{2,aq} + OH_{aq} \rightarrow ONOOH_{aq}$	$1.99x10^{-11}$
$NO_{2,aq} + H_{aq} \rightarrow HNO_{2,aq}$	$1.67x10^{-11}$
$NO_2^-_{aq} + O_{3,aq} \rightarrow NO_3^-_{aq} + O_{2aq}$	$5.48x10^{-16}$
$NO_{3,aq} + H_2O_{aq} \rightarrow HNO_{3,aq} + OH_{aq}$	$4.8x10^{-14}$
$N_2O_{3,aq} + H_2O_{aq} \rightarrow HNO_{2,aq} + HNO_{2,aq}$	$1.93x10^{-17}$
$N_2O_{4,aq} + H_2O_{aq} \rightarrow HNO_{2,aq} + HNO_{3,aq}$	$1.33x10^{-18}$
$N_2O_{5,aq}\ H_2O_{aq} \rightarrow NO_{2,aq} + NO_{3,aq} + H_2O_{aq}$	$1.4x10^{-19}$
$N_2O_{5,aq} + H_2O_{aq} \rightarrow HNO_{3,aq} + HNO_{3,aq}$	$2.0x10^{-21}$
$N_2O_{5,aq} + H_2O_{aq} \rightarrow ONOOH_{aq} + ONOOH_{aq}$	$2.0x10^{-21}$
$H_2O_{2,aq} + NO_2^-_{aq} + H_3O^+_{aq} \rightarrow ONOOH_{aq} + H_2O_{aq} + H_2O_{aq}$	$3.04x10^{-39}$
$ONOOH_{aq} + H_2O_{aq} \rightarrow H_3O^+_{aq} + NO_3^-_{,aq}$	$2.9x10^{-23}$
$ONOOH_{aq} + H_2O_{aq} \rightarrow OH_{aq} + NO_{2,aq} + H_2O_{aq}$	$1.24x10^{-23}$

$HNO_{aq} + O_{2aq} \rightarrow HO_{2,aq} + NO_{aq}$	8.01×10^{-21}
$HNO_{aq} + O_{3aq} \rightarrow O_{2,aq} + HNO_{2,aq}$	9.61×10^{-15}
$HNO_{aq} + OH_{aq} \rightarrow H_2O_{aq} + NO_{aq}$	8.00×10^{-11}
$O_2NO_2^-{}_{aq} \rightarrow NO_2^-{}_{aq} + O_{2,aq}$	1.0×10^{0}
$HO_2NO_{2,aq} + HNO_{2,aq} \rightarrow HNO_{3,aq} + HNO_{3,aq}$	1.99×10^{-20}
$HO_2NO_{2,aq} \rightarrow HNO_{2,aq} + O_{2,aq}$	7.0×10^{-4}
$HO_2NO_{2,aq} \rightarrow HO_{2,aq} + NO_{2,aq}$	4.6×10^{-3}
$e^-_{aq} + H_2O_{aq} \rightarrow H_{aq} + OH^-_{aq}$	3.04×10^{-20}
$e^-_{aq} + e^-_{aq} + 2\ H_2O_{aq} \rightarrow H_{2,aq} + 2\ OH^-_{aq}$	4.096×10^{-55}
$e^-_{aq} + H_{aq} + H_2O_{aq} \rightarrow H_{2,aq} + OH^-_{aq}$	6.4×10^{-32}
$e^-_{aq} + OH_{aq} \rightarrow OH^-_{aq}$	4.80×10^{-11}
$e^-_{aq} + H_3O^+_{aq} \rightarrow H_{aq} + H_2O_{aq}$	3.68×10^{-11}
$e^-_{aq} + H_2O_{2,aq} \rightarrow OH_{aq} + OH^-_{aq}$	1.76×10^{-11}
$e^-_{aq} + HO_2^-{}_{aq} + H_2O_{aq} \rightarrow OH_{aq} + 2\ OH^-_{aq}$	8.96×10^{-33}
$e^-_{aq} + O_{2,aq} \rightarrow O_2^-{}_{aq}$	3.04×10^{-11}
$e^-_{aq} + H_2O_{aq} \rightarrow H_2O^-{}_{aq}$	5.0×10^{-15}

Finally, it is important to mention that the liquid in our model is pure water, with 4.8 ppm O_2 and 8.9 ppm N_2 initially dissolved into it (equilibrium values with air). The experiments were performed in a buffered solution at pH 7.3 (pH of PBS), so the concentrations of H_3O^+ and OH^- in the liquid were fixed throughout the entire simulation at values which correspond to this pH. This also means that in the model no solutes are present (*e.g.*, Cl^-), which can have a scavenging effect on CAP-generated species (see results Chapter 4).

3.3 Results and discussion

3.3.1 Comparison of model and experiment

The different CAP treatment conditions investigated are listed in Table 3.3.

TABLE 3.3: Plasma treatment conditions applied for creating pPBS, for both the chemical analysis and the effect on the cancer cell cytotoxicity. The gap is the distance between the nozzle and the surface of the liquid substrate.

Condition	Gas flow rate (slm)	Gap (mm)	Treatment time (min)
1	1	10	5
2	1	10	9
3	1	15	5
4	1	15	9
5	1	30	5
6	1	30	9
7	2	20	7
8	3	10	5
9	3	10	9
10	3	30	5
11	3	30	9

Figure 3.4 presents the measured concentrations of NO_2^- and H_2O_2 under the 11 conditions listed in Table 3.3 above. The ratios of the concentrations of NO_2^- and H_2O_2 are also indicated in the Figure. It is clear that the concentration of H_2O_2 is always larger than that of NO_2^-. Comparing conditions where the gas flow rate and gap are kept constant but only the plasma treatment time is varied, tells us that the ratio of the concentrations remains the same, except for conditions 8 and 9, where the concentration of NO_2^- is extremely low. Thus, a high gas flow rate and small gap (conditions 8 and 9) favour the formation of H_2O_2 compared to NO_2^-. Vice versa, at a low gas flow rate and a large gap (conditions 5 and 6), the concentrations of NO_2^- and H_2O_2 are comparable, indicating that the formation of NO_2^- is promoted. Note that the densities reported are spatially averaged densities over the entire volume of the liquid. Indeed, it is known that strong gradients in the density of species exist (especially during CAP treatment)[25], but this cannot be accounted for in this 0D model.

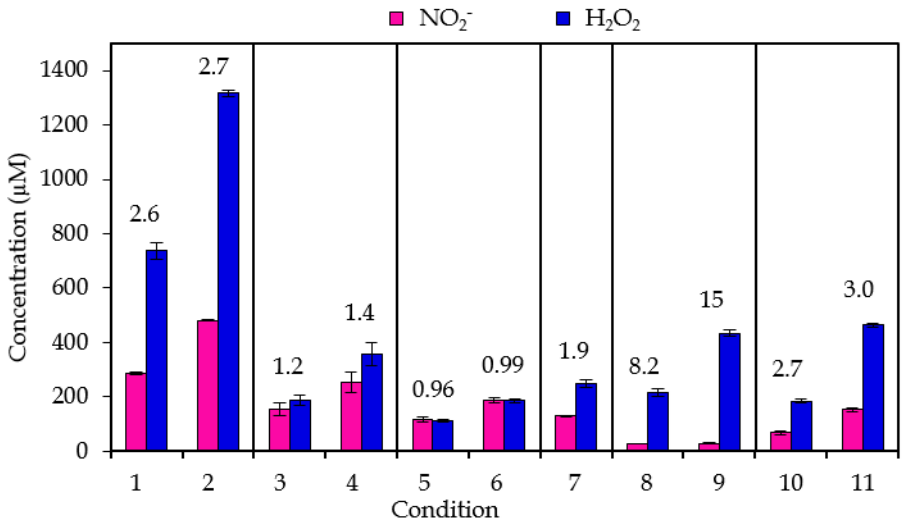

FIGURE 3.4: Concentrations of NO_2^- and H_2O_2 in pPBS at the 11 plasma treatment conditions listed in Table 3.3. Conditions for which only the plasma treatment time differs are indicated within one frame. The concentrations are plotted as the mean of at least three repetitions, and the error bars indicate the standard deviations of the mean. The numbers above the signals indicate the ratio of the concentration of H_2O_2 to the concentration of NO_2^- for that condition.

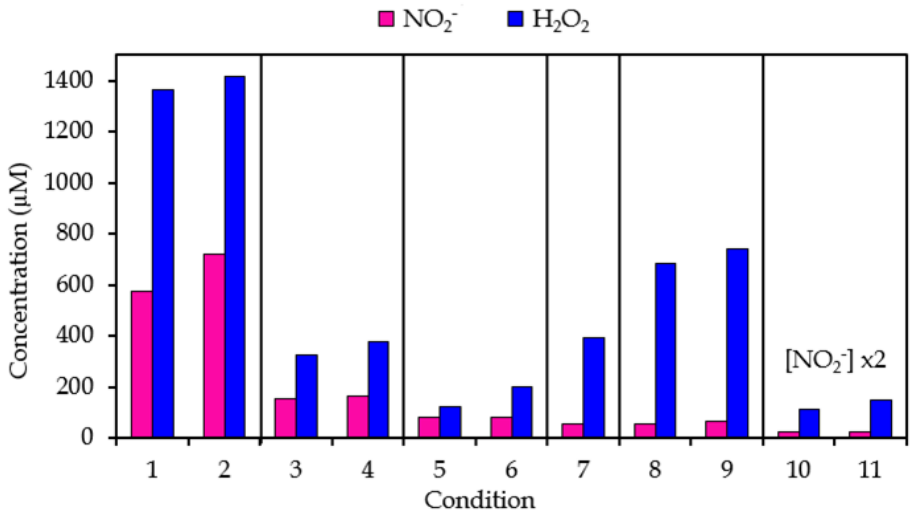

FIGURE 3.5: Concentrations of NO_2^- and H_2O_2 at the 11 plasma treatment conditions listed in Table 3.1, as obtained from the chemical kinetics model. Conditions for which only the plasma treatment time differs are again indicated within one frame.

The fact that different concentrations of species are formed by varying the plasma treatment conditions might be important in terms of the application, as some species will be more effective in killing the cancer cells, or might act even more selectively towards cancer cells than normal cells, in comparison to other species. Thus, by varying the plasma treatment parameters, the concentration of these particular species can be promoted.

Figure 3.5 presents the calculated liquid-phase concentrations of NO_2^- and H_2O_2 as obtained from the chemical kinetics model, at the 11 conditions listed in Table 3.3. When comparing these results to the experimental data of Figure 3.4, a reasonable agreement is observed both qualitative as well as quantitative. Indeed, although an exact agreement cannot be expected, due to the many assumptions made when using a chemical kinetics model, similar trends are observed in both the calculations and the experiments, in terms of (i) absolute values (quantitative agreement), (ii) higher H_2O_2 vs NO_2^- concentrations at (nearly) all conditions, and (iii) variations in concentrations as a function of plasma treatment time, gas flow rate, gap, and the presence of discharges onto the liquid surface (quantitative agreements). This indicates that the chemical kinetics model provides a realistic picture of the gas-phase and liquid-phase chemistry over the entire range of conditions investigated, and can thus be used to elucidate the underlying mechanisms at these various conditions.

A general scheme which highlights the main pathways leading to the generation and loss of H_2O_2 and NO_2^-, as predicted by the model, is depicted in Figure 3.6. This scheme shows the main formation and loss pathways for species included in the generation process of H_2O_2 and NO_2^-. Note that not all reactions that are present in the chemistry set are included in this figure. Indeed, only those reactions that play an important role are presented for the sake of clarity. The arrows in between different species represent reactions taking place to form the 'final' species from the reacting species. Moreover, scavenging reactions by components present in the treated liquid (*e.g.*, Cl^- in PBS) are not taken into account in this model. This could be introduced by including sink reactions, which ensures that a certain number of reactive

species is removed in each time step (as these specific components themselves are not included in the chemistry set). However, as there is not enough data available on how each of components reacts with all CAP-generated RONS, we chose to exclude these processes.

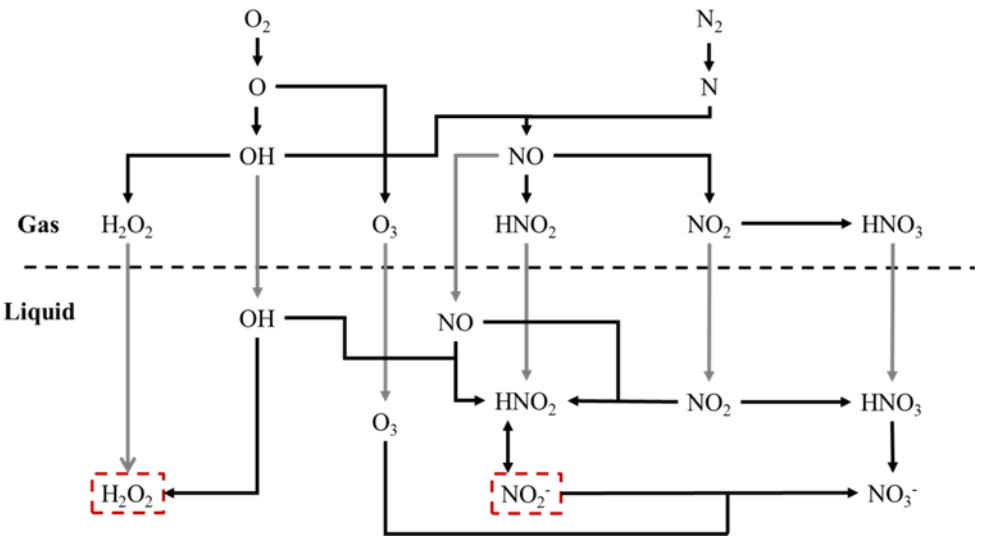

FIGURE 3.6: Main pathways in both the gas and liquid chemistry leading to the generation of NO_2^- and H_2O_2. The relative contributions of the different processes (*i.e.* chemical reactions (black lines) or diffusion processes (gray lines)) depend on the specific treatment conditions (see below). The gas-liquid interface is illustrated by the dashed horizontal line.

3.3.2 Generation of aqueous H_2O_2

H_2O_2 in the liquid phase originates back from O atoms in the plasma effluent. These radicals are mostly generated by electron-impact dissociation (R.1) or by collisions of O_2 with excited N_2 molecules (R.2).

$$O_2 + e^- \rightarrow O + O + e^- \quad \text{(R.1)}$$

$$O_2 + N_2^* \rightarrow O + O + N_2 \quad \text{(R.2)}$$

The O atoms react further with H_2O molecules (present in the ambient air and as impurities in the feed gas), generating $^\bullet OH$ (R.3).

$$O + H_2O \rightarrow {}^\bullet OH + {}^\bullet OH \quad \text{(R.3)}$$

From here, two processes can lead to the generation of H_2O_2 in the liquid phase, of which the relative contribution depends on the gap between the

nozzle and the liquid. For larger gap, the •OH will have the time to recombine in the plasma effluent, generating H_2O_2 in the gas phase, which is subsequently transported into the liquid layer (R.4). For shorter gap, the gaseous •OH will be transport into the liquid themselves (R.5), where most of them recombine to aqueous H_2O_2 (R.6).

$$^{\bullet}OH_g + {}^{\bullet}OH_g + M \rightarrow H_2O_{2,g} + M \rightarrow H_2O_{2,aq} \quad \text{(R.4)}$$

$$^{\bullet}OH_g \rightarrow {}^{\bullet}OH_{aq} \quad \text{(R.5)}$$

$$OH_{aq} + {}^{\bullet}OH_{aq} \rightarrow H_2O_{2,aq} \quad \text{(R.6)}$$

The calculated relative contributions of both pathways for the different conditions are listed in Table 3.4. This illustrates that in cases where the time it takes for the plasma effluent to reach the liquid is short (*i.e.* short gap and high flow rate), •OH that are transported into the liquid layer (where they recombine) are the main source for aqueous H_2O_2. For longer gap and lower flow rates, aqueous H_2O_2 mainly originates from gaseous H_2O_2, which is generated by •OH recombination in the gas phase.

TABLE 3.4: Contribution of gas phase H_2O_2 (R.4) and of •OH from the liquid phase (R.5-6), to the generation of aqueous H_2O_2.

Condition	Contribution (%)	
	R.4	R.5-6
1 - 2	14	86
3 - 4	29	71
5 - 6	98	2
7	15	85
8 - 9	2	98
10 - 11	41	59

The different treatment conditions not only affect the contribution of different pathways leading to the generation of H_2O_2, but they also affect the absolute amount of H_2O_2 generated in the liquid, as is clear from Figure 3.4 and 3.5. Indeed, at high flow rates and short gap, a large fraction of gaseous •OH survive transportation into the liquid. Thus, the aqueous •OH concentration will be significant, which promotes the recombination of •OH into H_2O_2 in the liquid, as this reaction rate is linearly dependent on the •OH concentration squared. On the other hand, at lower flow rates and longer gaps, many of the

gaseous •OH will already recombine in the gas phase. This recombination will, however, occur mostly with N-species (such as NO or NO_2), because their gas density is much higher than that of O-species (~80% of ambient air consists of N_2). This has a double effect on the aqueous H_2O_2 concentration: (i) the gaseous density of H_2O_2 will not increase upon increasing gap, so its contribution to the aqueous H_2O_2 is very similar in all cases (at the same flow rate), but (ii) because the aqueous •OH concentration is significantly lower at larger gap, the recombination rate into H_2O_2 in the liquid phase will be much lower. Consequently, the aqueous H_2O_2 concentration will decrease upon increasing the gap distance. The very high concentration of H_2O_2 observed at the shortest gap and lowest flow rate is attributed to the occurrence of discharges onto the liquid surface. Due to these discharges, a large number of electrons reaches the liquid substrate, which leads to the generation of OH radicals due to electron-impact reactions with H_2O molecules. Moreover, when discharges on the liquid occur, an electric current will pass through the liquid substrate, potentially enabling the electrolysis of water molecules.

3.3.3 Generation of aqueous NO_2^-

For NO_2^-, a similar analysis can be done. NO_2^- in the liquid is in balance with HNO_2 (see Figure 3.6). The latter is mainly generated in the liquid by three processes:

$$^{\bullet}OH_g + {}^{\bullet}NO_g \rightarrow HNO_{2,g} \rightarrow HNO_{2,aq} \quad \text{(R.7)}$$

$$^{\bullet}OH_{aq} + {}^{\bullet}NO_{aq} \rightarrow HNO_{2,aq} \quad \text{(R.8)}$$

$$^{\bullet}NO_{aq} + {}^{\bullet}NO_{2,aq} + H_2O_{aq} \rightarrow HNO_{2,aq} + HNO_{2,aq} \quad \text{(R.9)}$$

The relative contribution again depends on the treatment conditions and is shown in Table 3.5. At 1 slm flow rate, ambient air species can easily diffuse into the plasma effluent, and thus the HNO_2 concentration will already become very large in the gas phase, which explains why it is the most important source of aqueous HNO_2. Upon increasing flow rate, it will become more difficult for ambient air species to diffuse into the plasma effluent. Moreover, the species that are initially generated in the gas phase (*i.e.* •OH and •NO) have less time to recombine before reaching the liquid phase. Hence,

the relative contribution of R.7 decreases (most prominent when compared at 10 mm gap). By increasing the gap, the species have again more time to recombine in the gas phase, and thus the contribution of R.7 will increase again compared to R.8 (most prominent when compared at 3 slm).

TABLE 3.5: Contribution of different pathways to the generation of aqueous NO_2^-.

Condition	Contribution (%)		
	R.7	**R.8**	**R.9**
1 – 2	67	26	7
3 – 4	67	25	8
5 – 6	68	5	27
7	63	31	6
8 - 9	27	68	5
10 - 11	53	43	4

In order to explain the absolute concentrations of NO_2^- for the different conditions investigated, we have to keep in mind that to generate any of the HNO_2 (and thus NO_2^-) generating species (cf. R.7-9), both O_2 and N_2 are required. As mentioned before, by increasing the flow rate, the ability of these ambient air species to diffuse into the plasma effluent will drop. Therefore, the HNO_2 concentration measured in the liquid is much more dependent on the gas flow rate than H_2O_2, as can be derived from Figure 3.4 and 3.5.

Moreover, Figure 3.6 illustrates that the main loss process of NO_2^- is the reaction with O_3:

$$NO_2^-{}_{aq} + O_{3,aq} \rightarrow NO_3^-{}_{aq} + O_{2,aq} \qquad \text{(R.10)}$$

By increasing the gap, the amount of O_2 that can diffuse into the plasma effluent will rise, and thus also the amount of O_3 generated in the plasma effluent. This gaseous O_3 is subsequently transported into the liquid, where it will react with NO_2^-. This explains the drop in NO_2^- concentration upon increasing gap (see Figure 3.4 and 3.5).

In summary, our model predicts that both H_2O_2 and NO_2^- can be generated either (i) from diffusion of these species from the gas phase, or (ii) from aqueous reactions of short-lived species, and the relative contribution of

both pathways strongly depends on the treatment conditions (flow rate and gap).

3.3.4 Correlation between RONS and cell cytotoxicity

With the knowledge of which species are generated at what amounts in the different treatment conditions, it is possible to find correlations between the cell cytotoxicity assay (performed by Wilma Van Boxem) and specific alterations in the RONS mixture composition. Note that in these experiments, PBS was treated by plasma (forming pPBS) and administered to the different cell lines afterwards.

Figure 3.7 presents the percentages of cell cytotoxicity (percentage of total cells that are dead after treatment) for the three cell lines, along with the concentrations of NO_2^- and H_2O_2 shown in Figure 3.4, at exactly the same conditions to make the correlation between both. In these experiments, we only looked at cells being either death or alive, without focussing on different cell death mechanisms (*e.g.*, apoptotic versus necrotic cell death), although this would be very important to address in a follow-up study. Although not much is known regarding the differences between these human GBM cell lines, researchers have illustrated that LN229 and U251 can be classified as expansive-growth cells, whose proliferation rate is large and invasion ability is weak. U87-cells, on the other hand, are so-called cluster invasion cells, who showed rapid migration and the highest invasion ability.[113] In order to compare the concentrations of NO_2^- and H_2O_2 with the percentage of cell cytotoxicity for all conditions investigated, it is important to note that the results of the latter are always limited to a maximum of 100 % cell cytotoxicity, while the concentrations of NO_2^- and H_2O_2 are not limited and can be higher than the concentrations needed to achieve 100 % cell cytotoxicity.

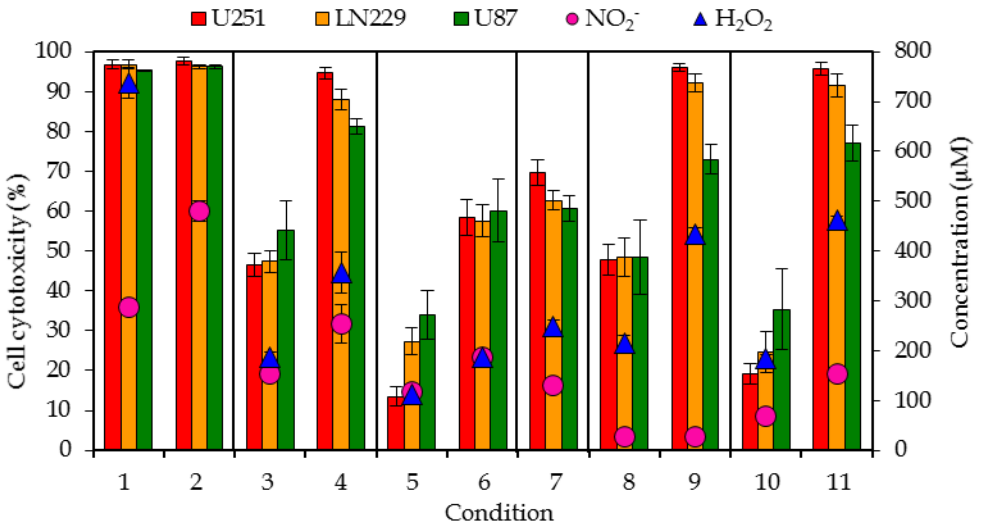

FIGURE 3.7: Effect of pPBS on cancer cell cytotoxicity for three different GBM cell lines (U251, LN229 and U87) (left y-axis), and comparison with the concentrations of NO_2^- and H_2O_2 in pPBS (right y-axis), for the 11 conditions listed in Table 3.3. Note that the H_2O_2 concentration in condition 2 is 1317 µM, but this is deliberately out of scale, to better evaluate the correlation between cell cytotoxicity and chemical composition for all other conditions.

It is evident from Figure 3.7 that the percentages of cell cytotoxicity exhibit the same trends as the concentrations of H_2O_2, but do not correlate with the concentrations of NO_2^-. Indeed, when the concentration of H_2O_2 raises, a higher percentage of cell cytotoxicity is obtained, and vice-versa. On the other hand, at conditions 8 and 9, there is almost no NO_2^- present in pPBS, while we observe a high percentage of cell cytotoxicity. Likewise, at conditions 3 and 11, the concentration of NO_2^- in pPBS is very similar, while condition 11 causes twice as much cell cytotoxicity as condition 3. Thus, we may conclude from this overview that H_2O_2 most probably plays a more important role in cancer cell cytotoxicity than NO_2^-, because the cell cytotoxicity follows the same trends as the H_2O_2 concentration over all the operating conditions. However, other species, like $^{\bullet}NO$, NO_3^- and ONOOH, can be important as well, either for killing the cancer cells, or for promoting the selectivity between cancer and normal cells (for which NO_2^- may also play an important role).

Further experiments, in which catalase was added to the pPBS after treatment, in order to remove H_2O_2 from the mixture, confirmed this finding. Indeed, after adding catalase, the cell cytotoxic effect of pPBS is removed entirely in all cases investigated, which means that H_2O_2 is the main species to induce cell death, which confirmed the findings of Sato *et al.*[29]

3.3.5 Cytotoxic effect of long-living RONS

Figure 3.8 presents the results of the experiments where we used H_2O_2- and/or NO_2^--rich PBS to compare the effect on cell cytotoxicity with pPBS. The concentrations of the reactive species added to PBS match these in the pPBS for the conditions considered. Firstly, it is clear that NO_2^- alone has no killing effect on GBM cancer cells in any case. Indeed, in some conditions, NO_2^--rich PBS even has a positive effect on the proliferation of cells (this is the case for cell lines LN229 and U87). This can be seen as an example of the hormesis effect often observed in biology, which means that a low dose can have a beneficial effect, whereas a higher dose has an inhibitory or toxic effect.[114] On the other hand, the H_2O_2-rich PBS is able to kill the cancer cells in all conditions for the U87 cell line. For U251 cells, the H_2O_2-rich PBS has only a killing effect for conditions 1 and 4, and for the LN229 cells H_2O_2 significantly kills cancer cells in all conditions, except 8. This reveals that H_2O_2 indeed contributes to the cancer cell cytotoxicity in most cases, but it cannot be the only important species.

When we consider both H_2O_2 and NO_2^- in PBS, there is mostly no additional killing effect observed, except for the U87 cell line, where in all cases a synergistic effect of H_2O_2 and NO_2^- is observed. We can conclude that the cell lines react differently on the addition of these reactive species, while the overall effect of pPBS on the three cell lines seems comparable (see above). Overall, it is unambiguous that H_2O_2 plays one of the major roles in the anti-cancer effect of pPBS, whereas NO_2^- is less important. However, the cell cytotoxicity of pPBS cannot be explained by H_2O_2-rich PBS alone, and other reactive species must contribute to the cell cytotoxicity as well, when using pPBS.

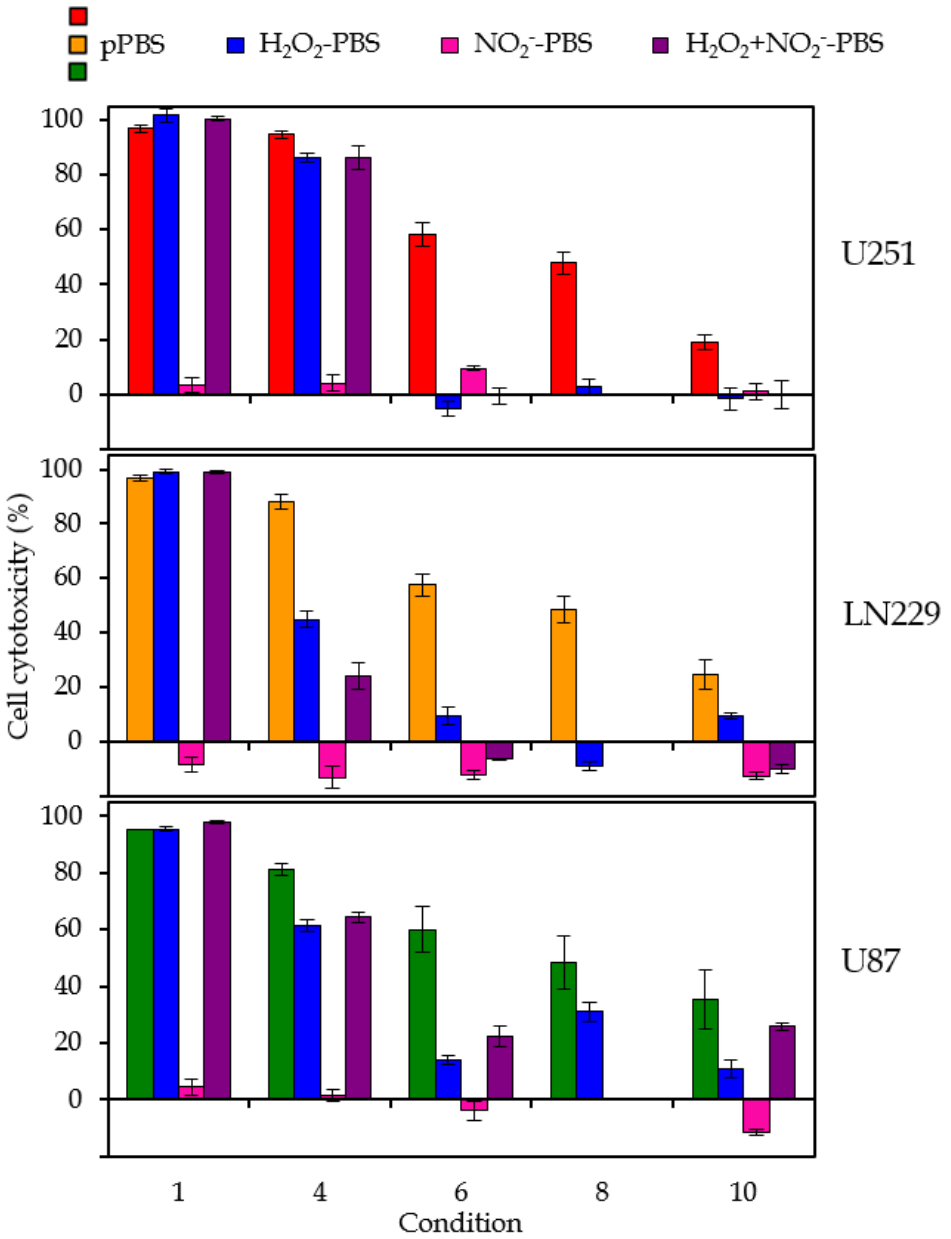

FIGURE 3.8: Comparison of the effect of pPBS with H_2O_2 and/or NO_2^--rich PBS on the cell cytotoxicity for three different GBM cell lines (U251, LN229 an U87). The concentrations of H_2O_2 and/or NO_2^- match these in the pPBS for the conditions considered (*i.e.* conditions 1, 4, 6, 8 and 10, which are listed in Table 3.3). For condition 8, no significant amount of NO_2^- is measured in the pPBS. Hence, only H_2O_2-rich medium is tested for that condition.

3.4 Conclusions

In collaboration with Wilma Van Boxem, we measured the chemical composition, more specifically the concentrations of NO_2^- and H_2O_2, of plasma-treated PBS (pPBS) with the kINPen®IND plasma jet, for different values of gas flow rate, gap and plasma treatment time, and we also evaluated the effect of this pPBS on cancer cell cytotoxicity for three different GBM cell lines, *i.e.*, U251, LN229 and U87, at exactly the same plasma treatment conditions. This should allow us to draw conclusions on the anti-cancer capacity of pPBS, and on the role of the two above-mentioned plasma species in pPBS for killing cancer cells.

First, it is clear from the experiments that varying the operating conditions during plasma treatment lead to different ratios of H_2O_2 and NO_2^- concentrations in pPBS, which can be important to consider when we know the exact role of individual species on cancer cell cytotoxicity and on their selectivity towards normal cells. To explain the generation processes of both H_2O_2 and NO_2^-, we developed a chemical kinetics model. We found that the H_2O_2 concentration is mostly determined by the time needed for $^{\bullet}OH$ to reach the liquid (affected by the gap and flow rate). Indeed, this determines whether the $^{\bullet}OH$ will recombine into H_2O_2 (at high $^{\bullet}OH_{aq}$ concentrations) or whether they will be consumed by N-species, forming HNO_2-HNO_3. For the NO_2^- concentration, on the other hand, our model predicts that (i) by increasing the flow rate, fewer ambient air species are able to diffuse into the effluent, thereby lowering the NO_2^- concentration, and (ii) by increasing the gap, more O_3 will be generated, which will consume NO_2^-, hence again lowering the NO_2^- concentration.

Furthermore, the experiments revealed that H_2O_2 is a major contributor to cancer cell cytotoxicity, while NO_2^- plays a minor role, but other reactive species should also play a role in the anti-cancer activity of pPBS. A synergistic effect between H_2O_2 and NO_2^- is found for the U87 cell line, but not for the U251 and LN229 cell lines.

TABLE 3.6: Summary. The effect of gap, gas flow rate, plasma treatment time, the occurrence of discharges at the liquid surface, and the stability of pPBS and pPBS with medium, on the concentrations of NO_2^- and H_2O_2 in pPBS and on the anti-cancer capacity of pPBS for three different cancer cell lines.

	NO_2^-	H_2O_2	U251	LN229	U87
Gap ↗	↘	↘	↘	↘	↘
Gas flow rate ↗	↘	↗	↗	↗	↗
Effect of plasma treatment time: ± linear?	✓	✓	✓	✓	✗
Discharges at the liquid surface	↗ x2	↗ x4	↗ ≥ x2	↗ ≥ x2	↗ ≥ x2

Table 3.6 summarizes the results of the effects of all plasma treatment parameters on the NO_2^- and H_2O_2 concentrations in pPBS, and on the cell cytotoxicity of the three different cancer cell lines. Increasing the gap results in lower concentrations of both NO_2^- and H_2O_2, as well as reduced cell cytotoxicity. This is logical because the plasma species are not so efficiently transferred into the liquid, which is less effective for killing the cancer cells. Increasing the gas flow rate leads to a drop in the NO_2^- concentration, because this species will not be formed so efficiently in the gas phase, as the N_2 and O_2 from the surrounding air come less in contact with the reactive plasma species. On the other hand, a higher gas flow rate yields a higher H_2O_2 concentration and also more cell cytotoxicity. This indicates that the anti-cancer capacity of pPBS is more related to the presence of H_2O_2 in the liquid than to the presence of NO_2^-. Increasing the plasma treatment time yields a more or less linear increase in both the NO_2^- and H_2O_2 concentrations in pPBS, and in the percentage cell cytotoxicity, except for the U87 cell line, although it is a bit dangerous to draw final conclusions on the linearity for the cancer cell cytotoxicity, based on only a few data points.

We also investigated the effect of the occurrence of discharges at the liquid surface on the NO_2^- and H_2O_2 concentrations in pPBS and on the cancer cell cytotoxicity, and observed that these discharges have a significant influence, yielding a factor 2 and 4 higher NO_2^- and H_2O_2 concentration in the liquid, as well as at least a factor 2 higher anti-cancer capacity of the pPBS. Indeed, these discharges allow electrons to reach the liquid and to produce more reactive species in the liquid due to electron impact reactions. This is important to

realize as a small variation of the gap (in our case between 10 and 15 mm) results in either the presence or absence of discharges at the liquid surface.

CHAPTER 4

Model development and applications of the COST-jet

The majority of the results presented in this chapter were published in:

Y. Gorbanev, J. Van der Paal, W. Van Boxem, S. Dewilde and A. Bogaerts. Reaction of chloride anion with atomic oxygen in aqueous solutions: can cold plasma help in chemistry research? *Phys.Chem.Chem.Phys.* **21**, 4117 (2019).

4.1 Introduction

As discussed in Chapter 1, the major focus of this thesis is the use of CAPs for medical applications. However, the immense potential of CAPs has also been shown in many other fields, such as green chemistry, materials chemistry and chemical synthesis.[115–117] As is the case in the medical applications of CAPs, this potential is defined by the large variety of highly reactive RONS, created by plasma.[118] RONS are mostly generated in the gas phase plasma and further interact with targets,[119] which are often represented by liquid solutions.[99] In Chapter 1, we discussed the two main methods of cold plasma application, *i.e.*, either (i) direct exposure to CAPs, or (ii) indirect treatment, using plasma-treated media (PTM; usually aqueous solutions).[7,26,30] Depending on the type of treatment, various RONS are responsible for the plasma-induced effects: persistent chemical species as in PTM (H_2O_2, NO_2^-, etc.) are combined with short-lived ones (radicals, atoms) during direct plasma application.[120]

Secondary chemistry involving chloride in aqueous solutions exposed to plasma was suggested by several groups.[121,122] The reactions of Cl^- with $^{\bullet}OH$ or $O_2^{\bullet-}$ radicals leading to ClO^- are known.[123] Very recently, Kondeti *et al*. suggested that in oxygen-containing plasmas, the main reaction leading to ClO^- formation may be a reaction of Cl^- and atomic O (R.1).[124]

$$Cl^- + O \rightarrow ClO^- \qquad \text{(R.1)}$$

Such a reaction may be very important for medical applications of plasmas, as Cl^- is present in buffers often used in cell line experiments (*e.g.*, PBS, see Chapter 3) and ClO^- is a very important biologically-active species[19,76,124] To the best of our knowledge, this chemical reaction has not been reported before. Generally, literature on the chemistry of atomic O in liquid phase is limited due to its high reactivity and the absence of simple chemical systems for its generation. The investigation of such a process is important for fundamental chemistry purposes, and also has large implications for biomedical plasma research. Direct evidence is required to assess the feasibility of this reaction.

In this work, we studied which RONS can oxidise Cl- to ClO- in plasma-treated solutions. We used the COST plasma jet, which was created as a 'standard' plasma jet, and its chemistry is well studied both computationally and experimentally.[13] It was previously shown that all reactive species are created inside the COST jet, and undergo further reactions in the effluent.[125] Importantly, it was also shown to be an efficient source of O atoms, which were detected in aqueous solutions.[126,127]

Note: The experiments included in this chapter were performed by Yury Gorbanev, and will therefore not be discussed in detail in this thesis.

4.2 Methodology

4.2.1 Experimental set-up

The plasma was ignited inside the jet using a feed gas of He with O_2 admixtures operated with two mass flow controllers (MFCs) (Figure 4.1), at a total flow rate of 1 $L.min^{-1}$ (all experimental details can be found in the supporting information of our paper[128]). We studied the formation of ClO^- in phosphate buffered saline (PBS) exposed to plasma. PBS is often used in biomedical plasma research, especially as PTM.[22] Plasma exposure conditions were similar to those used in previous works with the COST jet.[26,125] To assess the interaction of He+O_2 plasma with Cl^- in aqueous media, we measured the concentrations of plasma-induced RONS in two solutions: PBS and PB (the same as PBS, but without Cl^-). Different set-ups (propagation of the effluent into ambient air or inside an air-free reactor) and measuring techniques (EPR measurements using different spin-traps or colourimetry with different reagents) were used to measure different CAP-generated species in the treated liquid (including O, O_3, $^1O_2$, $^{\bullet}OH$, $^{\bullet}OOH$, H_2O_2 and NO_2^-).

To analyse the chemistry occurring in the gas phase under these different operating conditions, I developed a chemical kinetics model of the COST-jet, and validated it against the experimental measurements of the above mentioned species.

4.2.2 Chemical kinetics model

The approach of using a chemical kinetics model of the COST-jet is identical as described in the previous chapter, section 3.2.2. Indeed, as was the case in the chemical kinetics model of the kINPen, a cylindrical volume element is followed along the jet stream, thereby assuming a homogenous plasma along the radial axis.

As mentioned in Chapter 3, a chemical kinetics model calculates the density of all species as a function of time. By assuming a certain velocity profile of the feed gas, however, we can couple this time to the position of the volume element along the axis, which allows us to obtain information on the species densities as a function of distance. Furthermore, a gas temperature profile along the plasma axis is required to calculate the exact rate coefficients of all reactions of the heavy species, which are usually gas temperature dependent. Moreover, as the electron impact reactions depend on the EEDF, the reduced electric field is also required, which is in turn calculated based on the deposited power density. The power density profile applied is based on the electrode set-up of the COST-jet (see Figure 4.1).

Being a cross-field jet (see Figure 4.1), the COST-jet does not have a visible effluent, in contrast to the parallel-field kINPen IND, which has a typical visible effluent of 9-12 mm, as discussed in Chapter 3. As the densities of exited species (responsible for the visible effluent) in our model drop immediately as soon as the applied power is removed, this translates, for the case of the COST-jet, in a constant power density profile in the source, which drops to zero as soon as the effluent is reached. This is different from the kINPen IND, in which power was still applied in the first 9 mm of the effluent (see Chapter 3).

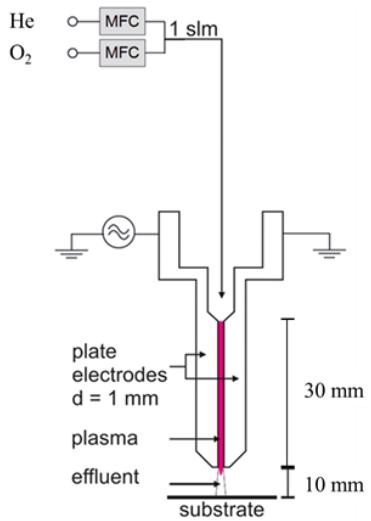

FIGURE 4.1: Schematics illustration of the set-up and dimensions of the COST-jet. The treatment distance was 10 mm for all results reported (both experimentally as well as in the simulations).

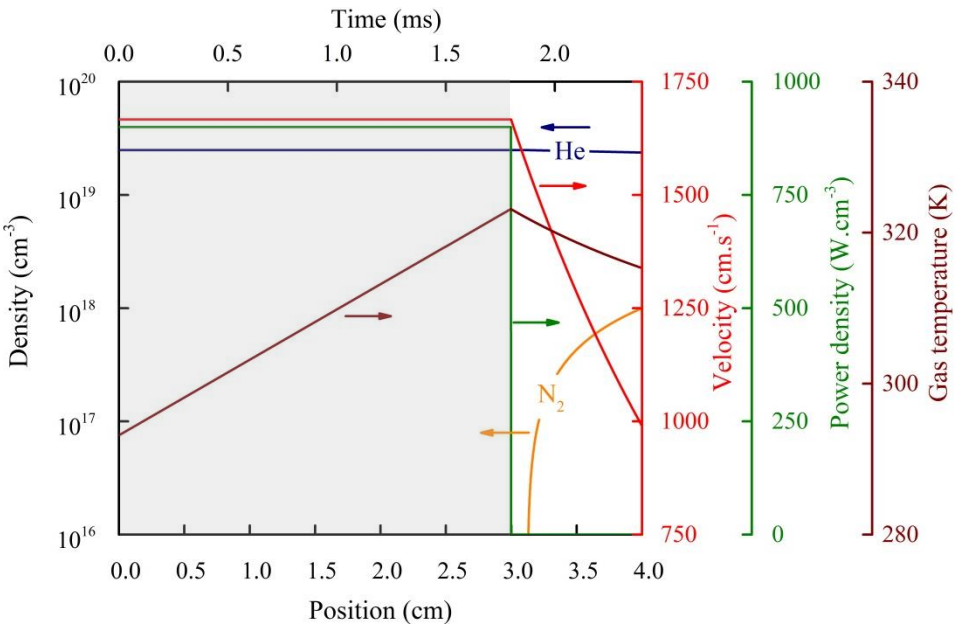

FIGURE 4.2: Illustration of the different input profiles used in the 0D simulations of the COST-jet. The grey zone (position 0-3 cm) indicates the region inside the source. Outside the source, the power density drops to zero, and as a result, the electron production rate drops to zero as well. Mixing with ambient air starts 0.12 cm outside of the jet, which is based on 2D fluid simulations (performed by Wilma Van Boxem). Ambient air species include N_2 (shown as a representative example), O_2 and H_2O.

Lastly, to mimic the mixing of (humid) air species into the effluent of the plasma jet, these species (N_2, O_2 and H_2O) are added into the effluent, assuming a certain air mixing rate (based on 2D fluid simulations). The profiles used as input for the model (axial velocity, power density, gas temperature and ambient air densities) are illustrated in Figure 4.2. The velocity profile is based on 2D fluid dynamics simulations, whereas the gas temperature and power density are assumptions based on experimental measurements[13].

The chemistry set of the gas phase reactions used in this study is identical to that used in chapter 3. It is largely taken from Murakami *et al*.[111], and extended with the reactions describing the behaviour of biomedically relevant species (*e.g.*, H_2O_2, $^{\bullet}OOH$, HNO_3 or HNO_2), adopted from the chemistry set of Van Gaens and Bogaerts[112]. This yields a total chemistry set of 91 different species and 1390 reactions.

4.3 Results and discussion

4.3.1 Results of the gas phase model

In a first set-up, the concentration of ROS (O_3, $^1O_2$, O) created by CAP were measured. Of these, only the reaction of O_3 with Cl^-, yielding ClO^- in aqueous solution, is known (R.2).[129]

$$Cl^- + O_3 \rightarrow ClO^- + O_2 \qquad \text{(R.2)}$$

The ROS concentration was measured based on electron paramagnetic resonance (EPR) spectroscopy analysis of the stable nitroxide TEMPO, formed in the reaction of the spin trap TEMP (2,2,6,6-tetramethylpiperidine) with O and $^1O_2$ (Figure 4.3).

Although we previously observed oxidation of TEMP by O_3,[119] later all formed TEMPO was ascribed to the reaction of TEMP with O (in the absence of $^1O_2$).[130] To investigate this further, the plasma effluent was not exposed to ambient air, but instead propagated inside an air-free reactor.[125,131] Since $^1O_2$ and O are short-lived, the exhaust of the reactor could contain only O_3: its

presence was confirmed by the oxidation of 3,3′,5,5′-tetramethylbenzidine (TMB) in PB exposed to the reactor exhaust. When a solution of TEMP was exposed to the reactor exhaust for 2 min, no formation of TEMPO was observed. This was consistent with the findings by Elg *et al.*, where O_3 at CAP-induced concentrations did not oxidise TEMP.[130] Thus, we conclude that all of the formed TEMPO observed under these experimental conditions was due to the oxidation of TEMP by O and $^1O_2$. Increasing the O_2 concentration in the feed gas above 0.2 % led to a decreasing amount of TEMPO formation. This can be attributed to an increased oxidation of O to O_3 (see modelling results in Figure 4.4), which in turn does not oxidize TEMP (see above). Note that other species (*e.g.*, $^{\bullet}OH$ or $O_2^{\bullet-}$) might react with TEMP, but these will not lead to the formation of TEMPO.

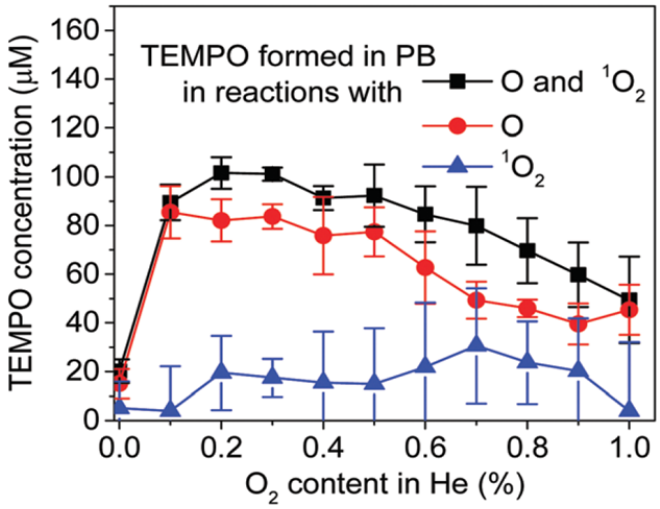

FIGURE 4.3: Concentrations of spin trapped O/$^1O_2$ in PB by He+O_2 plasma. The error bars are standard deviations between three measurements. Concentrations of $^1O_2$-induced TEMPO were obtained as a difference between experimental results with and without NaN_3; errors bars are sums of those in the two experimental conditions used.

Next, the introduction of an $^1O_2$ scavenger (NaN_3) enabled distinguishing between TEMPO formed by O and $^1O_2$.[119] The resulting trends of O and $^1O_2$ concentrations in the liquid compared very well with the trends of their gas phase concentrations predicted by our chemical kinetics model (Figure 4.4), once again confirming that TEMPO here was formed only by these ROS.

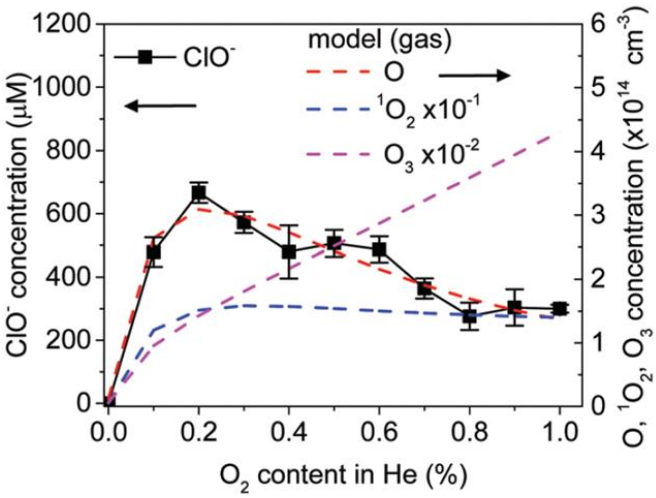

FIGURE 4.4: Concentration of ClO^- in plasma-treated PBS as determined by UV-vis spectrophotometry, and gas phase concentrations of O, $^1O_2$ and O_3 (dashed lines) as predicted by the chemical kinetics model. The error bars are the standard deviations between three measurements.

The observed trend of TEMPO concentration was virtually the same in PBS and PB, except that the concentrations were slightly lower in PBS, both with and without added NaN_3 (comparison of Figures 4.3 and 4.5 for results in PB and PBS, respectively).[128]

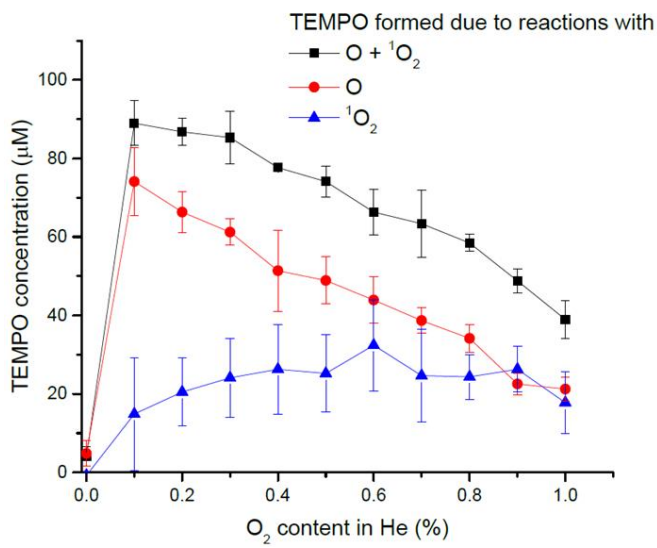

FIGURE 4.5: Formation of TEMPO in PBS as measured by EPR. The error bars the represent the standard deviation of three measurements.

This is probably due to the partial scavenging of O atoms by Cl^-. The total concentration of Cl^- in PBS is ca. 140 mM,[132] and TEMP was used at 20 mM concentration. Since the concentration of the formed TEMPO changed only marginally in the presence of Cl^-, the reaction rate coefficient of O with Cl^- is likely around 2–3 orders of magnitude lower than that of O with TEMP. Further kinetic studies are required for precise evaluation of this reaction.

Further, we assessed the amounts of other plasma-induced RONS such as NO_2^-, H_2O_2, $^{\bullet}OH$ and $^{\bullet}OOH/O_2^{\bullet-}$ in plasma-treated PB and PBS (Figure 4.6 a–c). H_2O_2 and NO_2^- were detected using colourimetry with Ti(IV) and the Griess reagent, respectively, and the radicals were detected by EPR, as described in previous works.[26,119,125]

With the COST jet, H_2O_2 can be either formed in the liquid from $^{\bullet}OH$ radicals, or delivered into the liquid already in its molecular form.[125] However, while low concentrations were detected in PB, no H_2O_2 was detected in PBS (Figure 4.6a). This suggests that either $^{\bullet}OH$ or H_2O_2 (or both) were scavenged by Cl^- ((R.3) and (R.4)).

$$Cl^- + {}^{\bullet}OH + {}^{\bullet}OH \rightarrow ClO^- + H_2O \qquad \text{(R.3)}$$

$$Cl^- + H_2O_2 \rightarrow ClO^- + H_2O \qquad \text{(R.4)}$$

Unlike H_2O_2 which was detected in the liquid after the CAP treatment (and thus was largely affected by further reactions in PBS, involving Cl^- and/or ClO^-), the radicals were spin trapped during the plasma exposure. The EPR analysis with 5-diethoxyphosphoryl-5-methyl-1-pyrroline N-oxide (DEPMPO) spin trap showed that the concentrations of the radicals decreased dramatically in both PBS and PB when O_2 was added to He (Figure 4.6b). The experimentally measured concentrations of H_2O_2 and the radical adducts DEPMPO–OOH and DEPMPO–OH generally agreed with the trends of the concentrations obtained by chemical kinetics modelling (dashed line in Figure 4.6a and Figure 4.7).

While very good agreements between the model and the experiments were achieved for $^{\bullet}OOH/O_2^{\bullet-}$, for $^{\bullet}OH$ the model predicted a low amount of

DEPMPO-OH at 0% O_2 in He. The experiments showed a higher concentration of DEPMPO-OH at 0% O_2 in He (see Figure 4.6b). We tentatively speculate that this was probably because plasma generates a large amount of He* metastables in the absence of admixtures to the feed gas. These metastables can reach the liquid and generate additional $^{\bullet}OH$ from H_2O, probably from a dense layer of vapour above the liquid solution.[120] The latter process could not be accounted for in the model.

These data together suggest that H_2O_2 detected in PB was delivered to the solution at least partially in molecular form, and was not detected in PBS due to the reaction with Cl^- (leading to ClO^-)[129] and/or with the formed ClO^-[133] ((R.4) and (R.5)).

$$ClO^- + H_2O_2 \rightarrow Cl^- + H_2O + O_2 \qquad (R.5)$$

NO_2^- was formed due to the interaction of the plasma effluent with ambient air. The NO_2^- concentration dropped below the detection limit in both PBS and PB with O_2 in the feed gas (Figure 4.6c). This could happen due to the reaction between NO_2^- and the formed ClO^- in PBS.[134] However, since the same trend was also observed in PB and was predicted by the model (see dashed line in Figure 4.5c), and as the latter did not include Cl^- chemistry, we propose that this was due to the further oxidation of NO_2^- to NO_3^-, or of NO_2^- precursors to N_2O_5 (Figure 4.7b). Most importantly, the results show that the main species present in the system, and which can oxidise Cl^- to ClO^- is indeed atomic oxygen. This species is delivered to the solutions in high concentrations by the COST jet operated with O_2 admixtures, making this CAP system a unique tool for the selective O induction in liquid.

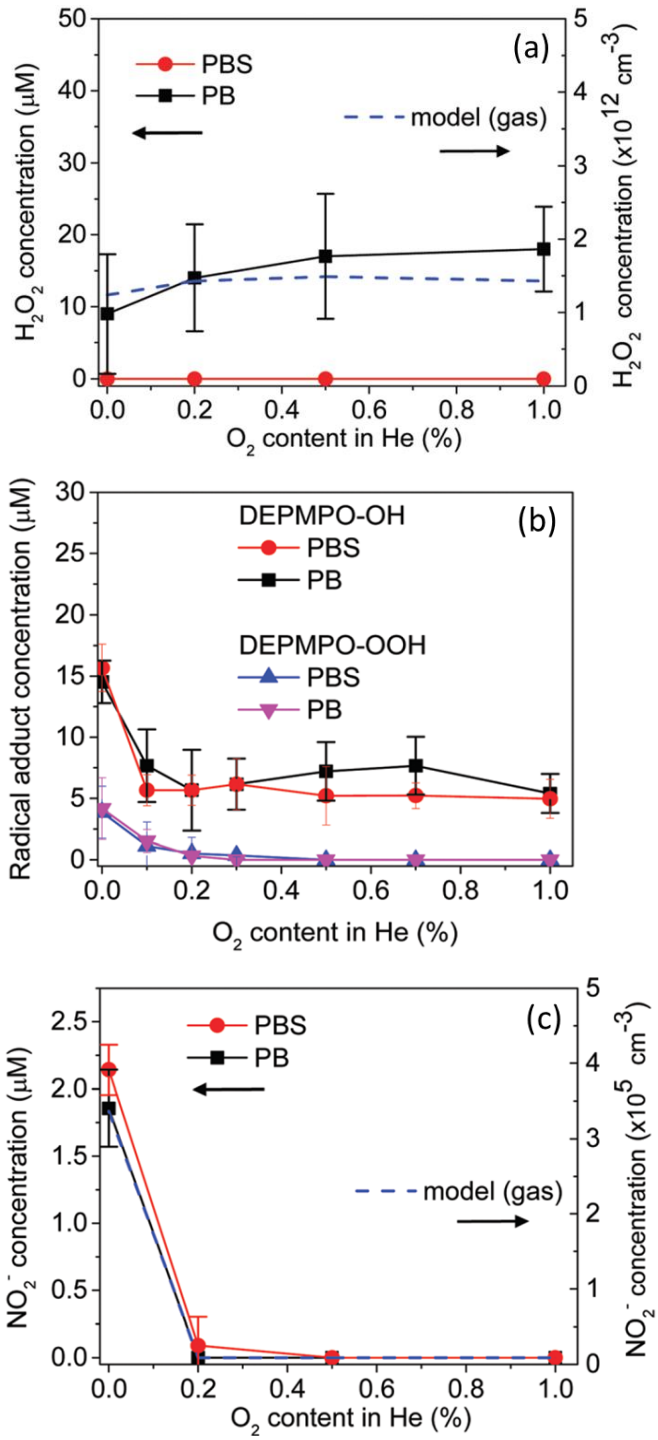

FIGURE 4.6: Concentrations of (a) H_2O_2, (b) spin trapped $^{\bullet}OH$ and $O_2^{\bullet-}$/$^{\bullet}OOH$ radicals, and (c) NO_2^- in both PB and PBS. The error bars are the standard deviations between three measurements. Gas phase modelling data is shown with dashed lines.

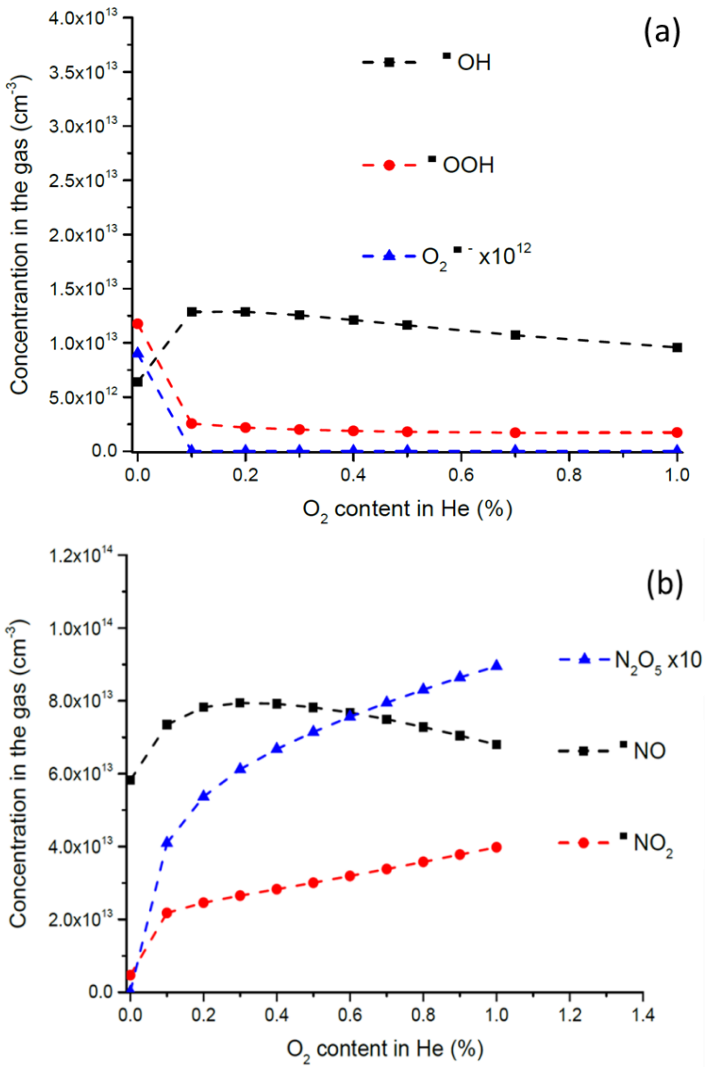

FIGURE 4.7: Concentrations of (a) $^{\bullet}$OH, $^{\bullet}$OOH and $O_2^{\bullet-}$, and (b) $^{\bullet}$NO, $^{\bullet}NO_2$ and N_2O_5 in the gas phase, as predicted by the chemical kinetics model. The trends of $^{\bullet}$OOH and $O_2^{\bullet-}$ agree well with the experimental data (see Figure 4.6b): in aqueous media, DEPMPO-OOH adduct may represent adducts with both $^{\bullet}$OOH and $O_2^{\bullet-}$ radicals.[115,129] Note that the RONS obtained at 0% O_2 originate from impurities in the feed gas (O_2, N_2 and H_2O), or from ambient air in the effluent.

Finally, we assessed the formation of ClO^- in PBS by exposure to plasma. A facile and sensitive measurement of ClO^- presents a challenge. Reports on ClO^- detection in CAP-exposed water suggest the possible use of L-tyrosine,[135] or describe deep UV spectrophotometry with a high detection limit.[123,124] In this study, we used a recently reported colourimetric method based on the

oxidation of TMB,[136] which allowed us to detect ClO^- with a lower limit of 1–2 mM. Since TMB can react with several oxidising species,[136] we investigated the applicability of the method for selective ClO^- detection in plasma-treated PBS, *i.e.* the interference of other possible CAP-induced primary and secondary reactive species. ClO_3^- and ClO_4^- (possible products of further oxidation of ClO^-) and H_2O_2 did not oxidise TMB in concentrations of up to 1 mM, whereas ClO_2^- did, but only after a long incubation time, in contrast with ClO^-.[128] In any case, we did not detect ClO_2^-, ClO_3^- or ClO_4^- in plasma-treated PBS using ion chromatography. NO_2^- (added as $NaNO_2$) used in concentrations detected in plasma-treated PB or PBS did not oxidise TMB either. Furthermore, PB exposed to He + O_2 plasma with any studied O_2 content did not oxidise TMB, clearly indicating the absence of any residual O_3 remaining in solution after plasma treatment. Thus, the presented method is both selective and highly sensitive, and can be used for the detection of ClO^- in PTM. It also enables the detection of ClO^- in a regular plate reader without requiring deep UV spectrophotometers. However, it is not applicable *in situ* during the treatment, due to the oxidation of TMB by O_3 and possibly other plasma RONS.

The trend of the measured ClO^- concentration as a function of the O_2 content in the feed gas is shown in Figure 4.4. Remarkably, the trend of ClO^- concentration coincided with that of the O atom concentration calculated by the computational model (Figure 4.4). At the same time, the O_3 concentration in the gas phase increased with higher content of O_2, while the $^1O_2$ concentration stayed nearly the same at 0.2–1% O_2. Additionally, when PBS was first exposed to the O_3-rich exhaust of the air-free reactor (as described above) and then analysed with TMB, no ClO^- was detected. Therefore, we conclude that most of the ClO^- was formed due to the reactions with atomic O. Thus, we were able to confirm the reaction between Cl^- and atomic O, which yields ClO^- from (i) the similarity of the experimentally obtained trends of the formed ClO^- concentration and TEMPO formed by O, (ii) nearly identical trends of formed ClO^- and the model-predicted gas phase concentration of atomic O, and (iii) the reduced amounts of TEMPO formed in PBS compared to PB (Figure 4.3, 4.4 and 4.5). These observations are in perfect alignment

with a recent paper of Jirasek et al.[137] who also suggested a reaction between Cl^- and O-atoms leading to the formation of ClO^-.

One important note to make is that CAPs rarely generate $^{\bullet}OH$ without also creating H_2O_2 in the gas phase.[26] Therefore, although ClO^- may be formed from Cl^- by $^{\bullet}OH$ radicals, it will be consumed by H_2O_2 (R.5) or NO_2^- in CAPs operating with air.[134,135] In other words, while ClO^-, possessing high biomedically relevant properties,[124] may potentially be formed in Cl-rich solutions such as PBS by almost all plasmas *in situ*, its effect on biological or other substrates will depend on the rate of its decay by other CAP-produced RONS.

4.3.2 Development and results of the liquid phase model

Note: The model discussed in this section was developed after publishing the paper discussed above. It is added to this chapter as it regards an improved chemical kinetics model of the liquid phase, applied to the COST-jet.

Introduction

In Chapter 3, we already discussed the development of a chemical kinetics model to investigate the chemistry in a liquid substrate treated by the kINPen IND. However, it was clear from this chapter that, although the general trends of the experimental results could be captured by our chemical kinetics model, for certain conditions the overlap was not entirely satisfactory (see Figures 3.3 and 3.4 in Chapter 3). Therefore, we improved this model in order to try to capture the experimental observations better. As the gas phase of the COST-jet is thoroughly validated by experiments in this Chapter, we present here the chemical kinetics model for this source. In future research, we will try to implement the same approach in different CAP sources, including the kINPen IND[14], SOFT-jet[15] and FE-DBD device[27].

Model set-up

The coupling of the gas and liquid phase is similar as discussed in Chapter 3. Indeed, to investigate the chemistry occurring in the PTL, a second set of species and a separate chemistry set were included in the chemical kinetics

model. First, a duplicate solvated species was added for each important gas phase species (*e.g.*, O_{3aq} for O_3). The importance of each species was either based on the final gas phase density of these species or their relevance for the biomedical applications. These aqueous species and the liquid reactions are restricted to the liquid module only (and are thus not taken into account in the gas phase module). The species in these two modules can only interact through the gas-liquid interphase by means of diffusion into or out of the liquid. In general, the densities of the liquid species are given by:

$$\frac{\partial n_{s,l}}{\partial t} = \sum_{i=1}^{j}\left[\left(a_{s,i}^{R} - a_{s,i}^{L}\right).R_i\right] + S\,.\,D_s\frac{(h_s.n_{s,g} - n_{s,l})}{h_s} \qquad (4.6)$$

in which $n_{s,l}$ is the liquid phase density of species s (m^{-3}), j the total number of reactions, $a_{s,i}^{L}$ and $a_{s,i}^{R}$ the stoichiometric coefficients at the left hand side and right hand side of the reaction, and R_i the reaction rate (in $m^{-3}.s^{-1}$). D_s is the liquid diffusion coefficient of gas phase species s, $n_{s,g}$ is the final gas phase density of species s and h_s the Henry constant of species s. The scaling constant S is required in these simulations, due to the lack of dimensions in the chemical kinetics model (similar to the scaling factor discussed in Chapter 3, which was taken from Lietz *et al.*[94]). This constant is dependent on the experimental set-up, accounting for, *e.g.*, dimensions of the source (area of the effluent), flow rate, volume and surface area of the treated liquid. This formula is slightly different from that used in the model discussed in Chapter 3 (see equations 3.7 and 3.8), although the general idea is the same (*i.e.*, transport based on diffusion coefficient and henry's constant).

Furthermore, this model is an improved version compared to the model discussed in Chapter 3, as the liquid is now divided into two regions, *i.e.*, the interface and the bulk liquid (see Figure 4.8). Equation 4.6 is therefore, in a first step, used to describe the transport of gas phase species to the interface (based on the final density of all species in the gas phase simulation) and subsequently, in a second step, the transport from the interface to the bulk liquid (based on the final density of all species in the interface simulation).

The chemistry set used for the gas phase simulation of the COST-jet is similar to the set presented in Chapter 3, although modifications are made to accommodate for helium as feed gas, instead of argon. The liquid phase chemistry set is also slightly different to that used in Chapter 3. Indeed, before, the reaction rate coefficients of reactions involving short- and longer-lived species had to be reduced to mimic the decreasing concentration of short-lived species in the bulk of the liquid (see section 3.2.4). As we now use two different liquid simulations to separately account for the interface and bulk liquid, we don't need this approach anymore, and therefore, we could use the reaction rate coefficients presented by Lietz *et al*.[94]

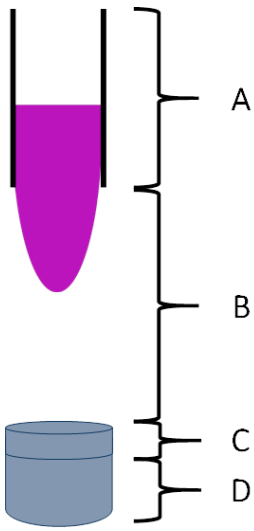

FIGURE 4.8: Schematic illustration of the different regions described in the chemical kinetics model. The gas phase simulation follows an infinitesimal volume-element along the plasma axis from inside the source (A) towards the effluent (B), until the substrate is reached. The gas phase species are then transported in the interface region of the liquid (C), before being transported into the bulk of the liquid (D). It has to be noted that the liquid in the model is just water (at pH 7.3, *i.e.*, the pH of PBS and PB), which is different from what is used experimentally (either PB or PBS). This means it does not contain solutes, which are present in the experiment (*e.g.* Cl^- or PO_4^-).

The operating conditions of the COST-jet used in this study are slightly different from the conditions used before in this Chapter. Instead of O_2, different amounts of H_2O are added to the helium feed gas (0%, 5% or 20% H_2O vapour admixture). These conditions were chosen to allow a comparison

with the recent measurements of H_2O_2 and NO_2^- concentrations in PTL, presented in a publication of Privat-Maldonado *et al.*[26]

Validation of the liquid model

Validation of the liquid phase simulations is based on comparison of the concentrations of H_2O_2 and NO_2^- between the model and experiments, as mentioned above.[26] This comparison is shown in Figure 4.9.

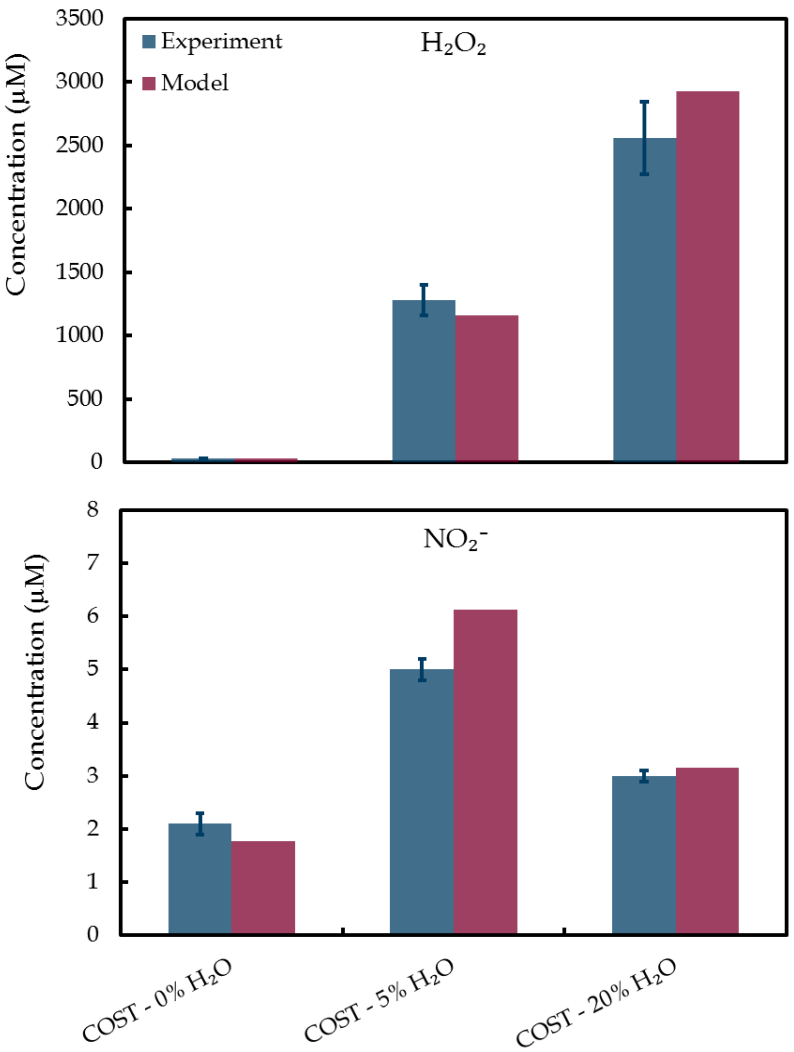

FIGURE 4.9: Comparison of the bulk liquid concentrations of H_2O_2 and NO_2^- obtained by model and experiment. In all conditions, 200 µL PBS was treated at a flow rate of 1 slm, with a treatment distance of 10 mm and treatment time of 3 minutes.

The assumptions made in the gas phase simulations are the same as discussed in section 4.2.2 of this Chapter. The value of the scaling constant used in the interface simulation is based on the value used in our previous work (discussed in Chapter 3), *i.e.*, 2.59×10^{9} m^{-2}. The value of the scaling constant used in the bulk simulation (1.2×10^{8} m^{-2}) is determined to match the absolute values of the liquid concentrations measured experimentally. The duration of the interface simulation is 5 s, after which the bulk liquid simulation starts, which takes 3 minutes, to mimic the experimental treatment time.[26] As can be seen from Figure 4.9, the agreement is quite satisfying. Of course, we use scaling constants to reach the same order of magnitude, but the latter are taken as the same for all conditions (*i.e.*, all H_2O admixtures), and Figure 4.9 shows that the trends of measured concentrations as a function of H_2O addition are correctly reproduced by the model.

After this validation, reaction rate analysis of the different source and loss terms allows us to identify the main pathways leading to all species included in the model.

General overview of the gas and liquid phase chemistry

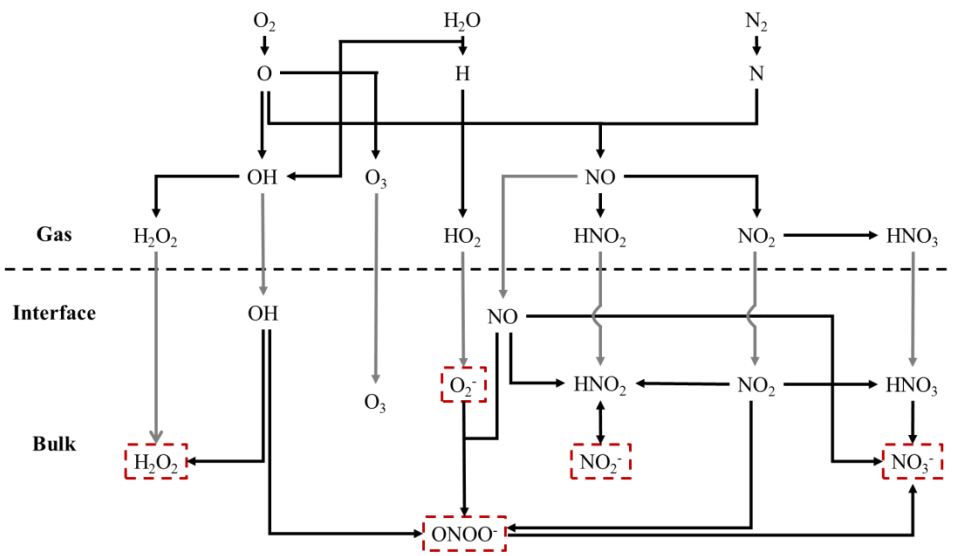

FIGURE 4.10: Reaction scheme depicting the main pathways leading to the stable aqueous species (depicted in red frames). The black arrows involve chemical reactions, whereas the grey arrows depict the diffusion of gas phase species into the liquid.

Based on a full reaction analysis of all major species in the gas and liquid phase, Figure 4.10 depicts the general reaction scheme that can be constructed to illustrate the pathways leading to the major species in both phases. The liquid phase concentrations of the five long-lived RONS are listed in Table 4.1, for the different feed gas compositions. In the following sections, the reaction analysis of these species is discussed separately.

TABLE 4.1: Calculated concentrations of the long-lived RONS in the liquid, obtained by the chemical kinetics model. The concentrations are given in μM.

Aqueous species	Dry He	He +5% H_2O	He + 20% H_2O
H_2O_2	31.4	1158.7	2929.3
NO_2^-	1.8	6.1	3.2
NO_3^-	3.1	2.8	1.5
$O_2^{\bullet-}$/$^\bullet$OOH	$5.3.10^{-3}$	$29.4.11^{-3}$	$39.7.10^{-3}$
$ONOO^-$/ONOOH	$14.6.10^{-3}$	$10.5.10^{-3}$	$5.8.10^{-3}$

Hydrogen peroxide — H_2O_2

The formation of H_2O_2 is dominated by the recombination of $^\bullet$OH in the gas phase. Depending on the feed gas (*i.e.*, H_2O admixture), these radicals are either created inside the jet (R.7 or R.8; *i.e.*, in the case of H_2O addition), or in the effluent (R.9 or R.10; in the case of dry helium gas flow), as is illustrated in Figure 4.11.

Jet	$H_2O + e^- \rightarrow {}^\bullet OH + {}^\bullet H + e^-$	(R.7)
	$H_2O + He^* \rightarrow {}^\bullet OH + {}^\bullet H + He$	(R.8)
Effluent	$^\bullet OOH + {}^\bullet H \rightarrow {}^\bullet OH + {}^\bullet OH$	(R.9)
	$^\bullet OOH + {}^\bullet O \rightarrow {}^\bullet OH + O_2$	(R.10)

The position of 3 cm indicates the end of the jet, *i.e.*, where the power is removed (see Figure 4.2). At this point, all radicals start to recombine, which explains why the density of $^\bullet$OH decreases. In the case of dry helium, however, a small increase can be seen, due to the recombination of $^\bullet$H and $^\bullet$OOH (R.9). At the position of 3.12 cm, the density of $^\bullet$OH increases again (in all cases, but most prominent in dry helium), due to the mixing with ambient

air (see Figure 4.2). At this position, •H still present in the effluent will react with O_2, leading to the formation of •OOH. •OOH in turn, will be converted in •OH according to R.9 and R.10. In the far effluent (position > 3.12 cm), the •OH density decreases faster with increasing humidity of the feed gas. This is because the density of all other ROS (*e.g.*, •OOH or H_2O_2) is higher in this case, which serve as scavengers of •OH. Therefore, the lower their density (*i.e.*, lowest in the case of dry helium), the longer •OH can survive in this effluent.

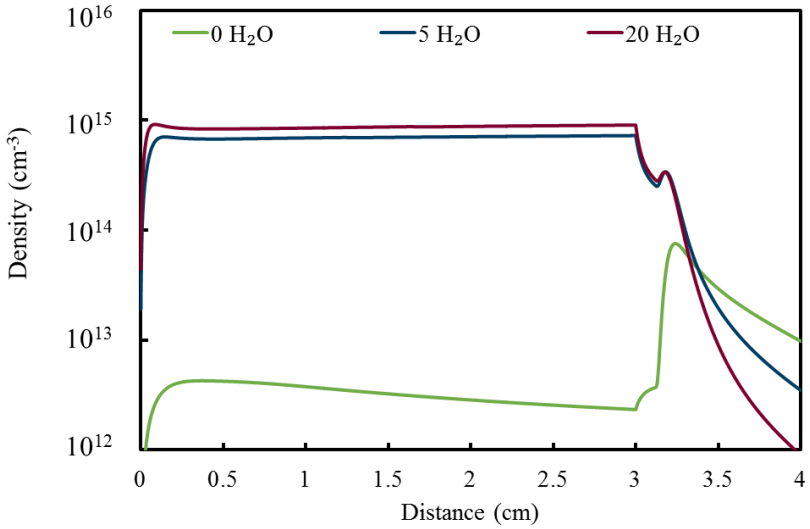

FIGURE 4.11: •OH density profile in the gas phase along the plasma axis, for the different feed gas compositions.

As H_2O_2 is generated by the recombination of •OH, the density profiles of H_2O_2 follow those of •OH. This means that when H_2O is added to the feed gas, almost all H_2O_2 is generated inside the jet itself, whereas in the case of dry helium, all H_2O_2 is generated in the effluent.

Moreover, the contribution of (i) diffusion of gaseous H_2O_2 into the liquid (R.11), versus (ii) the recombination of solvated •OH in the liquid (R.12) to the total generation of aqueous H_2O_2 in the interface also depends on the exact operating conditions.

$$^{\bullet}OH_g + {}^{\bullet}OH_g \rightarrow H_2O_{2,g} \rightarrow H_2O_{2,aq} \quad \text{(R.11)}$$

$$^{\bullet}OH_g \rightarrow {}^{\bullet}OH_{aq} + {}^{\bullet}OH_{aq} \rightarrow H_2O_{2,aq} \quad \text{(R.12)}$$

The contribution of both possible pathways is listed in Table 4.2 for each operating condition. By adding H_2O to the feed gas, the contribution of gas phase H_2O_2 to the generation of aqueous H_2O_2 increases significantly. This is because (i) the gas phase density increases by increasing the humidity of the feed gas and (ii) the number of $^{\bullet}OH$ that reach the surface decreases with increasing H_2O concentration in the feed gas (see Figure 4.11).

TABLE 4.2: Contribution of diffusion of gas phase H_2O_2 (R.11) and recombination of $^{\bullet}OH$ in the liquid phase (R.12) to the total H_2O_2 concentration in the liquid interface.

Feed gas	Contribution (%)	
	R.11	R.12
Dry helium	63	37
Helium + 5% H_2O	99	1
Helium + 20% H_2O	98	2

As $^{\bullet}OH$ rapidly recombines in the interface, the only contribution to H_2O_2 in the bulk of the liquid is the diffusion from the interface towards the bulk. Overall, we can conclude that the increasing H_2O_2 concentration upon increasing H_2O admixture observed in the experiments (Figure 4.9) can be attributed to the increasing $^{\bullet}OH$ density inside the source.

Nitrite — NO_2^-

The formation of NO_2^- in the liquid phase (note, this deprotonated form of HNO_2 is most stable at the working pH of 7.3 in PBS) is, under all conditions investigated, entirely dependent on the formation of HNO_2. As is the case for H_2O_2, the formation of HNO_2 can occur in the gas phase (R.13), or, due to recombination of radicals that reach the liquid surface, *in situ* in the liquid interface. Figure 4.12 illustrates the density profiles of HNO_2 in the gas phase, along the plasma axis for the different H_2O admixture.

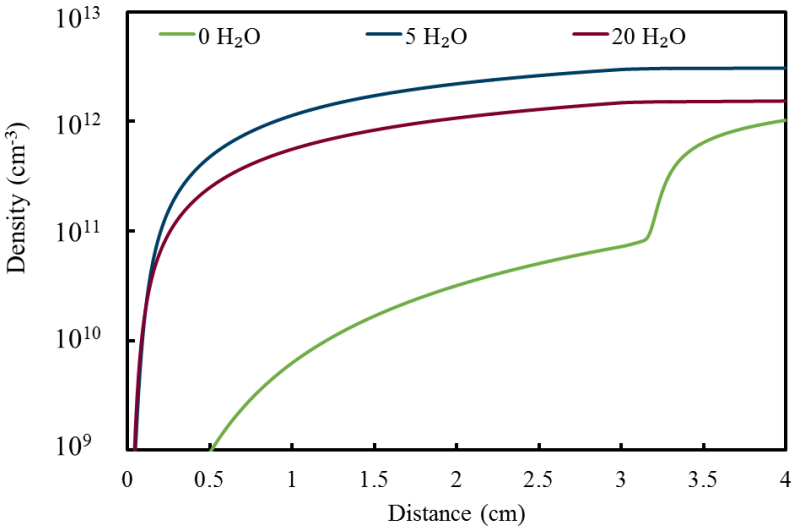

FIGURE 4.12: HNO_2 density profile along the plasma axis for the different feed gas compositions.

Similar to H_2O_2, in the case of dry helium, HNO_2 is mostly formed in the effluent of the COST-jet, due to recombination of $^{\bullet}OH$ and $^{\bullet}NO$ radicals (R.13). When H_2O is added to the feed gas, on the other hand, the largest fraction of HNO_2 is already generated inside the source (due to the high density of $^{\bullet}OH$ inside the jet, see Figure 4.12), although the mechanism is the same in all cases (R.13).

$$^{\bullet}OH + {}^{\bullet}NO + He \rightarrow HNO_2 + He \qquad (R.13)$$

The generation of aqueous HNO_2 in the liquid interface, in turn, is again a sum of both diffusion of gaseous HNO_2 (R.14), or recombination of short-lived RONS in the interface (R.15-R.20). The exact contribution of these pathways depends on the feed gas composition (Table 4.3).

$$^{\bullet}OH_g + {}^{\bullet}NO_g \rightarrow HNO_{2,g} \rightarrow HNO_{2,aq} \qquad (R.14)$$

$$^{\bullet}OH_g \rightarrow {}^{\bullet}OH_{aq} \qquad (R.15)$$

$$^{\bullet}NO_g \rightarrow {}^{\bullet}NO_{aq} \qquad (R.16)$$

$$^{\bullet}OH_{aq} + {}^{\bullet}NO_{aq} \rightarrow HNO_{2,aq} \qquad (R.17)$$

$$^{\bullet}NO_{2,g} \rightarrow {}^{\bullet}NO_{2,aq} \qquad (R.18)$$

$$^{\bullet}NO_{2,aq} + {}^{\bullet}NO_{2,aq} + H_2O_{aq} + H_2O_{aq} \rightarrow HNO_{2,aq} + NO_{3^-,aq} + H_3O^+_{aq} \quad (R.19)$$

The increasing contribution of diffusion of gas phase HNO_2 to the generation of aqueous HNO_2/NO_2^- (*i.e.*, pathway R.14) upon adding H_2O to the feed gas, is explained by the rising overall concentration of HNO_2 in the gas phase (see Figure 4.12). As far as the bulk liquid is concerned, similar to H_2O_2, the formation of NO_2^- in the bulk liquid is entirely dependent on the diffusion from the interface.

TABLE 4.3: Contribution of diffusion of gas phase HNO_2 (R.14) and recombination of short-lived RONS in the liquid interface (R.15-R19) to the total HNO_2 concentration in the interface. R.15-R.17 indicates the pathway of $^{\bullet}OH$ and $^{\bullet}NO$ radicals, whereas R.18-R.19 regards the disproportionation of $^{\bullet}NO_2$.

Feed gas	Contribution (%)		
	R.14	R.15-R.17	R.18-R.19
Dry helium	61	38	1
Helium + 5% H_2O	99	0	1
Helium + 20% H_2O	100	0	0

Based on the main generation pathways, we would assume that the HNO_2 concentration should increase upon increasing humidity of the feed gas, as this will lead to a higher $^{\bullet}OH$ density, which is involved in most generation pathways (R.14 and R.17). However, the main destruction pathway of HNO_2 also involves $^{\bullet}OH$ (R.20), which explains why overall, the experimentally obtained NO_2^- concentration reaches a maximum at 5% H_2O admixture, and drops upon higher H_2O admixtures in the feed gas (Figure 4.9)

$$HNO_{2,g} + {}^{\bullet}OH_g \rightarrow {}^{\bullet}NO_{2,g} + H_2O_g \quad (R.20)$$

Nitrate — NO_3^-

The formation of NO_3^- in the interface depends on both the diffusion of HNO_3 from the gas phase (R.21-R.22), as well as several aqueous reactions (R.23-R.25).

$$^{\bullet}OH_g + {}^{\bullet}NO_{2,g} \rightarrow HNO_{3,g} \rightarrow HNO_{3,aq} \quad \text{(R.21)}$$

$$^{\bullet}OOH_g + {}^{\bullet}NO_g \rightarrow HNO_{3,g} \rightarrow HNO_{3,aq} \quad \text{(R.22)}$$

$$^{\bullet}OH_{aq} + {}^{\bullet}NO_{2,aq} \rightarrow HNO_{3,aq} \quad \text{(R.23)}$$

$$O_2^{\bullet-}{}_{aq} + {}^{\bullet}NO_{aq} \rightarrow NO_3^-{}_{aq} \quad \text{(R.24)}$$

$$ONOOH_{aq} + H_2O_{aq} \rightarrow NO_3^-{}_{aq} + H_3O^+{}_{aq} \quad \text{(R.25)}$$

The profiles of the gas phase density of HNO_3 under different feed gas compositions are identical to those of HNO_2, displayed in Figure 4.12. The contribution of the two main formation pathways of HNO_3 in the gas phase (R.21 and R.22) depends on the feed gas composition (see Table 4.4). By adding H_2O to the feed gas, the contribution of the $^{\bullet}OH$ pathway (R.21) to the formation of gas phase HNO_3 increases (due to the significant increase of $^{\bullet}OH$ in the gas phase, see Figure 4.12). Moreover, as the concentration of gas phase HNO_3 increases by adding H_2O to the feed gas (similar to HNO_2, see Figure 4.12), the overall contribution of gaseous HNO_3 to the aqueous HNO_3/NO_3^- concentration also increases (see Table 4.4, increase in contribution of R.21).

TABLE 4.4: Contributions of the different pathways leading to the formation of aqueous NO_3^-.

Feed gas	Contribution (%)				
	R.21	**R.22**	**R.23**	**R.24**	**R.25**
Dry helium	5.8	1.7	46.8	24.3	21.3
Helium + 5% H_2O	32.4	0.7	3.4	46.9	18.9
Helium + 20% H_2O	30.7	0.8	0.4	48.7	19.4

Furthermore, Table 4.4 also lists the contributions of the different liquid reaction pathways leading to the formation of aqueous NO_3^-. The aqueous $^{\bullet}OH$ pathway (R.23) contributes for almost 50% in the case of dry helium, but its contribution decreases significantly when adding H_2O to the feed gas, due to the lower amount of $^{\bullet}OH$ reaching the substrate, as illustrated and discussed above (see Figure 4.12). In contrast, the superoxide anion ($O_2^{\bullet-}$) pathway (R.24) becomes much more important upon H_2O addition, with a contribution of almost 50%. This is due to the increase of the aqueous $O_2^{\bullet-}$

concentration with increasing humidity of the feed gas (see Table 4.1 and discussion below).

Superoxide anion — $O_2^{\bullet-}$

The formation of superoxide anions in the liquid is entirely dependent on the generation of $^{\bullet}OOH$ in the gas phase (the simulation results show that there is no net production due to liquid phase chemistry, see Fig 4.10). Indeed, once diffused into the solution, $^{\bullet}OOH$ (pK_a = 4.88) will be deprotonated at the working pH of 7.3. The formation of $^{\bullet}OOH$ in the gas phase occurs in the effluent of the jet, and is dominated by two processes (R.26 and R.27), of which the contributions are listed in Table 4.5.

$$^{\bullet}H + O_2 + He \rightarrow {}^{\bullet}OOH \qquad \text{(R.26)}$$

$$^{\bullet}OH + H_2O_2 + He \rightarrow {}^{\bullet}OOH + H_2O \qquad \text{(R.27)}$$

TABLE 4.5: Contributions of different pathways leading to the formation of $^{\bullet}OOH$ in the gas phase.

Feed gas	Contribution (%)	
	R.26	**R.27**
Dry helium	99.2	0.1
Helium + 5% H_2O	85.1	13.8
Helium + 20% H_2O	66.3	32.8

The reaction of H-atoms with molecular oxygen (O_2) (R.26) is clearly dominant, but as the concentration of H_2O_2 increases with increasing humidity of the feed gas, the contribution of R.28 increases as well. This also leads to an increasing concentration of aqueous $^{\bullet}OOH$, as shown in Table 4.1. In the bulk of the liquid, $O_2^{\bullet-}$ is lost, as it is converted into NO_3^- (R.24) or $ONOO^-$ (R.28).

$$^{\bullet}NO_{aq} + O_2^{\bullet-}{}_{aq} \rightarrow ONOO^-{}_{aq} \qquad \text{(R.28)}$$

Peroxynitrite — $ONOO^-$

As $ONOO^-$ is not included in the gas phase chemistry (due to a lack of data regarding its gas phase kinetics), the accumulation of peroxynitrite (or peroxynitrous acid, pK_a = 6.8) depends on the liquid chemistry in our model.

The generation of these species is controlled by two formation pathways (R.28 and R.29), of which the relative contributions are listed in Table 4.6.

$$^{\bullet}OH_{aq} + {}^{\bullet}NO_{2,aq} \rightarrow ONOOH_{aq} \qquad (R.29)$$

TABLE 4.6: Contributions of different pathways leading to the formation of aqueous $ONOO^-$/ONOOH

Feed gas	Contribution (%)	
	R.28	**R.29**
Dry helium	42.1	57.9
Helium + 5% H_2O	100.0	0.0
Helium + 20% H_2O	100.0	0.0

Upon adding H_2O to the feed gas, the density of $^{\bullet}OOH_{aq}$ increases, whereas that of $^{\bullet}OH_{aq}$ decreases, which explains why the contribution of R.28 increases and that of R.29 decreases upon increasing humidity of the feed gas. In the bulk of the liquid, ONOOH is converted into NO_3^-, according to R.25.

4.4 Conclusions

To summarize, in the first part of this chapter, we demonstrated, using a combination of experimental and modelling approaches: (1) a new reaction of Cl^- with atomic oxygen yielding ClO^-; (2) the high dependence of ClO^- stability in PTM on other CAP-generated RONS. This emphasises the importance of liquid phase reactions in plasma-exposed solutions. The generation of the secondary reactive species (either short-lived *in situ*, or persistent in PTM) from solution components could affect biological substrates, similarly to the primary plasma RONS. In addition, we also presented a facile method for ClO^- detection in plasma-treated aqueous solutions. Finally and most importantly, we illustrated that cold plasma can serve as a unique tool for the generation of short-lived RONS, such as O atoms, much sought-after in chemical applications.

In the second part of this chapter, we presented an improved version of our chemical kinetics model to investigate the liquid phase chemistry. In this improved version, we try to better mimic the experimental treatments by

differentiating between the interface and the bulk of the liquid. The results obtained with this new liquid model showed a very good agreement with the experimental measurements. Furthermore, reaction analysis allowed us to identify the main generation and destruction pathways of several important RONS. Knowledge of the importance of different gas and liquid phase reactions, in turn, allowed us to give an explanation for the experimental measurements. Indeed, we were able to explain that the concentration of H_2O_2 increases significantly when adding H_2O to the feed gas, due to a higher $^{\bullet}OH$ density in the source, whereas the $HNO_2/NO2^-$ density remained quite constant, as $^{\bullet}OH$ is both involved in the main source as well as the main loss processes.

CHAPTER 5

Cholesterol and RONS permeation

The results presented in this chapter were published in:

J. Van der Paal, C. Verheyen, E. C. Neyts and A. Bogaerts. Hampering effect of cholesterol on the permeation of reactive oxygen species through phospholipid bilayers as possible plasma cancer selectivity filter. *Sci. Rep.* **7**, 39526 (2017).

5.1 Introduction

The anti-cancer capacity of cold plasma has been suggested by many researchers in the past years (mainly in *in vitro* work).[2–4,22,26,30,86–91,98,138] Some of these investigations also illustrated that cancer cells are more susceptible to CAP-induced cell death, in comparison to healthy cells, which would allow us to treat them selectively.[2–4] However, on the other hand, other researchers have shown that there is no differentiation between cancer cells and healthy cells when treating them with CAP, or that cancer cells even are more resistant to CAP-induced cell death.[5–7] The variety of results obtained by different researchers stresses the clear need for more fundamental insight into possible underlying mechanisms during CAP treatment of cancer and healthy cells.[45] Indeed, as there are many differences between cell lines (*e.g.*, differences in lipid or protein expressions, see Chapter 1), increasing our knowledge on how CAPs interact with cells might increase our understanding of why different cell lines behave differently when exposed to CAP.

Over the last years, multiple theories have been proposed, but there is no consensus regarding the observed selectivity. All these models, however, stress the key role of reactive oxygen and nitrogen species (RONS) which are generated by the plasma.[20] Healthy cells are thought to deal better with this increased oxidative stress because they will take up less exogenous RONS and can neutralize these species more efficiently.[61] The main objective of this research was to provide new insights in the search for an explanation for this observed selectivity. Continuing upon the assumption that one of the major reasons behind the selectivity is that cancer cells absorb RONS faster compared to their healthy counterparts, a new question imposes itself: what difference between both cell types is responsible for this different uptake rate?

A possible explanation could be the increased expression of aquaporins (AQPs), a membrane protein family responsible for facilitating the diffusion of water across cellular membranes, in cancer cells. Indeed, it is shown that different cancer cell lines possess elevated levels of certain AQPs.[71–74] Breast

cancer cell lines for example, show increased levels of AQP1, 4 and 5[73,74], whereas AQP 1, 4, 8 and 9 are highly expressed in glioblastoma cell lines.[71,72,74] Due to the similarity of hydrogen peroxide (H_2O_2 - one of the most important RONS) and water, AQPs are also able to facilitate the passive diffusion of this reactive species through the plasma membrane[139], which results in an increased oxidative stress. An important note, however, is that not all AQPs are able to transport H_2O_2 across the membrane equally efficiently.[140] This is due to the central pore present in each AQP, which acts as a selective filter. The central pore diameter of AQP1, for example, is only 2.8 Å which is too small to allow for an easy diffusion of H_2O_2, resulting in a very low permeability for H_2O_2 across this specific AQP.[140] AQP8, on the other hand, has a central pore diameter of 3.2 Å, enabling it to very efficiently transport H_2O_2.[140] The combination of the altered expression levels of certain AQPs together with the different central pore diameters of these AQPs could be used to explain the sensitivity of different cancer cell lines towards CAP treatment.[24]

In this chapter, however, we focus on yet another difference between the cell membrane of cancer cells and healthy cells, which is the cholesterol fraction of the membrane. It is known that the metabolism of cholesterol is altered in cancer cells. Indeed, a decreased concentration is observed in metastatic cells[67–69], whereas multidrug resistant cells display elevated levels of cholesterol[69]. This might be a very important difference since cholesterol is of great importance in maintaining the proper fluidity and rigidity in the plasma membrane of all animal cells[141–144], in which it is one of the most abundant lipids with concentrations up to 50%.[145,146] Therefore, over the last years, the cholesterol fraction of cell membranes has been the subject of many computational[147–149] and experimental[150,151] investigations. These studies have provided a detailed understanding of the condensing and ordering effects of cholesterol. Due to these effects, an alteration of the cholesterol fraction might have a big effect on the permeation of RONS through the membrane of both cancer and healthy cells. In our previous work[1] we showed that if lipid peroxidation occurs (a process in which the impinging RONS oxidize the

phospholipids of the membrane), a decreased cholesterol concentration will lead to a weakened membrane, eventually leading to pore formation, which did not occur when membranes contain elevated levels of cholesterol. This finding is illustrated in Figure 5.1.

Since the observed pore diameters were in the order of 15 Å, these pores could serve as channels through which H_2O_2, as well as other RONS, would be able to penetrate the membrane easily, leading to an increase of the intracellular oxidative stress, which, in turn, can cause cell death.

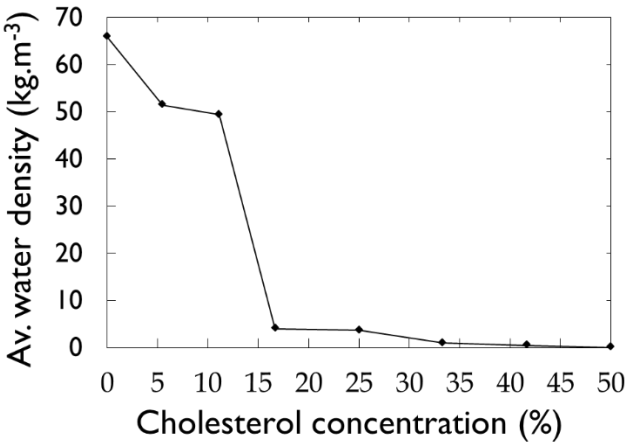

FIGURE 5.1: Water density inside the core of the membrane, averaged over the entire membrane, in the case of a fully oxidized lipid membrane, as obtained from MD simulations.[152] This shows that from ~ 11 mol% of cholesterol upwards, the membrane will resist pore formation, even if it fully oxidized. If the cholesterol content is lower, lipid oxidation can lead to the formation of nanopores, which will facilitate RONS permeation.

However, for these pores to be formed, oxidation degrees of over 60 % were required[1], at least on the simulated time scale. Since these high oxidation degrees might not be achievable during plasma treatments (no experimental data are available on the exact oxidation degree), the question arises what the effect of cholesterol on its own (without lipid peroxidation) would be on the permeation of different ROS through a lipid membrane. Therefore, in this chapter, MD simulations are performed to calculate the free energy profile (FEP) of H_2O_2, O_2, $^{\bullet}OH$ and $^{\bullet}OOH$ across phospholipid membrane structures

containing a varying cholesterol concentration, using the umbrella sampling (US) technique. This technique is used to improve the sampling of the entire system, which would be hindered in a traditional MD simulation due to the presence of hydrophilic and hydrophobic regions in a phospholipid bilayer. From the obtained FEPs, free energy barriers for permeation across the bilayer systems can be derived. MD studies have been used frequently in the past in the field of plasma oncology and plasma medicine in general.[92] Several of these studies have shown the applicability of the US method. Indeed, Cordeiro used this method to calculate the FEPs of similar ROS through a POPC membrane and found a good agreement with experimental results for the permeation free energy barrier of H_2O_2.[153] Furthermore, Wennberg *et al*. used US simulations to investigate the effect of cholesterol on solute (*e.g.*, ammonia, ethanol or benzene) partitioning into different phospholipid bilayer structures by varying the cholesterol concentration, lipid head group and lipid tail saturation.[154] One of their most important observations was the correlation between the area per phospholipid and the transfer free energy $\Delta G_{w\rightarrow tails}$ for moving a solute from water into the lipid tail region, which was also in line with previous experimental results.

In the following sections, we will first describe how the membranes were constructed and simulated. Subsequently, the most important results are shown and the implications for plasma oncology are explained. It is important to note that similar reactive species as the ones investigated in this paper are also important in other, more traditional treatment methods.[155,156] Therefore, the research findings from this paper can be expanded to other oxidative stress inducing modalities such as radiation or e-beam therapy. However, CAP treatment is emphasized here due to the observed selectivity (as mentioned above).

5.2 Methodology

5.2.1 Model systems construction

The model systems used in the simulations each contain in total 128 lipids. These lipids are either 1,2-dioleoyl-sn-glycero-3-phosphocholine (DOPC) or cholesterol. The chemical structure of both lipids is shown in Figure 5.2.

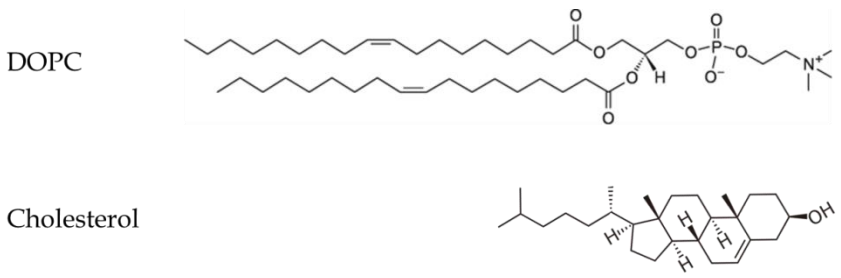

FIGURE 5.2: Chemical structures of DOPC and cholesterol

To examine the effect of the cholesterol concentration, 6 different systems were constructed which contain 0, 10, 20, 30, 40 or 50 mol% cholesterol. These concentrations were chosen to scan the full range of cholesterol fractions reported in literature for both cancer cells (23-32 mol%[67,68]) as well as healthy cells (38-50 mol%[67,68,145]). All membranes were generated using the Packmol package[157] according to the following three rules:

(i) Cholesterol and DOPC molecules are equally divided over both bilayer leaflets.

(ii) Within each leaflet, the lipids are randomly distributed in the xy-plane.

(iii) To avoid unrealistically large forces at the beginning of the MD simulation, atoms from different lipids are separated by at least 2 Å.

The Packmol package is a software code that calculates the pairwise distance between any two atoms from different molecules and, iteratively, optimizes the structure until all molecules satisfy the above mentioned geometric constraints.[157] To create a hydrated membrane, the lipids were surrounded by 8000 water molecules (4000 in each leaflet). Each system was initially placed in

a simulation box with dimensions 8 x 8 x 14 nm^3. An example of one of the systems, containing 30 mol% cholesterol, is shown in Figure 5.3.

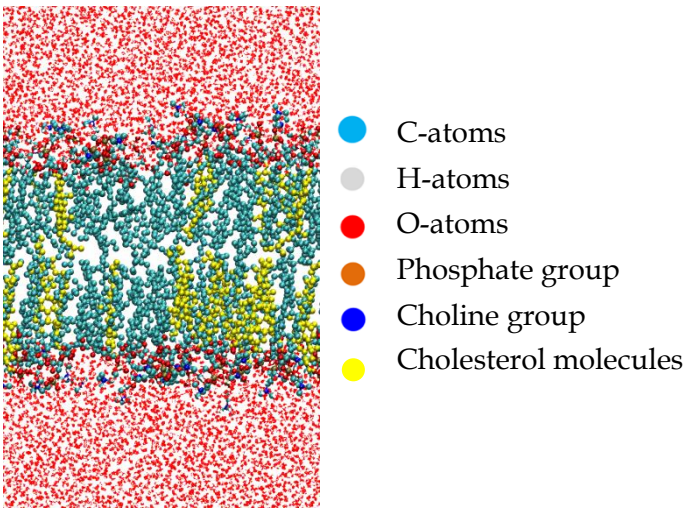

FIGURE 5.3: Structure of a bilayer containing 90 DOPC molecules (70 mol%), 38 cholesterol molecules (30 mol%) and 8000 water molecules. Phospholipids and water molecules are colored by atom type, whereas the cholesterol molecules are entirely colored in yellow, for the sake of clarity.

5.2.2 Simulation set-up

The general set-up of MD simulations has been discussed in Chapter 2 of this thesis. After constructing the hydrated bilayers, discussed in section 5.2.1, the systems were energy minimized using the steepest descent algorithm. During this energy minimization, the lipids are free to move in all directions, which leads to an optimization of the initial structure generated by the Packmol package (see above). Thereafter, the systems were equilibrated for 20 ns using the non-reactive united-atom GROMOS43A1-S3 force field[158] for all lipids, with a time-step of 2 fs. Force field parameters for the different ROS that are investigated were taken from Cordeiro.[153] The simulations were performed in the NPT ensemble (ensemble that maintains a constant number of particles (N), pressure (P) and temperature (T)), using the Nosé-Hoover thermostat[159] (with a reference temperature of 310 K and a coupling constant of 0.2 ps) together with the semi-isotropic Parrinello-Rahman barostat[160] (with a reference pressure of 1 atmosphere, a compressibility of 4.5×10^{-5} bar^{-1} and a

coupling constant of 1 ps). During these simulations, the coordinates and velocities of all atoms were listed every 100 ps for further use in the analysis of the membranes. Moreover, periodic boundary conditions were applied in all Cartesian directions. For the van der Waals interactions, a 1.0 nm cut-off was imposed, whereas for the electrostatics, the PME (Particle Mesh Ewald) method[161,162] was used with 1.0 nm cut-off for real-space interactions and a 0.15 nm grid spacing for the reciprocal-space interactions, together with a fourth-order B-spline interpolation. All simulations, as well as the analysis, were carried out using the GROMACS 5.1 software package.[163]

5.2.3 Umbrella sampling simulations

The umbrella sampling technique, as originally developed by Torrie and Valleau[164,165], uses the addition of an extra energy term, also called bias, to the system to ensure efficient sampling across an entire reaction coordinate. The sampling across the reaction coordinate can be executed in one simulation or in different simulations whose distributions overlap. These overlapping distributions are called the umbrella sampling windows. The exact mathematical description on how the bias is added, and how the unbiased free-energy differences are recovered afterwards, can be found elsewhere.[166]

Starting structures for the US simulations were taken as the last frame of the equilibration. A total of 150 US windows were defined along the bilayer normal (*i.e.*, the z-axis is the reaction coordinate in our systems), separated by 0.5 Å. As such, the sampling windows spanned the entire membrane system, starting from the lower water leaflet, crossing the lipid bilayer structure, and ending in the upper water leaflet. The umbrella windows were sampled in different simulations; however, to save computational resources, five umbrella windows were sampled during each simulation, keeping a distance of 15 Å between consecutive windows, which is illustrated in Figure 5.4.

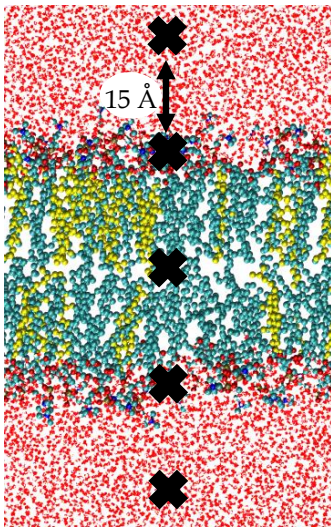

FIGURE 5.4: Illustration of the US simulation set-up. Five umbrella windows separated by 15 Å (position of ROS depicted by block crosses) are sampled in one simulation, thereby saving computational resources. In consecutive simulations, each species is shifted by 0.5 Å. To sample the entire membrane system, 30 simulations are performed, yielding a total of 150 umbrella histograms from which a FEP is constructed.

During these US simulations, reactive species were free to move in the xy-plane but their motion in the z-direction was restricted by applying a harmonic bias with a force constant of 1000 $kJ.mol^{-1}.nm^{-2}$. After an extra equilibration of 2 ns (same conditions as in the previous equilibration simulations), a 3 ns simulation was performed during which the US histograms were collected. FEPs were constructed by using a periodic version of the weighted histogram analysis method (WHAM)[167], as implemented in the g_wham tool of GROMACS. The final FEPs shown in all figures following were obtained by averaging over 10 independent simulations (*i.e.*, starting from independently equilibrated structures). It is important to note that we are mostly interested in differences between the obtained FEPs, rather than the absolute values. Indeed, the focus of this study was to assess the effect of the cholesterol content on the permeation of RONS, and therefore, we focus on differences in the FEPs in membranes containing different amounts of cholesterol.

5.2.4 Analysis

To characterize the different membrane systems, and to be able to explain the observed trends in the FEPs, the (i) bilayer thickness, (ii) area per lipid, (iii) minimum interlipid distance and (iv) lipid density were calculated. The values shown below were calculated using the last 5 ns of each equilibration run.

The bilayer thickness was defined as the average distance along the z-axis between the center of mass (COM) of the phosphorus atoms of both leaflets. The area per lipid was calculated from the average box size (in the xy-plane), which was then divided by the number of lipids in one leaflet, *i.e.*, 64. This value gives thus an average area over both phospholipids and cholesterol. The minimum interlipid distance is defined as the smallest distance between two atoms from the lipid tails of different lipids (both phospholipids and cholesterol). Finally, for the calculation of the lipid density, the simulation box is divided in 100 slices (along the z-axis). Then, the average density of the lipid atoms in each slice is calculated.

5.3 Results and discussions

5.3.1 Effect of reactive species on FEP

To illustrate how the different reactive species behave when travelling through the bilayer, Figure 5.5 shows the averaged FEPs for all ROS investigated across a pure DOPC membrane. Note that, although RNS are equally important in the field of plasma medicine, these were not investigated in this study due to the lack of corresponding force field parameters of most RNS. However, in a non-reactive force field, we expect RNS to behave similar compared to ROS due to similarities in polarity and size. In fact, preliminary results show similar behaviour between NO and O_2. The free energy barriers associated with the profiles shown in Figure 5.5 are listed in Table 5.1. Starting from the water layer, all hydrophilic ROS (H_2O_2, $^{\bullet}OOH$ and $^{\bullet}OH$) display an energy minimum at the phospholipid head group region, which originates from the stronger Coulombic interactions with these charged head groups. Consequently, due to the more polar character of this region (compared to the

water layer), the hydrophobic O_2-molecule shows a small increase in free energy. Continuing towards the bilayer core, the role of the membrane as a permeation barrier can be derived from the increase in free energy of the hydrophilic ROS. O_2 on the other hand displays an energy minimum in the center of the membrane, which will result in an accumulation of molecular oxygen in the bilayer core.[168]

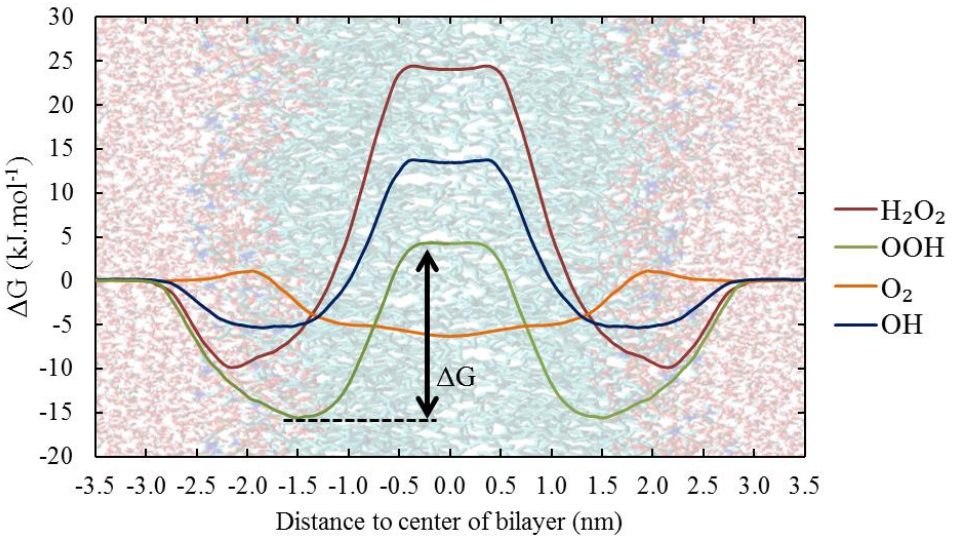

FIGURE 5.5: FEPs of different ROS across a pure DOPC membrane. The membrane structure is shown as a background to give an indication as to where the different regions (water layer, head group region, hydrophobic lipid core) are located. The transfer free energy barriers ($\Delta G_{lipid \rightarrow tail}$) which are listed in the tables below are always calculated as the difference between the maximum and minimum value in the FEP (see Figure).

TABLE 5.1: Transfer free energies of all investigated ROS in a pure DOPC bilayer. The error bars are derived from the transfer free energies of all 10 independent profiles.

ROS	$\Delta G_{water \rightarrow tail}$ (kJ.mol^{-1})
H_2O_2	34.6 ± 3.3
$^{\bullet}OOH$	20.1 ± 2.3
$^{\bullet}OH$	19.9 ± 2.8
O_2	1.3 ± 0.4

When comparing the transfer free energy barriers of all species, it is clear that the permeation of H_2O_2 is most hindered. The free energy barriers of $^{\bullet}OOH$ and $^{\bullet}OH$ are very similar and there is almost no significant barrier for O_2, which is in agreement with experimental evidence concerning the permeability of these different species[169]. The value of the free energy barrier of H_2O_2 (34.6±3.3 kJ.mol^{-1}) is in good agreement with other both computational (33±4 kJ.mol^{-1})[153] and experimental findings (36.8 kJ.mol^{-1})[170]. Furthermore, the significantly higher free energy barrier observed for H_2O_2 and the hydrophilic ROS can be explained by the number of hydrogen bonds these species can establish with surrounding water molecules. This number determines how easily the reactive species will lose their hydration shell upon penetrating into the membrane. Indeed, Cordeiro[153] determined that H_2O_2 can establish twice as many H-bonds (combination of H-bonds as donor and acceptor gives a total of 4.5) compared to $^{\bullet}OOH$ (2.3) and $^{\bullet}OH$ (2).

5.3.2 Effect of cholesterol fraction in membrane on FEP

In the following sections, the effect of the cholesterol fraction is discussed for each of the species investigated separately.

Hydrogen peroxide - H_2O_2

The FEPs of H_2O_2 across DOPC membranes containing a varying amount of cholesterol are shown in Figure 5.6. The membrane shown on the background is only an indication on where the different regions of the system are located. This is important to note, because the bilayer thickness (and thus the position of the head groups etc.) depends on the cholesterol concentration (Figure 5.7a). This increasing bilayer thickness, which is accompanied by a decreasing area per lipid (Figure 5.7b), is known as the condensing effect of cholesterol.[171,172]

Figure 5.6 shows that the cholesterol fraction has an influence on (i) the width and (ii) the height of the free energy barrier, and (iii) the shape of the FEP in the center of the bilayer. Because the minima of the FEPs are located around the head group region of the bilayer (see above), the width of the free energy barrier is a measure for the bilayer thickness. The variation in width

can thus be explained by the increase in bilayer thickness (Figure 5.7a). The consequence of this widening, however, is that the bilayer core is stabilized entropically at higher cholesterol concentrations, which will slow down the diffusion of H_2O_2 across the membrane.

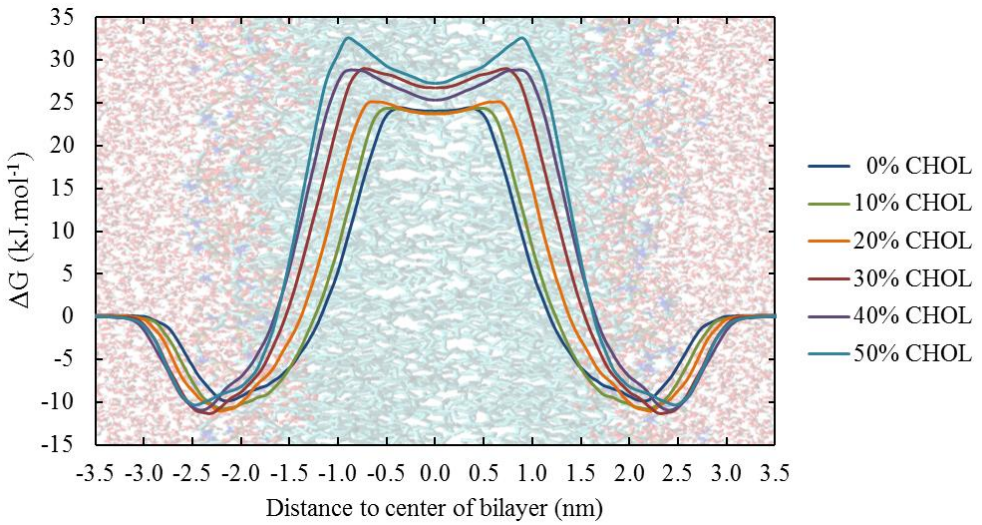

FIGURE 5.6: Effect of the cholesterol fraction in the cell membrane on the FEP of H_2O_2.

A possible explanation for the increasing trend of the height of the free energy barrier can be found in the minimum interlipid distance, which is included in Table 5.2. Due to the condensing effect of cholesterol and the associated decreasing area per lipid, the minimum interlipid distance will decrease upon increasing the cholesterol fraction, as has been suggested in literature.[173] We assume that this will impede the penetration of H_2O_2 across the bilayer which results in an increasing barrier. The last important observation that could be derived from Figure 5.6, *i.e.*, the appearance of a local minimum in the center of the bilayer when increasing the cholesterol fraction, can be explained by looking at the lipid density throughout the bilayer along the z-axis, which is plotted in Figure 5.8.

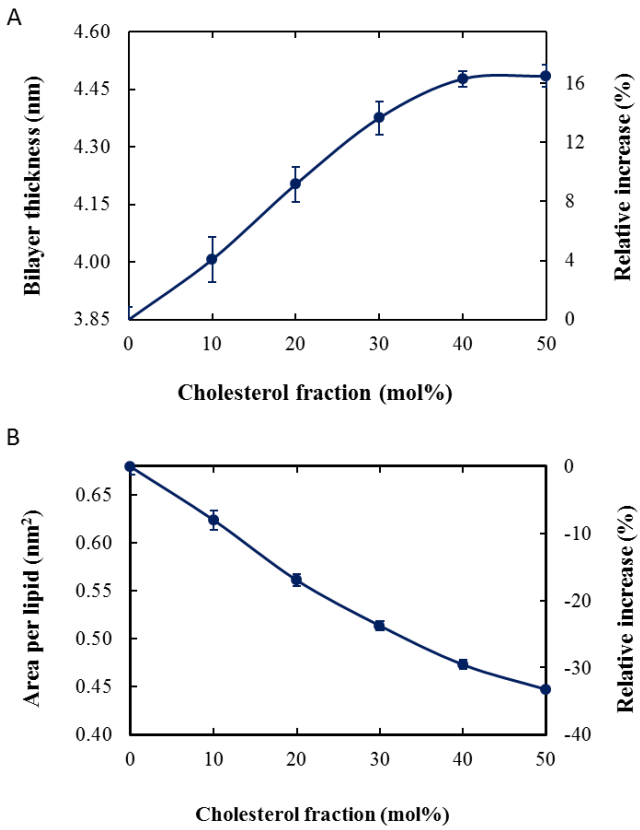

FIGURE 5.7: Bilayer thickness (A) and area per lipid (B) as a function of the cholesterol concentration of the membrane. Absolute values are shown on the left axis, while relative values (with respect to the non-oxidized system) are depicted on the right axis.

TABLE 5.2: Transfer free energy barrier of H_2O_2 in DOPC bilayers containing a varying fraction of cholesterol (column 2). Column 3 shows the averaged minimal interlipid distances in these systems.

Cholesterol fraction (mol%)	$\Delta G_{water->tail}$ (kJ.mol^{-1})	Interlipid distance (Å)
0	34.6 ± 3.3	3.063 ± 0.002
10	36.3 ± 2.9	2.926 ± 0.018
20	36.7 ± 3.0	2.772 ± 0.012
30	40.8 ± 4.1	2.660 ± 0.035
40	40.5 ± 3.7	2.589 ± 0.036
50	43.4 ± 3.8	2.558 ± 0.046

Figure 5.8 illustrates that upon increasing the cholesterol fraction (i) the lipid density increases between z ≈ ±1.0-1.5 nm, while (ii) the lipid density decreases in the center of the bilayer. The increase around z ≈ ±1.0-1.5 nm can be assigned to a dense packing of the bulky rings present in cholesterol (as can be derived from the cholesterol density profile, also plotted in Figure 5.8), while the decrease in the center of the bilayer is due to the smaller structure of cholesterol. As the OH-group of cholesterol will ensure cholesterol to be located in the lipid-water interface, due to favourable interactions, the smaller size of cholesterol causes a depletion of lipids in the center. We thus assume that the combination of the increase in lipid density around the bulky rings together with the decrease in the center, are the underlying reason for the local minimum in the binary systems containing both phospholipids and cholesterol. Moreover, the higher the cholesterol fraction, the more pronounced is this local minimum (as can be derived from Figure 5.6).

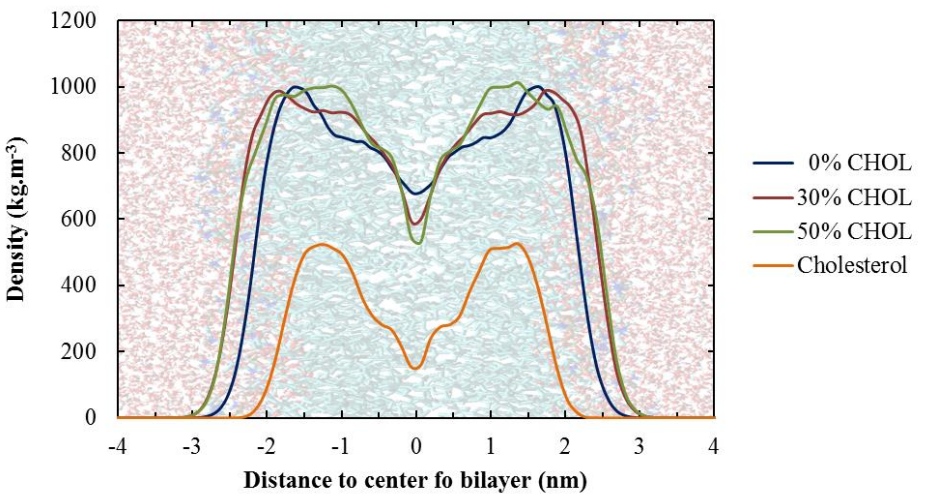

FIGURE 5.8: Total lipid density along the z-axis in membranes containing 0, 30 and 50% cholesterol, and the cholesterol density in systems containing 50% cholesterol.

The increasing height of the energy barrier, combined with the appearance of a local minimum as well as the increased width of the barrier, will all contribute to hamper the penetration of H_2O_2 across membranes with higher cholesterol fractions. This is an important observation in the context of plasma oncology because the plasma membrane of cancer cells is known to possess

lower amounts of cholesterol compared to healthy cells, which thus facilitates the penetration of H_2O_2, one of the most important ROS generated by CAPs, in these cells.

Based on the Eyring equation, we can estimate the rate of permeation from the energy barriers mentioned in Table 5.2. According to this equation, the rate constant (k) can be calculated as follows:

$$k = \frac{k_B\, T}{h} e^{\frac{-\Delta G}{RT}} \tag{5.1}$$

In this equation, k_B is the Boltzmann constant (1.381×10^{-23} J.K^{-1}), T the gas temperature (310 K) and h Planck's constant (6.626×10^{-34} J.s). A barrier of 40 kJ.mol^{-1} would thus translate to a rate constant of permeation of 1.18×10^{6} s^{-1}, whereas a barrier of 30 kJ.mol^{-1} results in a rate constant of 5.69×10^{7} s^{-1}.

Hydroperoxyl radical - $^{\bullet}$OOH

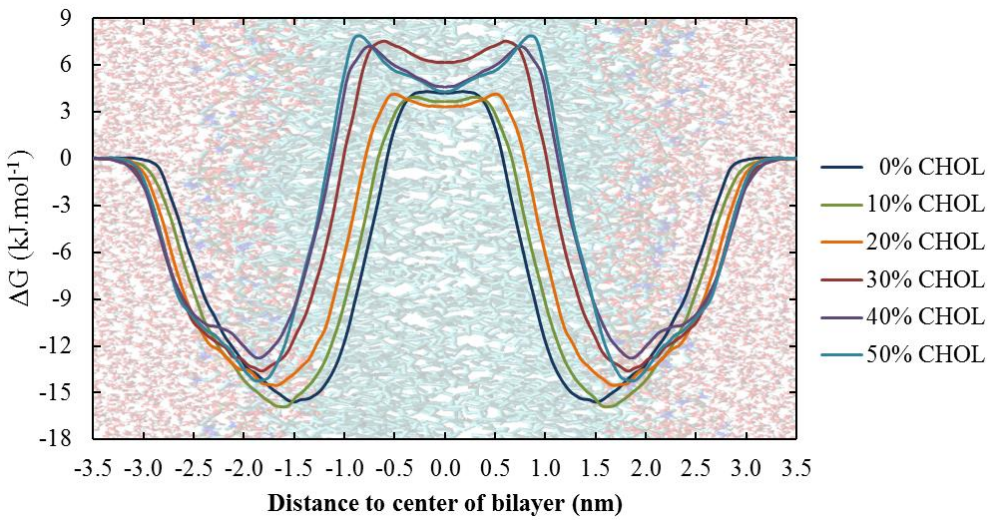

FIGURE 5.9: Effect of the cholesterol fraction in the cell membrane on the FEP of $^{\bullet}$OOH.

The FEPs of $^{\bullet}$OOH across all simulated systems are shown in Figure 5.9, with the associated transfer free energy barriers in Table 5.3. In general, the effect of cholesterol on the FEP of $^{\bullet}$OOH is very similar compared to H_2O_2, *i.e.*, (i) the energy barrier becomes wider and (ii) a local minimum appears in the center of the bilayer. The height of the free energy barrier is less affected compared to

hydrogen peroxide, which is probably because $^{\bullet}OOH$ is smaller than H_2O_2 making it less dependent on the decreasing interlipid distance. Moreover, we note that the depth of the energy minimum in the vicinity of the head groups decreases upon increasing the cholesterol fraction.

TABLE 5.3: Transfer free energy barrier of $^{\bullet}OOH$ in DOPC bilayers containing a varying fraction of cholesterol.

Cholesterol fraction (mol%)	**$\Delta G_{water->tail}$ (kJ.mol^{-1})**
0	20.1 ± 2.3
10	20.8 ± 3.1
20	19.4 ± 2.2
30	21.9 ± 2.7
40	21.0 ± 3.0
50	23.2 ± 2.8

Hydroxyl radical - $^{\bullet}OH$

Figure 5.10 shows the FEPs of the transport of an $^{\bullet}OH$ radical through membranes containing a varying amount of cholesterol. The accompanying transfer free energy barriers are listed in Table 5.4.

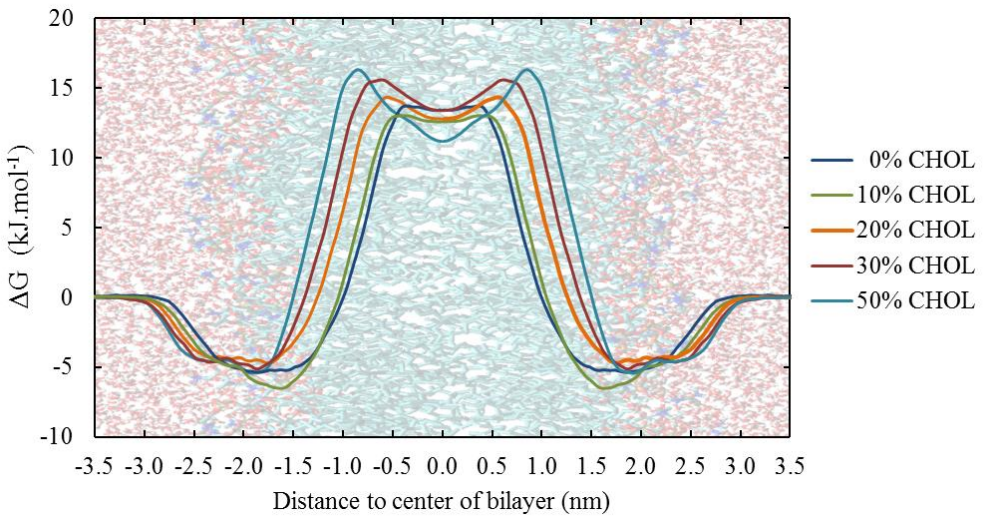

FIGURE 5.10: Effect of the cholesterol fraction in the cell membrane on the FEP of $^{\bullet}OH$.

TABLE 5.4: Transfer free energy barrier of •OH in DOPC bilayers containing a varying fraction of cholesterol.

Cholesterol fraction (mol%)	$\Delta G_{water->tail}$ (kJ.mol^{-1})
0	19.9 ± 2.8
10	20.4 ± 3.2
20	19.9 ± 2.8
30	22.3 ± 2.1
40	21.1 ± 2.3
50	22.1 ± 2.4

The general trends discussed in the sections above also appear in these graphs, *i.e.* an increasing barrier width and the formation of a local free energy minimum in the center of the bilayer. In contrast to •OOH, the depth of the free energy minimum in the vicinity of the head group region is not affected by the cholesterol fraction in the case of an •OH (in line with H_2O_2, see Figure 5.6). The barrier height did not change significantly upon altering the cholesterol fraction, as was also the case for •OOH (see above).

Molecular oxygen - O_2

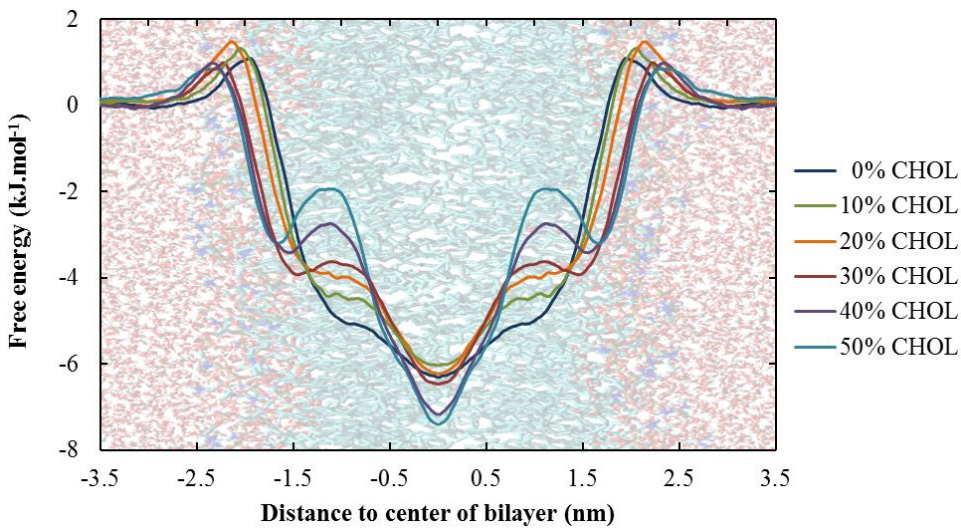

FIGURE 5.11: Effect of the cholesterol fraction in the cell membrane on the FEP of O_2.

The FEPs of the last reactive oxygen species investigated, O_2, are shown in Figure 5.11. The exact values of the transfer free energy barrier are omitted since these barriers are not significant (as can be derived from Figure 5.11). Due to the hydrophobic nature of this species, the FEPs are entirely different compared to all above (see discussion in Section 5.3.1). Upon increasing the cholesterol fraction (i) the free energy decreases in the center of the bilayer and (ii) a new barrier is formed at z ± 1.0 nm. The further decrease in free energy at the center of the bilayer will probably lead to an even more pronounced accumulation of O_2 in the bilayer core of membranes with higher cholesterol concentrations.

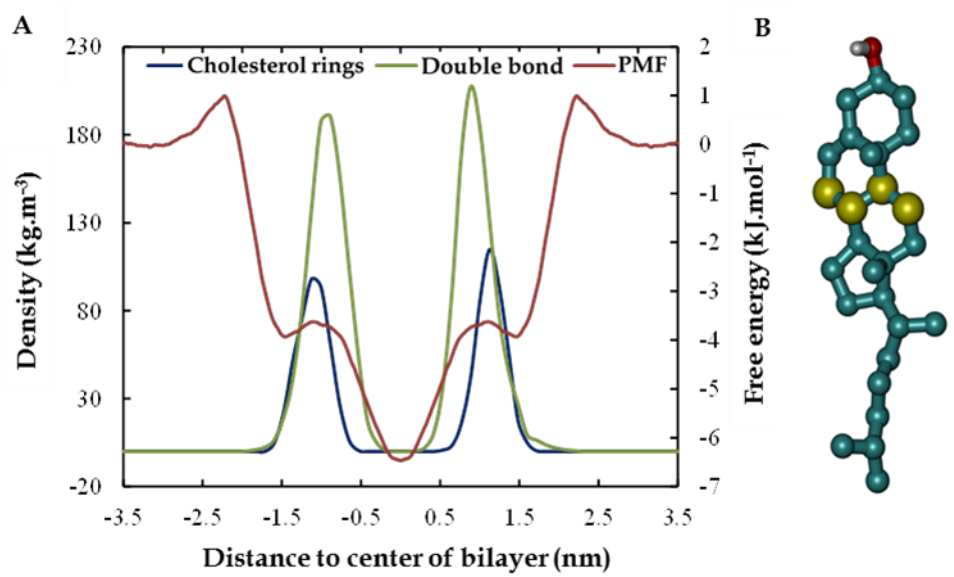

FIGURE 5.12: Illustration of the overlap between the position of the cholesterol rings, the double bonds of DOPC and the extra free energy barrier for O_2 in the bilayer around z = ±1.0 nm (A). The density of the carbon atoms which are shared between the second and third ring of cholesterol is plotted on the left axis, while the FEP of O_2 across a 30:70 CHOL:DOPC membrane is plotted on the right axis. The exact atoms of cholesterol whose density is plotted in Figure A are depicted in yellow (B). These atoms are chosen since they are located in the middle of the bulky sterol rings.

However, in the context of plasma oncology, the second trend, *i.e.*, the formation of a new energy barrier is probably more important. This new barrier is most likely caused by the bulky rings of cholesterol and the double

bonds present in DOPC, which can be illustrated by comparing the location of these atoms in the membrane with the location of the extra barrier. This comparison is shown in Figure 5.12 for the case of membranes containing 30 % cholesterol.

The combination of the bulky rings and the double bonds make the region around z ≈ 1.0 nm the most rigid part of the entire membrane, due to which the penetration of O_2 will be most hampered here. Although this new barrier is only a few kJ.mol^{-1} in height, it can be very important because, as mentioned before, O_2 is required in the propagation step of the lipid peroxidation process. The extra free energy barrier in the vicinity of the double bonds, upon increasing cholesterol concentration, would lead to a depletion of O_2 in this region and this can drastically lower the lipid peroxidation rate.

5.4 Conclusions

United-atom molecular dynamics simulations were applied to investigate the effect of the cholesterol fraction in cell membranes on the permeation of different reactive oxygen species across these membranes. The results obtained in this study illustrate that, depending on the specific species, cholesterol is able to affect multiple aspects of the FEP, including (i) the height and (ii) width of the barrier, and (iii) the overall shape of the FEP (including the shape at the head group region, at the center of the membrane and at the sterol rings). Two of the most important shape-changing observations include (i) the appearance of local minima in the center of the bilayer in the FEPs of all hydrophilic ROS, which deepens upon increasing the cholesterol fraction, and (ii) the appearance of a free energy barrier at the double bond region in the FEP of O_2, which increases when increasing the cholesterol fraction.

The appearance of a local minimum in the center of the bilayer is important because this will hamper the penetration of ROS towards the intracellular environment, even when the ROS succeed to penetrate into the membrane core.

Furthermore, although all FEPs shown indicate that cholesterol definitely has an influence on the penetration of certain ROS, even for systems without cholesterol, the free energy barriers are still significantly high for species to easily travel through the membrane. This leads to the conclusion that, in order to explain an increased vulnerability of cancer cells over healthy cells during CAP treatment, (i) either extra elements should be in play to explain a stronger ingress of RONS in cancer cells, or that (ii) cancer cells are more vulnerable to the ingress of RONS due to their decreased capacity to reduce redox damage. One possibility to explain an increased ingress of RONS could be the expression of certain AQPs (see above). Another possibility would be the pores generated during the lipid peroxidation process, which will cause the membrane to lose its primary biological function (regulating transport from the extracellular to the intracellular matrix and vice versa), as illustrated in our previous work.[1] By breaching this barrier, RONS would be able to permeate into the cell, causing oxidative stress, which might lead to cell death. In this regard, the extra free energy barrier for O_2 in the vicinity of the double bonds could be of great importance because it can drastically decrease the occurrence of this process. Indeed, one of the requirements for lipid peroxidation to occur is exactly the presence of O_2 at the double bonds region. Consequently, in healthy cells, the ingress of RONS will be slowed down significantly due to the higher cholesterol fraction in their cell membrane.

In conclusion, our results provide a possible explanation as to why cancer cells, containing lower amounts of cholesterol, would absorb RONS faster compared to their healthy counterparts (containing higher levels of cholesterol), which is assumed to be one of the primary reasons behind the experimentally observed selectivity of CAP cancer treatment.

CHAPTER 6

Electric field and RONS permeation

The results presented in this chapter were published in:

M. Yusupov, J. Van der Paal, E. C. Neyts and A. Bogaerts. Synergistic effect of electric field and lipid oxidation on the permeability of cell membranes. *Biochimica et Biophysica Acta.* **1861**, 839-847 (2017).

6.1 Introduction

In the context of plasma medicine, several experimental investigations have been performed on phospholipid (PL) vesicles as simple models for cell membranes, to study the oxidation of lipids, their structural and chemical modifications, as well as the transport of ROS across the PL membranes (see also Chapter 8).[174–179] For example, Hammer *et al.* showed that a three minute CAP treatment of liposomes leads to an increase in the fluidity of the PL bilayer (PLB).[175] Maheux *et al.* reported a more negative zeta potential after CAP treatment of small unilamellar vesicles.[176] The authors indicated that a larger number of chemical modifications takes place on the PLs, leading to a more negatively charged surface of the treated liposomes.[176] Further, Hong *et al.* showed that CAP treatment of PL vesicles can lead to an ingress of ROS into the vesicles without damaging the cell membrane integrity.[177] They also observed a significant reduction of the transfer efficiency of ROS into the vesicles in the presence of serum.[180] The permeation of $^{\bullet}OH$ as well as their ability to induce lipid oxidation were observed using giant unilamellar vesicles.[178] Furthermore, Tero *et al.* observed the formation of pores (with sizes of 10 nm - 50 nm) induced by CAP on artificial planar lipid bilayers formed at solid-liquid interfaces.[179] Thus, to summarize, CAP treatment of the cell membrane leads to oxidation of the lipids, which subsequently affects the bilayer fluidity and lipid disorder, thereby altering the permeability of the membrane to reactive plasma species.

Similar conclusions were made in numerical studies applying MD simulations on oxidized PLBs.[1,181–183] In general, the simulations reveal an overall increase in the membrane permeability[181], a change in the lipid mobility in the PLB[182], pore creation and bilayer disintegration[183] upon introduction of oxidized lipids, as well as a protective role of cholesterol[1]. This protective effect of cholesterol is in agreement with the experimental study of Svarnas *et al.*, in which they found that liposomes containing 50 mol% cholesterol are resistant against disruption by the plasma, whereas cholesterol fractions below 50 mol% lead to increased disruption of liposomes.[184]

It is important to realize that in addition to the creation of reactive species, some CAP sources also generate strong electric fields, ranging from a few up to 100 kV.cm^{-1} (see *e.g.*, [185–191]). These electric fields may play an important and synergistic role in plasma-cell interactions[191], as they are high enough to induce pore formation in membranes[192]. Thus, in order to gain insight in the plasma-cell interactions, the effect of electric fields should be taken into account together with the effect of reactive plasma species.

The application of high electric fields can indeed disturb the integrity of the membrane, through the creation of pores either temporarily or permanently, which leads to cell membrane permeabilization. This method is known as electroporation and nowadays is employed in different fields, including medicine.[193–195] Electroporation is widely used for the delivery of chemical species, such as ions and small molecules, dyes, drugs or genetic materials into cells[194,196,197] and it is successfully applied for cancer treatment[198,199]. Thorough discussions on electroporation and its applications are given in excellent reviews.[192,196,198–200] There are also MD studies devoted to electroporation, where various investigations are conducted using PLB model systems, *e.g.*, the study of the mechanisms of membrane electroporation[201,202], the effect of cholesterol on the electroporation threshold[203], transport of siRNA through lipid membranes[204], the phosphatidylserine translocation[205] as well as calcium-induced adsorption of DNA on a lipid membrane[206]. More information about MD studies on electroporation can be found in.[207,208] Although much research has been performed in the field of electroporation, still little is known about the synergy between ROS and the electric field, and more specifically on how this affects the cell membrane permeability.

Thus, based on the above mentioned considerations, in this chapter we investigate the combined effect of the electric field together with lipid oxidation, as both effects are important in plasma-cell interactions, and thus the combination of both is highly relevant for studying the effect of plasma on living cells. To the best of our knowledge, this combined effect has not yet been investigated before in the context of plasma medicine. Besides the direct

interest for plasma medicine, this study is also of broader interest for other applications where both strong electric fields and ROS come into play.

Note: The results presented in section 6.3.2 of this chapter were mainly obtained by Maksudbek Yusupov.

6.2 Methodology

6.2.1 Model systems construction

In this chapter, MD simulations are presented to study the electroporation process together with the effect of oxidation of the PLs. Firstly, we studied the translocation of ROS (more specifically $^{\bullet}OH$, $^{\bullet}OOH$, H_2O_2 and O_2) through native and oxidized PLBs, calculating their permeation FEPs to elucidate the penetration capabilities in the absence of an electric field. Secondly, the effect of the electric field on pore formation is assessed, again in native and oxidized bilayers.

As a model system we use the PLB shown in Figure 6.1, representing the cell membrane. It is composed of 128 lipids surrounded by two water leaflets, each of which contains 4000 water molecules (*i.e.*, in total 8000 water molecules), corresponding to a hydration level of 63 water molecules/lipid. The PL investigated is 1,2-dioleoyl-*sn*-glycero-3-phosphocholine (DOPC), which is illustrated in Figure 6.2. To study the effect of oxidized PLs, two oxidation products of DOPC are included in the simulated systems, *i.e.*, a peroxide and an aldehyde (see also Figure 6.2). The peroxide and aldehyde were chosen because it is shown that these are two of the major oxidation products.[209] The peroxide is the end product of the main lipid peroxidation reaction, whereas the aldehyde product is formed due to a ring closing and opening reaction of the intermediate lipid peroxide radical, which yields two aldehydes. To create multiple oxidized membranes, 10, 20, 30, 40 or 50 mol% of the DOPC molecules in the native PLB structure are replaced by one of both oxidized PLs. The Packmol package is used to create the different structures.[157]

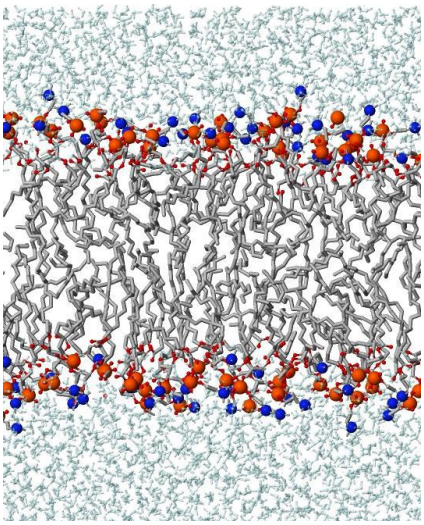

FIGURE 6.1: Native DOPC PLB to be treated with MD simulations. The PLB consists of 128 DOPC molecules with 8000 water molecules organized in two lamellae (*i.e.*, 64 DOPCs, with corresponding water layer, at the top and 64 at the bottom). The water layers, oxygen atoms and lipid tails are shown in cyan, red and gray colors, respectively. The P (orange) and N (blue) atoms are depicted with bigger beads, for the sake of clarity. The color legend also applies to the other similar Figures below.

Once the initial configurations of the membranes are generated, an energy minimization is performed using the steepest descent algorithm. Afterwards, the systems are equilibrated during 110 ns, of which the last 10 ns are used for further analysis. During all runs, the GROMOS43A1-S3 united atom force field is applied.[158] The ROS investigated in this study were, however, not present in this force field, so the relevant parameters are taken from literature.[153] The simulations are performed in the NPT-ensemble by applying the Nose-Hoover thermostat[159] and the semi-isotropic Parinello-Rahman barostat[160] (*i.e.* pressure coupling is isotropic in x and y direction, but different in z direction, which ensures that L_x=L_y). The applied reference temperature is 310 K combined with a coupling constant of 0.2 ps, whereas the applied reference pressure is 1 atmosphere combined with a compressibility of 4.5×10^{-5} bar^{-1} and a coupling constant of 1 ps. Periodic boundary conditions are applied in all Cartesian directions. Considering the non-bonded interactions, a 1.0 nm cut-off is applied for the van der Waals interactions. The electrostatic interactions, on the other hand, are calculated using the PME-method[162,163],

using a 1.0 nm cut-off for the real-space interactions in combination with a 0.15 nm spaced-grid for the reciprocal-space interactions and a fourth-order B-spline interpolation. All simulations and analyses mentioned in this study are performed using the GROMACS 5.1 package.[163]

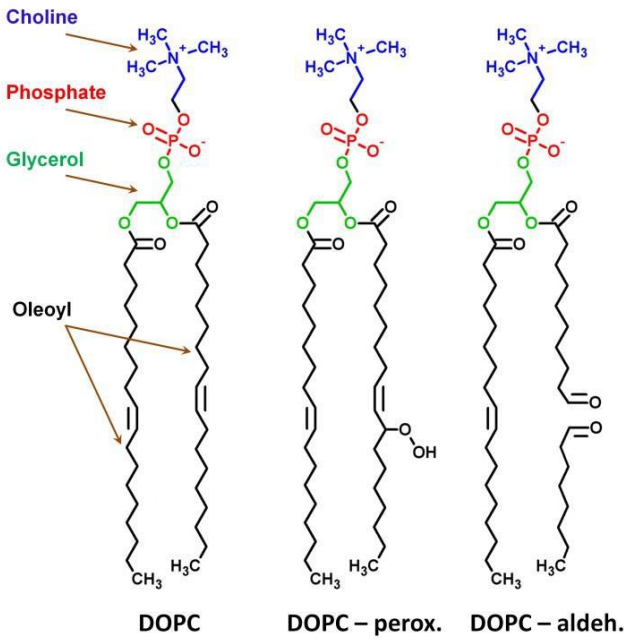

FIGURE 6.2: Schematic illustrations of the native (DOPC) and oxidized (DOPC-perox. and DOPC-aldeh.) PLs.

6.2.2 Free energy profiling

To understand the effect of lipid oxidation on the permeation of ROS, umbrella sampling (US) simulations are performed for H_2O_2 and O_2 molecules as well as for $^{\bullet}OOH$ and $^{\bullet}OH$, in native and 50% oxidized structures (both aldehyde and peroxide). Initial structures for these simulations are selected as random frames from the last ns of the corresponding equilibration simulation (see above). For each energy profile, 150 US windows are defined along the bilayer normal (z-axis), which are separated by 0.5 Å. In this manner, the sampling windows span the entire membrane system. Five US windows, separated by 15 Å, are sampled during each simulation to save computational resources. A harmonic bias with a force constant of 1000 $kJ.mol^{-1}.nm^{-2}$ is applied along the z-direction on the reactive species, to restrict their motion.

After an extra equilibration of 3 ns, a 2 ns simulation is performed during which the US histograms are collected. The conditions used in these simulations are identical to those used during the equilibration runs (see above). FEPs are constructed by using a periodic version of the weighted histogram analysis method (WHAM)[210], as is implemented in the *g_wham* tool of GROMACS. The final energy profiles are obtained by averaging over four US simulations, which differ from one another based on their starting structure, to allow for some statistical variations. Note that the US simulations need a lot of computational resources and are therefore computationally expensive. In total 1440 US simulations are performed for the calculation of the FEPs.

6.2.3 Electric field simulations

To investigate the effect of the electric field on the different membrane structures, additional simulations are performed using the last frame of each equilibrated structure as input, and applying an electric field of varying strength. In case of the oxidized structures, electric field strengths of 300, 400 and 500 $mV.nm^{-1}$ are investigated, whereas in the case of the native membrane, electric field strengths of 400, 450, 500, 550 and 600 $mV.nm^{-1}$ are used. Note that these are typical electric field values used in electroporation simulations (see *e.g.*,[201,202,204,206]). However, the values are much higher than the electric fields applied in electroporation experiments[191] or in plasma medicine applications[5,185–187,189,190,211]. Experimentally, applied field strengths might vary between 0.1 and 100 $kV.cm^{-1}$ (*i.e.*, between 0.01 and 10 $mV.nm^{-1}$), which are at least an order of magnitude lower than the fields used in MD simulations. In fact, the macroscopic field applied to the system in experiments is not equivalent, by any means, to the field which is felt by the membrane (and which is applied in MD simulations), and therefore these values should not be directly compared. Specifically, the macroscopic electric field used in experiments is only the spatially averaged electric field obtained from the applied voltage between electrodes, whereas the microscopic electric field across the membrane should be determined from the transmembrane potential. The latter is not straightforward to determine from the global value.

Therefore, a constant electric field is used in MD simulations to study the electroporation process. The transmembrane potential difference, in this case, is simply determined from a multiplication of this electric field to the size of the simulation box in the field direction (mostly z axis). The time dependent microscopic transmembrane potential was determined from the global value (*i.e.*, the macroscopic electric field) in [212,213] using a so-called distributed circuit model. The determined maximum value of the transmembrane potential (*i.e.*, > 2 V, when the external applied electric field is 10 $mV.nm^{-1}$ [212,213]) corresponds fairly well to the values of the transmembrane voltage needed for pore formation in MD simulations (see *e.g.*,[201,204] as well as below). Thus, despite the fact that the temporal behaviour is excluded, the applied constant electric fields in MD studies can give valuable information about the electroporation process on the atomic scale. Moreover, these microscopic electric fields can be correlated with the macroscopic electric fields through the transmembrane potential and the direct proportionality can be obtained between them.

The simulations are run for 20 ns, using the same simulation parameters as in the equilibration runs. By selecting 10 frames from the last 10 ns of the equilibration run (*i.e.*, one frame every ns), 10 independent electric field simulations are performed. For each simulation, the time until the occurrence of pore formation is calculated, which is then averaged over all independent simulations.

Although the pore formation by electric fields should be more reversible, in contrast with pore formation due to lipid oxidation, this effect is not taken into account in the MD simulations. Indeed, once electroporation occurs in the MD simulations, the overall structure of the small membrane system is completely lost, due to which this process is irreversible (at least on the timescale investigated in these MD simulations). This is, however, not a cause of concern, as we are only interested in studying the time needed to induce this pore.

6.2.4 Analysis

To analyze the various properties of the simulated membranes, the last 10 ns of each equilibration run is used. The bilayer thickness is defined as the average distance along the z-axis between the center of mass of the phosphorus atoms of both leaflets, using the *gmx_distance* command of GROMACS. The area per lipid is calculated from the average box size in the xy-plane, divided by the number of lipids in one leaflet, *i.e.*, $L_x \times L_y/64$. This value gives thus an average area over both native and oxidized PLs. The average box size in the xy-plane, as well as the average box size in the z-direction are calculated using the *gmx_energy* command. The error bars shown in the results below are all calculated using the block method of Hess.[214]

6.3 Results and discussion

As mentioned above, this study is composed of two parts. We first study the translocation of ROS (namely, $^{\bullet}OH$, $^{\bullet}OOH$, H_2O_2 and O_2) through native and oxidized PLBs. This gives us information about the penetration abilities of ROS through these bilayers, when there is no pore formed in the PLBs. Indeed, the effect of the electric field is excluded here, and the oxidation degree is up to 50%, which is high enough to observe the effect of oxidation, but low enough so that pore formation does not yet occur.[1] This allows us to elucidate whether or not the formation of pores is necessary in order to deliver ROS (and other molecules) into the cell interior. Subsequently, we investigate the effect of the electric field on pore formation, again in native and oxidized bilayers. This allows us to determine how the electric field facilitates pore formation, when oxidation takes place in the PLBs. Thus, in this study two research questions will be investigated, *i.e.*, (i) can ROS penetrate through a native or oxidized PLB in the absence of an electric field, and if not, (ii) which electric field strengths are needed to create pores in both native and oxidized PLB?

6.3.1 Translocation of ROS through native and oxidized PLBs

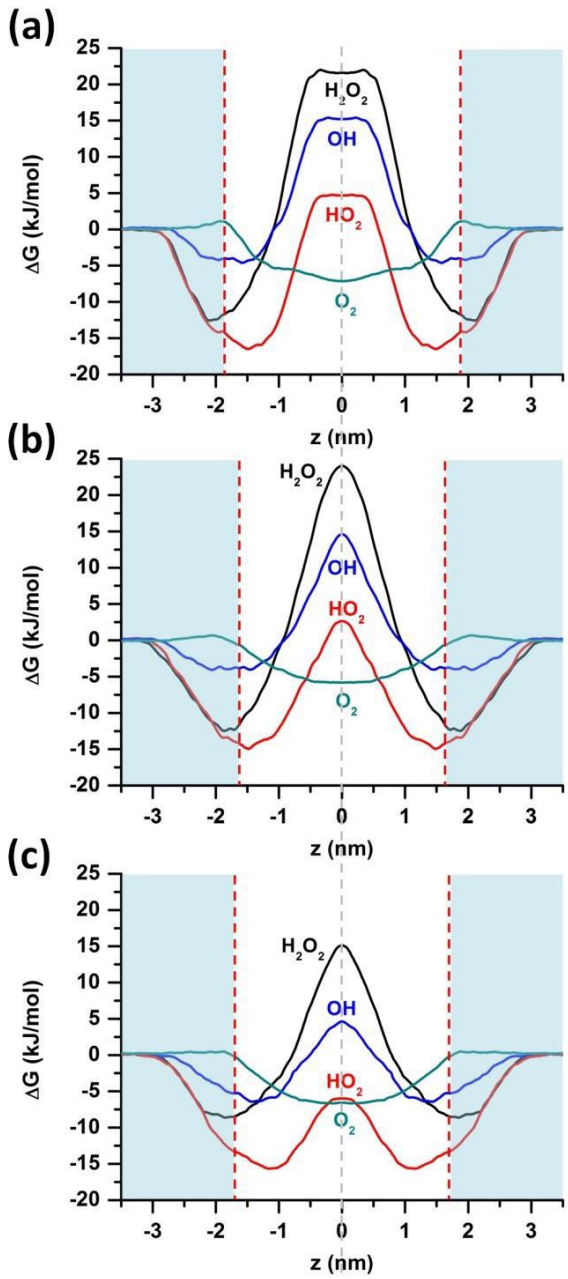

FIGURE 6.3: FEPs for the translocation of ROS across native (a), 50 mol% peroxidized (b) and 50 mol% aldehyde oxidized (c) PLBs. The red dashed lines indicate the average positions of the phosphate groups (*i.e.*, average bilayer thickness, cf. Table 6.2). The gray dashed line corresponds to the bilayer center. The water layers are highlighted by the light blue shaded color.

Figure 6.3 illustrates the FEPs of ROS across native and 50% oxidized PLBs, for both the peroxide and aldehyde oxidation products. We chose the 50% oxidized systems, but we expect that other oxidation degrees will give similar results, albeit less pronounced. Moreover, these calculations of the energy profiles are computationally expensive.

In all three cases hydrophobic O_2 molecules can easily travel towards the lipid tails without significant energy barriers for permeation. As soon as they reach the apolar center of the bilayer, they remain stable there, as their activation free energies from the center to the water layer are still relatively high (see Table 6.1). The H_2O_2 molecules have a free energy minimum near the head group region, *i.e.*, they prefer to stay close to the phosphate groups (see red dashed line in Figure 6.3). This is due to the favorable H-bond interactions with phosphate groups.[153] The $^{\bullet}$OOH and $^{\bullet}$OH radicals can stay deeper in the PLB. This is more pronounced for $^{\bullet}$OOH with significantly deeper free energy minima, *i.e.*, -16.5, -15.0 and -15.6 kJ.mol^{-1}, in the case of the native, 50% peroxidized and 50% aldehyde oxidized PLBs, respectively (see Figure 6.3).

The behaviour of these species can again be explained from the H-bonds they form.[153] $^{\bullet}$OOH radicals are better proton donors but weaker proton acceptors than water[153] and they more likely interact with ester groups found between the head groups and the lipid tails. $^{\bullet}$OH radicals, on the other hand, can act equally as H-bond donor or acceptor[153] and therefore they can locate close to both ester as well as head groups. Moreover, the presence of one additional oxygen atom in $^{\bullet}$OOH compared to $^{\bullet}$OH radicals results in stronger van der Waals interactions with lipid head groups[153], which might explain the deep free energy minimum shown for $^{\bullet}$OOH (see Figure 6.3). It should be mentioned here that H_2O_2 molecules are more stable in water solution, as they bind with water molecules at least with four hydrogen bonds, which was revealed in an *ab initio* MD study.[215] Moreover, H_2O_2 molecules establish about twice as many H-bonds in water as $^{\bullet}$OH or $^{\bullet}$OOH[153], which can explain why they cannot penetrate deeper in the membrane and they stay close to the aqueous phase and phosphate region (see Figure 6.3).

Nevertheless, all these hydrophilic ROS (*i.e.*, H_2O_2, $^{\bullet}OOH$ and $^{\bullet}OH$) experience permeation barriers by the membrane. This is consistent with experimental evidence, where $^{\bullet}OOH$ and H_2O_2 are found to be much less permeant than O_2.[216] The calculated free energy barriers for all ROS are given in Table 6.1.

TABLE 6.1: Calculated free energy barriers of ROS across native and 50% (peroxide and aldehyde) oxidized PLBs. The values given for H_2O_2, $^{\bullet}OOH$ and $^{\bullet}OH$ are the activation free energies for permeation, *i.e.*, to reach the bilayer center, whereas it is an activation free energy relative to the aqueous phase in the case of O_2 (cf. Figure 6.3).

System	Activation free energy (kJ.mol^{-1})			
	H_2O_2	**$^{\bullet}OH$**	**$^{\bullet}OOH$**	**O_2**
Native	34.5 ± 2.1	20.2 ± 2.1	21.3 ± 2.2	8.3 ± 1.1
50% peroxide	36.4 ± 3.4	18.6 ± 2.5	17.6 ± 2.6	6.5 ± 1.4
50% aldehyde	23.8 ± 1.7	11.1 ± 1.2	15.8 ± 1.7	7.5 ± 2.1

The activation free energy for H_2O_2 permeation in the native PLB is 34.5 ± 2.1 kJ.mol^{-1}, which is in reasonable agreement with the experimental value, *i.e.*, 36.8 kJ.mol^{-1}.[170]

As is clear from Table 6.1, with the exception of H_2O_2 in the 50% peroxidized system, an overall decrease of the activation free energies of H_2O_2, $^{\bullet}OOH$ and $^{\bullet}OH$ for permeation is observed in the case of oxidized PLBs, especially for aldehyde oxidized PLBs. Moreover, it is clear from Figure 6.3 that the FEPs of these species become narrower in the lipid center in the case of the oxidized PLBs. This indicates that in oxidized membranes the ROS are able to accumulate only around the head groups, except for the O_2 molecules (see Figure 6.3bc). The decrease of the free energy barriers and the sharpening of the profiles can be explained below after careful analysis of the effect of oxidation on the PLBs.

Thorough analysis of the effect of oxidation on the structural and dynamic properties of the PLB showed that oxidation of the lipids leads to a higher disordering of the lipid tails, thereby increasing the lipid area and decreasing the bilayer thickness (see Table 6.2).

TABLE 6.2: Summary of the area per lipid, the bilayer thickness and the box size in the z-direction, in case of the native membrane as well as the 50% (peroxide and aldehyde) oxidized membranes.

System	Area per lipid (nm^2)	Bilayer thickness (nm)	Lz (nm)
Native	0.673 ± 0.001	3.89 ± 0.04	9.61 ± 0.02
50% peroxide	0.784 ± 0.002	3.24 ± 0.04	8.26 ± 0.03
50% aldehyde	0.809 ± 0.003	3.33 ± 0.06	8.08 ± 0.05

The larger area per lipid and the drop in bilayer thickness are due to the bending of the polar oxidized groups from the hydrophobic core towards the water interface, which is also described in literature.[1,181] Table 6.2 also illustrates that in case of the aldehyde oxidation product, the increase of the area per lipid is more pronounced than for the peroxide oxidation product, whereas the decrease of the bilayer thickness is smaller. This means that the total bilayer volume is larger in case of aldehyde oxidation, compared to peroxidation of the membrane. This can only be explained by the permeation of water molecules into the membrane (or in the head group region), which would make the bilayer swell. This phenomenon is illustrated in Figure 6.4.

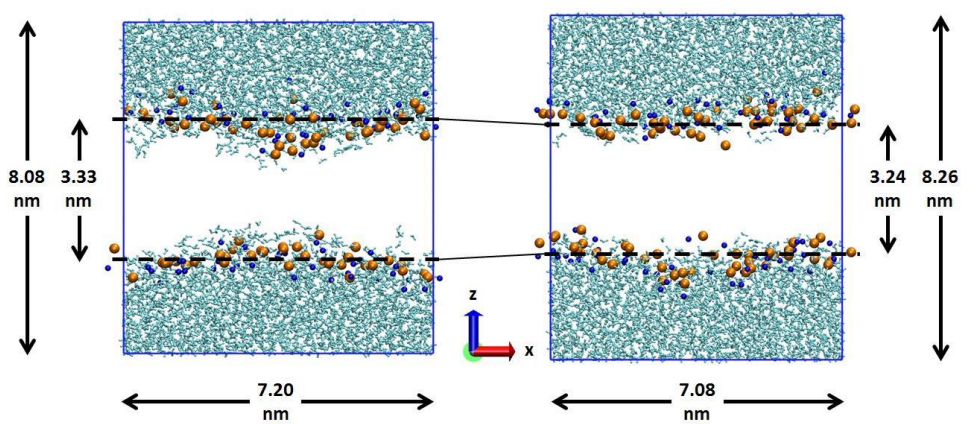

FIGURE 6.4: Schematic illustration of the effect of oxidation on the bilayer thickness and on the box size along the z- and x-axis in case of the 50 mol% aldehyde oxidized system (left) and 50 mol% peroxidized system (right). Note that the box sizes along the x- and y-axis are identical (L_x=L_y). The lipid tails are not shown for the sake of clarity.

The same conclusion can also be drawn by looking at the total size of the box along the z-axis (L_z). From Table 6.2, it is clear that L_z is smaller in the aldehyde oxidized system compared to its peroxidized counterpart, while the bilayer thickness is larger. This again can be explained by the permeation of water molecules into the lipid system, by which L_z decreases and the bilayer thickness increases.

Thus, in the case of aldehyde oxidation, the increase in permeability of the PLB is more pronounced compared to the peroxidation case. This explains the overall decrease of the energy barriers of the ROS in the oxidized PLBs, especially in the aldehyde oxidation case (see Figure 6.3 and Table 6.1). It should also be mentioned that in both oxidation cases the ROS cannot remain stable at the center of the bilayer (as is the case in the native PLB; cf. the flat profiles and even small minima in the profiles in Figure 6.3a), except for the O_2 molecules. This can again be explained by an increase in lipid disordering, which leads to an increase in fluidity of the PLB.

Generally we can conclude that oxidation of the lipid tails leads to a decrease of the lipid order, thereby increasing the bilayer fluidity as well as the permeability of the bilayer to ROS. However, the energy barriers still remain relatively high (order of tens of $kJ.mol^{-1}$), so the ROS will not easily penetrate through the lipid bilayer. This indicates that specific protein channels, like AQPs, or pores are required in order to deliver the ROS into the cell interior.

6.3.2 Effect of the electric field on pore formation

As mentioned above, strong electric fields, *i.e.*, in the range of 0.1 – 100 $kV.cm^{-1}$, can lead to pore formation in the membrane. Some CAP sources produce quite strong electric fields, in addition to reactive plasma species, such as ROS, which cause lipid oxidation. Thus, it is important to know how oxidation of the lipids can affect the threshold electric field for poration, as well as the pore formation time. Figure 6.5 demonstrates snapshots from MD simulations showing the typical pore formation process in a native PLB, under the effect of a constant electric field of 0.5 $V.nm^{-1}$ applied in the direction perpendicular to

the bilayer surface. As mentioned above, the values of the electric field used in the MD simulations are not equivalent to the experimentally applied electric fields, and a detailed clarification of this comparison was given in section 6.2.3 above. Therefore, the MD simulations are still very interesting to obtain information on the effect of electric fields on the electroporation process.

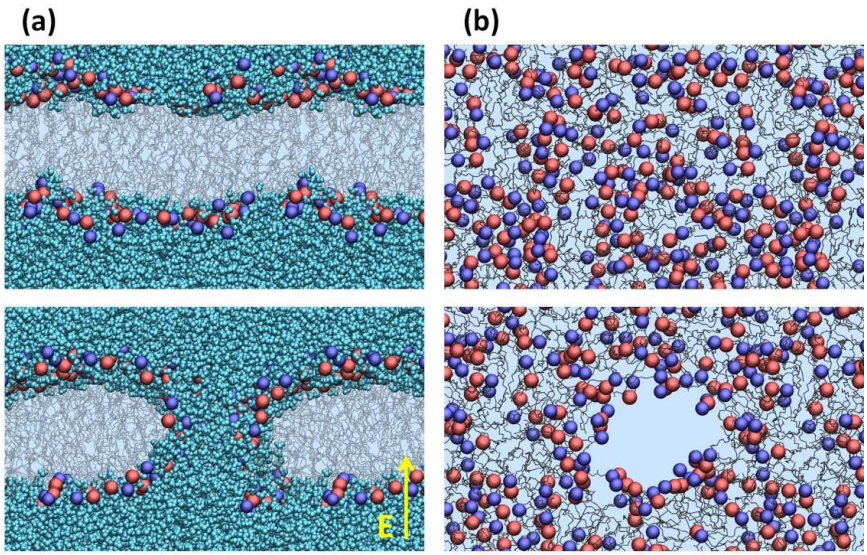

FIGURE 6.5: Snapshots from MD simulations, showing the pore formation in a native PLB after ~2 ns, upon effect of a constant electric field of 0.5 $V.nm^{-1}$, (a) side view and (b) top view. The water layers are removed from the top view picture, for the sake of clarity.

In short, the pore formation begins with the creation of a single-file water defect, which grows quickly (within a few ns) eventually leading to the pore formation. This process is well described in literature (see *e.g.*,[201]). This pore might allow reactive species and other molecules to penetrate deep into the cell interior.

The average time needed to initiate pore formation in a native PLB is plotted as a function of the electric field value in Figure 6.6. It is clear that a stronger electric field leads to a drop in the pore formation time. This behaviour is more or less exponential, which is in agreement with.[217]

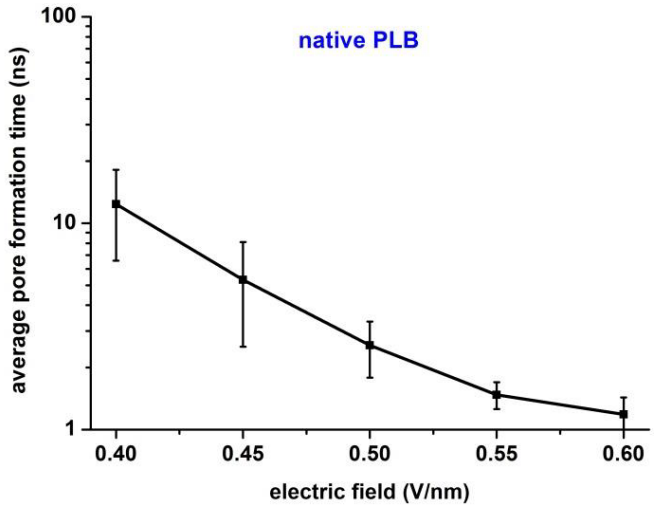

FIGURE 6.6: Average time needed to initiate pore formation in a native PLB, versus the applied electric field.

It should be mentioned that the pore formation is a stochastic process, and therefore, the poration time can fluctuate considerably, as is obvious from the error bars in Figure 6.6. Due to the stochastic nature of the process, there is an inherent uncertainty in the obtained values, which cannot be reduced by increasing the number of simulations.

Figure 6.7 illustrates the average poration time for three different electric field values, as a function of the oxidation degree of the PLB, for both aldehyde (a) and peroxide (b) oxidation. It is clear from Figure 6.7a that for aldehyde oxidation, a higher oxidation degree leads to a drop in the pore formation time. Moreover, electroporation can already occur upon applying lower electric fields compared to the native PLB (cf. Figure 6.6 and the missing data points in Figure 6.7a), which means that the lipid oxidation into aldehydes leads to a decrease of the threshold electric field needed for pore formation to occur. In the case of the peroxidation (see Figure 6.7b), we did not observe the same strong effect of the oxidation on the pore formation time, although again a small drop is noticed compared to the native PLB.

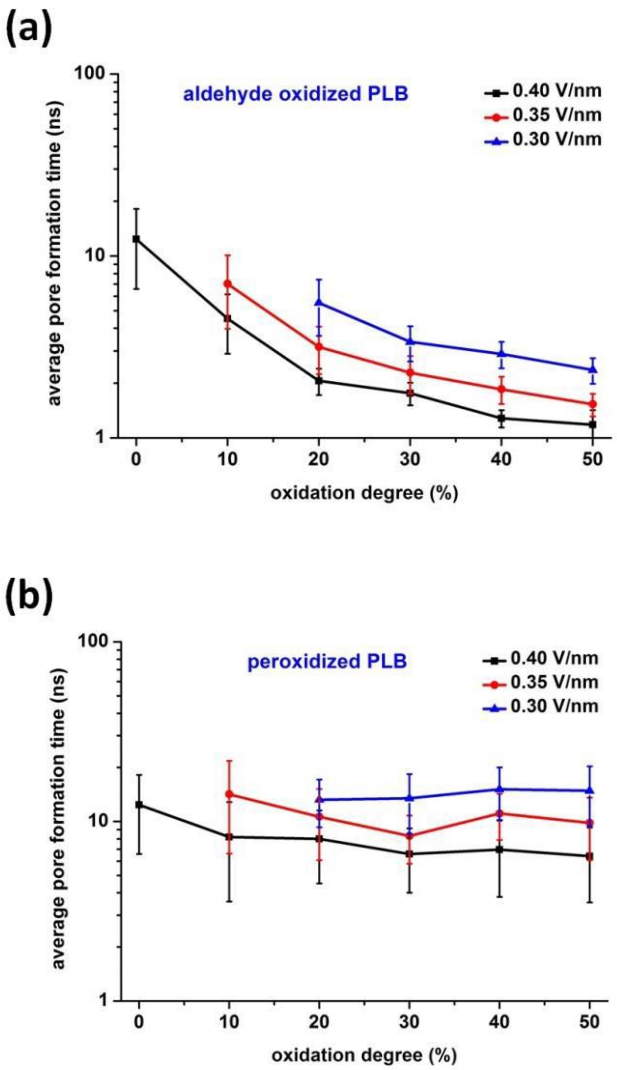

FIGURE 6.7: Average time needed to initiate pore formation, for different applied electric fields, versus oxidation degree, for aldehyde oxidation (a) and peroxidation (b).

The reason for this might be related to the permeability of water through the oxidized PLBs. Indeed, based on our results presented in Figure 6.3, we may expect that the permeation free energy barrier of water through peroxidized PLBs will be higher than for aldehyde oxidation. Since the pore formation process initiates with the creation of water defects (see above), and since the penetration of water molecules to the hydrophobic part of the bilayer will be

more difficult in the case of the peroxidized PLB, more time will be needed for pore formation, independent from the oxidation degree (cf. Figure 6.7).

It should be stressed again that in electroporation simulations the applied electric fields are much higher than the fields used in experiments, which are typically in the order of few $mV.nm^{-1}$.[5,191] As is mentioned above, these values should not be directly compared. For a more detailed clarification of this comparison, see section 6.2.3 above. Moreover, the average pore formation times obtained in MD simulations (see Figs. 6 and 7) cannot be directly related to the experimentally observed pore formation kinetics, which is expressed by a characteristic time (τ), as they are conceptually different. Briefly, τ is an ensemble averaged value which is independent of the size of the PL patch, whereas in MD simulations with small PL structures, the probability of an occurrence of a first pore depends on the patch size (*i.e.*, it increases with patch size). These issues were clarified in more detail in.[218] Thus, the attention should be paid on the trends and not on the exact values of the poration times and electric fields given in Figures 6.6 and 6.7.

In general, we can conclude that oxidation of the lipid tails in the PLB facilitates the pore formation, by lowering the threshold electric field needed for pore formation.

6.4 Conclusions

In this chapter, computer simulations were performed to obtain a better insight in the synergistic effect of an electric field in combination with lipid oxidation on the formation of pores in a PLB. First, the translocation of ROS through native and oxidized PLBs was investigated in the absence of an electric field. It was found that oxidation of the PLs leads to an overall decrease of the permeation free energy barriers of the ROS, especially in the case of aldehyde oxidation. This is due to the increasing fluidity of the PLB, thereby increasing the permeability of the bilayer to ROS. However, the energy barriers are still relatively high, and thus the ROS will still not be able to easily travel through the oxidized PLB. This indicates that there is a need

for specific protein channels, like AQPs, or that pores should be created in order to deliver reactive species into the cell interior.

The latter can be realized by applying an electric field, *i.e.*, so-called electroporation. As some CAP sources produce significant electric fields, besides ROS which may lead to lipid oxidation, we investigated the synergistic effect of the electric field and oxidation of the PLB. Our calculations reveal that a stronger electric field yields a shorter pore formation time. Moreover, oxidation of lipid tails leads to a drop in the average time needed to initiate electroporation, as well as a lower threshold electric field needed for pore formation. This effect was most apparent for aldehyde oxidation, while it was rather minor for peroxidation of the PLB. The latter may be explained by the higher permeation free energy barrier of water through a peroxidized PLB, as the pore formation process is initiated by the creation of water defects.

The results presented in this Chapter provide atomic-level insight into the mechanisms of the combined effect of an electric field and lipid oxidation, as produced, *e.g.*, by cold atmospheric plasma, on living cells.

CHAPTER 7

CAP for transdermal drug delivery

The results presented in this chapter are accepted for publication in:

J. Van der Paal, G. Fridman and A. Bogaerts. Ceramide cross-linking leads to pore formation: potential mechanism behind CAP enhancement of transdermal drug delivery. *Plasma Processes and Polymers*. e1900122.

7.1 Introduction

Transdermal drug delivery (TDD) is an innovative and very attractive drug administration method, as it possesses many advantages over other administration methods, including, *e.g.*, avoiding the first-pass effect of the liver (when compared to oral administration of drugs), reducing side effects (such as pain during hypodermic injections) and the ease of (self-)administration of the drug.[219] To date, TDD systems are already being used in the treatment of a variety of diseases, *e.g.*, to deliver chemotherapeutics or vaccines.[220,221] The first applications of a TDD system date back to 1979, when a 3-day patch was developed to treat motion sickness.[219] The most famous application of a TDD system, however, is undisputedly nicotine patches, which were developed a decade later. Since then, the use of TDD systems in the delivery of drugs has grown rapidly.

One of the main challenges of TDD, however, is that very few drugs can be administered transdermally. Indeed, to achieve an effective concentration of the applied drug in the body, there are very strict limitations to the molecular weight and lipophilicity of the drug molecule.[222] Therefore, TDD is nowadays combined with systems that enhance the permeability of the skin, either mechanically or chemically.

Effective chemical enhancers of the skin permeability are amphiphilic molecules (a compound containing both hydrophilic and lipophilic properties) which actively disturb the lipid order in the skin, thereby creating nanometer-sized defects in the skin. Such defects are, however, often accompanied by skin irritation. If chemical enhancers that have minimal impact on skin irritation are used, the actual enhancement of the permeability of hydrophilic compounds is again very limited, which limits their applicability. In this framework, a lot of research is devoted to using, *e.g.*, peptides[223] or microemulsions[224] as drug carrier systems, which seems to possess a lot of potential. Furthermore, also very promising results are being obtained using styrene-maleic acid lipid particles (SMALPs), in which amphiphilic styrene-

maleic acid copolymers insert themselves into a lipid bilayer (forming a SMALP) and thereby drastically increase its permeability.[225] Mechanically enhancing the skin permeability is based on a process called iontophoresis. By applying an electric field over the skin structure, highly charged drug molecules will be moved due to electrophoresis, while weakly charged or neutral drug molecules will be transported due to the electro-osmotic flow created by the movement of water molecules,[226,227] which is in turn caused by the movement of mobile cations, such as sodium ions (Na^+), present in the skin structure.[228] The downside of this technique is that, as the skin structure itself is not modified, only very small, highly charged drug molecules can be easily transported through the skin. If larger or weakly charged molecules need to be transported at a rate high enough to achieve a therapeutically active drug concentration in the body, very high electric fields need to be applied, which is accompanied with skin irritation and pain.[229] Other enhancement techniques include, *e.g.*, ultrasound, which relies on oscillating pressure waves,[230] electroporation, in which strong electric fields temporarily disrupt the lipid bilayer structures in the skin[231]. All of these techniques, however, have their own limitations.[219]

The discussion above clearly shows that, up until now, each of these enhancement techniques struggle with the balance of enhancing the delivery of drugs to achieve a biologically active level, while avoiding side effects in the process.[232] The challenge of getting drugs through the skin tissue and into the blood vessels is a function of (i) the chemical composition of the drug, as well as (ii) the skin structure. When focusing on the skin structure, research has shown that the outermost layer of the skin, *i.e.*, the stratum corneum (SC), forms the greatest barrier for the transdermal delivery of drugs.[222,232,233] Various studies revealed that the structure of the SC, being only a few hundred micron thick, consists out of keratine-rich cells, the so-called corneocytes or horny cells, which are embedded in a lipid matrix. This matrix contains stacked bilayers of fully extended ceramides (*i.e.*, six main ones that differ from each other mainly in the head group), cholesterol, and free fatty acids.[234–236] A simple schematic of the SC structure is shown in Figure 7.1.

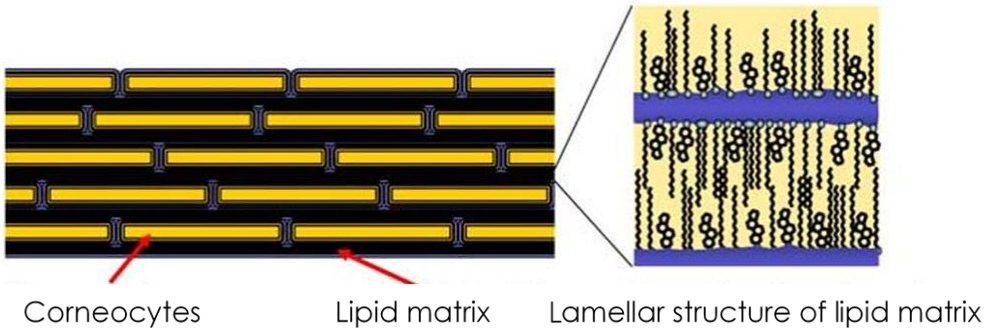

FIGURE 7.1: Schematic illustration of the brick-and-mortar structure of the SC. The corneocytes (bricks) are embedded in a lipid matrix of ceramides, cholesterol and free fatty acids (mortar).

When looking at the structure of the skin, different routes can be identified for drug molecules to reach the underlying skin layers, which are illustrated in Figure 7.2. The predominant path of a drug molecule passing the SC structure is shown to be the intercellular route, in which drug molecules avoid the corneocytes or horny cells, but rather pass through the lipid matrix (see Figures 7.1 and 7.2).[237,238] Indeed, it is reported that permeation through the SC does not significantly depend on biological processes, but rather is more of a passive diffusion process, as the TDD rate for *in vitro* studies is roughly the same as for *in vivo* human trials.[239]

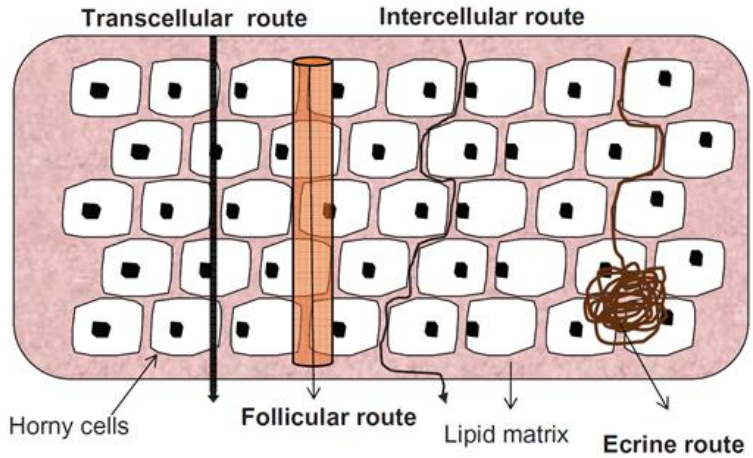

FIGURE 7.2: Illustration of the different pathways for the penetration of drug molecules through the SC.[240]

Recently, it has been demonstrated that CAPs have the ability to enhance the transdermal uptake of drugs in a very gentle way, *i.e.*, while avoiding side

effects such as deeper tissue damage, and without inducing structural changes to the drug or carrier system.[241–246] In these studies, FE-DBDs are used, due to which a synergy of (i) electric fields and (ii) plasma-generated RONS can potentially occur. Moreover, during treatment, plasmas can also promote synergistic biological processes, next to the enhancement of TDD itself, including, *e.g.*, a reduction of the bacterial load[247] and acidification of the skin environment[248]. However, the exact processes occurring during CAP treatment of skin structures remains to be identified. In search of an explanation behind this plasma-induced increase in permeability of the SC, we suggest a reversible pore formation mechanism, as illustrated in Figure 7.3.

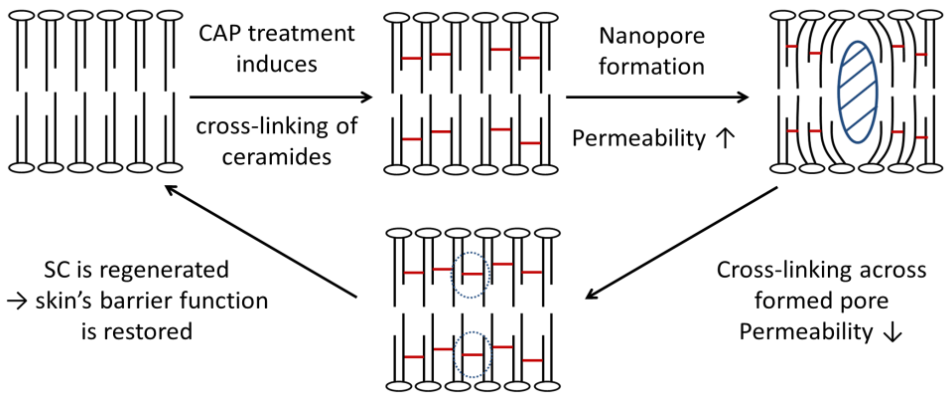

FIGURE 7.3: Proposed mechanism of plasma-induced reversible pore formation in the SC. ROS present in cold plasma induce lipid oxidation in the unsaturated lipid tails of the ceramides in the SC. This leads to the formation of cross-linkages between neighboring lipids. The formation of oligomers of ceramides leads to the generation of voids in between different oligomers. This will enhance the permeability of the SC. Upon prolonged CAP treatment, the entire system will eventually be cross-linked (on a local scale), which will suppress the initial increase of the SC's permeability. As this process only occurs on a nanoscale, the continuous regeneration of the skin will ensure that no prolonged damage occurs.

In this process, lipid oxidation due to CAP-generated reactive oxygen species (ROS; *e.g.*, $^{\bullet}O$ or $^{\bullet}OH$ radicals) leads to the creation of cross-linkages between lipids present in the SC. A ceramide bilayer is taken as a model system of the SC, which can be seen as the target of CAPs to enhance TDD. Two possible mechanisms leading to the cross-linking of neighboring ceramides can be

identified. A first option is that cross-linking occurs due to a process called lipid peroxidation, which starts by the abstraction of an allylic hydrogen due to impinging CAP-generated radicals (*e.g.*, •O or •OH), followed by O_2 addition and the formation of an O-O bridge.[209,249] A second option is a polymerization process that does not involve the formation of an O-O bridge, in which the allylic carbon radical created after H-abstraction immediately reacts with the double bond of a neighboring ceramide (cf. free radical polymerization of alkenes). Either way, due to these cross-linkages, nanopores are generated in the SC structure, which will facilitate the passive diffusion of drug molecules through skin tissue. Since (i) these are nanoscale restructurings of the SC structure, and (ii) the SC is continuously regenerated, the barrier function of the skin can easily be restored.

This hypothesis is based on observations made by multiple other researchers. First of all, the process of lipid oxidation in the presence of ROS had been demonstrated extensively in literature.[209,250,251] As CAPs contain a variety of ROS, it is only logical to assume that oxidation of skin lipids is involved in the underlying mechanism of CAP-assisted TDD. Next, it has been shown by Melo *et al.* that ceramides containing saturated lipid tails are not oxidized when applying oxidative stress (induced by •OH generated under Fenton reaction conditions) .[252] This suggests that if CAP-generated ROS reach the skin lipids, they can only react with unsaturated lipid tails. In this case, cross-linking of these tails, which have the same structure as the aliphatic tail of free fatty acids, is very likely to occur, as has already been demonstrated by multiple researchers.[253–256]

In this chapter, we explore the validity of the proposed reversible pore formation mechanism by employing MD simulations. By comparing bilayer systems containing different numbers of cross-linked lipids, we test if this process can explain the increase in permeability of the SC. Such MD simulations can give us molecular level insight in the effect of cross-linked (CL) ceramides. Indeed, this type of simulations has already been applied successfully to examine the dynamic and structural behaviour of lipid structures under oxidative stress.[152,257,258]

It has to be mentioned that although the SC is often mentioned as the major barrier for drug permeation (see discussion above), it is only one of many layers present in our skin. Even if drug molecules are able to penetrate through this layer, they still need to pass numerous other layers before reaching blood vessels (including, *e.g.*, the stratum lucidum, the stratum granulosum or the stratum spinosum).[224] Furthermore, next to cross-linking of ceramides, CAP-generated RONS could also lead to the formation of, *e.g.*, peroxides in the SC structure. Such oxidation products could also play a role in enhancing the permeability of hydrophilic molecules, as discussed in the previous chapter.

7.2 Methodology

As a model system for the SC, we mimic its structure by a ceramide bilayer, ignoring the presence of free fatty acids and cholesterol. This approach can be justified as ceramides are considered to be the most important determinant of the barrier function of the skin. [259] All simulated systems contain, in total, 1800 ceramides, surrounded by 72000 water molecules on each side. The initial structure was created using the Packmol program[157] and an energy minimization is performed, after which we performed a 900 ns simulation, employing a time step of 30 fs. This proved to be enough to equilibrate the structures, based on an analysis of the x, y and z-dimensions of the system, as well as the total potential energy of the system. The last 250 ns of this run were used to collect the data shown in the figures below. The systems were simulated in the NPT ensemble, using Bussi's velocity rescaling thermostat[260] (at 310 K) and the Parrinello-Rahman barostat[160] (at 1 atmosphere). The non-reactive, coarse-grained Martini force field was used in these simulations[261]. In a coarse-grained force field, multiple atoms are grouped into one bead, thereby reducing the number of particles used to represent each lipid. This allows us to simulate far bigger systems compared to what is possible with all-atom or united-atom force fields. Moreover, since non-reactive force fields do not allow existing bonds to be broken or new bonds to be created during a simulation, cross-linkages between different ceramides were defined in the

initial structures. This non-reactive approach was chosen as it allows to simulate longer time scales, as well as bigger length scales in comparison to the reactive counterpart,[92] and this is necessary to study the above mentioned hypothesis of cross-linking and pore formation. Cross-linked ceramides were added to the force field by including the required topology files. To construct the topology file of a ceramide dimer, a bond was added between neighboring beads, applying the same bond length and force constant present between other beads of the same types (C1 and C3 beads, see[261] for more information). The description of the additional angles, created by this new bond, was based on angles between identical beads as well. To construct oligomers containing more ceramides, the same approach was followed.

As mentioned above, two possible mechanisms leading to the cross-linking of ceramides can be identified. As the exact mechanism is unknown, we opted to implement a hybrid structure in our MD simulations. Indeed, although the lipid peroxidation mechanism involving an O-O bridge between ceramides is the most straightforward (as a free radical polymerization process is sterically hindered due to the large ceramide tails), this does require an additional step, and therefore the presence of O_2. If it would be only lipid peroxidation, a polar Martini bead (the Martini force field uses different types of beads to represent groups of atoms which differ in polarity) would need to be introduced in between the cross-linked ceramides, to account for the O-O bridge. If it would only be a free radical polymerization process, on the other hand, the double bonds would be lost during the reaction while the ceramide structures remain apolar. In the hybrid structure used in our simulations, the bead representing the double bond is preserved (cf. lipid peroxidation mechanism), but no polar bead is implemented in the structure (cf. the free radical polymerization mechanism), as is illustrated in Figure 7.4. Furthermore, as we are mainly interested in the effect of cross-linking ceramides on the overall membrane structure, regardless of the exact configuration of the polymerized chains, this hybrid structure is adequate to provide this information.

To investigate the effect of different cross-linking degrees, we constructed multiple systems, which contain 0, 400, 800, 1200 or 1600 cross-linked ceramides, corresponding to a cross-linking degree of 0, 22, 44, 66 or 88%. These values were chosen to scan the entire range of cross-linked fractions, which can experimentally be achieved by varying the duration of plasma treatment. Moreover, the effect of chain length of cross-linked ceramides was investigated as well (hereafter referred to as the degree of polymerization (DOP)), *i.e.*, we built structures with polymerized ceramide chains containing 5, 10 or 20 ceramides (DOP = 5, 10 or 20). The idea of the polymerized or cross-linked ceramide chains is illustrated in Figure 7.4.

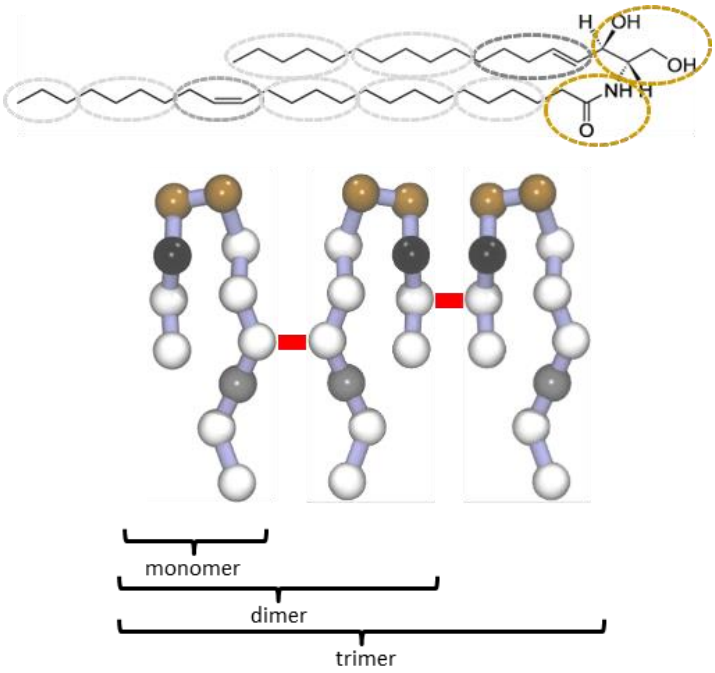

FIGURE 7.4: The top figure shows the all-atom representation of one native ceramide, whereas the bottom figure illustrates the Martini-interpretation of the same ceramide in trimer configuration (one monomer is one native ceramide; the same colors are used for the ovals (group of atoms) in the top figure and corresponding beads in the bottom figure; see text). Moreover, the bottom figure schematically illustrates how the cross-linked structures are built for the simulations. The longer chains (5-, 10- and 20-linked) are built in the same way. The color (and thus the type) of each bead is based on the polarity of the corresponding group of atoms which the bead represents.

The analysis was performed using a search and find algorithm, which calculates the void size in each system.[262] In a first step, the entire system was divided into cubic cells, with dimensions of 2.5x2.5x2.5 Å^3. Next, the system was scanned for free cells, *i.e.*, cells which don't contain any atoms. Afterwards, the volume of all free cells was summed up to get the total void size mentioned in the figures below. However, when calculating this void size, we only used larger clusters of cells, *i.e.*, clusters that contained at least 15 linked free cells. Using this boundary condition, we ignored very small voids between neighboring lipids, because these would have no effect on the permeability of larger drug molecules. The graphs shown below illustrate the relative increase in void size, which is calculated as follows:

$$\Delta_{Void\ size} = \frac{Void\ size_{CL} - Void\ size_{N}}{Void\ size_{N}} x100\ \% \qquad (7.1)$$

With $\Delta_{Void\ size}$ being the relative increase in void size, $Void\ size_{CL}$ the total void size in a system which contains cross-linked ceramides and $Void\ size_{N}$ the free void size in the native system, *i.e.*, the system containing only monomeric ceramides.

To determine the average void size and the associated error bars, 50 snapshots were selected from the last 250 ns of each simulation (*i.e.*, one every 5 ns). Furthermore, all systems were run in duplicate (starting from different lateral distributions of the lipids in the input geometry). The free void size was calculated for each individual snapshot, which renders a total of 100 values for all data points shown in the figures below.

To test the possibility of synergistic effects of cross-linked ceramides and electric fields, additional simulations are performed using the last frame of each equilibrated structure as input, and applying an electric field of varying strength. Electric field strengths of 262.5, 275, 300, 350 and 400 mV.nm^{-1} are investigated on systems with different cross-linking degrees, in the case of a DOP of 20. The simulations are run for 300 ns, using the same simulation parameters as in the equilibration runs. By selecting 10 frames from the last 10

ns of the equilibration run (*i.e.*, one frame every ns), 6 independent electric field simulations are performed. For each simulation, the time until the occurrence of pore formation is calculated, which is subsequently averaged over all independent simulations.

7.3 Results and discussion

7.3.2 Effect of cross-linking on the generation of voids

Figure 7.5 illustrates the calculated relative increase in void size for different cross-linking (CL) degrees and different degrees of polymerization (DOP). Upon increasing the cross-linking degree of the ceramides present in the SC structure up to 44%, the total void size increases drastically. The relative increase in void size, compared to a structure containing only monomeric ceramides, reaches about 40% for all DOPs investigated. However, when increasing the number of cross-linked ceramides even further, the relative increase in void size decreases again. Although the graphs show similar trends for all DOPs, the exact value of this threshold depends on the length of the polymerized ceramide chain. Indeed, for a DOP of 20, there is already a significant effect on the void size for a cross-linking degree of 22%, whereas for DOPs of 5 or 10, the effect is only significant for a cross-linked fraction of 44%.

In terms of application for TDD, these results indicate that the enhancement of the permeability of the SC by CAP will strongly depend on the treatment time. During treatment, the permeability of the SC will increase, reaching maximum enhancement for a certain treatment time. Prolonged treatment will have the opposite effect, suppressing the further increase in permeability. The optimal treatment time will be determined by the composition of the SC (patient specific) as well as the CAP source used.

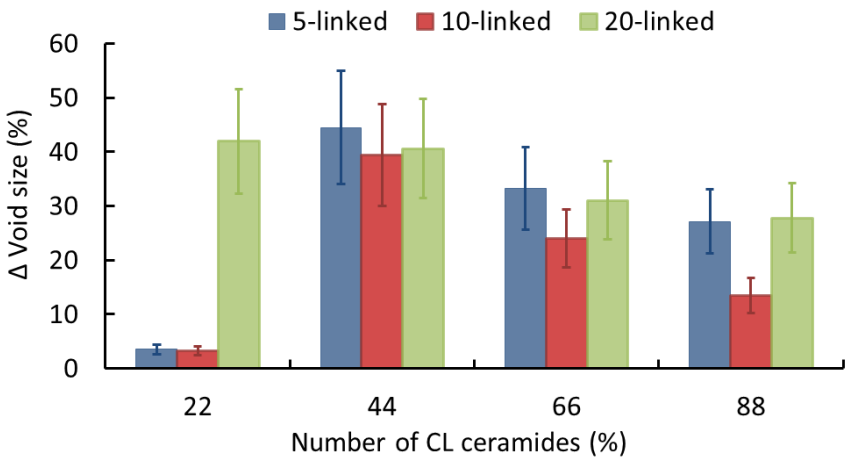

FIGURE 7.5: Effect of the cross-linking (CL) fraction and degree of polymerization (DOP) on the relative increase in total void size with respect to the system without cross-linking. Upon increasing the cross-linked fraction of the system, the free void size first increases (up to cross-linked fractions of 44%), after which the total free void size decreases again. The DOP does not have a big effect on this trend.

It has to be acknowledged that the error bars shown in Figure 7.5 are quite large (~20% of the average value). However, performing additional simulations or increasing the sampling time period did not reduce these error bars. This is due to the combination of (i) the dynamic nature of the lipids in the bilayer and (ii) the analysis tool used in this study. Indeed, the flexible lipid tails can easily cross through one of the cells that is part of a bigger cluster, due to which the cluster could be broken into two smaller parts, which separately would not be included in the calculations anymore (see above). This artefact cannot be avoided in our analysis, but we do believe that this is the best analysis tool available.

The correlation between the increase in void size in the SC and the permeability of water molecules is illustrated in Figure 7.6, by looking at the distribution of water molecules across the structure when introducing cross-linked ceramides into the SC. Indeed, this Figure shows that after polymerization, the tendency of water molecules to populate the bilayer interior increases. Although no water molecules are able to reach the center of

the membrane (in agreement with the absence of pore formation in our simulations), this increase in water permeability can still allow for an increase of the permeability of drugs, *e.g.*, in the case of the presence of an electric field over the SC structure (present in, *e.g.*, floating-electrode DBDs).[263]

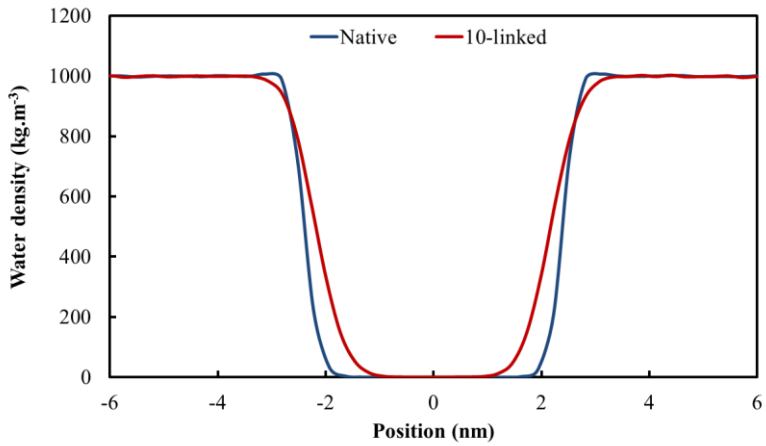

FIGURE 7.6: Water density across the SC along the bilayer normal, in a structure containing no cross-linked ceramides versus a structure consisting of 44% of 10-linked ceramides (shown as representative example of a cross-linked SC system).

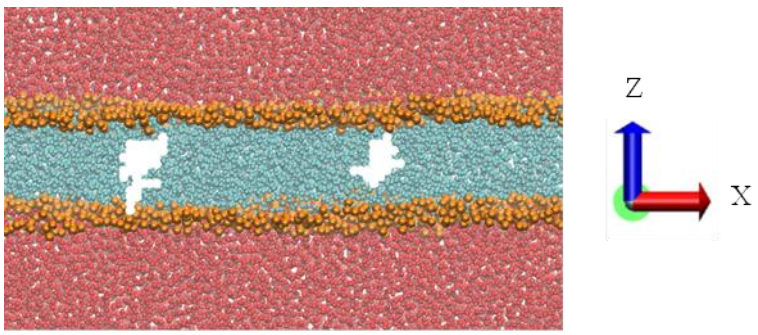

FIGURE 7.7: Front view of a ceramide bilayer system. The water molecules above and below the bilayer are depicted as red spheres, the ceramide head group are depicted as orange spheres and the lipid tails in cyan. The two biggest voids observed in this system are depicted in white. In this system (DOP = 10, 44% of CL ceramides), around 10% of the entire membrane is void.

In Figure 7.7, a snapshot of one of the SC structures investigated is shown, which illustrates the pores created (visualized using the VMD program[264]). The seemingly rough edges of the pores shown in Figure 7.7 originate from

the method used, in which cubic cells are used to identify voids (see discussion above). Note that only a slice (along the xz-plane) is displayed in this Figure, to be able to visualize these voids.

7.3.2 Effect of the electric field on pore formation

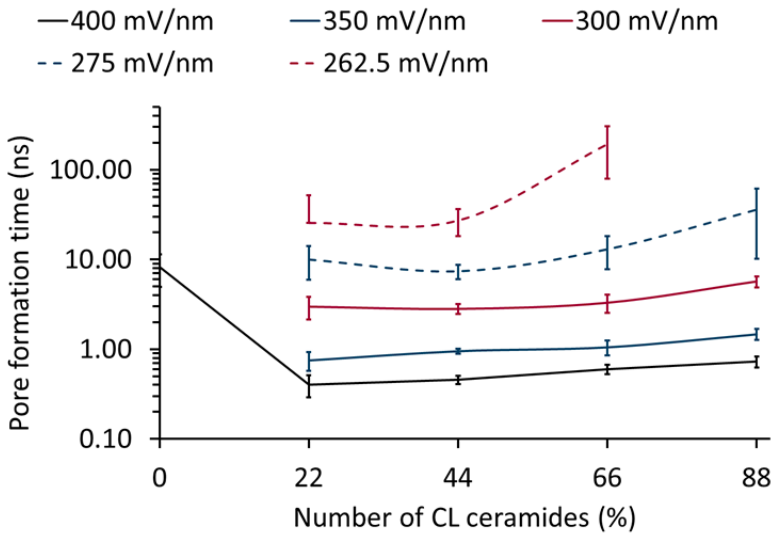

FIGURE 7.8: Average time needed to initiate pore formation, for different applied electric fields, versus cross-linking degree. In the case of the 0% cross-linked structures, no pore formation is observed within the 300 ns simulation for electric field strengths lower than 400 $mV.nm^{-1}$.

Figure 7.8 illustrates the average time needed to induce pore formation for five different electric field values, as a function of the cross-linking degree of the ceramide bilayer (DOP = 20). As expected, increasing the electric field strength leads to a reduction of the poration time. More interesting is the behaviour in the case of a fixed electric field strength when altering the cross-linking degree. These results show that initial cross-linking of ceramides (up to 22%) leads to a reduction of the poration time. However, when the cross-linking degree is increased further, this poration time increases again (although the longest time is always observed for the native SC structure). These results confirm the hypothesis that cross-linking of ceramides can facilitate the permeation of molecules through these structures, and that electric fields (present in FE-DBDs often used in these applications) can exert a

synergistic effect. They also show the same trend as observed in the results of the void size simulations, *i.e.*, initial cross-linking has the strongest effect (largest void size measured and shortest time needed to induce pore formation), whereas further cross-linking partially cancels this (decrease in void size and increase in poration time).

7.4 Conclusions

We have performed coarse-grained MD simulations in search of the mechanism behind CAP-enhanced TDD. The hypothesis put forward is that lipid tail oxidation, induced by plasma-generated ROS, leads to the formation of cross-linkages between neighboring ceramides. This, in turn, leads to the generation of nanopores, which facilitate the diffusion of drug molecules through skin tissue, as observed experimentally. Our MD simulations reveal that cross-linking of the ceramides indeed induces the creation of voids in the SC structure, which can facilitate the diffusion of drugs. Next to this, a synergistic effect is observed when an external electric field is applied on native or cross-linked ceramide structures. Furthermore, our results predict that there will be an optimal treatment time to achieve maximum enhancement of the SC permeability, which, experimentally, will depend on the exact composition of the SC, as well as on the plasma source used. Indeed, both the void size calculation results, as well as the results of the electroporation simulations show that initial cross-linking has the strongest effect, whereas these effects are weakened when further cross-linked ceramides are introduced. Overall, our results indicate that the induction of ceramide cross-linking can be an explanation for the experimentally observed ability of CAP to enhance transdermal drug delivery.

CHAPTER 8

Lipid composition and RONS permeation

The results presented in this chapter are accepted for publication in:

J. Van der Paal, S.-H. Hong, M. Yusupov, N. Gaur, J.-S. Oh, R. D. Short, E. J. Szili and A. Bogaerts. How membrane lipids influence plasma delivery of reactive oxygen species into cells and subsequent DNA damage: An experimental and computational study. *Phys. Chem. Chem. Phys.*. **21**, 19327-19341 (2019).

8.1 Introduction

Targeted cell membrane therapy has the potential to shape the future of how we treat and manage chronic diseases such as cancers. In order to continue improving cell membrane therapies, it is necessary to improve our fundamental understanding of how the unique features of diseased *versus* healthy cell membranes can be exploited for treatment of the disease with minimal damage to healthy cells and tissue. Indeed, in a wide range of diseases, the cell membrane composition is altered and membrane function is perturbed.[265,266] New approaches for the treatment of chronic diseases, including cancers, target these perturbations in membrane composition and function.[266] For example, cancer cells display a higher phosphatidylethanolamine (PE) content in the outer leaflet of the bilayer membrane, as they lose their ability to maintain PE asymmetry in both leaflets of the plasma membrane.[70] Raised PE content enhances the susceptibility of the cell membrane to perforation in response to peptide-based anti-cancer therapy and has been shown to lead to eventual cell death.[267] Another relatively new strategy is the use of molecular drugs, such as Minerval® (2-hydroxyoleic acid), which interfere with lipid structures within the cell membrane to kill cancer cells.[268]

When focussing on targeted membrane therapy for cancer treatment, a major issue still to be addressed is to increase our understanding of how the complex interplay between the array of membrane lipids and other membrane components influences the cell response to anti-cancer therapies. This problem is exacerbated by the fact that there are more than 1000 different lipids in any eukaryotic cell.[145,269] On one hand, the overall structure of the membrane is determined by the chemical structure of each of these individual lipids. The fluidity of the membrane, for example, increases when introducing lipids which contain shorter lipid tails, unsaturated cis-double bonds, and decreases when cholesterol is added to the system.[46] On the other hand, the overall composition of a membrane is only one part of the picture. As the lipids are free to move throughout the plane of the membrane, lipids with long

saturated carbon tails and cholesterol molecules tend to cluster together due to strong van der Waals interactions, leading to the formation of transient microdomains or rafts.[46]

In the development of therapeutics that leverage on differences in cell membranes, the starting point has been to focus on the (currently known) few global differences in the membrane lipid composition between a diseased (*e.g.*, cancerous) cell and its healthy equivalent cell.[265] In the case of cancer, cancerous cell membranes compared to their healthy, normal counterpart are typically characterised by (i) a higher number of aquaporin channels[71,74], (ii) a lower amount of cholesterol[67,68], (iii) increased levels of unsaturated lipids[67,68], and (iv) altered amounts of certain lipid types (*e.g.*, PE as mentioned above).[70] These unique features of cancer cells are currently being investigated as potential targets for anti-cancer therapies. This is particularly applicable for therapies that induce oxidative stress in cancer cells (*e.g.*, chemotherapy, radiation therapy and in the context of this study, plasma therapy) through the production of ROS, which (once inside the cell) can lead to biochemical changes in the cell such as irreversible DNA damage, resulting in eventual cell death.[270]

Owing to the complexity of cell membranes, simple models usually comprising one or two phospholipid types have been developed to gain new insights into the role of specific cell membrane components in regulating cellular processes, both experimentally, *e.g.*, with phospholipid vesicle cell models, and by computational simulations of lipid bilayers.[271] These model systems have also been utilised to study the response of specific components of the cell membrane to oxidative stress. For example, it was observed that the membrane of phospholipid vesicles is more prone to destabilisation through oxidation processes when the membrane cholesterol content is below 50 mol%[272], and MD simulations of lipid peroxidation products have revealed that at reduced levels of cholesterol, membranes are less capable of self-repair from physical damage induced by oxidation of the membrane lipids.[152]

This chapter aims to provide new insight into how plasma-generated ROS interact with vesicles comprising lipids typical found in healthy and cancer cells. More specifically, by experiment and computational modelling, we investigate how ROS interact and penetrate vesicles comprising different proportions of saturated and unsaturated lipids, and how the addition of cholesterol and changes in PL head group influence these interactions and the transport of ROS to the vesicle interior. The subsequent ability of ROS to induce DNA damage within the vesicles is measured using a molecular beacon (MB). Vesicles were subjected to a mixture of ROS, including, *e.g.*, $^{\bullet}OH$, $O_2^{\bullet-}$ and H_2O_2, all generated using an APPJ. These plasma jets are being intensively investigated for cancer therapies with promising patient outcomes already seen in initial clinical case studies.[273] The main mode-of-action of plasma jets in treating cancers is thought to arise from the rich mixture of ROS and RNS delivered by plasma jets into cells and tissue, targeting the destruction of cancer cells and tumours through oxidative stress.[21] Vesicle experiments are supported by umbrella sampling (US) MD simulations, investigating the effect of the membrane composition on the permeation of H_2O_2, which is known to be one of the major longer-lived ROS generated by plasma jets in aqueous liquids[274], and is an important cellular signalling molecule.[275]

An exciting feature of plasma as a cancer treatment therapy, versus radiation therapy, is that plasma is non-ionizing and is therefore possibly "gentler" on bystander (non-cancerous) cells.[276,277] Further, it is possible to scale down the plasma beam to the single-cell-level, enabling highly-targeted treatment.[278,279] Plasma devices are also much more affordable: for instance, current commercial medical plasma devices retail as low as few tens of thousands of USD, which is significantly less than the costs of new linear accelerators of around 1M USD.

Note: The MD simulations discussed in this chapter were performed by Maksudbek Yusupov.

8.2 Methodology

8.2.1 General set-up

Figure 8.1 illustrates the plasma jet treating vesicles in solution with the location of the voltage probe, current monitor and the spectrometer for optical emission spectroscopy (OES).

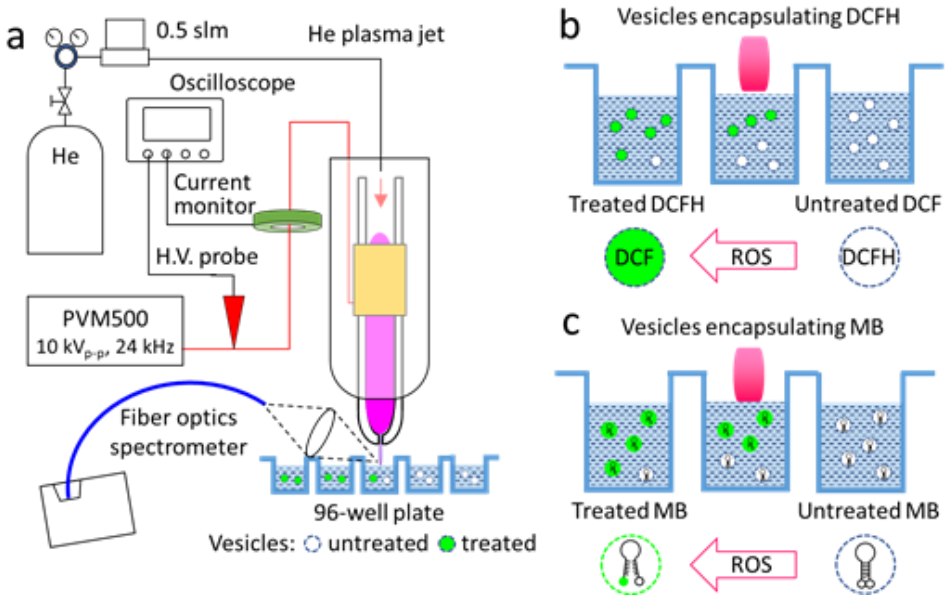

FIGURE 8.1: (a) Illustration of the plasma jet configuration used for the treatment of the vesicle solutions, and the location of the voltage and current probes and OES for the plasma diagnostics. Illustration of the induction of fluorescence in vesicles containing (b) encapsulated 2,7-dichlorodihydrofluorescein (DCFH) or (c) MB.

The plasma jet was described in detail elsewhere.[97] A grounded plate was placed below the 96-well plate, which served as a counter electrode for the powered ring electrode. Helium (He) gas (BOC, high purity grade) flow was fixed at 0.5 standard litres per minute (slpm) throughout all experiments using a digital mass flow controller (Apex, 0–2 slpm flow range). A sinusoidal voltage of 10 kV_{p-p} (peak-to-peak) at 24 kHz was applied to the external electrode with a PVM500 power supply (Information Unlimited). The treatment distance, measured between the nozzle of the plasma jet and the top of the 96-well plate, was fixed at 3 mm.

The applied voltage and current were measured using a ground-referenced high voltage probe (Pintek Electronics, HVP-18HF) directly connected to the HV cable and a current monitor (Pearson 2877) placed around the insulated part of the high voltage cable. The discharge current was determined by subtracting the current measured during operation of the plasma jet from the baseline current measured at the applied voltage but without helium flow (*i.e.* without plasma discharge).

A fibre optic spectrometer (OceanOptics, Model – Flame-TX-R1-ES, Grating – #31-500/250) was used for measuring the optical emission between 200-1000 nm. All the measurements were taken in a custom-built "dark box" to prevent interference from ambient light.[97] The optical emission from the visible effluent of the plasma jet was recorded during treatment of the vesicle solutions. The integration time of the spectrometer (T) was set to 100 ms.

8.2.2 Phospholipid vesicle synthesis

Ten different vesicle compositions were synthesized, which all contained different concentrations of 1,2-dioleoyl-*sn*-glycero-3-phosphocholine (DOPC), 1,2-dipalmitoyl-*sn*-glycero-3-phosphocholine (DPPC), 1,2-dipalmitoyl-*sn*-glycero-3-ethanolamine (DPPE), and cholesterol. All compositions are shown in Table 8.1.

These specific lipids were chosen, as lipids containing a phosphatidylcholine (PC) head group are the most common lipids in all cellular membranes (up to almost 60 mol% in specific membranes).[67,280,281] Moreover, C18 lipids are also one of the most abundant fraction of lipids found in cellular membranes, both in healthy cells, as well as in cancerous cells.[67,281] Furthermore, lipids containing a phosphatidylethanolamine (PE) head group were added to this study as certain diseased cells, such as cancer cells, display a higher phosphatidylethanolamine (PE) content in the outer leaflet of the bilayer membrane.[70] Lastly, by investigating DOPC, DPPC and DPPE, we were able to systematically alter one lipid parameter (head group or saturation degree), while keeping all others fixed.

The concentrations of DPPE were chosen because the PE concentration in the cell membrane is approximately 25%.[280] In healthy cells, all PE lipids are in the inner leaflet, but cancer cells lose the ability to maintain this asymmetry, with PE being expressed also in the outer leaflet.[267] In this study, we assume that the RONS will affect the outer leaflet first. Therefore, we chose to mimic the increasing concentration of PE in the outer leaflet of cancer cells up to 25 mol%. The concentration of cholesterol investigated in this study is also based on concentrations observed in human cells.[282]

TABLE 8.1: Composition of the synthesized phospholipid vesicles.

Mixture	Cholesterol (mol%)	DOPC (mol%)	DPPC (mol%)	DPPE (mol%)
1	10	0	85	5
2	15	0	80	5
3	25	0	70	5
4	10	85	0	5
5	15	80	0	5
6	25	70	0	5
7	25	0	75	0
8	25	0	50	25
9	25	75	0	0
10	25	50	0	25

The different lipid compositions used in the ten vesicle types synthesized allowed us to tailor (i) the saturation degree of the phospholipid membranes with DOPC and DPPC, (ii) the cholesterol fraction within the membranes, and (iii) the size of the lipid head group with DPPE (which has a relatively small lipid head group compared to DOPC and DPPC). The key features of DOPC, DPPC, DPPE and cholesterol that were tested in this study are shown in Figure 8.2.

The vesicles were synthesized by mixing 100 µL of a 0.1 mM stock solution of each vesicle (in chloroform) with 200 µL of chloroform, after which the solutions were dried with nitrogen gas until only a thin film of the lipids on the bottom of the vial was left. Afterwards, 2.5 mL of the pre-prepared MB

or DCFH solution (in HEPES) was added, and the mixture was heated to 70 °C for 10 min for DCFH or 50 °C for the MB (lower temperature to prevent unwanted conformational changes to the MB). Subsequently, the mixture was extruded 15 times through two 100 nm polycarbonate membranes in a hand-held syringe extruder (Avanti Polar Lipids, model # 610000). This extruded solution was then transferred to a Sephadex G25 column, to purify the mixture and remove non-encapsulated dye. Finally, the eluate was stored overnight at 4°C. Before CAP jet treatment, the vesicles were diluted by adding 4 mL of 4-(2-hydroxyethyl)piperazine-1-ethanesulfonic acid (HEPES) to the solution. The details of the buffers used in this synthesis can be found in the Appendix A, section A2).

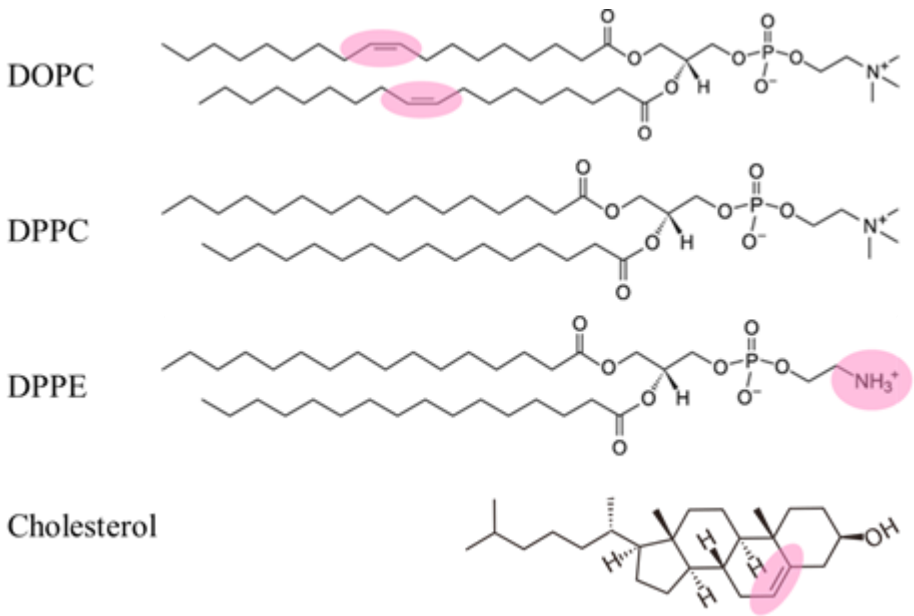

FIGURE 8.2: Schematic representation of the structures of DOPC, DPPC and DPPE lipids, and cholesterol. The parts highlighted in pink indicate key differences in the structure of each molecule that was tested in this study.

8.2.3 2,7-dichlorodihydrofluorescein (DCFH): assessment of ROS ingress into vesicles

A 1 mg/mL DCFH solution was prepared by dissolving 5 mg of DCFH-diacetate (Sigma-Aldrich, catalogue number D6883) in 5 mL of neat ethanol.

This solution was stored at -18 °C until use. Ester hydrolysis was induced by adding 500 μL of the DCFH solution to 2 mL of a 10 mM sodium hydroxide solution and incubating at 25 °C for 30 minutes at ambient temperature, before adding 10 mL of HEPES buffer to neutralise the solution.

8.2.4 Molecular beacon (MB): assessment of DNA strand breaks

The MB consisted of a single-stranded loop and double-stranded stem structure with a fluorophore and quencher moiety at the end of each DNA strand. With the MB intact, the quencher inhibits fluorescence of the fluorophore. If the DNA strand of the MB breaks, the quencher is separated from the fluorophore, resulting in a switch-on of fluorescence (as a positive indication of DNA strand breaks).[283] 37 nmol of MB (Sigma Aldrich, 3017672631, FAM-5-GCACTGAAGCGCCGCACGCCATGTCG-ACGCGCTTCAGTGC–3′-BHQ-1), as supplied in each bottle, was dissolved in 372 μL of 10 mM Tris-base buffer (pH 7.6), giving a final concentration of 0.1 mM. To ensure the correct configuration of the MB, the solution was first heated to 95 °C to (reversibly) denature the DNA, after which the MB was incubated overnight in the dark at ambient temperature, allowing the MB structure to slowly reform to its correct configuration. The MB solution was further diluted (1:5) in HEPES leading to a final working concentration of 16.7 μM for encapsulation within the vesicles.

8.2.5 Microplate reader measurements

After CAP jet treatment of the 200 μL test solutions, 100 μL of the solution was transferred to a fresh 96-well plate for absorbance or fluorescence measurements on a BMG Labtech Fluostar Omega microplate reader. Fluorescence of the MB or DCFH was recorded at an excitation wavelength of 485 nm and emission wavelength of 520 nm. Absorbance of the OPD was measured at a wavelength of 450 nm. Unless otherwise stated, all samples were measured directly after treatment. Where applicable, the normalised intensities were calculated by dividing the measured intensity of the test (CAP jet treated) solution by the non-treated solution.

8.2.6 Simulation: H_2O_2 delivery across different membrane compositions

We performed MD simulations to study the permeation of H_2O_2 across lipid bilayers with various compositions. Although CAPs generate many different RONS, we choose to focus on H_2O_2 as (i) we demonstrated in our previous work[263,284] that all polar RONS behave in the same way as H_2O_2, and (ii) as the vesicles are treated in a liquid solution, so a large fraction of the short-lived RONS generated by the plasma jet (e.g., •OH) will recombine before reaching the vesicles, making H_2O_2 the most abundant reactive species present in the solution. As in the experiments, ten different bilayers were constructed, of which the composition was chosen to mimic the composition of the vesicles studied experimentally, *i.e.*, the bilayers contained different concentrations of DPPE and cholesterol in DPPC or DOPC systems. All these bilayers contained a total of 128 lipids, hydrated by 6000 water molecules surrounding the bilayer structure on both sides. The MD simulations thus only included a small patch of a membrane, which then served as a model system for the entire vesicle. The construction of the systems, as well as the equilibration procedure and the details of the US simulations, are provided in Appendix A, sections A2 and A4, respectively).

8.2.7 Simulation: Area per lipid calculation

The surface area per lipid was determined by dividing the total surface area of the membrane (averaged over the 200 ns, by sampling the data after every 200 ps) by the number of lipids of one leaflet of the phospholipid bilayer (PLB) (*i.e.*, Lx × Ly/64, where Lx and Ly are the x and y dimensions of the PLB, respectively, and 64 is the number of lipids present in one layer).

8.2.8 Simulation: Radial distribution function calculation

The radial distribution function (RDF) determines the probability of finding a particle at a certain distance from a fixed reference particle. We calculated the RDF between phosphorus atoms of neighboring DOPC molecules in membranes containing either 0 or 25% DPPE, using the last 200 ns of the equilibration run (by sampling the data after every 200 ps) and applying the gmx rdf tool of GROMACS.

8.2.9 Statistical analysis

Statistical analysis was performed on the data presented in figures 4, 6 and 7, using an unpaired Student t-test assuming unequal variances. A *p* value of less than 0.05 or 0.001 was considered to be significantly different (95% and 99.9% confidence, respectively).

8.3 Methodology

8.3.1 CAP jet as a source of oxidative molecules

The basic electrical and optical properties of the CAP jet were characterised in order to determine how the physicochemical properties of the CAP jet relate to the delivery of ROS into the vesicle solution. Figure 8.3a shows the voltage and current waveforms during CAP jet treatment of a vesicle solution. The same voltage waveform with amplitude of 10 kV_{p-p} at 24 kHz was maintained for all of the experiments (Figure 8.3a). Figure 8.3a also shows the typical positive and negative discharge current peaks expected for a dielectric barrier discharge CAP jet.[285] The average discharge power was calculated to be 0.79 W.

Optical emission spectroscopy (OES) was used to determine the high-energy components of the CAP jet that facilitate ROS (and RNS) chemistry. Figure 8.3b shows a typical optical emission spectrum profile of the CAP jet during treatment of the vesicle solution including the N_2 2nd positive system ($C^3\Pi_u$–$B^3\Pi_g$) and the N_2^+ 1st negative system ($B^2\Sigma_u^+$–$X^3\Sigma_g^+$) between 300-400 nm, and the $^{\bullet}OH$ at 308 nm.[286]

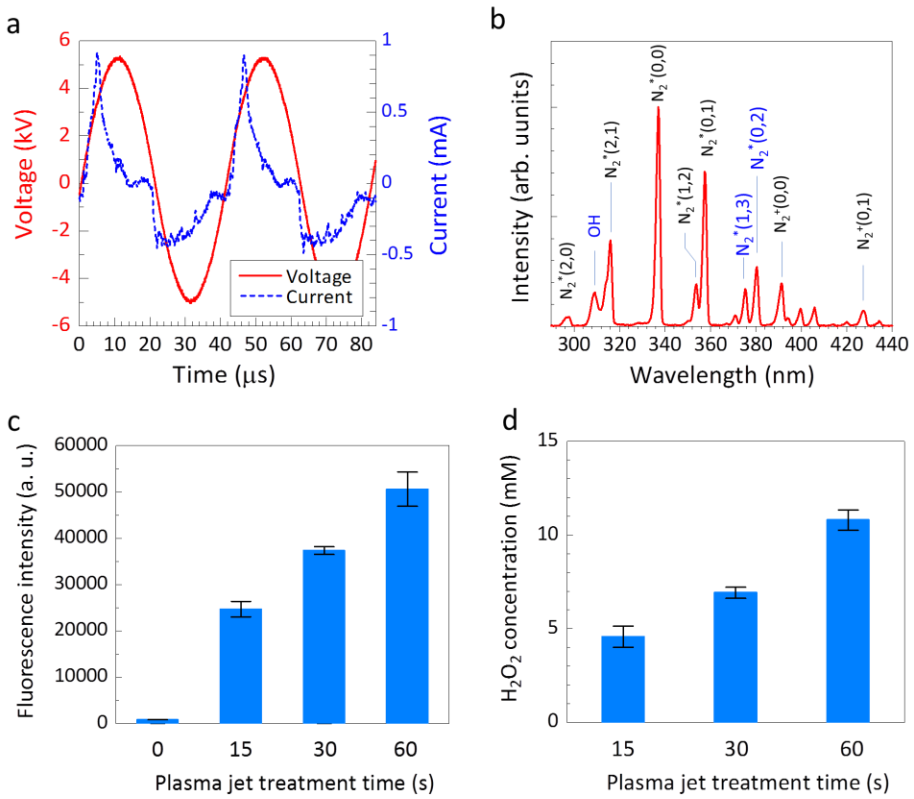

Figure 8.3: Electrical and optical characteristics of the CAP jet and its generation of oxidative molecules in HEPES buffer. (a) Applied voltage and current waveforms at 10 kV_{p-p} and 24 kHz; (b) optical emission spectrum profile between 280–440 nm; (c) ROS and RNS generated in HEPES with the CAP jet, as measured by fluorescence of the DCFH molecular probe after oxidation by ROS and RNS; (d) H_2O_2 concentrations generated in HEPES with the plasma jet as measured by the OPD/HRP molecular probe system.

Using the theoretical calculation of the N_2 2nd positive system [N_2^*(1,3) and N_2^*(0,2)] with the spectrum simulator of the N_2^* 2nd positive system kindly provided by Professor Hiroshi Akatsuka at Tokyo Institute of Technology [287], we obtained the best fitted spectra with the rotational temperature (T_r) of 0.028 eV. T_r is considered the gas temperature because of the rapid rotational relaxation through inelastic collisions between molecules and atoms[288], and was calculated to be 290 K. Here, the T_r of N_2 molecules is in very good agreement with our previous calculations.[289–291] The vibrational temperature

(T_v) of 0.28 eV was higher than our previous studies. This is probably due to the higher frequency of 24 kHz used to operate the CAP jet in this study compared to our previous studies (below 10 kHz), which probably resulted in increased inelastic collisions between electron and N_2 molecules in the ambient air. In Figure 8.3b, a prominent peak is seen at 308 nm representative of the $^{\bullet}OH$, which is a key species that can produce longer-term ROS chemistry in solution, particularly through recombination of neighboring $^{\bullet}OH$ molecules producing H_2O_2 [292,293]. H_2O_2 can persist in solution on the timescale of days or longer.[294,295]

We used DCFH as a broad range molecular probe for ROS (and RNS) molecules to qualitatively determine the CAP jet production of these molecules in the buffered solution. As shown in Figure 8.3c, the fluorescence of DCFH (after oxidation by ROS and RNS) increased as function of the CAP jet treatment time. As mentioned above, H_2O_2 is usually the most abundant longer-lived ROS generated by CAP jets in solution. Figure 8.3d shows that the concentration of H_2O_2 increased as function of CAP jet treatment time in the concentration range 4-12 mM. We anticipated that this H_2O_2 concentration range would be sufficient to observe changes in the vesicles.[296]

8.3.2 ROS delivery into vesicles with different membrane compositions

Having established that the vesicles remained intact after CAP jet treatment (Appendix A, section A6), we next set out to study how different components of the vesicle membranes influence the ingress of ROS into the vesicle interior. Enhanced ingress of ROS into biological cells induces a higher level of oxidative stress on the cells, and excessive or sustained levels of ROS are toxic to all cells, which for some applications can be used for the targeted destruction of cells (*e.g.*, in cancer therapy).[297] The specific membrane components studied were: (i) unsaturated and saturated phospholipids; (ii) cholesterol fraction; and (iii) DPPE. For these experiments, DCFH encapsulated within the vesicles was used as a fluorescence probe for detection of ROS (and RNS).

8.3.3 ROS delivery across cell membranes

Oxidation of non-fluorescent DCFH to fluorescent DCF was used to qualitatively measure the amount of ROS that had entered vesicles after CAP jet treatment. In the context of the CAP jet used herein, H_2O_2 is produced in abundance in the mM range; other molecular ions such as nitrate (NO_3^-) and nitrite (NO_2^-) are produced at much lower concentrations in the μM range.[298] We looked at (i) the effect of the saturation degree of the phospholipids, (ii) the cholesterol fraction and (iii) the amount of DPPE included within the membrane. Below, the experimental results of synthetic vesicles are combined with MD simulations for all three elements separately.

Effect of lipid tail saturation degree

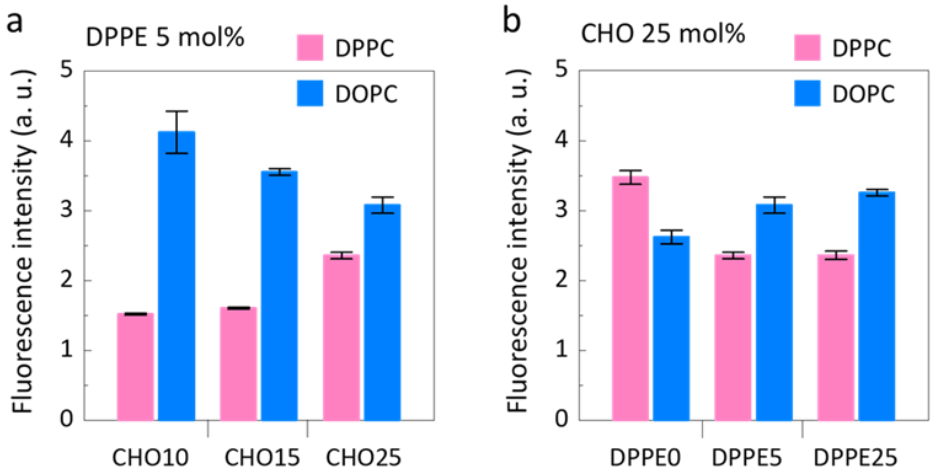

FIGURE 8.4: Effect of either DPPC or DOPC on the ingress of ROS into vesicles following CAP jet treatment, at a treatment time of 60 s. The vesicles in the left graph contain different concentrations of cholesterol (10, 15 or 25 mol%) with fixed concentration of DPPE (5 mol%), whereas the vesicles in the right graph contain different concentrations of DPPE (0, 5 and 25 mol%) at fixed cholesterol concentration (25 mol%).

To examine the effect of the saturation degree of the phospholipids on the ROS ingress in vesicles, vesicles were synthesised to incorporate equal amounts of cholesterol and DPPE, and contain either DOPC (C18:1) or DPPC (C16:0); *i.e.*, we compare vesicle systems 1-3, 7 and 8 (containing DPPC) with systems 4-6, 9 and 10 (based on DOPC) (Table 1). The results are illustrated in

Figure 8.4, which shows the fluorescence intensity of DCF in different vesicle systems, which is a measure for the amount of ROS ingress into the vesicles.

With a single exception in the case where vesicles contain no DPPE (discussed in following paragraph), Figure 8.4 shows that there is greater ingress of ROS in the vesicles containing DOPC (*i.e.*, the unsaturated lipids) when compared to those containing DPPC ($p < 0.001$), for which two likely explanations can be found. First, DOPC has a lower phase transition temperature of 256 K compared to DPPC (314 K).[299] Therefore, at an average temperature of approximately 298 K, the membrane containing DOPC will be much more fluid compared to that containing DPPC, which could facilitate the passive diffusion of ROS into the vesicle interior. The second explanation is that the double bond within the lipid tails of DOPC presents a potential site for lipid oxidation, with highly-reactive ROS which reach the vesicle membrane (the oxidation rate of unsaturated hydrocarbons by $^{\bullet}OH$ is 10 to 20 times higher compared to that of saturated hydrocarbons).[300] Oxidation increases (i) the polarity of the membrane interior (in extreme cases even aqueous pores can be formed [258,284]) and (ii) the fluidity of the membrane; both are expected to facilitate passive diffusion of polar ROS and RNS, such as, H_2O_2, NO_2^- or NO_3^-, as previously demonstrated.[284] Figure 4 also indicates one exception, *i.e.*, for membranes containing the highest amount of cholesterol (25 mol%) and the lowest amount of DPPE (0 mol%). In this case, the DPPC-containing membrane was more susceptible to ROS permeation than the DOPC membrane. This is attributed to the opposite effects that cholesterol and DPPE exert in either saturated (DPPC) or unsaturated (DOPC) membranes, and will be discussed in more detail in the later sections, in which we focus on the effect of both cholesterol and DPPE separately.

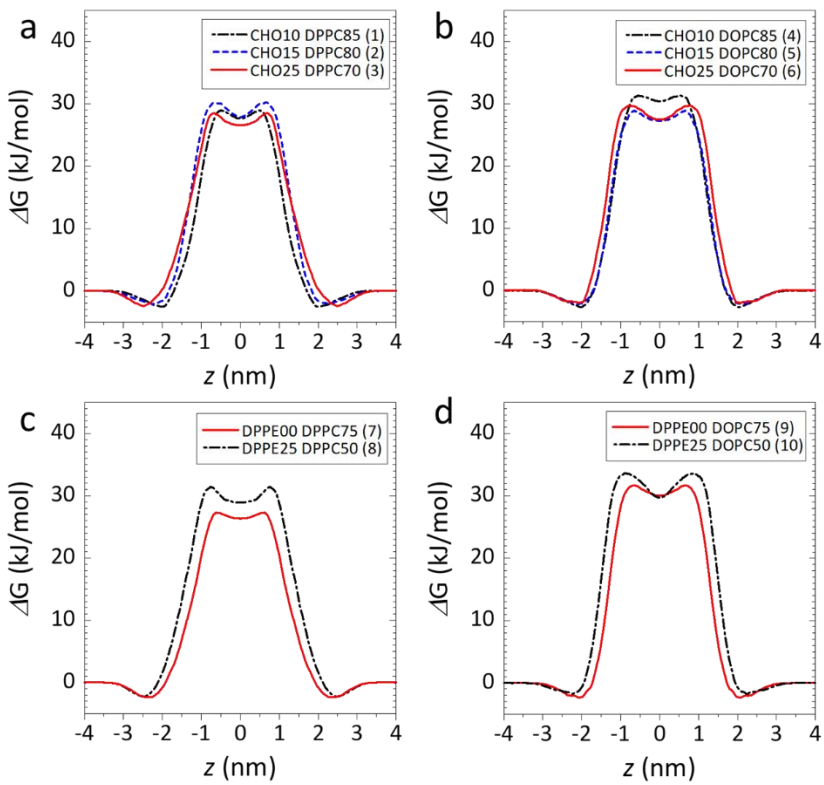

FIGURE 8.5: FEPs obtained from the US simulations for all different membrane compositions. The numbers mentioned in the legend indicate the molar fraction of each component in the lipid bilayer. (a) and (b) compare the effect of DPPC and DOPC, respectively, when varying the cholesterol content (keeping the DPPE content fixed at 5 mol%), whereas in the membranes investigated in (c) and (d) the DPPE content is varied, keeping the cholesterol content fixed at 25 mol%, for either (c) DPPC or (d) DOPC.

MD simulations of PLBs were performed to investigate the importance of DOPC and DPPC on ROS ingress. The obtained FEPs for H_2O_2 (major ROS produced by the CAP jet in this study) are shown in Figure 8.5, which are a measure for the barrier of passive diffusion of H_2O_2 across the membrane.

Figure 8.5 shows almost no difference between the height of the FEPs of bilayers containing either DOPC or DPPC (comparing Figure 8.5a with 8.5b, or Figure 8.5c with 8.5d). This means that the passive diffusion rate across all these membranes would be almost identical. This indicates that the differences observed in the vesicle experiments are more likely to arise from lipid

oxidation occurring at the unsaturated bonds in DOPC, and not due to differences in fluidity (arising from differences in phase transition temperature). An important note, however, is that these simulations only focus on the diffusion of H_2O_2, thereby ignoring other smaller species (*e.g.*, the $^{\bullet}OH$), which will be discussed later in more detail.

Effect of cholesterol

To determine the effect of variations in the cholesterol content on ROS delivery, vesicle systems 1 to 6 (Table 8.1) were compared; these vesicles contained 10, 15 or 25 mol% cholesterol in combination with 5 mol% DPPE, and either DOPC or DPPC. The results of the DCFH measurements are shown in Figure 8.6.

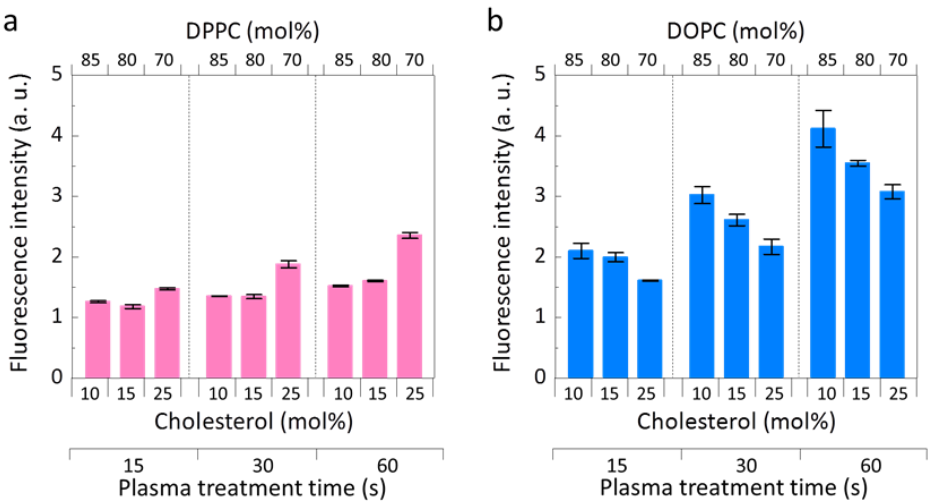

FIGURE 8.6: Effect of cholesterol membrane content on the ingress of ROS during CAP jet treatment of (a) DPPC or (b) DOPC vesicles. The DPPE content is fixed at 5 mol%.

First, these graphs illustrate opposite trends in vesicles containing mostly either (a) DPPC or (b) DOPC. In the DPPC-containing vesicles (pink bars), ROS ingress is increased with increasing cholesterol fraction, while in the DOPC membranes (blue bars), the opposite trend is seen. Specifically, at lower cholesterol fractions of 10 and 15 mol%, a significantly higher amount of ROS was detected in the DOPC vesicles ($p < 0.001$). On the other hand, the difference in the amount of ROS detected in both vesicles was insignificant (p

> 0.05) at the highest cholesterol fraction of 25 mol% (due to ROS ingress increasing for DPPC vesicles and decreasing for DOPC vesicles at the highest cholesterol fraction). Moreover, Figure 8.6 shows that in the case of the DOPC vesicles, in comparison to the DPPC vesicles, (i) the overall ROS ingress is higher, as was also clear from Figure 8.4; but also that (ii) the increase in ROS ingress upon increasing treatment time is much more pronounced. Indeed, the fluorescence intensity in each of the DPPC vesicles is almost constant as a function of treatment time, while the DOPC vesicles show a clear increase with increasing treatment time from 15 s up to 60 s. This corresponds with our conclusion above; *i.e.*, that the ingress in the DOPC vesicles is mostly governed by lipid oxidation, which facilitates permeation of the membrane, and the latter increases upon longer treatment time, while in the DPPC-containing vesicles, only a small accumulation of ROS due to passive diffusion is observed.

An explanation as to why opposing trends are observed upon altering the cholesterol fraction in either DPPC or DOPC vesicles can also be found in the ability of plasma species to oxidize these different lipids.[300] In DPPC vesicles lacking cholesterol, oxidation is not likely to occur.[301] However, when cholesterol is added to the membrane, the unsaturated bonds present in these molecules can be oxidized by impinging ROS. Due to this oxidation, the polarity of the membrane core would increase slightly, which facilitates further permeation of CAP-generated ROS.[302] Therefore, if the concentration of cholesterol increases in the DPPC vesicles, the permeation of ROS increases as well, as is observed in Figure 8.6. In DOPC vesicles, on the other hand, even without the presence of cholesterol, lipid oxidation already occurs due to the double bond in the lipid tails. Replacing DOPC by cholesterol reduces the total number of reactive sites per vesicle present in the lipid core (each molecule of DOPC contains two double bonds, whereas cholesterol only contains one double bond), thereby lowering the overall reactivity of the membrane. This explains why a reduced amount of intracellular ROS is measured in the DOPC vesicles upon increasing cholesterol fraction (Figure 8.6). Furthermore, the rigid nature of cholesterol also strongly increases the

lipid packing in unsaturated membranes, which would hamper passive ROS permeation further, as was shown previously.[152]

Effect of DPPE content

To examine the effect of the concentration of DPPE on the ingress of CAP-generated ROS, vesicles containing 0, 5 or 25 mol% of DPPE were synthesized. Throughout these experiments, the cholesterol content was fixed at 25 mol%. The results of the broad-range ROS measurements are shown in Figure 8.7.

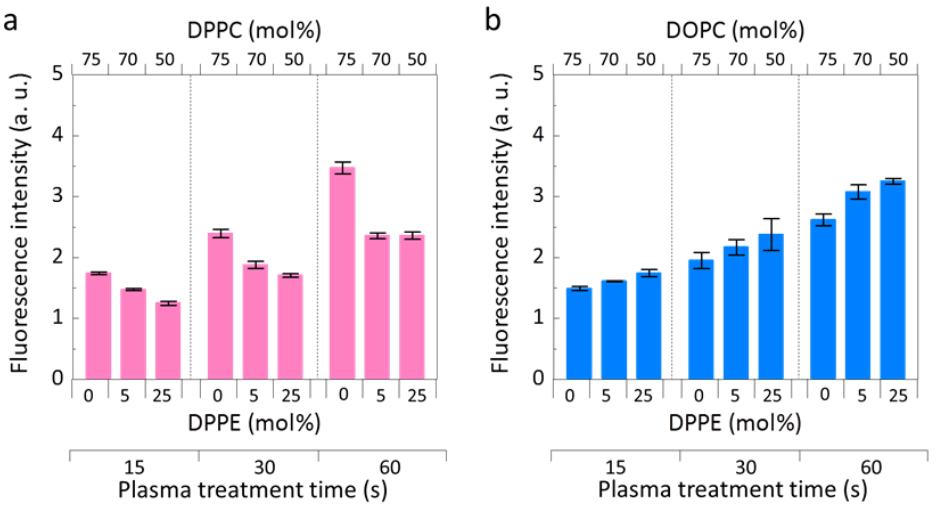

FIGURE 8.7: Effect of DPPE content in the vesicles on the ingress of ROS during CAP jet treatment of (a) DPPC or (b) DOPC vesicles. The cholesterol content was fixed at 25 mol%.

Adding DPPE to the vesicles clearly exerts the opposite effect to that of adding cholesterol (cf. Figure 8.6 to 8.7); *i.e.*, adding DPPE leads to a decreasing permeability in the DPPC vesicles (a), but an increase of ROS ingress in the DOPC vesicles (b). The effect of DPPE on ROS ingress is particularly noticeable when comparing vesicles with 5 mol% and 25 mol% DPPE. At 5 mol% DPPE, ROS ingress between DPPC and DOPC is not significant ($p > 0.05$), whereas a significantly ($p < 0.05$) higher amount of ROS ingress was observed for DOPC vesicles at 25 mol% DPPE (compared to DPPC vesicles). In the DPPC vesicles, lipid tail oxidation effects are not expected to play any role, as DPPC by DPPE contain identical lipid tails. The differences observed must thus be explained by structural changes between DPPC and DPPE, *i.e.*, a

different head group of the lipid. Indeed, DPPC contains a phosphatidylcholine (PC) group (PO_4^--$N(CH_3)_3^+$), whereas DPPE contains a phosphatidylethanolamine (PE) group (PO_4^--$N(H_3)_3^+$) (Figure 8.2).

The PE head group of DPPE is less bulky than the PC head group in DPPC. Thus, when replacing DPPC by DPPE, the lipids can be packed closer together, which makes passive permeation of ROS more difficult, as indeed observed in the DCFH measurements. This is also confirmed in the MD simulations, by comparing the average area per lipid in the different membrane structures, as shown in Table 8.2.

TABLE 8.2: Calculated values of the area per lipid for the different membranes.

Vesicle type	Area per lipid (nm^2)	
	0 mol% DPPE	**25 mol% DPPE**
DPPC	0.451 ± 0.004	0.435 ± 0.001
DOPC	0.506 ± 0.002	0.449 ± 0.001

Increasing the DPPE content in either the DPPC or the DOPC vesicles increases the packing of the lipids, and thus leads to a decreasing area per lipid (Table 8.2). Thus, upon increasing the DPPE fraction, the passive diffusion of reactive species should be hampered in both systems. For the DPPC vesicles, this is also observed in the US simulations, which show that upon increasing DPPE fraction, the free energy barrier of H_2O_2 permeation increases (see Figure 8.5c).

However, in the DOPC vesicles, the DCFH measurements indicate an increasing permeability upon increasing DPPE fraction, which does not correlate with the results in Table 8.2. The explanation for this is not straightforward, even more so when we consider that when DOPC is replaced by DPPE, the total number of reactive sites in the membrane decreases, which should result in a decrease in the likelihood of pore formation due to lipid oxidation, and thereby also the chances of ROS permeating the membrane. Therefore, we suspect that a different effect is taking place, which counteracts the effects of both an increase in lipid packing density and a decrease in lipid oxidation.

One possibility is that the presence of DPPE leads to the creation of lipid rafts in the membrane structures, *i.e.*; lipids of the same type pack together to form patches with an enhanced local concentration of this lipid inside the membrane. It is known that cholesterol tends to form such rafts together with sphingolipids and other saturated lipids.[46,303] These saturated lipids contain an aliphatic tail, which is also present in DPPE (see Figure 8.2), but not in DOPC (which contains a double bond in each lipid tail). Therefore, upon increasing the DPPE concentration, lipid rafts could be generated, containing elevated levels of DPPE and cholesterol. As the overall molar fraction of each lipid type is fixed in the vesicles, this would mean that other parts of the vesicle membrane are enriched in DOPC. Thus, due to the generation of lipid rafts, enriched in DPPE and cholesterol, other parts of the membrane might be enriched in DOPC, which serve as the 'weak spot' of these membranes, being extremely vulnerable to pore formation upon lipid oxidation. In previous research, we have shown that in order to create pores in lipid membranes, very high lipid oxidation degrees are locally required[16], which can indeed only occur if these oxidised lipids are grouped together in membrane patches.

To analyse possible lipid raft formations in these membrane structures, we compare the radial distribution functions (RDFs) of the P-P distance of neighboring DOPC lipids, in systems containing 0 and 25 mol% DPPE in Figure 8.8. These RDFs are a measure for the probability of finding a particle (in this case, any P-atom) at a certain distance from a fixed reference particle (the reference P-atom).

In the system containing only DOPC and cholesterol (red curve), the first peak (at a distance of 0.45 nm) corresponds to two DOPC molecules placed next to each other. The second peak, at a distance of 0.55 nm, most likely occurs from DOPC molecules separated by a cholesterol molecule. Upon adding DPPE to the system, the black curve clearly shows that the peak of neighboring DOPC molecules increases, which means that more DOPC molecules are grouped together. At first sight, this is counterintuitive, as there are more non-DOPC lipids in the system, so the chance of DOPC being organised directly next to each other should decrease. Therefore, these results

might indicate that lipid raft formation does occur in these systems, creating rafts that are either enriched in DOPC (explaining this higher peak) or in DPPE/cholesterol. As mentioned before, these DOPC rafts serve as the membrane's 'weak spot' for lipid oxidation and pore formation, which explains the increased ROS ingress in Figure 8.7 upon increasing DPPE content, for the DOPC vesicles. In DPPC vesicles, such rafts will not be created as both DPPC and DPPE contain the same aliphatic lipid tails. Therefore, their interaction with cholesterol will be equally strong. It has to be kept in mind, however, that the model membranes only contain 64 lipids in each leaflet, which makes it difficult to mimic the actual raft formation process that could take place in the vesicle systems.

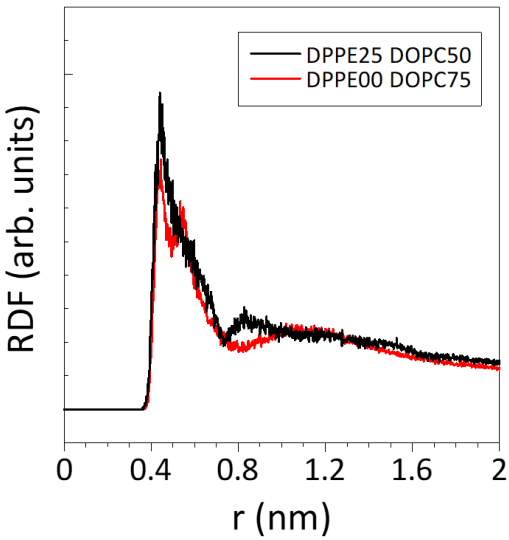

FIGURE 8.8: RDFs of the P-P distance of neighboring DOPC lipids in systems containing 0 or 25 mol% DPPE. The numbers mentioned in the legend indicate the molar fraction of each component in the vesicles. The cholesterol content is fixed at 25 mol%.

A combination of different processes discussed above (lipid oxidation and raft formation) can also explain the anomaly observed in Figure 8.4, *i.e.*, why DPPC vesicles containing 0 mol% DPPE and 25 mol% cholesterol are more vulnerable to ROS ingress compared to the DOPC equivalent. As is discussed above, increasing the cholesterol fraction reduces oxidation in DOPC vesicles, whereas it increases oxidation in DPPC vesicles. Moreover, because the DOPC

vesicles lack DPPE, raft formation will not occur. This means that the cholesterol molecules are dispersed homogeneously through the membrane, protecting it from pore formation after lipid oxidation of DOPC. In DPPC vesicles, on the other hand, cholesterol itself is oxidised due to impinging ROS, thereby losing its ability to strengthen the membrane.

8.3.4 CAP induced DNA double strand breaks

Finally, we investigate the ability of CAP to induce DNA strand breaks of a MB encapsulated within vesicles, focusing on the effect of cholesterol in combination with the saturation degree of the lipids. Therefore, only vesicles 1, 3, 4 and 6 were taken into account, which contain either 10 or 25 mol% cholesterol, 5 mol% DPPE, combined with either DPPC or DOPC. The fluorescence intensity of the MB encapsulated in these vesicles was measured after 60 seconds plasma treatment. Higher fluorescence intensity correlates with an increased number of DNA strand breaks induced during CAP treatment. The results of these measurements are shown in Figure 8.9.

Upon altering the saturation degree of the main lipid that comprises the vesicle, cholesterol was observed to have opposite effects on the ability of the CAP jet to induce DNA strand breaks within the vesicles. Although the differences are rather small, this observation is in line with that of the ROS measurements discussed above. In the vesicles comprising mainly of a saturated lipid, *i.e.*, containing mostly DPPC, increasing the cholesterol content increases the number of DNA strand breaks, just as it increases the total ROS ingress, due to passive ROS diffusion. On the other hand, in the DOPC vesicles, increasing the cholesterol content leads to a decrease in the number of DNA strand breaks, attributed to the lower DOPC content, and thus less lipid oxidation, yielding less pore formation.

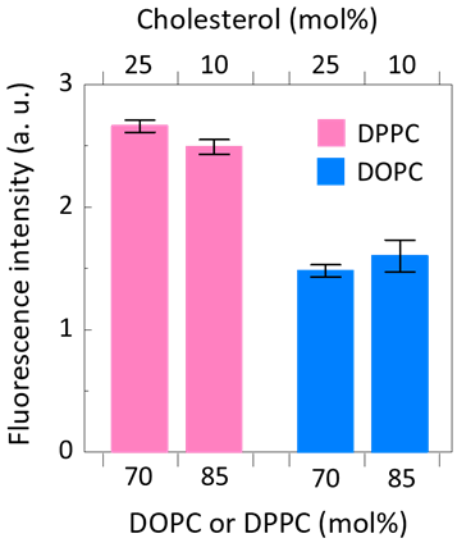

FIGURE 8.9: Relative amount of DNA strand breaks within vesicles following 60 s CAP jet treatment of DPPC (pink bars) or DOPC vesicles (blue bars), with a membrane cholesterol content of 10 mol% and 25 mol%, and a fixed DPPE content of 5 mol%.

A perhaps somewhat surprising significant result, is that the total number of DNA strand breaks is significantly lower in the DOPC vesicles compared to the DPPC vesicles, which does not correlate with the total ROS ingress measured in the DCFH vesicle experiments (see Figure 8.4). Short-lived ROS (*e.g.*, the $^{\bullet}OH$, with an intracellular half-life of 10^{-9} s) are much more effective species to induce DNA strand breaks, rather than long-lived ROS (*e.g.*, H_2O_2, with an intracellular half-life of 10^{-3} s). [19,97] Therefore we need to consider how these short-lived, reactive species are likely to interact with the different components of the vesicle membrane. In DOPC vesicles, the double bonds of the DOPC lipids serve as a highly-reactive site, effectively scavenging these short-lived ROS before they can reach the vesicle interior. [300] The ROS measurements discussed above, measure the total number of ROS (and RNS) entering the vesicles, without differentiating between species with different lifetimes. The combination of both assays (DCFH and MB) indicates that in DOPC vesicles, more ROS are able to penetrate the vesicle membrane, but we surmise these are mostly longer-lived ROS, while in DPPC vesicles, a lower number of ROS is able to diffuse through the membrane, but these are mostly shorter-lived ROS. Generally, the latter are much smaller, which facilitates

their ability to diffuse through the membrane. Indeed, previous research has shown that the energy barrier for passive diffusion across a membrane of short-lived ROS, such as $^{\bullet}OH$ or $^{\bullet}OOH$, is significantly lower compared to that of *e.g.*, H_2O_2. [258]

8.4. Conclusions

CAP treatment of lipid vesicles was combined with MD simulations to study the effect of different membrane lipid compositions on the ability of plasma-derived ROS to diffuse through these membranes. We varied the saturation degree of the lipid tails, the cholesterol content of the membrane, and the type of lipid head group (*i.e.*, PE vs. PC head group). We selected these characteristics because different cell types, including healthy and cancerous human cells, sometimes also show variations in these types of lipid characteristics, as explained in the introduction of this Chapter. [67,68,71,74,304]

Our results indicate that CAP can potentially be utilised to induce specific cellular effects (oxidative stress and DNA damage) by targeting interactions of plasma-derived ROS with specific cell membrane lipid components. The ROS measurements show that generally vesicles containing more unsaturated lipids (DOPC) are significantly more vulnerable to ROS ingress compared to those containing more saturated lipids (DPPC). However, adding cholesterol to both types of vesicles makes the DOPC vesicles less vulnerable, while it increases the vulnerability of DPPC vesicles to ROS ingress. Similarly, the addition of DPPE, which contains a smaller head group compared to DOPC and DPPC, also exerts opposite effects in either the DOPC or the DPPC vesicles. In DOPC membranes, the addition of DPPE makes the vesicles more susceptible to ROS permeation, whereas in DPPC membranes, it has a 'protecting' role. To determine the possible underlying mechanisms causing these observations, we performed MD simulations. Although these simulations cannot be seen as absolute evidence for the underlying mechanisms, they show that multiple effects can potentially play a role, including (i) lipid oxidation of unsaturated phospholipids and cholesterol, (ii)

lipid packing due to the head group volume, and (iii) formation of lipid rafts due to strong interactions between lipids of the same type.

We also assessed the ability of a CAP jet to induce DNA strand breaks within vesicles encapsulating a MB. This led to the surprising observations that, although DOPC vesicles are more susceptible to ROS permeation compared to DPPC vesicles, the MB within DPPC vesicles is more susceptible to CAP jet-derived ROS damage. This can be explained by the fact that the double bonds present in DOPC serve as scavenging sites for short-lived ROS, thereby preventing them from entering the vesicle interior. On the other hand, due to the reaction of the double bonds with these short-lived species, the polarity of the bilayer interior increases, facilitating the overall permeation of other impinging ROS. In DPPC vesicles, no reactive sites are present, which allows short-lived ROS to diffuse through the membrane. Once they reach the vesicle interior, these species are very efficient in inducing DNA strand breaks. However, without lipid oxidation occurring, the membrane's hydrophobic environment is sustained, thereby hindering the overall ingress of impinging larger and more stable ROS (*e.g.*, H_2O_2).

In the last decades, CAP technology has emerged as a potential solution to help alleviate escalating healthcare problems, such as cancers. [276,305] However, the full clinical benefits of CAP are yet to be realised, possibly due to our lack in understanding of how CAP can be used to target desired effects in specific cell type types. This paper aimed to provide new insights into how different membrane lipid components, of relevance for treatment of certain diseases such as some cancers, can be exploited by CAP technology for targeted membrane therapy such as for cancer treatment. As the oxidative stress provoked by CAP is considered the main mode-of-action to induce cellular effects, it is important to develop our understanding of how the cell membrane landscape influences the cell's response to oxidative stress. To aid this research, more advanced models will need to be developed both experimentally and computationally, as a means of scientifically testing the potential of CAP technologies in biology and medicine. This includes increasing the number of different lipid types present in the vesicles, as well

as taking, *e.g.*, serum proteins or membrane-associated proteins into account, which can serve as scavengers of CAP-generated RONS, in which secondary RONS can be generated.

Future outlook

Although each investigation presented in this thesis relates to the use of CAP for medical applications (with a special focus on cancer treatment), the different chapters can roughly be divided into three distinguished aspects of these treatments.

1. Chapters 3 and 4 focus on the chemistry occurring inside the plasma source, effluent or liquid, by means of chemical kinetics models.
2. Chapters 5, 6 and 7 employ molecular dynamics (MD) simulations to investigate the underlying mechanisms of the interactions of CAP-generated RONS and electric fields with biological substrates (cellular membranes or skin layers).
3. Chapter 8 assesses the permeation of RONS and intracellular DNA damage into synthetic cells by means of lipid vesicle experiments, which allows for a controlled environment. These experiments are linked with the reported MD simulations, as we can use the results of these MD simulations to explain our experimental observations.

Although promising results were obtained in each of these three divisions, the results also allow room for further investigations. Indeed, regarding the gas phase chemical kinetics models developed in Chapters 3 and 4, in the future, we want to expand these models to investigate different CAP sources used in our research group for medical applications, which include, next to the already discussed COST-jet, the SOFT-jet and a FE-DBD device. Subsequently, the new version of the liquid chemical kinetics model discussed in Chapter 4 can be used for these sources, as well as for the kINPen IND (of which only results obtained with the initial liquid model were discussed in this thesis). By increasing our knowledge of the reactive species generated in these different sources, we can try to correlate biological outcomes with the species generated, look for similarities and differences between these sources and assess optimal conditions to generate a desirable chemical cocktail.

Furthermore, umbrella sampling MD simulations, similar to those discussed in Chapters 5 and 6, have been used by other researchers in our group for different systems. In the future, such simulations will remain very valuable to assess the interactions between CAP-generated RONS and different proteins, known to be over-expressed in cancerous cells, or to assess the effect of CAP-induced modifications of these proteins on proteins-ligand or protein-protein interactions (which might, *e.g.*, be involved in signal-transduction pathways).

Lastly, we hope that the results presented in Chapter 8 will motivate researchers in the future to determine the lipid composition of different cell lines, both healthy and cancerous. This knowledge, in turn, would allow developing more realistic vesicle models for different cell lines, by which the exact effect of the lipid composition can be assessed with regard to the biological outcome of CAP treatment of the very same cell lines (*e.g.*, cell death).

As discussed throughout this thesis, many *in vitro* and *in vivo* studies are being devoted to study the mechanisms and effects of CAPs in the treatment of cancer. Furthermore, some clinical results are already obtained by Metelmann et al., which highlight the great potential of plasma as a cancer treatment modality.[306,307] Although this kind of pre-clinical testing and compassionate case use is very important in the development of the field, if we want this technology to become a real adjuvant cancer treatment therapy, which can be used by clinicians in addition to more traditional therapies, there is a need for actual clinical trial studies. Now that multiple CAP sources have received certification for use on human patients[308], we can start using them in clinical trials to move this technology forward. A first big step here is taken by researchers in the US, who received FDA approval to start a Phase I clinical trial on 20 patients.[309] In this study, cold plasma will be used to treat remaining cancer cells or tissue after surgical removal of a solid tumor mass, which is a great example of how CAP can be used in synergy with traditional treatment methods. At the same time, more fundamental (pre-clinical) research should be performed to unravel the mechanism at which plasma

operates on different cancer and healthy cells, as this knowledge will help optimizing treatments in the future.

List of publications

Related to this thesis

1. **J. Van der Paal**, S.-H. Hong, M. Yusupov, N. Gaur, J.-S. Oh, R. D. Short, E. J. Szili and A. Bogaerts. How membrane lipids influence plasma delivery of reactive oxygen species into cells and subsequent DNA damage: An experimental and computational study. *Physical Chemistry Chemical Physics*, 10.1039/C9CP03520F (2019).

2. **J. Van der Paal**, G. Fridman and A. Bogaerts. Plasma-induced lipid cross-linking can enhance transdermal drug delivery. *Plasma processes and Polymers*, 10.1002/ppap.201900122 (2019).

3. Y. Gorbanev, **J. Van der Paal**, W. Van Boxem, S. Dewilde and A. Bogaerts. Reaction of chloride anion with atomic oxygen in aqueous solutions: can cold plasma help in chemistry research? *Physical Chemistry Chemical Physics*, **8**, 4117-4121 (2019).

4. W. Van Boxem, **J. Van der Paal**, Y. Gorbanev, S. Vanuytsel, E. Smits, S. Dewilde and A. Bogaerts. Anti-cancer capacity of plasma-treated PBS: effect of chemical composition on cancer cell cytotoxicity. *Scientific Reports*, **7**, 16478 (2017).

5. **J. Van der Paal**, C. Verheyen, E.C. Neyts and A. Bogaerts. Hampering Effect of Cholesterol on the Permeation of Reactive Oxygen Species through Phospholipids Bilayer: Possible Explanation for Plasma Cancer Selectivity. *Scientific Reports*, **7**, 29526 (2017).

6. M. Yusupov, **J. Van der Paal**, E.C. Neyts and A. Bogaerts. Synergistic effect of electric field and lipid oxidation on the permeability of cell membranes. *Biochimica et Biophysica Acta - General Subjects*, **1861**, 839-847 (2017).

7. **J. Van der Paal**, E.C. Neyts, C.C.W. Verlackt and A. Bogaerts. Effect of lipid peroxidation on membrane permeability of cancer and normal cells subjected to oxidative stress. *Chemical Science*. **7**, 489-498 (2016).

Other publications

1. A. Bogaerts, M. Yusupov, J. Razzokov and **J. Van der Paal**. Plasma for cancer treatment: How can RONS penetrate through the cell membrane? Answers from computer modeling. *Frontiers of Chemical Science and Engineering*, 1-11 (2019).

2. S. Vermylen, J. Dewaele, S. Vanuytsel, J. De Backer, **J. Van der Paal**, *et al*. Cold atmospheric plasma treatment of melanoma and glioblastoma cancer cells. *Plasma Processes and Polymers*, **13**, 1195-1205 (2016).

3. A. Bogaerts, N. Khosravian, **J. Van der Paal**, *et al*. Multi-level molecular modelling for plasma medicine. *Journal of Physics D: Applied Physics*, **49**, 054002 (2015).

4. **J. Van der Paal**, C.C.W. Verlackt, M. Yusupov, E.C. Neyts and A. Bogaerts. Structural modification of the skin barrier by OH radicals: a reactive molecular dynamics study for plasma medicine. *Journal of Physics D: Applied Physics*, **48**, 155202 (2015).

5. A. Bogaerts, M. Yusupov, **J. Van der Paal**, C.C.W. Verlackt, E.C. Neyts. Reactive molecular dynamics simulations for a better insight in plasma medicine. *Plasma Processes and Polymers*, **11**, 1156-1168 (2014).

6. **J. Van der Paal**, S. Aernouts, A.C.T. Van Duin, E.C. Neyts and A. Bogaerts. Interaction of O and OH radicals with a simple model system for lipids in the skin barrier: a reactive molecular dynamics investigation for plasma medicine. *Journal of Physics D: Applied Physics*, **46**, 395201 (2013).

List of presentations

1. J. Van der Paal, S.-H. Hong, M. Yusupov, N. Gaur, J.-S. Oh, E. Szili and A. Bogaerts. How the cell membrane composition influences plasma-induced cellular effects. *24th International Symposium on Plasma Chemistry (ISPC24),* Naples, Italy, July 2019. (**Oral presentation)**

2. J. Van der Paal, Y. Gorbanev, E. Helsen, W. Van Boxem, E. Biscop and A. Bogaerts. Comparison of reactive species generation in different cold plasma sources. *24th International Symposium on Plasma Chemistry (ISPC24),* Naples, Italy, July 2019. (**Poster presentation)**

3. J. Van der Paal, S.-H. Hong, M. Yusupov, N. Gaur, J.-S. Oh, E. Szili and A. Bogaerts. Cell membrane response to oxidative stress for anti-cancer therapies: an experimental and computational study. *5th International Workshop on Plasma for Cancer Treatment (IWPCT5)*, Antwerp, Belgium, April 2019. (**Poster presentation)**

4. J. Van der Paal, S. Heijkers, J. Slaets, G. Busco, E. Robert, J.-M. Pouvesle and A. Bogaerts, Chemical kinetics model for hypoxia effect in the afterglow of an argon plasma jet. *23rd International Symposium on Plasma Chemistry (ISPC23),* Montréal, Canada, July 2017. (**Poster and Oral flash presentation)**

5. J. Van der Paal, G. Fridman, A. Fridman, E. C. Neyts and A. Bogaerts. In search of the plasma poration mechanism during plasma treatment of skin. *23rd International Symposium on Plasma Chemistry (ISPC23),* Montréal, Canada, July 2017. (**Oral presentation)**

6. J. Van der Paal, S. Heijkers, J. Slaets, E. Robert and A. Bogaerts Chemical kinetics model for hypoxia effect in the afterglow of a Helium plasma jet. *9th International Workshop on Microplasmas (IWM9),* Garmisch-Partenkirchen, Germany, June 2017. (**Oral presentation)**

7. J. Van der Paal, G. Fridman, A. Fridman and A. Bogaerts. Cold plasma interactions with model systems of skin and cellular membranes: investigation of underlying mechanisms. *4th International Workshop on Plasma for Cancer Treatment (IWPCT4)*, Paris, France, April 2017. (**Poster presentation)**

8. J. Van der Paal, M. Yusupov, C. Verheyen, E. .C. Neyts and A. Bogaerts. Effect of cholesterol on the permeation of ROS through a phospholipids bilayer: Possible explanation for CAP cancer selectivity? *6th International Conference on Plasma Medicine (ICPM6)*, Bratislava, Slovakia, September 2016. (**Poster presentation)**

9. J. Van der Paal, E. C. Neyts and A. Bogaerts. Can cholesterol and lipid peroxidation explain the selectivity of CAP treatment towards cancer cells? A molecular dynamics study. *3rd International Workshop on Plasma for Cancer Treatment (IWPCT3)*, Washington DC, USA, March 2016. (**Oral and Poster presentation)**

10. J. Van der Paal, S. Vermeylen, J. De Waele, E. Marcq, J. Van Audenaerde, K. Leyssens, E. Smits, S. Dewilde and A. Bogaerts. Cold atmospheric plasma treatment of cancer cells: effect of cell malignity and treatment time. *3rd International Workshop on Plasma for Cancer Treatment (IWPCT3)*, Washington DC, USA, March 2016. (**Poster presentation)**

11. J. Van der Paal, E. C. Neyts and A. Bogaerts. Consequences of lipid peroxidation for the cell membrane permeability: Implications for plasma oncology. Young Professionals Workshop on Plasma Medicine, Rostock, Germany, September 2015. (**Oral presentation)**

Awards and grants

Awards

1. **Bob Barker Best Student Paper Award**, *International Workshop on Plasma for Cancer Treatment (IWPCT)*, Paris, France, 2017.

2. **KVCV award** for the most meritorious Chemistry student graduating from the University of Antwerp. Awarded by the Royal Flemish Chemical Society (KVCV), 2015.

Grants

1. **FWO PhD Fellowship** (2 + 2 years), October 2015-September 2019.

2. FWO travel grant for a research visit to the University of South Australia in Adelaide, March–May 2018.

Appendix A

A1: Preparation of buffers

The 4-(2-hydroxyethyl)-1-piperazineethanesulfonic acid (HEPES) buffer was prepared by dissolving the following components in 100 mL of purified water:

- HEPES—238.3 mg
- NaCl—624 mg
- NaOH—22.4 mg
- EDTA—29.22 mg

The pH of the solution was adjusted to 7.4 with 10 mM NaOH solution. The buffer was filtered through a 0.2 μm syringe filter before use. HEPES buffer was used for the preparation and dilution of the vesicles for the experiments.

A concentrated buffer of 1M Tris buffer was prepared by dissolving 12.11 g of Tris-base in 80 mL water. The pH was adjusted to 7.6 by adding concentrated HCl (6.2 M), after which the final volume was adjusted to 100 mL. The concentrated Tris buffer was diluted to 10 mM in water for the preparation of the molecular beacon (MB) stock solution (see below).

A2: System set-up and equilibration

All simulations, i.e., energy minimization, equilibration and umbrella sampling runs, were performed using the GROMACS-5.1 package [163]. For the interatomic interactions the GROMOS 54A7 force field parameters were applied [310] in combination with the SPC water model [311]. Specifically, the GROMOS-type parameters for the DOPC, DPPC, DPPE, cholesterol and H_2O_2 molecules were adopted from[312], [313], [314], [302] and [153], respectively. After constructing the initial configurations using the Packmol package[157], an energy minimization of all systems was performed using the steepest-descent algorithm. These simulations, as well as all the following ones (*i.e.*, equilibration and umbrella sampling runs), were performed using the GROMACS-5.1 package[163] in combination with the GROMOS 54A7 force

field[310]. After the energy minimization, all systems were equilibrated for 400 ns in the NPT ensemble (*i.e.*, constant number of particles, pressure and temperature). The temperature at which the systems were equilibrated was different for systems containing either DOPC or DPPC, *i.e.*, at 298 K or 323 K, respectively. These temperatures were chosen based on the transition temperatures of both lipids (253 K for DOPC and 314 K for DPPC), to ensure that all simulated bilayers were in the liquid state, as was the case with the vesicles studied experimentally.[315] The reference pressure used in the simulations was the same for all bilayers, *i.e.*, 1 atmosphere. The NPT ensemble was employed using the Parrinello-Rahman barostat[160] with compressibility and coupling constant of 4.5×10^{-5} bar^{-1} and 2 ps, respectively, as well as the Nose–Hoover thermostat[159] with a coupling constant of 0.5 ps. Considering the non-bonded interactions, the particle mesh Ewald method was used to treat electrostatic interactions with cut-off radius of 1.0 nm for Coulomb interactions.[162] The same cut-off radius was applied for the van der Waals interactions. This cut-off radius was chosen after scanning different values and evaluating the results based on the agreement of the obtained area per lipid with experimental values (0.63 nm^2 for both DOPC and DPPC bilayers in native form, see [315–318] and references therein). All simulations were carried out using a time step of 2 fs, and periodic boundary conditions were applied in all three directions.

A3: Umbrella sampling (US) simulations

To investigate the ability of H_2O_2 permeation through the different bilayers, US simulations were performed to determine FEPs of H_2O_2 across all systems.[165,166] From the last 40 ns of the equilibration run, five membrane structures were extracted, which served as the initial configurations for the US runs. In each US simulation, 32 H_2O_2 molecules were added to the structure, distributed over eight layers along the bilayer normal (*i.e.* four molecules in each plane). These molecules were restrained to move along the *z*-axis by a harmonic bias with force constant of 2000 $kJ.mol^{-1}.nm^{-2}$. Furthermore, their movement in the *xy*-plane was also restrained by using the so-called flat-bottomed position restraint, with a radius of 0.5 nm and a force constant of

500 kJ.mol^{-1}.nm^{-2}. To obtain a FEP, 160 US windows were used, which were separated by 0.5 Å. The US simulations were performed in the NPT ensemble, with the same parameters as in the equilibration runs. The total simulation time of these runs was 5 ns, of which the last 2 ns were used as sampling time. The convergence of the free energy results was evaluated based on the symmetricity of the profiles to the centre of the bilayer. From each initial structure, four different FEPs were obtained (one for each H_2O_2 molecule placed in each US window). By using five different initial structures (see above), a total of 20 FEPs was obtained for each bilayer composition. These profiles were averaged, leading to the FEPs shown in the Figure 8.5 shown in Chapter 8. Each FEP was calculated using a periodic version of the weighted histogram analysis method (WHAM), by utilizing the gmx wham tool of GROMACS.[210]

A4: Ortho-phenylenediamine (OPD)/horseradish peroxidase (HRP) H_2O_2 indicator

OPD (Sigma-Aldrich, P9187) was dissolved in 20 mL of PBS supplemented with 125 ng /ml of horseradish peroxidase (HRP) (Sigma-Aldrich, catalogue number P6782). The solution was stored at 4 °C until use. The OPD/HRP solution was used to determine the concentration of H_2O_2 generated by the plasma jet in solution. This involved adding 200 µL of the OPD/HRP solution to wells of a 96-well plate and then treating the solution with the plasma jet. After 10 min of incubation at ambient temperature (to allow time for the HRP to catalyse the oxidation of the OPD in the presence of H_2O_2, into a yellow coloured product), 100 µL of the OPD/HRP solution was transferred to a fresh 96-well plate for measurement. The H_2O_2 concentration in the plasma jet treated was determined according to a calibration curve (see below).

A5: Determination of H_2O_2 concentration

The H_2O_2 concentration generated by the plasma jet treatments in the HEPES buffer (presented in Figure 8.3d in Chapter 8) was determined according to a calibration curve. The calibration curve was determined by adding 10 µL of known H_2O_2 concentrations to 80 µL of OPD/HRP solution (see above) and

incubating for 10 min at ambient temperature (same incubation time as is used in the manuscript, which was determined to be sufficient to develop the solution). Afterwards, absorbance of the OPD solution was recorded on a microplate reader, as described in section 2.5 of the manuscript. The absorbance data were plotted as function of the H_2O_2 concentration as shown in Figure A1 below. The data covered the full range of absorbance data (both below and above) achieved by the plasma jet treatments. The calibration curve was near linear (R^2 = 0.9987) with the equation from the curve (y = 0.1043x) used to derive the unknown H_2O_2 concentration produced by the plasma jet treatments.

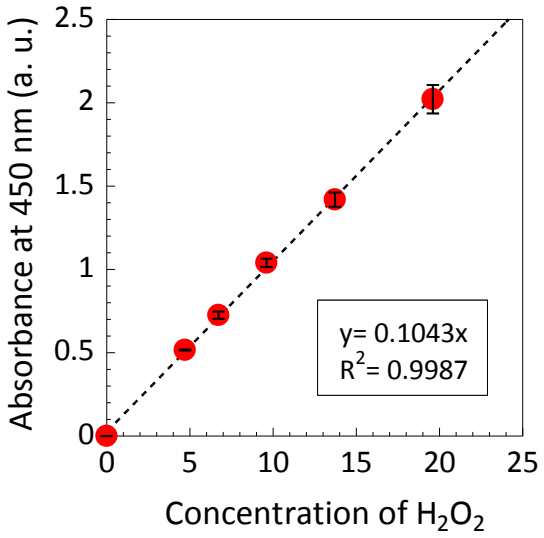

FIGURE A1: Calibration curve used to derive the H_2O_2 concentration produced by the plasma jet treatments of the HEPES solution, as shown in Figure 8.3d in Chapter 8.

A6: Carboxyfluorescein (CF): assessment of vesicle rupture

Vesicles encapsulating CF were used to analyse the possibility of the vesicle membrane being ruptured by the plasma jet treatment. In these experiments, 50 mM of CF was encapsulated within the vesicles, at which concentration CF is self-quenched inside the intact vesicles. However, if the vesicles were ruptured by the plasma jet treatment, the CF would be released and diluted into the HEPES buffer containing the vesicles, resulting in a switch-on of fluorescence (*i.e.* a positive indication of vesicle rupture). To prepare a 50 mM

concentration of the carboxyfluorescein (CF) encapsulation buffer, the following components were dissolved in 13 mL of purified water:

- CF—244 mg
- NaCl—7.6 mg
- NaOH—70.2 mg
- EDTA—3.7 mg
- HEPES —31 mg

The pH was adjusted to 7.4, and the solution was stored shielded from ambient light at 4 °C until use. Figure A2 shows the results of a typical vesicle rupture assay for vesicles encapsulating CF. This Figure shows the results of a 2 minute plasma treatment of vesicle system 10 (50 mol% DOPC, 25 mol% DPPE and 25 mol% cholesterol - see Table 7.1 in Chapter 7), which is harsher than any treatment conditions used in the paper. As seen in Figure A2, there was no increase in the CF fluorescence signal even after this more pro-longed plasma jet treatment. As a positive control, Triton X-100 was added to completely lyse the vesicles, which was seen by a prominent increase in fluorescence (Figure A2).

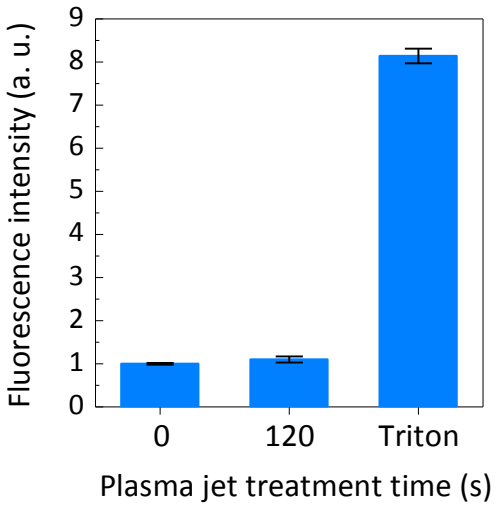

FIGURE A2: Result of a typical vesicle rupture assay for different plasma jet treatment times. The vesicle membrane composition comprised of 50 mol% DOPC, 25 mol% DPPE and 25 mol% cholesterol (vesicle system 10, Table 7.1 in Chapter 7). Positive control of vesicle rupture was Triton X-100.

Bibliography

1 J. Van der Paal, E. C. Neyts, C. C. W. Verlackt and A. Bogaerts, *Chem. Sci.*, 2016, **7**, 489–498.

2 R. Guerrero-Preston, T. Ogawa, M. Uemura, G. Shumulinsky, B. L. Valle, F. Pirini, R. Ravi, D. Sidransky, M. Keidar and B. Trink, *Int. J. Mol. Med.*, 2014, **34**, 941–946.

3 S. Kalghatgi, E. Cerchar, J. Azizkhan-, A. Fridman and G. Friedman, *Plasma Med.*, 2011, **1**, 249.

4 A. Siu, O. Volotskova, X. Cheng, S. S. Khalsa, K. Bian, F. Murad, M. Keidar and J. H. Sherman, *PLoS One*, 2015, **10**, e0126313.

5 A. M. Hirst, F. M. Frame, M. Arya, N. J. Maitland and D. O. Connell, *Tumor Biol.*, 2016, **37**, 7021–7031.

6 N. K. Kaushik, N. Kaushik, D. Park and E. H. Choi, *PLoS One*, 2014, **9**, e103349.

7 P. Girard, A. Arbabian, M. Fleury, G. Bauville, V. Puech, M. Dutreix and J. S. Sousa, *Sci. Rep.*, 2016, **6**, 29098.

8 J. J. Thompson, *Philos. Mag. Ser.*, 1879, **44**, 293–316.

9 I. Langmuir, *Proc. Natl. Acad. Sci. U. S. A.*, 1928, **14**, 627–637.

10 A. Bogaerts, E. Neyts, R. Gijbels and J. Van Der Mullen, *Spectrochim. Acta Part B*, 2002, **57**, 609–658.

11 M. Laroussi, *Plasma*, 2018, **1**, 47–60.

12 A. Dubuc, P. Monsarrat, F. Virard, N. Merbahi, J. Sarrette, S. Laurencin-dalicieux and S. Cousty, *Ther. Adv. Med. Oncol.*, 2018, **10**, 1–12.

13 J. Golda, J. Held, B. Redeker, M. Konkowski, P. Beijer, A. Sobota, G. Kroesen, N. St, J. Braithwaite, S. Reuter, M. M. Turner, T. Gans, D. O 'connell and V. Schulz-Von Der Gathen, *J. Phys. D Appl. Phys*, 2016, **49**, 84003–11.

14 S. Reuter, T. von Woedtke and K. Weltmann, *J. Phys. D. Appl. Phys.*, 2018, **51**, 233001.

15 P. Attri, J. Gaur, S. Choi, M. Kim, R. Bhatia, N. Kumar, J.-H. Park, A. E. Cho, E. H. Choi and W. Lee, *Sci. Rep.*, 2017, **7**, 2636.

16 J. Winter, R. Brandenburg and K. Weltmann, *Plasma Sources Sci. Technol.*, 2015, **24**, 064001.

17 N. K. Kaushik, N. Kaushik, N. N. Linh, B. Ghimire and et al, *Nanomaterials*, 2019, **9**, 1–19.

18 G. Isbary, T. Shimizu, Y. Li, W. Stolz, H. M. Thomas, G. E. Morfill and J. L. Zimmermann, *Expert Rev.*, 2013, **10**, 367–377.

19 B. C. Dickinson and C. J. Chang, *Nat Chem Biol.*, 2012, **7**, 504–511.

20 D. B. Graves, *J. Phys. D. Appl. Phys.*, 2012, **45**, 263001.

21 M. Keidar, *Plasma Sources Sci. Technol.*, 2015, **24**, 033001.

22 W. Van Boxem, J. Van der Paal, Y. Gorbanev, S. Vanuytsel and E. Smits, *Sci. Rep.*, 2017, **7**, 16478.

23 T. von Woedtke, S. Reuter, K. Masur and K. D. Weltmann, *Phys. Rep.*, 2013, **530**, 291–320.

24 D. Yan, A. Talbot, N. Nourmohammadi, X. Cheng, J. Canady, J. Sherman and M. Keidar, *Sci. Rep.*, 2015, **5**, 18339.

25 P. Heirman, W. Van Boxem and A. Bogaerts, *Phys. Chem. Chem. Phys.*, 2019, **21**, 12881.

26 A. Privat-Maldonado, Y. Gorbanev, S. Dewilde, E. Smits and A. Bogaerts, *Cancers (Basel).*, 2018, **10**, 394.

27 A. Lin, Y. Gorbanev, J. De Backer, J. Van Loenhout, W. Van Boxem, F. Lemière, P. Cos, S. Dewilde, E. Smits and A. Bogaerts, *Adv. Sci.*, 2019, **6**, 1802062.

28 J. M. Joslin, J. R. Mccall, J. P. Bzdek, D. C. Johnson and B. M. Hybertson, *Plasma Med.*, 2016, **6**, 135–177.

29 T. Sato, M. Yokoyama and K. Johkura, *J Phys D Appl Phys*, 2011, **44**, 372001.

30 S. Vermeylen, J. De Waele, S. Vanuytsel, J. De Backer, M. Ramakers, K. Leyssens, E. Marcq, E. L. J. Smits, S. Dewilde and J. Van Der Paal, *Plasma Process. Polym.*, 2016, **13**, 1195–1205.

31 D. Yan, N. Nourmohammadi, K. Bian, F. Murad, J. H. Sherman and M. Keidar, *Sci. Rep.*, 2016, **6**, 26016.

32 K. Wende, P. Williams, J. Dalluge, W. Van Gaens, H. Aboubakr, J. Bischof, T. Von, S. M. Goyal, K. Weltmann, A. Bogaerts, K. Masur, P. J. Bruggeman and P. Williams, *Biointerphases*, 2017, **10**, 029518.

33 D. Boehm, C. Heslin, P. J. Cullen and P. Bourke, *Sci. Rep.*, 2016, **6**, 21464.

34 D. Yan, H. Cui, W. Zhu, N. Nourmohammadi, J. Milberg, L. G. Zhang, J. H. Sherman and M. Keidar, *Sci. Rep.*, 2017, **7**, 4479.

35 C. Klinkhammer, C. Verlackt, F. Kogelheide, A. Bogaerts, N. Metzler-nolte, K. Stapelmann, M. Havenith and J. Lackmann, *Sci. Rep.*, 2017, **7**, 13828.

36 A. Görlach, *Antioxid. Redox Signal.*, 2005, **7**, 1398–1406.

37 A. Stancampiano, T. Chung, S. Dozias, J. Pouvesle, L. M. Mir and E. Robert, in *ISPC24*, 2019, pp. 1–4.

38 P. Viegas, E. Slikboer and A. Obrusník, *Plasma Sources Sci. Technol.*, 2018, **27**, 094002.

39 D. B. Graves, *IEEE Trans. Radiat. Plasma Med. Sci.*, 2018, **2**, 594–607.

40 M. Laroussi, *IEEE Trans. Plasma Sci.*, 1996, **24**, 1188–1191.

41 M. G. Kong, G. Kroesen, G. Morfill, T. Nosenko, T. Shimizu, J. Van Dijk and J. L. Zimmermann, *New J. Phys.*, 2009, **11**, 115012.

42 J. Schlegel, J. Köritzer and V. Boxhammer, *Clin. Plasma Med.*, 2013, **1**, 2–7.

43 F. Judée, J. Vaquero, S. Guégan, L. Fouassier and T. Dufour, *J Phys D Appl Phys*, 2019, **52**, 245201.

44 E. Freund, K. R. Liedtke, J. Van Der Linde, H. Metelmann, C. Heidecke, L. Partecke and S. Bekeschus, *Sci. Rep.*, 2019, **9**, 634.

45 D. B. Graves, *Plasma Process. Polym.*, 2014, **11**, 1120–1127.

46 B. Alberts, A. Johnson, J. Lewis, M. Raff, K. Roberts and P. Walter, *Molecular biology of the cell*, Garland Science, 5th edn., 2008.

47 J. L. Barnes, M. Zubair, K. John, M. C. Poirier and F. L. Martin, *Biochem. Soc. Trans.*, 2018, **46**, 1213–1224.

48 K. Grønbæk, C. Hother and P. A. Jones, *J. Pathol. Microbiol. Immunol.*, 2007, **115**, 1039–1059.

49 A. Goodspeed, L. M. Heiser, J. W. Gray and J. C. Costello, *Mol Cancer Res*, 2016, **14**, 3–13.

50 M. O. Palumbo, P. Kavan, W. H. M. Jr, L. Panasci, S. Assouline, N. Johnson, V. Cohen, F. Patenaude, M. Pollak, R. T. Jagoe and G. Batist, *Front. Pharmacol.*, 2013, **4**, 1–9.

51 A. Makkouk and G. J. Weiner, *Cancer Res.*, 2014, **75**, 5–10.

52 M. Witek, E. Blomain, M. S. Magee, B. Xiang, S. A. Waldman and A. E. Snook, *Int J Radiat Oncol Biol Phys*, 2014, **88**, 1188–1195.

53 R. R. Allison, R. J. Amdur, J. D. Bradley, D. J. Brenner, R. A. Bucholz, H. R. Cardenes, W. H. Choi, L. C. Cho and et al, *Technical basis of radiation therapy*, Springer, 2006.

54 J. L. Glover, P. J. Bendick, W. J. Link and R. J. Plunkett, *Lasers Surg. Med.*, 1982, **2**, 101–106.

55 D. Schardt, T. Elsässer and D. Schulz-ertner, *Rev. Mod. Phys.*, 2010, **82**, 383–425.

56 D. Dolmans, D. Fukumura and R. Jain, *Nat. Rev. Cancer*, 2003, **3**, 380–387.

57 G. L. Semenza, *Nat. Rev. Cancer*, 2003, **3**, 721–732.

58 A. Thomas, B. A. Teicher and R. Hassan, *Lancet Oncol.*, 2016, **17**, e254–62.

59 A. Coulson, A. Levy and M. Gossell-Williams, *West Indian Med. J.*, 2014, **63**, 650–654.

60 T. N. Seyfried and L. C. Huysentruyt, *Crit Rev Oncog.*, 2013, **18**, 43–73.

61 D. Trachootham, J. Alexandre and P. Huang, *Nat. Rev. Drug Discov.*, 2009, **8**, 579–591.

62 T. P. Szatrowski and C. F. Nathan, *Cancer Res.*, 1991, **51**, 794–799.

63 S. Kawanishi, Y. Hiraku, S. Pinlaor and N. Ma, *Biol. Chem.*, 2006, **387**, 365–372.

64 S. Toyokuni, K. Okamoto, J. Yodoi and H. Hiai, *FEBS Lett.*, 1995, **358**, 1–3.

65 C. Wiel, K. Le Gal, M. X. Ibrahim, P. Lindahl, V. I. Sayin, M. O. Bergo, C. Wiel, K. Le Gal, M. X. Ibrahim, C. A. Jahangir, M. Kashif and H. Yao, *Cell*, 2019, **178**, 330–345.

66 L. Lignitto, S. E. Leboeuf, H. Homer, M. Pagano, L. Lignitto, S. E. Leboeuf, H. Homer, S. Jiang and M. Askenazi, *Cell*, 2019, **178**, 316–329.

67 W. J. van Blitterswijk, G. de Veer, J. H. Krol and P. Emmelot, *BBA - Biomembr.*, 1982, **688**, 495–504.

68 M. Shinitzky, *Biochim. Biophys. Acta*, 1984, **738**, 251–61.

69 N. Bernardes and A. M. Fialho, *Int. J. Mol. Sciiences*, 2018, **19**, 3871.

70 L. T. Tan, K. Chan, P. Pusparajah, W. Lee, L. Chuah, T. M. Khan, L. Lee, B. Goh, S. Pace and L. Lee, *Front. Pharmacol.*, 2017, **8**, 1–6.

71 S. Saadoun, M. C. Papadopoulos, D. C. Davies, B. A. Bell and S. Krishna, *Br. J. Cancer*, 2002, **87**, 621–623.

72 S. juan Zhu, K. jian Wang, S. wei Gan, J. Xu, S. ye Xu and S. quan Sun, *Biochem. Biophys. Res. Commun.*, 2013, **440**, 173–177.

73 Z. Shi, T. Zhang, L. Luo, H. Zhao, J. Cheng, J. Xiang and C. Zhao, *J. Surg. Oncol.*, 2012, **106**, 267–272.

74 M. C. Papadopoulos and S. Saadoun, *Biochim. Biophys. Acta - Biomembr.*, 2015, **1848**, 2576–2583.

75 G. Bauer, *Anticancer Res.*, 2014, **34**, 1467–1482.

76 G. Bauer, *Redox Biol.*, 2015, **6**, 353–371.

77 A. Lin, B. Truong, S. Patel, N. Kaushik, E. H. Choi, G. Fridman, A. Fridman and V. Miller, *Int. J. Mol. Sci.*, 2017, **18**, 966.

78 V. Miller, A. Lin and A. Fridman, *Plasma Chem Plasma Process*, 2016, **36**, 259–268.

79 D. Dobrynin, G. Fridman, G. Friedman and A. Fridman, *New J. Phys.*, 2009, **11**, 115020.

80 S. Kalghatgi, C. M. Kelly, E. Cerchar, B. Torabi, O. Alekseev, A. Fridman, G. Friedman and J. Azizkhan-Clifford, *PLoS One*, 2011, **6**, 1–11.

81 A. Lin, N. Chernets, J. Han, Y. Alicea, D. Dobrynin, G. Fridman, T. A. Freeman, A. Fridman and V. Miller, *Plasma Process. Polym.*, 2015, **12**, 1117–1127.

82 N. Y. Babaeva and M. J. Kushner, *J Phys D Appl Phys*, 2013, **46**, 025401.

83 M. Wang, B. Holmes, X. Cheng, W. Zhu, M. Keidar and L. G. Zhang, *PLoS One*, 2013, **8**, e73741.

84 N. Barekzi and M. Laroussi, *J. Phys. D. Appl. Phys.*, 2012, **45**, 422002.

85 J. Y. Kim, J. Ballato, P. Foy, T. Hawkins, Y. Wei, J. Li and S. O. Kim, *Biosens. Bioelectron.*, 2011, **28**, 333–338.

86 L. I. Partecke, K. Evert, J. Haugk, F. Doering, L. Normann, S. Diedrich, F.-U. Weiss, M. Evert, N. O. Huebner, C. Guenther, C. D. Heidecke, A.

Kramer, R. Bussiahn, K.-D. Weltmann, O. Pati, C. Bender and W. von Bernstorff, *BMC Cancer*, 2012, **12**, 473.

87 G. Pasqual-Melo, R. K. Gandhirajan, I. Stoffels and S. Bekeschus, *Clin. Plasma Med.*, 2018, **10**, 1–8.

88 R. M. Walk, J. A. Snyder, P. Srinivasan, J. Kirsch, S. O. Diaz, F. C. Blanco, A. Shashurin, M. Keidar and A. D. Sandler, *J. Pediatr. Surg.*, 2013, **48**, 67–73.

89 J. Köritzer, V. Boxhammer, A. Schäfer, T. Shimizu, T. G. Klämpfl, Y. F. Li, C. Welz, S. Schwenk-Zieger, G. E. Morfill, J. L. Zimmermann and J. Schlegel, *PLoS One*, 2013, **8**, e64498.

90 M. Vandamme, E. Robert, S. Dozias, J. Sobilo, S. Lerondel, A. Le Pape and J.-M. Pouvesle, *Plasma Med.*, 2011, **1**, 27–43.

91 M. Vandamme, E. Robert, S. Lerondel, V. Sarron, D. Ries, S. Dozias, J. Sobilo, D. Gosset, C. Kieda, B. Legrain, J. M. Pouvesle and A. Le Pape, *Int. J. Cancer*, 2012, **130**, 2185–2194.

92 A. Bogaerts, N. Khosravian, J. Van der Paal, C. C. W. Verlackt, M. Yusupov, B. Kamaraj and E. C. Neyts, *J. Phys. D. Appl. Phys.*, 2016, **49**, 054002.

93 S. Pancheshnyi, B. Eismann, G. J. M. Hagelaar and L. C. Pitchford, *ZDPlasKin: a new tool for plasmachemical simulations*, 2008.

94 A. M. Lietz and M. J. Kushner, *J. Phys. D. Appl. Phys.*, 2016, **49**, 425204.

95 K. Pluhackova and R. A. Böckmann, *J. Phys. C Condens. Matter*, 2015, **27**, 323103.

96 S. O. Yesylevskyy, T. Rivel and C. Ramseyer, *Sci. Rep.*, 2017, **7**, 16078.

97 E. J. Szili, N. Gaur, S.-H. Hong, H. Kurita, J.-S. Oh, M. Ito, A. Mizuno, A. Hatta, A. J. Cowin, D. Graves and R. D. Short, *J Phys D Appl Phys*, 2017, **50**, 274001.

98 S. Bekeschus, A. Käding, T. Schröder, K. Wende, C. Hackbarth, K. R. Liedtke, T. von Woedtke, C. Heidecke and L. Partecke, *Anticancer Agents Med Chem*, 2018, **18**, 824–831.

99 P. J. Bruggeman, M. J. Kushner, B. R. Locke, J. G. E. Gardeniers, W. G. Graham, D. B. Graves, R. C. H. M. Hofman-Caris, D. Maric, J. P. Reid, E. Ceriani and et al, *Plasma Sources Sci. Technol.*, 2016, **25**, 053002.

100 F. Judée, C. Fongia, B. Ducommun and M. Yousfi, *Sci. Rep.*, 2016, **6**, 21421.

101 T. Adachi, S. Nonomura, M. Horiba, T. Hirayama and T. Kamiya, *Sci. Rep.*, 2016, **6**, 20928.

102 N. Kurake, H. Tanaka, K. Ishikawa and T. Kondo, *Arch. Biochem. Biophys.*, 2016, **605**, 102–108.

103 S. Agnihotri, K. E. Burrell and A. Wolf, *Arch. Immunol. Ther. Exp.*, 2013, **61**, 25–41.

104 D. N. Louis, H. Ohgaki, O. D. Wiestler, W. K. Cavenee, P. C. Burger, A. Jouvet, B. W. Scheithauer and P. Kleihues, *Acta Neuropathol.*, 2007, **114**, 97–109.

105 R. Stupp, M. E. Hegi, W. P. Mason, M. J. Van Den Bent, M. J. B. Taphoorn, R. C. Janzer, S. K. Ludwin and A. Allgeier, *Lancet Oncol.*, 2009, **10**, 459–466.

106 G. M. Eisenberg, *Ind. Eng. Chem. Anal. Ed.*, 1943, 327–328.

107 J. B. J. Fox, *Anal. Chem.*, 1979, **51**, 1493–1502.

108 G. J. M. Hagelaar and Pitch, *Plasma Sources Sci. Technol.*, 2005, **14**, 722–733.

109 M. A. Lieberman and A. J. Lichtenberg, *Principles of Plasma Discharges and Materials Processing*, Wiley Interscience, 2nd edn., 2005.

110 C. C. W. Verlackt, W. Van Boxem and A. Bogaerts, *Phys. Chem. Chem. Phys.*, 2018, **20**, 6845–6859.

111 T. Murakami, K. Niemi, T. Gans, D. O 'connell, W. G. Graham, D. O'Connell and W. G. Graham, *Plasma Sources Sci. Technol.*, 2013, **22**, 015003.

112 W. Van Gaens and A. Bogaerts, *J. Phys. D. Appl. Phys.*, 2013, **46**, 275201.

113 W. Diao, X. Tong, C. Yang, F. Zhang, C. Bao and H. Chen, *Sci. Rep.*, 2019, **9**, 1–9.

114 M. P. Mattson, *Ageing Res Rev.*, 2008, **7**, 1–7.

115 J. Harris, N. Phan, Anh and K. Zhang, *Green Chem.*, 2018, **20**, 2578–2587.

116 F. Rezaei, Y. Gorbanev, M. Chys, A. Nikiforov, P. Cos, A. Bogaerts, N. De Geyter and S. W. H. Van Hulle, *Plasma Process. Polym.*, 2018, **15**, e1700226.

117 Y. Gorbanev, D. Leifert, A. Studer, D. O'Connell and V. Chechik, *Chem. Commun.*, 2017, **53**, 3685–3688.

118 I. Adamovich, S. D. Baalrud, A. Bogaerts, P. J. Bruggeman, C. M and et al, *J. Phys. D. Appl. Phys.*, 2017, **50**, 323001.

119 Y. Gorbanev, D. O. Connell and V. Chechik, *Chem. Eur. J.*, 2016, **22**, 3496–3505.

120 Y. Gorbanev, A. Privat-maldonado and A. Bogaerts, *Anal. Chem.*, 2018, **90**, 13151–13158.

121 M. A. C. Hänsch, M. Mann and K. Weltmann, *J. Phys. D. Appl. Phys.*, 2015, **48**, 454001.

122 Z. Ke, Z. Chen and Q. Huang, *Plasma Process. Polym.*, 2017, **15**, e1700153.

123 I. M. Piskarev, *High Energy Chem.*, 2017, **51**, 297–301.

124 V. S. S. K. Kondeti, C. Q. Phan, K. Wende, H. Jablonowski, U. Gangal, J. L. Granick, R. C. Hunter and P. J. Bruggeman, *Free Radic. Biol. Med.*, 2018, **124**, 275–287.

125 Y. Gorbanev, C. C. W. Verlackt, S. Tinck, E. Tuenter, K. Foubert and P. Cos, *Phys. Chem. Chem. Phys.*, 2018, **20**, 2797–2808.

126 M. M. Hefny, C. Pattyn, P. Lukes and J. Benedikt, *J. Phys. D. Appl. Phys.*, 2016, **49**, 404002.

127 J. Benedikt, M. M. Hefny, A. Shaw, B. R. Buckley, F. Iza, S. Schäckermann and J. E. Bandow, *Phys. Chem. Chem. Phys.*, 2018, **20**, 12037–12042.

128 Y. Gorbanev, J. Van der Paal, W. Van Boxem, S. Dewilde and A. Bogaerts, *Phys. Chem. Chem. Phys.*, 2019, **21**, 4117–4121.

129 Z. C. Liu, L. Guo, D. X. Liu, M. Z. Rong, H. L. Chen and M. G. Kong, *Plasma Process. Polym.*, 2017, **14**, 1600113.

130 D. T. Elg, I. Yang and D. B. Graves, *J. Phys. D. Appl. Phys.*, 2017, **50**, 475201.

131 Y. Gorbanev, R. Soriano, D. O'Connell and V. Chechik, *J. Vis. Exp.*, 2016, **117**, e54765.

132 A. A. Green, *J. Am. Chem. Soc.*, 1933, **55**, 2231–2236.

133 A. M. Shams El Din and R. A. Mohammed, *Desalination*, 1998, **115**, 145–153.

134 J. M. Cachaza, J. Casado, A. Castro and M. A. Lopez Quintela, *Can. J. Chem*, 1976, **54**, 3401–3406.

135 K. Wende, P. Williams, J. Dalluge, W. Van Gaens, H. Aboubakr, J. Bischof, T. Von, S. M. Goyal, K. Weltmann, A. Bogaerts, K. Masur, P. J. Bruggeman and P. Williams, *Biointerphases*, 2015, **10**, 0298518.

136 Y. Guo, Q. Ma, F. Cao, Q. Zhao and X. Ji, *Anal. Methods*, 2015, **7**, 4055–4058.

137 V. Jirasek and P. Lukes, *Plasma Sources Sci. Technol.*, 2019, **28**, 035015.

138 H. J. Ahn, K. Il Kim, N. N. Hoan, C. H. Kim, E. Moon, K. S. Choi, S. S. Yang, J.-S. Lee, S. Kalghatgi, C. Kelly, E. Cerchar, B. Torabi, O. Alekseev, H. Ahn, K. Kim, G. Kim, E. Moon, S. Yang, Y. Hong, J. Kang, H. Lee, H. Uhm, E. Moon, S. Rupf, A. Lehmann, M. Hannig, B. Schäfer, A. Schubert, T. Yamamori, H. Yasui, M. Yamazumi, Y. Wada, Y. Nakamura, R. Mittler, S. Vanderauwera, N. Suzuki, G. Miller, V. Tognetti, Y. Bae, H. Oh, S. Rhee, Y. Yoo, R. Davis, M. Torres, C. Tournier, P. Hess, D. Yang, J. Xu, T. Turner, H. Aoki, P. Kang, J. Hampe, K. Yoshimura, T. Noma, G. Kim, G. Kim, S. Park, S. Jeon, H. Seo, G. Kim, W. Kim, K. Kim, J. Lee, K. Kim, G. Kim, Y. Hong, S. Yang, H. Lee, C. Shon, Y. Kim, S. Kim, G. Kim, X. Zhang, M. Li, R. Zhou, K. Feng, S. Yang, G. Fridman, A. Shereshevsky, M. Jost, A. Brooks, A. Fridman, K. Kim, J. Choi, Y. Hong, G. Kim, E. Noh, K. Kim, G. Kim, Y. Oh, T. Park, D. Han, D. Dobrynin, A. Fridman, A. Yu, J. Köritzer, V. Boxhammer, A. Schäfer, T. Shimizu, T. Klämpfl, R. Franco, M. Panayiotidis, J. Cidlowski, S. Cook, P. Sugden, A. Clerk, J. Lindsay, M. Esposti, A. Gilmore, A. Chalah, R. Khosravi-Far, D. Brenner, T. Mak, D. Zorov, M. Juhaszova, S. Sollott, A. Laurent, C. Nicco, C. Chéreau, C. Goulvestre, J. Alexandre, K. Arjunan, G. Friedman, A. Fridman, A. Clyne, S. Kim, S. Kim, B. Kim, S. Rah, S. Chung, M. Marletta, J. Sun, X. Zhang, M. Broderick, H. Fein, N. Oleinik, N. Krupenko, S. Krupenko, K. Mikule, B. Delaval, P. Kaldis, A. Jurcyzk and P. Hergert, *PLoS One*, 2014, **9**, e86173.

139 G. P. Bienert and F. Chaumont, *Biochim. Biophys. Acta - Gen. Subj.*, 2014, **1840**, 1596–1604.

140 A. Almasalmeh, D. Krenc, B. Wu and E. Beitz, *FEBS J.*, 2014, **281**, 647–656.

141 F. de Meyer and B. Smit, *Proc. Natl. Acad. Sci. U. S. A.*, 2009, **106**, 3654–3658.

142 T. Rog, M. Pasenkiewicz-Gierula, I. Vattulainen and M. Karttunen, *Biochim. Biophys. Acta - Biomembr.*, 2009, **1788**, 97–121.

143 S. Raffy and J. Teissié, *Biophys. J.*, 1999, **76**, 2072–2080.

144 M. Sok, M. Sentjurc and M. Schara, *Cancer Lett.*, 1999, **139**, 215–220.

145 G. van Meer, *Annu. Rev. Cell Biol.*, 1989, **5**, 247–278.

146 E. Sackmann, in *Structure and Dynamics of Membranes*, eds. R. Lipowsky and E. Sackmann, Elsevier, Amsterdam, 1995, pp. 1–64.

147 B. N. Olsen, P. H. Schlesinger and N. A. Baker, *J Am Chem Soc*, 2009, **131**, 4854–4865.

148 E. Falck, M. Patra, M. Karttunen, M. T. Hyvönen and I. Vattulainen, *Biophys. J.*, 2004, **87**, 1076–91.

149 C. Hofsäß, E. Lindahl and O. Edholm, *Biophys. J.*, 2003, **84**, 2192–2206.

150 P. L. Yeagle, *Biochimie*, 1991, **73**, 1303–1310.

151 T. P. W. McMullen and R. N. McElhaney, *Curr. Opin. Colloid Interface Sci.*, 1996, **1**, 83–90.

152 J. Van Der Paal, E. C. Neyts, C. C. W. Verlackt and A. Bogaerts, *Chem. Sci.*, 2015, **7**, 489–498.

153 R. M. Cordeiro, *Biochim. Biophys. Acta - Biomembr.*, 2014, **1838**, 438–444.

154 C. L. Wennberg, D. Van Der Spoel and J. S. Hub, *J. Am. Chem. Soc.*, 2012, **134**, 5351–5361.

155 M. F. Renschler, *Eur. J. Cancer*, 2004, **40**, 1934–1940.

156 M.-Y. Liou and P. Storz, *Free Radic Res.*, 2010, **44**, 1–31.

157 L. Martínez, R. Andrade, E. G. Birgin and J. M. Martínez, *J. Comput. Chem.*, 2009, **30**, 2157–2164.

158 S. W. Chiu, S. A. Pandit, H. L. Scott and E. Jakobsson, *J. Phys. Chem. B*, 2009, **113**, 2748–2763.

159 W. G. Hoover, *Phys. Rev. A*, 1985, **31**, 1695–1697.

160 M. Parrinello and A. Rahman, *J. Appl. Phys.*, 1981, **52**, 7182–7190.

161 T. Darden, D. York and L. Pedersen, *J. Chem. Phys.*, 1993, **98**, 10089.

162 U. Essmann, L. Perera, M. L. Berkowitz, T. Darden, H. Lee and L. G. Pedersen, *J Chem Phys*, 1995, **103**, 8577–8593.

163 M. J. Abraham, T. Murtola, R. Schulz, S. Pall, J. C. Smith, B. Hess and E. Lindah, *SoftwareX*, 2015, **1-2**, 19–25.

164 G. M. Torrie and J. P. Valleau, *Chem. Phys. Lett.*, 1974, **28**, 578–581.

165 G. M. Torrie and J. P. Valleau, *J. Comput. Phys.*, 1977, **23**, 187–199.

166 J. Kästner, *WIREs Comput. Mol. Sci.*, 2011, **1**, 932–942.

167 S. Kumar, J. M. Rosenberg, D. Bouzida and R. H. Swendsen, *J Comput Chem*, 1992, **13**, 1011–1021.

168 W. K. Subczynski and J. S. Hyde, *Biophys. J.*, 1983, **41**, 283–6.

169 M. N. Möller, J. R. Lancaster Jr and A. Denicola, in *Free Radical Effects on Membranes*, ed. S. Matalon, Elsevier, Amsterdam, 2008, vol. Volume 61, pp. 23–42.

170 J. C. Mathai and V. Sitaramam, *J. Biol. Chem.*, 1994, **269**, 17784–17793.

171 R. A. Demel, L. L. M. Van Deenen and B. A. Pethica, *Biochim. Biophys. Acta*, 1967, **135**, 11–19.

172 W.-C. Hung, M.-T. Lee, F.-Y. Chen and H. W. Huang, *Biophys. J.*, 2007, **92**, 3960–3967.

173 S. W. Chiu, E. Jakobsson, R. J. Mashl and H. L. Scott, *Biophys. J.*, 2002, **83**, 1842–1853.

174 E. J. Szili, S. Hong and R. D. Short, *Biointerphases*, 2015, **10**, 029511.

175 M. U. Hammer, E. Forbrig, S. Kupsch, K. Weltmann and S. Reuter, *Plasma Med.*, 2013, **3**, 97–114.

176 S. Maheux, G. Frache, J. S. Thomann, F. Cl, C. Penny, T. Belmonte and D. Duday, *J. Phys. D. Appl. Phys.*, 2016, **49**, 344001.

177 S.-H. Hong, E. J. Szili, A. T. A. Jenkins and R. D. Short, *J. Phys. D. Appl. Phys.*, 2014, **47**, 362001.

178 S. H. Ki, J. K. Park, C. Sung, C. B. Lee, H. Uhm, E. H. Choi and K. Y. Baik, *J. Phys. D. Appl. Phys.*, 2016, **49**, 085401.

179 R. Tero, R. Yamashita, H. Hashizume, Y. Suda, H. Takikawa, M. Hori and M. Ito, *Arch. Biochem. Biophys.*, 2016, **605**, 26–33.

180 S. Hong, E. J. Szili, A. T. A. Jenkins and R. D. Short, *J. Phys. D. Appl. Phys.*, 2014, **47**, 362001.

181 J. Wong-ekkabut, Z. Xu, W. Triampo, I. Tang and D. P. Tieleman, *Biophys. J.*, 2007, **93**, 4225–4236.

182 L. Beranova, L. Cwiklik, P. Jurkiewicz, M. Hof and P. Jungwirth, *Langmuir Lett.*, 2010, **26**, 6140–6144.

183 L. Cwiklik and P. Jungwirth, *Chem. Phys. Lett.*, 2010, **486**, 99–103.

184 P. Svarnas, S. H. Matrali, K. Gazeli and S. G. Antimisiaris, *Plasma*

Process. Polym., 2015, **12**, 655–665.

185 A. Bourdon, T. Darny, F. Pechereau, J.-M. Pouvesle, P. Viegas, S. Iseni and E. Robert, *Plasma Sources Sci. Technol.*, 2016, **25**, 035002.

186 A. Begum, M. Laroussi and M. Rasel Pervez, *AIP Adv.*, 2013, **3**, 062117.

187 G. B. Sretenovic, I. B. Krsti, V. V. Kovacevic, B. M. Obradovic and M. M. Kuraica, *J. Phys. D. Appl. Phys.*, 2014, **47**, 102001.

188 A. Shashurin, M. N. Schneider and M. Keidar, *Plasma Sources Sci. Technol.*, 2012, **21**, 034006.

189 N. Y. Babaeva and M. J. Kushner, *J. Phys. D. Appl. Phys.*, 2010, **43**, 185206.

190 N. Y. Babaeva, W. Tian and M. J. Kushner, *J. Phys. D. Appl. Phys.*, 2014, **47**, 235201.

191 J. C. Weaver, K. C. Smith, A. T. Esser, R. S. Son and T. R. Gowrishankar, *Bioelectrochemistry*, 2012, **87**, 236–243.

192 M. L. Yarmush, A. Golberg, G. Sersa, T. Kotnik and D. Miklavˇ, *Annu. Rev. Biomed. Eng.*, 2014, **16**, 295–320.

193 S. Lakshmanan, G. K. Gupta, P. Avci, R. Chandran, M. Sadasivam, A. Elisa and M. R. Hamblin, *Adv. Drug Deliv. Rev.*, 2014, **71**, 98–114.

194 S. Haberl, D. Miklavcic, G. Sersa, W. Frey and B. Rubinsky, *IEEE Electr. Insul. Mag.*, 2013, **29**, 29–37.

195 J. Villemejane and L. M. Mir, *Br. J. Pharmacol.*, 2009, **157**, 207–219.

196 M. Breton and L. M. Mir, *Bioelectromagnetics*, 2012, **33**, 106–123.

197 J. Gehl, *Acta Physiol Scand*, 2003, **177**, 437–447.

198 A. Gothelf, L. M. Mir and J. Gehl, *Cancer Treat. Rev.*, 2003, **29**, 371–387.

199 S. J. Beebe, N. M. Sain and W. Ren, *Cells*, 2013, **2**, 136–162.

200 C. Chen, S. W. Smye, M. P. Robinson and J. A. Evans, *Med Biol Eng Comput*, 2006, **44**, 5–14.

201 M. Tarek, *Biophys. J.*, 2005, **88**, 4045–4053.

202 P. T. Vernier and M. J. Ziegler, *J. Phys. Chem. B*, 2007, **111**, 12993–12996.

203 M. Breton, L. Delemotte, A. Silve, L. M. Mir and M. Tarek, *JACS communcuations*, 2012, **134**, 13938–13941.

204 P. T. Vernier, M. J. Ziegler, Y. Sun, W. V Chang, M. A. Gundersen and D. P. Tieleman, *JACS communcuations*, 2006, **128**, 6288–6289.

205 A. Y. Antipina and A. A. Gurtovenko, *J. Phys. Chem. B*, 2015, **119**, 6638.

206 M. Casciola and M. Tarek, *BBA - Biomembr.*, 2016, **1858**, 2278–2289.

207 S. J. Marrink, A. H. De Vries and D. P. Tieleman, *BBA - Biomembr.*, 2009, **1788**, 149–168.

208 T. He, D. Liu, H. Xu, D. Xu and D. Li, *J. Phys. D. Appl. Phys.*, 2016, **49**, 205204.

209 A. Reis and C. M. Spickett, *Biochim. Biophys. Acta*, 2012, **1818**, 2374–2387.

210 J. S. Hub, B. L. De Groot and D. Van Der Spoel, *J. Chem. Theory Comput.*, 2010, **6**, 3713–3720.

211

212 Q. Hu, S. Viswanadham, R. P. Joshi, S. J. Beebe and P. F. Blackmore, *Phys. Rev. E*, 2005, **71**, 031914.

213 Q. Hu, R. P. Joshi and K. H. Schoenbach, *Phys. Rev. E*, 2005, **72**, 031902.

214 B. Hess, *J Chem Phys*, 2002, **209**, 209–217.

215 S. T. Moin, T. S. Hofer, B. R. Randolf and B. M. Rode, *Comput. Theor. Chem.*, 2012, **980**, 15–22.

216 M. N. Möller, J. R. J. Lancaster and A. Denicola, *Curr. Top. Membr.*, 2008, **61**, 24–42.

217 A. A. Gurtovenko and A. S. Lyulina, *J. Phys. Chem. B*, 2014, **118**, 9909–9918.

218 R. A. Böckmann, B. L. De Groot, S. Kakorin, E. Neumann, H. Grubmu and R. A. Bo, *Biophys. J.*, 2008, **95**, 1837–1850.

219 M. R. Prausnitz and R. Langer, *Nat. Biotechnol.*, 2008, **26**, 1261–1268.

220 M. A. Moses, H. Brem and R. Langer, *Cancer Cell*, 2003, **4**, 337–341.

221 G. M. Glenn and R. T. Kenney, *Curr Top Microbiol Immunol*, 2006, **304**, 247–268.

222 M. R. Prausnitz, S. Mitragotri and R. Langer, *Nat. Rev. Drug Discov.*, 2004, **3**, 115–124.

223 B. Chaulagain, A. Jain, A. Tiwari, A. Verma and S. K. Jain, *Artif. Cells, Nanomedicine, Biotechnol.*, 2018, **46**, S472–S487.

224 T. Shukla, N. Upmanyu, M. Agrawal, S. Saraf, S. Saraf and A. Alexander, *Biomed. Pharmacother.*, 2018, **108**, 1477–1494.

225 K. S. Simon, N. L. Pollock and S. C. Lee, *Biochem. Soc. Trans.*, 2018, **46**, 1495–1504.

226 Y. N. Kalia, A. Naik, J. Garrison and R. H. Guy, *Adv. Drug Deliv. Rev.*, 2004, **56**, 619–658.

227 A. K. Banga, *Electrically-Assisted Transdermal and Topical Drug*, Taylor & Francis, London, 1998.

228 M. J. Pikal, *Adv. Drug Deliv. Rev.*, 2001, **46**, 281–305.

229 R. Prausnitz, *Adv. Drug Deliv. Rev.*, 1996, 395–425.

230 L. Machet and A. Boucaud, *Int. J. Pharm.*, 2002, **243**, 1–15.

231 A. Denet, R. Vanbever and D. P. Gale, *Adv. Drug Deliv. Rev.*, 2004, **56**, 659–674.

232 H. Marwah, T. Garg, A. K. Goyal and G. Rath, *Drug Deliv.*, 2016, **23**, 564–578.

233 A. Naik, Y. N. Kalia, R. H. Guy and R. H. Guy, *Pharm. Sci. Technolo. Today*, 2000, **3**, 318–326.

234 I. Iwai, H. Han, L. den Hollander, S. Svensson, L.-G. Öfversfedt, J. Anwar, J. Brewer and M. Bloksgaard, *J. Invest. Dermatol.*, 2012, **132**, 2215–2225.

235 B. Forslind and M. Lindberg, *Skin, hair and nails*, CRC Press, 1st edn., 2003.

236 J. A. Bouwstra, F. E. R. Dubbelaar, G. S. Gooris and M. Ponec, *Acta Derm Venereol*, 2000, **208**, 23–30.

237 J. J. Escobar-Chávez, V. Merino-Sanjuan, M. Lopez-Cervantes, Z. Urban-Morlan, E. Pinon-Segundo, D. Quintanar-Guerrero and A. Ganem-Quintanar, *J. Pharm. Pharm. Sci.*, 2008, **11**, 104–130.

238 J. Hadgraft, *Int. J. Pharm.*, 2001, **224**, 1–18.

239 S. Mitragotri, *Adv. Drug Deliv. Rev.*, 2013, **65**, 100–103.

240 J. J. Escobar-Chávez, R. Díaz-Torres, I. M. Rodríguez-Cruz, C. L. Domínguez-Delgado, R. S. Morales, E. Ángeles-Anguiano and L. M. Melgoza-Conteras, *Res. Reports Transdermal Drug Deliv.*, 2012, **1**, 3–17.

241 O. Lademann, H. Richter, M. C. Meinke, A. Patzelt, A. Kramer, P. Hinz,

K. Weltmann, B. Hartmann and S. Koch, *Exp. Dermatol.*, 2011, **20**, 488–490.

242 K. Shimizu, N. A. Tran, K. Hayashida and M. Blajan, *J Phys D Appl Phys*, 2016, **49**, 315201.

243 K. Shimizu, K. Hayashida and M. Blajan, *Biointerphases*, 2015, **10**, 029517.

244 M. Gelker, C. C. Müller-goymann and W. Viöl, *Clin. Plasma Med.*, 2018, **9**, 34–40.

245 A. Lehmann, F. Pietag and T. Arnold, *Clin. Plasma Med.*, 2017, **7**, 16–23.

246 J. Lademann, A. Patzelt, H. Richter, O. Lademann and G. Baier, *Laser Phys. Lett.*, 2013, **10**, 083001.

247 R. Laurita, A. Miserocchi, M. Ghetti, M. Gherardi, A. Stancampiano, V. Purpura, D. Melandri, P. Minghetti, E. Bondioli and V. Colombo, *IEEE Trans. Radiat. Plasma Med. Sci.*, 2017, **1**, 275–279.

248 A. Helmke, D. Hoffmeister, N. Mertens, S. Emmert, J. Schuette and W. Vioel, *New J. Phys.*, 2009, **11**, 115025.

249 A. Catalá, *Biochem. Biophys. Res. Commun.*, 2010, **399**, 318–323.

250 H. S. El-beltagi and H. I. Mohamed, *Not Bot Horti Agrobo*, 2013, **41**, 44–57.

251 G. Barrera and L. Peroxidation, *Int. Sch. Res. Netw. Oncol.*, 2012, 137289.

252 T. Melo, E. Maciel, M. M. Oliveira, P. Domingues and M. R. M. Domingues, *Eur. J. Lipid Sci. Technol.*, 2012, **114**, 726–732.

253 W. J. Muizebelt and M. W. F. Nielen, *J. Mass Spectrom.*, 1996, **31**, 545–554.

254 H. W. Gardner, *Free Radic. Biol. Med.*, 1989, **7**, 65–86.

255 M. A. R. Meier, O. J. Metzger and U. S. Schubert, *Chem. Soc. Rev.*, 2007, **36**, 1788–1802.

256 F. S. Güner, Y. Yagci and A. T. Erciyes, *Prog. Polym. Sci.*, 2006, **31**, 633–670.

257 S. E. Feller, *Curr. Opin. Colloid Interface Sci.*, 2000, **5**, 217–223.

258 J. Van der Paal, C. Verheyen, E. C. Neyts and A. Bogaerts, *Sci. Rep.*, 2017, **7**, 39526.

259 J. Mutanu Jungersted, L. I. Hellgren, J. K. Kogh, T. Drachmann, G. B.

Jemec and T. Agner, *Acta Derm Venereol*, 2010, **90**, 350–353.

260 G. Bussi, D. Donadio and M. Parrinello, *J Chem Phys*, 2007, **126**, 014101.

261 S. J. Marrink, J. H. Risselada, S. Yefimov, P. D. Tieleman and A. H. De Vries, *J. Phys. Chem. B*, 2007, **111**, 7812–7824.

262 P. Sane, E. Salonen, E. Falck, J. Repakova, F. Tuomisto, J. M. Holopainen and I. Vattulainen, *J. Phys. Chem. Lett. B*, 2009, **113**, 1810–1812.

263 M. Yusupov, J. Van der Paal, E. C. Neyts and A. Bogaerts, *BBA - Gen. Subj.*, 2017, **1861**, 839–847.

264 W. Humphrey, A. Dalke and K. Schulten, *J. Mol. Graph.*, 1996, **14**, 33–38.

265 P. V Escribá, *Trends Mol. Med.*, 2006, **12**, 34–43.

266 P. V Escribá, J. M. González-Ros, F. M. Goñi, L. Vigh, L. Sánchez-magraner, A. M. Fernández, X. Busquets, I. Horváth and G. Barceló-coblijn, *Transl. Med.*, 2008, **12**, 829–875.

267 B. Leite, A. Aufderhorst-roberts, M. S. Palma, S. D. Connell, R. Neto and P. A. Beales, *Biophys. J.*, 2015, **109**, 936–947.

268 J. Martínez, V. Oliver, J. Casa, F. Barcel, R. Alemany, J. Prades, T. Nagy, C. Baamonde, P. G. Kasprzyk, S. Terés, C. Saus and P. V Escriba, *Mol. Pharmacol.*, 2005, **67**, 531–540.

269 M. Sud, E. Fahy, D. Cotter, A. Brown, E. A. Dennis, C. K. Glass, A. H. M. Jr, R. C. Murphy and C. R. H. Raetz, *Nucleic Acids Res.*, 2007, **35**, 527–532.

270 T. Ozben, *J. Pharm. Sci.*, 2007, **96**, 2181–2196.

271 Y.-H. M. Chan and S. G. Boxer, *Curr. Opin. Chem. Biol.*, 2007, **11**, 581–587.

272 P. Svarnas, S. H. Matrali, K. Gazeli and S. G. Antimisiaris, *Plasma Process. Polym.*, 2015, **12**, 655–665.

273 H. R. Metelmann, C. Seebauer, V. Miller, A. Fridman, G. Bauer, D. B. Graves, J. M. Pouvesle, R. Rutkowski, M. Schuster, S. Bekeschus, K. Wende, K. Masur, S. Hasse, T. Gerling, M. Hori, H. Tanaka, E. Ha Choi, K. D. Weltmann, P. H. Metelmann, D. D. Von Hoff and T. von Woedtke, *Clin. Plasma Med.*, 2018, **9**, 6–13.

274 E. A. Veal, A. M. Day and B. A. Morgan, *Mol. Cell*, 2007, **26**, 1–14.

275 S. Bekeschus, J. Kolata, C. Winterbourn, A. Kramer, R. Turner, K. D. Weltmann, B. Br and K. Masur, *Free Radic Res.*, 2014, **48**, 542–549.

276 M. Keidar, R. Walk, A. Shashurin, P. Srinivasan, A. Sandler, S. Dasgupta, R. Ravi, R. Guerrero-Preston and B. Trink, *Br. J. Cancer*, 2011, **105**, 1295–1301.

277 E. A. Ratovitski, X. Cheng, D. Yan, J. H. Sherman, J. Canady, B. Trink and M. Keidar, *Plasma Process. Polym.*, 2014, **11**, 1128–1137.

278 R. Kakei, A. Ogino, F. Iwata and M. Nagatsu, *Thin Solid Films*, 2010, **518**, 3457–3460.

279 J. Y. Kim, Y. Wei, J. Li, P. Foy, T. Hawkins, J. Ballato and S. Kim, *Small*, 2011, **7**, 2291–2295.

280 G. Van Meer, D. R. Voelker and G. W. Feigenson, *Nat. Rev.*, 2008, **9**, 112–124.

281 T. Harayama and H. Riezman, *Nat. Publ. Gr.*, 2018, **19**, 281–296.

282 T. Rivel, C. Ramseyer and S. Yesylevskyy, *Sci. Rep.*, 2019, **9**, 5627.

283 H. Kurita, T. Nakajima, H. Yasuda and K. Takashima, *Appl. Phys. Lett.*, 2011, **99**, 191504.

284 J. Razzokov, M. Yusupov, R. M. Cordeiro and A. Bogaerts, *J. Phys. D. Appl. Phys.*, 2018, **51**, 365203.

285 J. Oh, Y. Aranda-gonzalvo and J. W. Bradley, *J Phys D Appl Phys*, 2011, **44**, 365202.

286 A. G. Gaydon, *The Identification of Molecular Spectra*, Springer Netherlands, 1st edn., 1976.

287 S. Koike, T. Sakamoto, S. Kobori, H. Matsuura and H. Akatsuka, *Jpn. J. Appl. Phys.*, 2004, **43**, 5550–5557.

288 J. Kurihara, N. Iwagami and K. Oyama, *TERRAPUB*, 2013, 33–39.

289 J. Oh, H. Furuta, A. Hatta and J. W. Bradley, *Jpn. J. Appl. Phys.*, 2015, 01AA03.

290 J. Oh, M. Kakuta, H. Furuta, H. Akatsuka and A. Hatta, *Jpn. J. Appl. Phys.*, 2016, 06HD01.

291 J. Oh, E. J. Szili, N. Gaur and S. Hong, *J. Phys. D. Appl. Phys.*, 2016, **49**, 304005.

292 H. Y. Kim, Y. J. Hong, K. Y. Baik, G. C. Kwon, J. J. Choi, G. S. Cho, U. Han Sup, D. Y. Kim and E. H. Choi, *Plasma Chem Plasma Process*, 2014, 457–472.

293 P. Attri, Y. H. Kim, D. H. Park, J. H. Park, Y. J. Hong, H. S. Uhm, K. Kim, A. Fridman and E. H. Choi, *Sci. Rep.*, 2015, 9332.

294 M. J. Traylor, M. J. Pavlovich, S. Karim, P. Hait, Y. Sakiyama, D. S. Clark and D. B. Graves, *J. Phys. D. Appl. Phys.*, 2011, 472001.

295 U. K. Ercan, H. Wang, H. Ji, G. Fridman, A. D. Brooks and S. G. Joshi, *Plasma Process. Polym.*, 2013, 544–555.

296 B. Halliwell and J. M. C. Gutteridge, *Free Radicals in Biology and Medicine.pdf*, Oxford University Press, 5th edn., 2015.

297 H. Pelicano, D. Carney and P. Huang, *Drug Resist. Updat.*, 2004, **7**, 97–110.

298 J. Oh, E. J. Szili, S. Ito and S. Hong, *Plasma Med.*, 2015, **5**, 125–143.

299 J. R. Silvius, *Thermotropic Phase Transitions of Pure Lipids in Model Membranes and Their Modifications by Membrane Proteins*, John Wiley & Sons, Inc., New York, 1982.

300 A. C. Lloyd, K. R. Darnall, A. M. Winer and J. N. J. Pitts, *J. Phys. Chem.*, 1976, **80**, 789–794.

301 M. Yusupov, K. Wende, S. Kupsch, E. C. Neyts, S. Reuter and A. Bogaerts, *Sci. Rep.*, 2017, **7**, 5761.

302 A. J. P. Neto and R. M. Cordeiro, *BBA - Biomembr.*, 2016, **1858**, 2191–2198.

303 E. Sezgin, I. Lavental, S. Mayor and C. Eggeling, *Nat Rev Mol Cell Biol.*, 2017, **18**, 361–374.

304 Q. Liu, Q. Luo, A. Halim and G. Song, *Cancer Lett.*, 2017, **401**, 39–45.

305 S. J. Kim and T. H. Chung, *Sci. Rep.*, 2016, **6**, 20332.

306 H. Metelmann, D. S. Nedrelow, C. Seebauer, M. Schuster, T. Von Woedtke, K. Weltmann, S. Kindler, P. Henriette, S. E. Finkelstein, D. D. Von Hoff and F. Podmelle, *Clin. Plasma Med.*, 2015, **3**, 17–23.

307 M. Schuster, C. Seebauer, R. Rutkowski, A. Hauschild, F. Podmelle, C. Metelmann, B. Metelmann, T. Von Woedtke, S. Hasse, K. Weltmann and H. Metelmann, *J. Cranio-Maxillofacial Surg.*, 2016, **44**, 1445–1452.

308 K. Weltmann and T. Von Woedtke, *Plasma Phys. Control. Fusion*, 2017, **59**, 014031.

309 K. Wiles, *Med. Xpress*, 2019.

310 N. Schmid, A. P. Eichenberger, A. Choutko, S. Riniker, M. Winger, A. E. Mark and W. F. Van Gunsteren, *Eur. Biophys. J.*, 2011, **40**, 843–856.

311 H. J. Berendsen, P. J. Postma, W. F. van Gunsteren and J. Hermans, *Interaction Models for Water in Relation to Protein Hydration*, Springer, Dordrecht, 14th edn., 1981.

312 D. Poger and A. E. Mark, *J. Chem. Theory Comput.*, 2010, **6**, 325–336.

313 D. Poger, W. F. V. A. N. Gunsteren and A. E. Mark, *J. Comput. Chem.*, 2009, **31**, 1117–1125.

314 T. J. Piggot, D. A. Holdbrook and S. Khalid, *J. Phys. Chem. B*, 2011, **115**, 13381–13388.

315 T. J. Piggot, Á. Piñeiro and S. Khalid, *J. Chem. Theory Comput.*, 2012, **8**, 4593–4609.

316 J. F. Nagle, *Biophys. J.*, 1993, **64**, 1476–1481.

317 N. Kučerka, J. F. Nagle, J. N. Sachs, S. E. Feller, J. Pencer, A. Jackson and J. Katsaras, *Biophys. J.*, 2008, **95**, 2356–2367.

318 J. Pan, S. Tristram-Nagle, N. Kučerka and J. F. Nagle, *Biophys. J.*, 2008, **94**, 117–124.